Cranfield University

David Anthony Darbyshire

Development of Lead-Free Thin-Film Dielectrics for Capacitor Applications

School of Applied Sciences
Microsystems and Nanotechnology Centre

PhD Thesis

Cranfield University

School of Applied Sciences
Microsystems and Nanotechnology Centre

PhD Thesis

2011

David Anthony Darbyshire

Development of Lead-Free Thin-Film Dielectrics for Capacitor Applications

Supervisors: Dr Paul B Kirby
Dr Qi Zhang

Academic Years: 2007-2010

Thesis submitted for the degree of Doctor of Philosophy

Abstract

This PhD project aims to develop lead-free thin-film dielectric materials for fixed value, voltage tunable and high-k zipping variable capacitors using growth techniques that can be scaled for silicon batch fabrication. The thesis specifically details the growth and characterisation of barium zirconate titanate (BZT) and bismuth zinc niobate (BZN) dielectric thin films. Fixed value and tunable capacitors have been realised through the use of low and high permittivity dielectric thin film materials in both the amorphous and crystalline states. Planar devices fabricated using BZT and BZN dielectric thin films were grown by sol-gel and RF magnetron sputtering, respectively. The effects of different bottom electrodes were also investigated. Capacitors in a metal-insulator-metal (MIM) [metal-ferroelectric-metal (MFM) for BZT] structure have been fabricated to characterise the dielectric films at low frequency to 300 kHz.

Finding alternative higher permittivity dielectrics to SiO_2 for various capacitor and isolation layer applications can be a challenge. Trials were conducted that looked at using amorphous BZT, nanocrystalline BZN and crystalline BZN as a low-k dielectric insulator. Dielectric constants of ~50 were typical for BZN, but much lower permittivity was achieved for amorphous BZT, between 2 and 15 when deposited on Au/Cr bottom electrode. Breakdown strength of amorphous BZT film grown on $Pt/Ti/SiO_2/Si$ substrate was extremely high (close to 2.0 MV/cm) and far superior to that of nanocrystalline BZN (0.25 MV/cm). The dielectric strength of BZN was increased to 0.56 MV/cm when BZN was grown on a BZT seed layer due to a change in the microstructure of the BZN film from granular to columnar. The development of a suitable dielectric (BZN) for use with polymer substrate was also investigated and MIM capacitors fabricated by sputter deposition. Preliminary results for nanocrystalline BZN thin film growth on Au coated liquid crystal polymer (LCP) substrates appeared encouraging with dielectric constant of 27 and loss 0.005.

Crystallised BZT thin films can be used to good effect as lead-free dielectric material in tunable devices. For BZT in the ferroelectric phase, excellent tunabilities of 80% were realised when deposited on platinised silicon. This was found not to be the case for BZT in the paraelectric phase where tunabilities tended to be ~60% at best. The dielectric properties of MIM thin-film capacitors can be enhanced by the use of lower resistivity bottom electrode such as Au. Previous research has failed to demonstrate growth and crystallisation of BZT on Au electrode due to the fact that it is technically difficult using the sol-gel method; films tend to crack after annealing. This research found that films can be stabilised, and the tunability of BZT thin film in the paraelectric phase can be increased significantly, by growing BZT on Au bottom electrode using a BZN buffer layer 25 nm thick. A peak tunability of 83% was achieved while maintaining a low dielectric loss of ~0.01. Novel BZT multilayer structures incorporating both ferroelectric and paraelectric compositions were grown on platinised silicon resulting in a tunability of 82% at a bias field 600 kV/cm.

Based on the success of growing good quality thin BZN films on Au bottom electrode, it was decided to use thin-film BZN as one of the high-k dielectrics in the zipping varactor, a miniature MEMS tunable device. Trials were performed that looked at depositing BZN on thick (800 nm) Au coated silicon and glass. This was successful on small sample pieces but failed when scaled up to full device wafer size (100 mm diameter) due to Au/Cr diffusion into the dielectric layer. To overcome this, a 300 nm thick BZN film was sputter deposited on Pt/Ti and Pt/Au/Ti coated 100 mm glass device wafers and processed to form the dielectric layer and bottom electrode of the capacitor. As part of the process the BZN layer required patterning. Wet etching of the small features was inappropriate due to undercutting of the structure; an anisotropic dry etching process was therefore necessary. Prior to this work there had been no reported activity on the dry etching of BZN, only wet etched using a 1:10 HF-deionised H_2O solution. In this work, thin-film BZN was reactively ion etched in CHF_3/Ar plasma at an etch rate of ~6 nm per minute with excellent selectivity over platinum of 6:1. Fabrication of the curved top electrode, final assembly and device testing were undertaken by a group at Imperial College London who were collaborators on a work programme entitled, “Integrated Functional Materials for System-in-Package Applications”.

Acknowledgements

First and foremost, I wish to thank Dr Paul Kirby and Dr Qi Zhang for their supervision of this PhD, for guidance and support, and for giving me the freedom to develop my own ideas. Also, without their timely encouragement and patience while undergoing personal difficulties, and for subsequently organising a generous extension, it would have been impossible for me to finish the research and write this thesis.

Appreciation goes to Dr Sue Impey (subject advisor) and Dr Bruce Jefferson (independent chairman of the thesis committee) for very frank and constructive criticism where necessary at and following my MPhil to PhD transfer review (first annual review) and during and after the second annual review.

Many thanks are due also to Arne Luker for much assistance at the outset of the experimental work; to Rob Wright and Carlos Fragkiadakis for practical assistance and many useful technical discussions; to Dr Chris Shaw, Andrew Stallard and Matthew Taunt for their technical support particularly at times when there were equipment reliability issues; to Christine Kimpton for invaluable assistance with scanning electron microscopy (SEM) and atomic force microscopy (AFM); to Dr Matthew Kershaw and Andrew Dyer for x-ray photoelectron spectroscopy (XPS) and focused ion beam (FIB) analysis; to Jane Hubble for inductively coupled plasma – mass spectrometry (ICP-MS); and not least to Enza Giaracuni for her constant and at times patient administrative support.

Grateful acknowledgement is made to the Engineering and Physical Sciences Research Council (EPSRC) for project sponsorship and financial support.

Finally, I would like to thank my family (wife Leigh, daughters Gemma and Kayte) for the support and encouragement throughout this process.

Table of Contents

List of Figures

List of Tables

1 Introduction

Although the first ferroelectric materials were developed as far back as the early 1940s with barium titanate ($BaTiO_3$), then lead zirconate titanate (PZT) in the 1950s, in more recent years considerable progress has been made in the characterisation and development of a range of dielectric materials including other lead- and barium-based oxides [1.1]. This has resulted in a plethora of published research, not only in the materials themselves, but also in the applications, including high dielectric constant capacitors, non-volatile memories, electro-optic devices, microelectromechanical systems (MEMS) and tunable microwave devices, to mention just a few [1.2-1.7]. Much of the underlying physics and modelling associated with the materials and devices is now well understood and documented [1.8-1.13]. Finding a nugget of new knowledge is not necessarily straightforward.

In the production of planar type capacitors it is possible to employ all forms of dielectric material including bulk ceramic, thick film, thin film, single crystal and polycrystalline. For planar device technology there are advantages to selecting a thin film approach rather than making use of thick film or bulk ceramic, particularly at high frequencies. For example, the use of thick ferroelectric films in planar microwave devices result in higher loss and worse tunability compared to the use of thin ferroelectric films. At microwave frequencies only a thin upper layer of the thick ferroelectric film contributes to the tuning. In effect, the thick film behaves as a non-tunable capacitance (bulk of thick film) connected in parallel with the tunable part of the film (thin upper layer) [1.3]. In addition, there are geometrical constraints imposed on the use of thick films compared to thin films for components which have micro- and nano-scale linear dimensions. Other attractive features of employing thin films in tunable applications are the low tuning voltages, relatively low production costs and simplicity of fabrication (e.g., when using techniques such as sol-gel thin film deposition). The simplest tunable component based on thin dielectric films is the parallel-plate capacitor. This is a metal-insulator-metal (MIM) [metal-ferroelectric-metal (MFM) for BZT (5/95)] structure and is ideal for the characterisation of the dielectric material.

A variety of approaches can be adopted for depositing thin and thick film dielectric materials using either, vapour phase processes including evaporation, RF magnetron sputtering, ion beam sputtering, pulsed laser deposition (PLD), metal-organic chemical vapour deposition (MOCVD), spray pyrolysis and electrophoresis, or liquid phase processes such as liquid phase epitaxy and chemical solution deposition (CSD). The use of PLD has increased significantly in recent years for depositing highly ordered ferroelectric films from which multilayer superlattice structures have emerged [1.14]. However, this is not a practicable method of depositing thin films over large area substrates, where sample size is typically restricted to a few square millimetres. According to much of the current literature, the preferred techniques for fabricating BZT and BZN dielectric thin films on large area substrates are CSD and sputtering, respectively.

The work reported on in this thesis focused specifically on two dielectric materials, barium zirconate titanate (BZT), a ferroelectric perovskite material, and bismuth zinc niobate (BZN), a non-ferroelectric cubic pyrochlore material. The aim has been to improve capacitor performance by attempting to replicate bulk dielectric properties in thin film form. The target specifications for these thin film materials are high permittivity (>100), low dielectric loss ($<10^{-2}$) and excellent electric field tunability (>40%). The tunability is roughly proportional to the dielectric constant. In order to control the material crystallography and microstructure, sol-gel and RF magnetron sputtering were the preferred methods for depositing thin-film BZT and BZN, respectively. Critical links between process parameters, microstructure and electrical performance have been established. Electrical performance of thin-film capacitors as a function of a range of material properties was investigated; these include, the use of seed layers, buffer layers, and multilayer structures involving BZT and BZN. An increased activity in the development of multilayer/heterolayer structures as tunable dielectrics [1.15-1.27] is evident especially those that incorporate perovskite material. Enhancement of electrical properties through the application of multilayer or composite structures has been demonstrated by other researchers in the case of BZT [1.28, 1.29] and BZN [1.30-1.35].

This thesis will consider the development of dielectric thin-film capacitors using BZT and BZN in three main applications (described below). In each of these application areas problems arise that require a research solution, the strategy for which is outlined in chapter 2. The solution in each case results in a significant contribution to knowledge. Note, the terms permittivity and dielectric constant are used interchangeably throughout the thesis.

- *Fixed value, linear dielectric capacitor*. Ferroelectric materials are of increasing importance to the silicon processing industry since alternative materials to SiO_2 with a higher dielectric constant are required [1.36]. These alternative materials are particularly useful for various capacitor and isolation layer applications in microelectronics. To fulfil this requirement, fixed value, amorphous BZT thin-film capacitors were fabricated and tested on a trial basis. The objective was to establish sufficiently low temperature processing of these alternative dielectric materials to ensure compatibility with silicon integrated circuit technology, such as in dynamic random access memories (DRAMs) or as a transistor gate dielectric in logic devices. To this end, thin-film BZN parallel-plate capacitors were also trialled since very low temperature (300^oC) crystallisation of the BZN could be achieved, resulting in material with a very high dielectric strength. The application of these dielectric materials will make it possible to use thicker insulating layers than currently used when employing SiO_2. The two-step sputtering deposition method was also trialled for BZN and proved successful as a technique for varying and controlling the dielectric constant of the thin films.

- *Voltage tunable capacitor*. In this programme of research the focus of attention was on developing barium zirconate titanate (BZT) as a lead-free ferroelectric material for tunable capacitors. The material is characterised by large dielectric constant, high dielectric tunability and low dielectric loss, even though high tunability generally leads to a high loss. This raises the research question as to whether improved capacitor performance can be realised in either the ferroelectric or paraelectric phase. It has been demonstrated that excellent tunability of planar capacitors can be achieved at low frequency for thin BZT films in the ferroelectric phase. However, the problem of how to improve the tunability of BZT in the paraelectric phase required a solution. This thesis highlights the growth of BZT thin film on Au bottom electrode made possible by the introduction of a BZN buffer layer. Improvement in the tunability of BZT in the paraelectric phase, to values comparable to those in the ferroelectric phase, has been demonstrated. An improvement in capacitor performance at low frequency can also be achieved using multilayer structures incorporating BZT of different compositions. This will be discussed, along with experimental evidence, in chapter 7 of this thesis. It is anticipated that many of these improvements to capacitor performance at low frequencies can be realised at higher frequencies and that this should be pursued as part of a further work programme.

- *High-k zipping varactor.* The main challenge was to find a dielectric material with sufficiently high permittivity and dielectric strength that allowed large capacitance variation in the zipping device. The successful growth of thin BZN films on Au bottom electrode was the impetus for developing a zipping variable capacitor that utilised a BZN dielectric layer. By using a thick (800 nm) Au bottom electrode the contact resistance can be significantly reduced to ~1Ω. The growth of BZN on thick Au was successful for small sample pieces but failed to work when scaled up to full device wafer size (100 mm diameter) due to Au/Cr diffusion from the bottom electrode into the BZN film. Other electrode metals were trialled with success and a new, improved heat treatment process enabled good quality, defect free, thin BZN films to be used as dielectric layer. The films were characterised by high permittivity (~100), low loss (0.0015) and very high dielectric strength (2.0 MV/cm). The high breakdown strength meant that larger device activation voltages could be supported. A further success, and not reported elsewhere, was the dry etching of BZN using an CHF_3/Ar gas plasma.

2 Research Strategy

2.1 Defining the Research Problem

Much of research involves solving a practical problem for which the solution is not obvious. This raises research questions that help to define a research problem. The research problem is motivated by incomplete knowledge and must be better understood if a solution is to be found. The research process is represented graphically in figure 2.1[2.1].

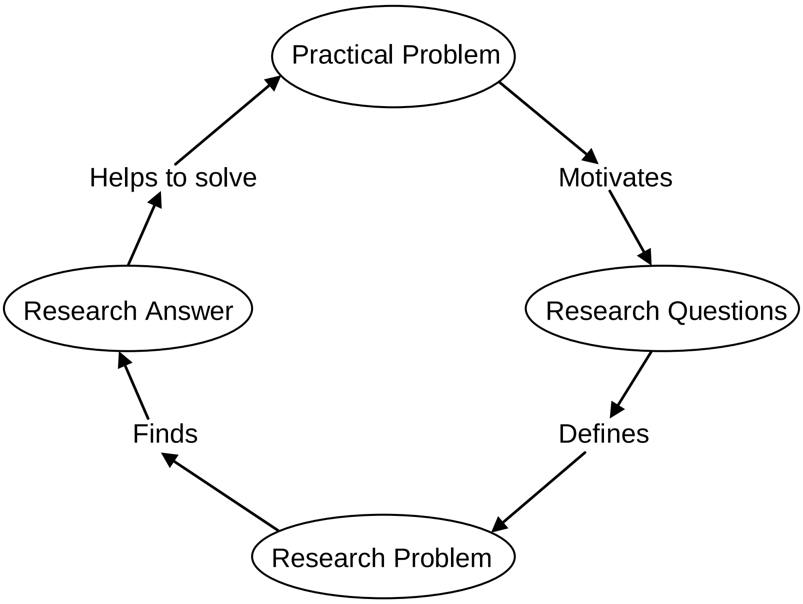

Figure 2.1 Research process involved in the solution of a practical problem [2.1].

Throughout this research there has been more than one problem to solve and often a new problem has arisen while trying to solve an existing one. This thesis is looking at solving problems in each of three main areas that are primarily applications driven. These areas are summarised in the introduction, and the experimentation, results and discussion developed to find research answers and to help solve the practical problems are presented in chapters 6 to 8.

Consider now an example of a practical problem related to improving the dielectric properties of BZT, a ferroelectric material for application to parallel-plate tunable capacitor. The challenge is associated with sol-gel derived BZT material in the paraelectric phase when grown on platinised silicon. Although the dielectric loss of thin film material in the paraelectric phase is lower than in the ferroelectric phase, the tunability is also lower. This has implications for the performance of tunable capacitor especially at high frequencies. For tunable devices the ratio of tunability to loss referred to as the figure of merit (FOM) must to be maximised. The following is an example taken from this thesis of implementing a research strategy from practical problem to research answer.

1. **Practical problem**: Reduced tunability of BZT thin film in the paraelectric phase when grown on platinised silicon using the sol-gel method.

2. **Research questions**: How can the tunability be increased? What have other researchers done, if anything? What methodology to use? Can the BZT thin film be grown on a lower resistivity bottom electrode material such as gold? What are the advantages? Are there fabrication issues?

3. **Research problem**: Not possible to grow and crystallise sol-gel derived BZT thin films directly on Au coated silicon due to stress in the films and Au/Cr diffusion. Requires a research solution.

4. **Research answer**: Use a very thin buffer layer inserted between the bottom electrode and dielectric layer. Thin-film BZN shown to be successfully grown and crystallised on Au without the problem of diffusion. A significant increase in tunability (60% to 82%) of BZT thin film in the paraelectric phase achieved when grown on Au coated silicon with intermediate 25 nm thick BZN buffer layer.

This basic research process was employed to define and solve other problems encountered throughout the work programme.

2.2 Research Objectives

Each of the research objectives relate to the dielectric materials BZT and BZN developed throughout this work, but are primarily applications rather than materials driven. The application lays the basis for material selection; examining the suitability of both ferroelectric (BZT) and non-ferroelectric (BZN) materials for application to fixed value, tunable and zipping variable capacitors. A research study of the important material parameters that determine dielectric properties and their dependence on growth conditions for both sol-gel and sputtering is presented. Although the materials investigation involved established materials, the aim was to improve capacitor performance by developing new processes using these materials. In line with this the primary research objectives were:

- To develop and characterise lead-free thin-film dielectrics as part of the material feasibility study. To characterise both amorphous and crystalline BZT and BZN thin films in terms of material and dielectric properties for use in fixed value and tunable capacitors.

- To develop the sol-gel and RF magnetron sputter deposition processes together with new thermal treatment procedures to control the material crystallography and microstructure more precisely.

- To identify critical links between process parameters, microstructure and electrical performance (e.g. the influence of annealing method and temperature on thin film crystallisation and dielectric loss).

- To address the fundamental issue of whether it is preferable to use the ferroelectric material (i.e. BZT) in its paraelectric or ferroelectric phase for tunable thin-film capacitor applications at low frequency.

- To investigate electrical performance of thin-film capacitors as a function of a range of material properties and processes including, for example, the use of seed and buffer layers and multilayer structures.

- To model the dielectric properties of bilayers (e.g. BZT thin film and BZN buffer layer) and multilayer BZT structures of two components.

- To develop a suitable method for processing BZN dielectric thin film and bottom electrode metallisation on glass device wafer as part of zipping varactor fabrication. Perform dry etching of thin-film BZN for the first time.

2.3 Contributions to Knowledge

An original contribution to knowledge has been achieved through the verification of key hypotheses. Experimental evidence is presented in chapters 6 to 8 of this thesis and a summary of the main features and achievements is given at the end of each of these sections. Significant contributions are listed below. The appropriate sub-sections within the thesis where details of the contributions can be found are shown in parenthesis.

- The two-step sputtering deposition method can be used to control the microstructure and dielectric constant of thin-film BZN (sub-section 6.3.4).
- Amorphous BZT is a suitable low-k dielectric material for insulator application when sol-gel grown on Pt and Au coated silicon substrates (sub-section 6.3.6).
- Sputtered thin BZN buffer layer improves dielectric strength and tunability of sol-gel derived BZT thin films in the paraelectric phase when grown on Au coated silicon - a hybrid processing method (sub-section 7.3.6).
- Sol-gel deposited BZT thin-film multilayer structures lead to improved dielectric properties compared to BZT single component films when grown on platinised silicon (sub-section 7.3.7).
- A novel low temperature, hybrid, two-stage annealing method for improved wafer-scale fabrication results in large area, defect free, dielectric films (sub-sections 8.4.1and 8.4.3).
- BZN thin films can be anisotropically dry etched using fluorine chemistry with good selectivity over photoresist and metal layers. BZN reactively ion etched (RIE) for the first time by using CHF_3/Ar reactive gas plasma (sub-section 8.4.4).

Successful outcomes were realised by careful planning and experimental rigour.

3 Background and Literature Review

This chapter will highlight the background information required to better understand the materials and processes used in the fabrication of dielectric thin-film capacitors of the types discussed in this thesis. A literature review will help to identify key areas of research to which a significant contribution to knowledge can be made.

3.1 Crystal Structure and Phase Transitions of BZT

3.1.1 Structural Properties of BZT

Barium titanate ($BaTiO_3$) material has an ABO_3 perovskite structure based on the prototype crystal calcium titanate ($CaTiO_3$). Ionic substitutions of barium or titanium in barium titanate ($BaTiO_3$) give rise to some interesting behaviour. The material characteristics are related to the type of ionic substitutes and to the degree of substitution. For example, barium strontium titanate $(Ba,Sr)TiO_3$ (BST), where the A-site Ba^{2+} ion in $BaTiO_3$ is substituted by the Sr^{2+} ion, exhibits enhanced dielectric properties such as high dielectric constant and low loss. As an alternative to BST, barium zirconate titanate $Ba(Zr,Ti)O_3$ (BZT), has received attention since some interesting dielectric properties related to the ferroelectric-to-paraelectric phase transition can be realised by the substitution of titanium (Ti) in the B site of $BaTiO_3$ by zirconium (Zr). Since BZT has lower dielectric loss than BST, it is an alternative choice in tunable microwave device applications. It is also recognized that Zr^{4+} is chemically more stable than Ti^{4+}, an important property in the fabrication of ceramic capacitors [3.1].

With the substitution of Zr^{4+} for Ti^{4+} in $BaTiO_3$ we have a complex perovskite system denoted as $A(B',B'')O_3$. In effect, the cation Zr^{4+} occupies the B site in the ABO_3 structure, where A is a monovalent or divalent metal (e.g., Ba^{2+} ion) and B is a tetravalent or pentavalent metal. Figure 3.1 shows an ordered perovskite unit cell in $A(B'_{0.5}B''_{0.5})O_3$. In the form $Ba(Zr_{0.5}Ti_{0.5})O_3$ the Zr^{4+} (B' ion) and Ti^{4+} (B" ion) are surrounded only by O^{2-} ions in an MO_6 octahedra arrangement so that no Zr^{4+} or Ti^{4+} ions are immediately adjacent to the divalent cation Ba^{2+}. In figure 3.1 the AB"O_3 (i.e. $BaTiO_3$) unit cell (Ba^{2+} ions at the cube corners) can be seen at the centre of the A(B'$_{0.5}$,B"$_{0.5}$)O_3 (i.e. $Ba(Zr_{0.5}Ti_{0.5})O_3$) unit cell. Naturally the B site is randomly occupied by either Zr^{4+} or Ti^{4+} ions due to the same valence states of Zr^{4+} and Ti^{4+} in BZT. However, Hotta *et al.* was able to control the order degree by means of superlattice techniques using the pulsed laser deposition (PLD) approach [1.14].

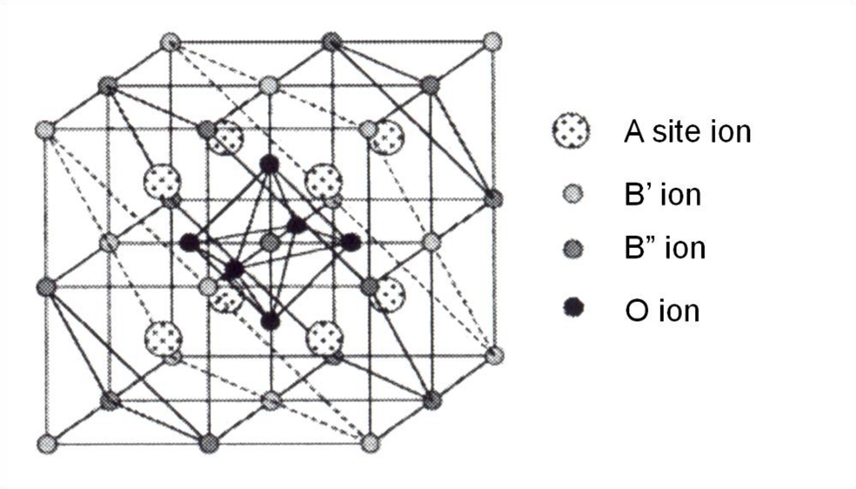

Figure 3.1 Complex perovskite crystal structure of order degree 100% [1.14].

The relaxor behaviour is very much dependent on the correct ordering of ion in the crystal. The B-site ions in $Ba(Zr,Ti)O_3$ are not normally ordered. In fact, for a mixture of ions (Zr and Ti) on one site there is evidence that these ions are randomly distributed. BZT films may contain paraelectric and ferroelectric mixed phases. Although it has been demonstrated that PLD can be used to control precisely the order degree state of BZT, the sol-gel approach can give good stoichiometric films through homogeneous mixing at the molecular level to form the sol. Other than controlling the order degree, there are distinct advantages of using sol-gel over PLD, and these have been highlighted in chapter 4.

3.1.2 Phase Transitions

Perovskite oxides such as $BaTiO_3$ readily form solid solutions with other oxides (such as $BaZrO_3$) so that ferroelectric materials with a variety of properties can be realised. In this study we substitute the isovalent cation Zr^{4+} for Ti^{4+} to form $Ba(Zr_xTi_{1-x})O_3$ thin films, where x can take the value 0 to 1. Hence, the composition can vary from $BaTiO_3$ (x=0) to $BaZrO_3$ (x=1) with interesting and varied room temperature dielectric properties. Barium zirconate ($BaZrO_3$) is paraelectric at all temperatures. The effect of isovalent impurity Zr^{4+} in $BaTiO_3$ material on the ferroelectric phase transition for x atomic% between 0 and 35 can be seen in the phase diagram (figure 3.2) [1.13].

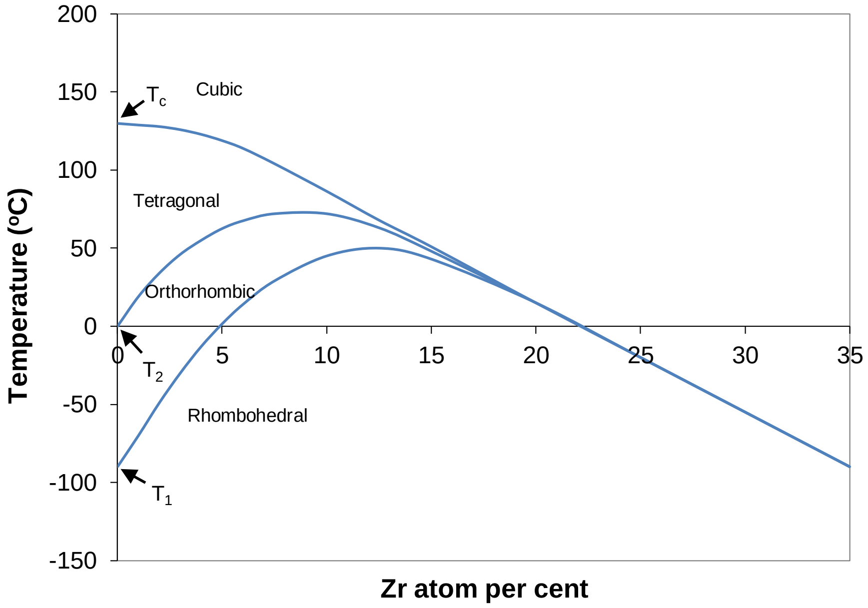

Figure 3.2 Phase diagram of $Ba(Zr,Ti)O_3$ for Zr at% of 0-35 and characteristic transition temperatures T_1, T_2 and T_c [1.13].

The introduction of impurities affects the crystallisation, and the dielectric and ferroelectric behaviour of the material. The properties of ferroelectric ceramics and thin films such as BZT can be modified by adjustments to the composition and microstructure. Substitution of alternative cations such as Zr^{4+} for Ti^{4+} can affect, for example, the transition temperature including the Curie point, domain wall motion, and crystallite size. As observed in the phase diagram for BZT (figure 3.2), the introduction of Zr^{4+} into the crystal structure effectively lowers the Curie point T_c. In normal ferroelectrics the Curie point marks a unique transition temperature at which the spontaneous polarisation falls to zero and the permittivity reaches a maximum. Below this temperature the material is ferroelectric and possesses a very high permittivity that varies with applied electric field and temperature. Above the Curie temperature the properties of the material change to those of a paraelectric (i.e., a normal dielectric) where the permittivity ε_r is reduced in accordance with the Curie-Weiss law:

$$\varepsilon_r = \frac{C}{T - T_c} \tag{3.1}$$

where C is the Curie-Weiss constant for a given material and T_c is the Curie point or temperature. Therefore ε_r reduces when $T>T_c$. Analysis of equilibrium behaviour near a phase transition is given by Landau theory [1.9].

In figure 3.2 the phase transition temperatures are displayed for Zr substitution $0<x\leq0.35$. At x=0, the material takes on the characteristic phase transitions commonly associated with $BaTiO_3$ as shown in figure 3.3 (P denotes the spontaneous polarisation). The a- and c-axis lattice constants for the three BZT compositions under investigation are given in appendix 1. Initially, for low Zr content, rhombohedral to orthorhombic and orthorhombic to tetragonal phase transition temperatures (T_1, T_2) increase; tetragonal to cubic phase transition temperature (T_c) decreases. The three transition temperatures then move closer until at ~20 at% Zr they merge near to room temperature. The phase transition temperature T_c continues to be suppressed with increasing Zr content.

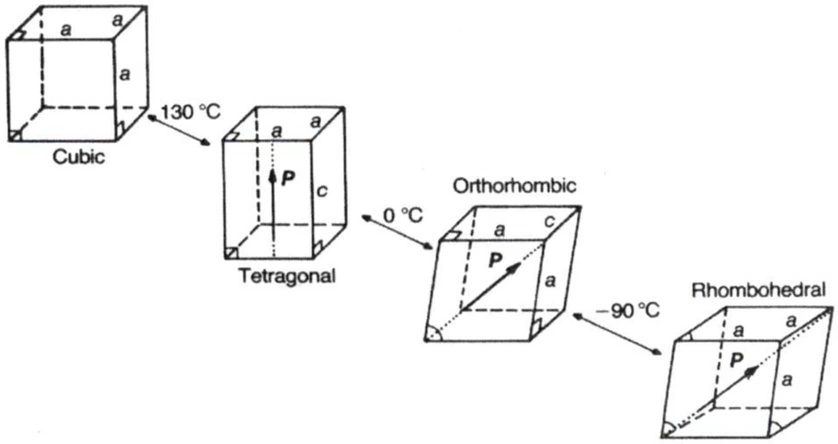

Figure 3.3 Unit-cell distortions associated with $BaTiO_3$ phase transitions [3.2].

The properties of BZT ceramics are composition dependent. When ions such as Zr^{4+} are substituted into the crystal lattice of $BaTiO_3$ there is a change from normal ferroelectric ($BaTiO_3$) to relaxor ferroelectric (relaxors). At room temperature, normal ferroelectric behaviour is observed for $0<x<0.15$, diffuse phase transition for $0.15<x<0.25$, and relaxor-like behaviour for $x\geq0.25$. Diffuse phase transitions, an intermediate state between ferroelectric and relaxor behaviour, are characterised by phase transitions showing broad capacitance maxima. Ferroelectrics with disordered structure (in particular B-site cation disorder) exhibit diffuse dielectric phase transition properties. The spontaneous polarisation of a relaxor does not abruptly fall to zero at T_c but decays to zero gradually. Relaxor ferroelectrics are characterised by a significant change in permittivity with frequency at temperatures in a transition region (Curie region). Frequency-relaxor behaviour results from dipole reorientation time dependency. The permittivity maintained large (ε_r~10^5) in a broad temperature interval makes these materials useful in high permittivity capacitors, sensors and transducers.

The composition $Ba(Zr_{0.05}Ti_{0.95})O_3$ was selected initially for this research programme since the material is ferroelectric at room temperature. Other compositions chosen were $Ba(Zr_{0.20}Ti_{0.80})O_3$ at or around a morphotropic phase boundary, and $Ba(Zr_{0.35}Ti_{0.65})O_3$ paraelectric at room temperature. The material contains a mixture of Ti^{4+} rich polar regions (nanopolar clusters of $BaTiO_3$) and Zr^{4+} rich regions ($BaZrO_3$). With low Zr content, the volume fraction of polar regions predominates. As the Zr content increases, the volume fraction of the polar regions is progressively reduced.

3.2 Crystal Structure of BZN

BZN ($Bi_{1.5}Zn_{1.0}Nb_{1.5}O_7$) is a non-ferroelectric pyrochlore material with the general composition $A_2B_2O_7$ and more specifically $A_2B_2O_6O'$ where the O' is bonded only to the A site (i.e. two different networks A_2O' and B_2O_6). The B_2O_6 framework consists of BO_6 octahedral sharing vertices. Within the pyrochlore family of oxides of stoichiometry $A_2B_2O_7$, A is a divalent or trivalent metal and B is a tetravalent or pentavalent metal. BZN has the cubic pyrochlore structure based upon the cubic fluorite structure (NaCa)(NbTa)O_6F/(OH). Since $Bi_{1.5}Zn_{1.0}Nb_{1.5}O_7$ exhibit a cubic pyrochlore structure Zn ions can occupy both the A and B sites [3.3]. Therefore, in the case of BZN we have the general formula $(Bi_{1.5}Zn_{0.5})(Zn_{0.5}Nb_{1.5})O_7$. It is thought that the B site is occupied first and that Bi and Zn are randomly mixed on the A site. Hence, a deficiency of zinc can result in vacancies at the A site. This reduces the polarisation under bias which in turn decreases the tunability. It is therefore important to sputter deposit the thin films from a stoichiometric $Bi_{1.5}Zn_{1.0}Nb_{1.5}O_7$ ceramic target. The BZN composition $(Bi_{1.5}Zn_{0.5})(Zn_{0.5}Nb_{1.5})O_7$ is also favoured for another reason. According to Wang *et al*. the Bi^{3+} occupies the A site due to its large ionic radius (1.17 Å), the Nb^{5+} ion occupies the B site due to its small radius (0.64 Å) and the Zn^{2+} can occupy both A site and B site because of its medium radius (0.9 Å) [3.4]. A detailed description of oxide pyrochlores is presented in a review by Subramanian *et al.* [3.5]. From figure 3.4, the pyrochlore structure can be seen based on corner shared BO_6 octahedra. The centre of the hexagons contain overlapping projections of one A cation and two O’ anions in the AO_8 polyhedron. Other descriptions of the structure have been proposed by various authors including a description of the ideal crystal structure of pyrochlore based on two interpenetrating networks of BO_6 octahedra and A_2O' chains (figure 3.5).

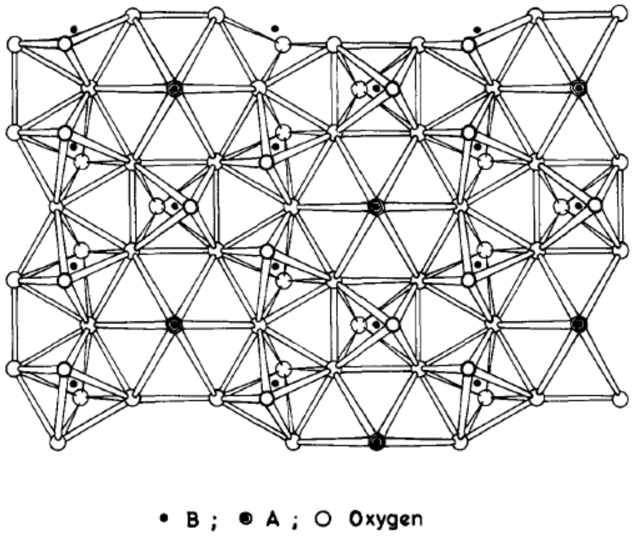

Figure 3.4 Pyrochlore structure showing the corner shared BO_6 octahedra in a zig-zag arrangement [3.5].

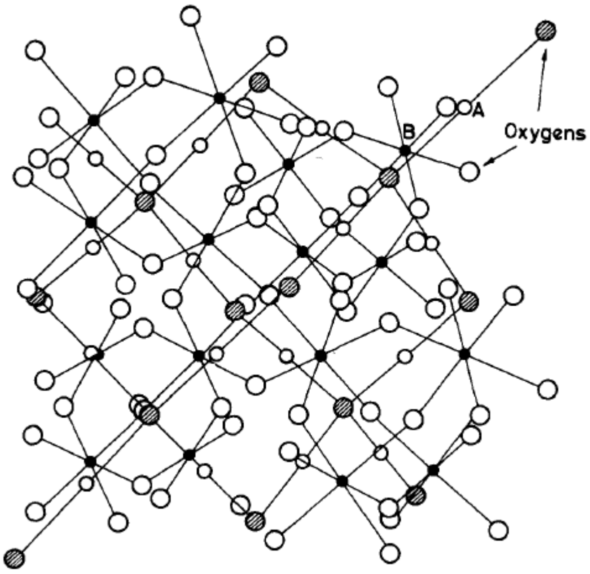

Figure 3.5 Pyrochlore structure based on two interpenetrating networks of BO_6 octahedra and A_2O' chains [3.5].

Although perovskite and pyrochlore structures both possess corner shared BO_6 octrahedral network, in perovskite the octahedra are arranged in a linear chain, whereas, in the pyrochlore structure the octahedra are aligned in a zig-zag arrangement, as clearly seen in figure 3.4.

3.3 Materials Research Review

3.3.1 Barium Zirconate Titanate (BZT)

Previous studies of BZT have shown that thin films of the material can be prepared using chemical solution deposition (CSD) [3.1, 3.6-3.17], sputtering [3.18-3.25] or pulsed laser deposition [3.26-3.28]. In the case of CSD (i.e. the sol-gel method), the starting materials are commonly barium acetate, zirconium isopropoxide and titanium isopropoxide. Substrates are generally Pt coated silicon ($Pt/Ti/SiO_2/Si$) although buffer layers or conductive oxide electrodes such as $LaNiO_3$ [3.9, 3.25] and lanthanum strontium manganite $LaSrMnO_3$ [3.28] are sometimes used. Thin films are invariably grown by sol-gel process by spin-coating several layers. Each layer is spun at ~ 3000 rpm for 20-30 seconds giving a layer thickness of a few 10s nm. Pyrolysis and annealing of individual layers is performed in air at temperatures of between 300°C and 700°C for 5 to 10 minutes. Since perovskite material often first form pyrochlore phases a final annealing at >700°C for 10–30 minutes takes place to ensure the equilibrium perovskite phase is achieved. In some cases this annealing is performed in either an O_2 atmosphere or in flowing O_2. Final film thickness is typically 300 nm to 500 nm. Results in terms of achievable dielectric constant and tunability are encouraging. Dielectric constants of between 200 and 300 have been achieved for films deposited by CSD and sputtering, and as high as 450 for films grown using PLD. The tunability of the material can be significantly increased by increasing the annealing temperature. For example, a tunability of 76% and a loss tangent of 0.0078 have been obtained for films deposited by RF magnetron sputtering at an increased annealing temperature of 1100°C [3.20, 3.21]. The influence of substrate temperature on the microstructure and dielectric properties of sputtered BZT thin films was investigated by Choi *et al*. [3.19].

Much has also been published on the properties of bulk ceramic and thick film BZT material prepared by solid-state synthesis [3.29-3.43]. Although this fabrication route is not particularly relevant to the thin film process, it is useful to compare the properties of thin films with those of bulk material. Generally, thin films exhibit lower dielectric constant and tunability and higher dielectric loss than bulk material of a similar composition. Ideally want the dielectric properties of the thin-film BZT to replicate those of bulk material, although with BZT this is difficult. For example, dielectric constant is typically an order of magnitude or so larger for bulk ceramic than it is for thin film. Some results obtained by Tang *et al.* for BZT bulk material are presented in table 3.1 [3.40]. For BZT ceramic of composition $Ba(Zr_{0.20}Ti_{0.80})O_3$ a peak tunability of 86% was achieved at a low bias field of 20 kV/cm. The tunability measured at room temperature (300 K) decreased with increasing Zr content. Although for $Ba(Zr_{0.25}Ti_{0.75})O_3$ the tunability was reduced (58%) compared to $Ba(Zr_{0.20}Ti_{0.80})O_3$, the figure of merit (FOM) defined as tunability/tanδ was 135, considerably higher than FOMs achieved for thin-film BZT, 30-40 typically. A FOM of 135 equated to a dielectric loss of 0.4%. Also, for thin-film BZT it is necessary to apply higher electric fields (100s kV/cm) in order to obtain comparable tunability to that of bulk material.

Table 3.1 Room temperature (300 K) tunability and figure of merit (FOM) of four bulk ceramic samples measured at an applied electric field of 20 kV/cm and at a frequency of 10 kHz [3.40].

	BZT20	BZT25	BZT30	BZT35
Tunability (%)	86	58	26	19
FOM	80	135	104	76

Within the literature, researchers have examined the effect of varying the Zr content of $Ba(Zr_xTi_{1-x})O_3$, (BZT, x = 0, 0.05, 0.08, 0.15, 0.18, 0.20, 0.25, 0.30, 0.35). Gao *et al*. [3.7] showed the effect of varying frequency 1 kHz to 1 MHz on the dielectric constant and loss of thin BZT films for different BZT compositions (figure 3.6a). BZT films were grown on $Pt/Ti/SiO_2/Si$ substrates by the sol-gel process. Above 100 kHz a significant deterioration in the dielectric constant and loss can be observed for films with reduced Zr. At a measured frequency of 100 kHz, Gao *et al*. plotted dielectric constant and tunability as a function of Zr content for thin-film BZT (figure 3.6b). They found that a Zr content of 15 at% gave the highest dielectric constant of ~ 350 and a peak tunability of ~ 47%.

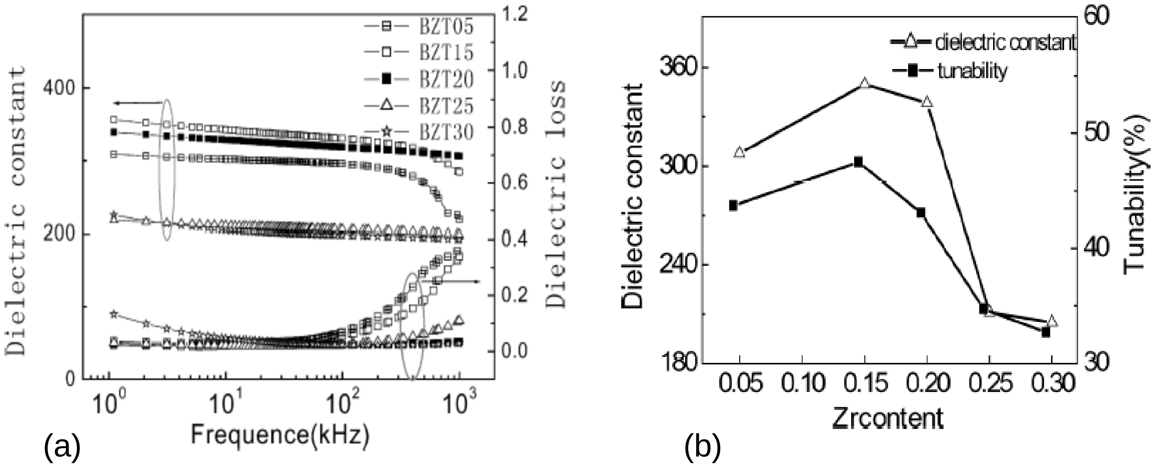

(a) (b)

Figure 3.6 (a) Variation in dielectric constant and loss with frequency for BZT thin films of different Zr content and (b) dielectric constant and tunability as a function of Zr content for BZT thin films measured at a frequency of 100 kHz [3.7].

Compare the results obtained by Gao *et al.* with those obtained by Zhai *et al*. [3.9] who deposited BZT thin film material on lanthanum nickelate ($LaNiO_3$) coated silicon substrates by the sol-gel process (table 3.2). Reduced dielectric loss and improved tunability is very evident.

Table 3.2 Measured dielectric constant (ε), dielectric loss (tan δ), tunability (%) and figure of merit (K) of BZT thin films of different Zr content [3.9].

BZT	$\varepsilon(0)$	ε (400 kV cm^{-1})	tan δ	Tunability (%) 1 MHz	K
$x = 0$	230	97	0.019	58	30
$x = 0.05$	332	120	0.017	64	38
$x = 0.15$	284	120	0.017	58	34
$x = 0.35$	214	88	0.017	59	35

For thin films the focus of attention is on lower Zr content, where x = 0.05 to 0.35, typically. As the Zr content is increased this induces a reduction in the average grain size, decreases the dielectric constant, and maintains a low stable leakage current. It is reported that this is possible because the Zr^{4+} ion has larger ionic size (0.087 nm) than Ti^{4+} (0.068 nm). The substitution of Ti by Zr ions leads to an expansion in the unit cell [3.7]. Surface morphology of films also demonstrates sensitivity to Zr content. It is observed that the average grain size decreases significantly with the increase of the Zr content. With increasing Zr content films become dense and smoother. Zhai *et al*. showed that varying the concentration of the sol (0.3 M, 0.1 M and 0.05 M) had a significant influence on the crystallisation, microstructure and dielectric properties (figure 3.7) of $Ba(Zr_{0.35}Ti_{0.65})O_3$ (BZT) films [3.11]. It is evident that the grain size decreases and the films become dense as the sol concentration decreases. However, as the grain size decrease, switching in films is relatively difficult. At a concentration of 0.3 M cracking of the film is observed. For 0.3, 0.1 and 0.05 M solution-deposited BZT thin films a tunability of 58%, 46% and 45% was achieved at a frequency of 1 MHz, respectively. Microstructure and surface morphology of BZT thin films are studied by x-ray diffraction (XRD), scanning electron microscopy (SEM) and atomic force microscopy (AFM).

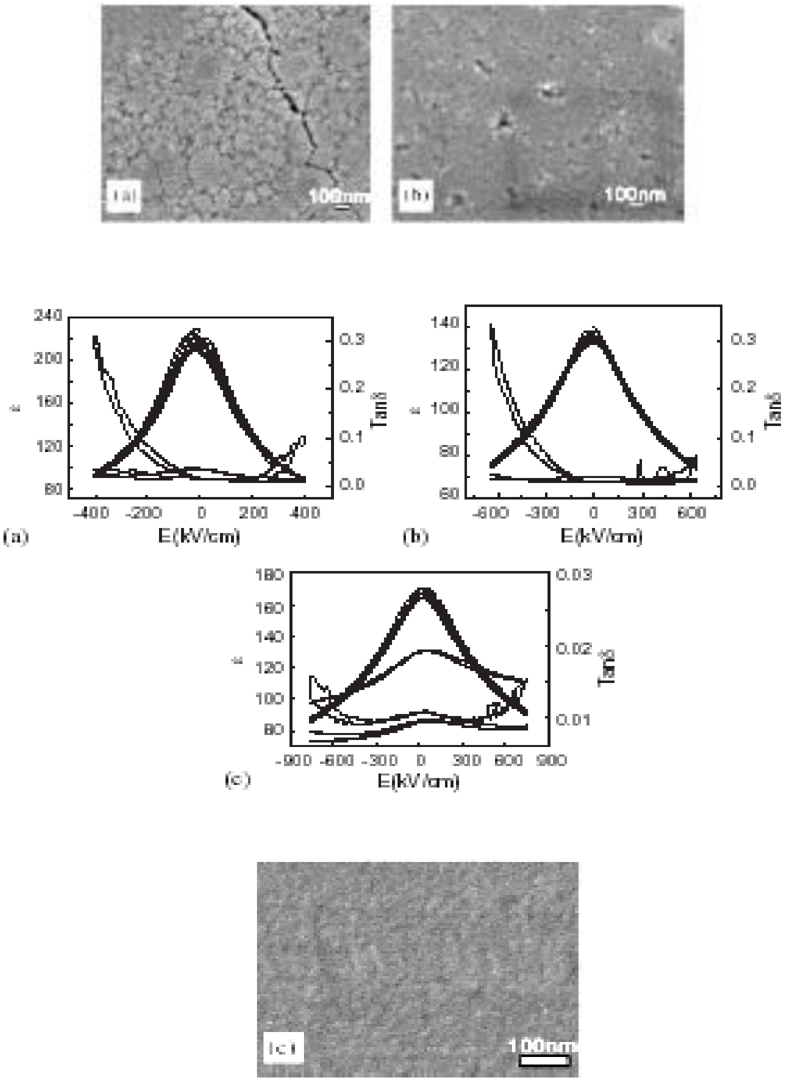

Figure 3.7 SEM micrographs of sol-gel deposited BZT thin films and corresponding variations in the dielectric properties as a function of applied electric field. Sol-gel deposited BZT thin films prepared from precursor solutions of (a) 0.3 M, (b) 0.1 M, and (c) 0.05 M concentration [3.11].

The influence of thickness on $Ba(Zr_xTi_{1-x})O_3$ thin films has also been reported [3.8]. For instance, permittivity is seen to decrease with decreasing film thickness. The dielectric properties of the ferroelectric thin films become closer to those of bulk material when the thickness of the films are greater than 2 μm. Dielectric properties of the thin films have been studied as a function of thickness, temperature and electric field [3.6].

Shy *et al.* have shown that an improvement in leakage current can be achieved using thin-film BZT compared to BST [3.25]. This is in part influenced by the substitution of Ti^{4+} ion with Zr^{4+} which expands the perovskite lattice and reduces electron “hopping” between Ti^{4+} and Ti^{3+} ions. The leakage current is also affected by the properties of the top and bottom electrodes. A low leakage current of ~10^{-9} A/cm^2 was obtained for BZT ceramics.

3.3.2 Bismuth Zinc Niobate (BZN)

Materials suitable for thin-film capacitors and ceramic resonators in microwave applications are required to have good dielectric properties (high tunability with low loss). Studies by various researchers have demonstrated that bismuth zinc niobate ($Bi_{1.5}Zn_{1.0}Nb_{1.5}O_7$) bulk ceramic and thin films have useful dielectric properties. Intense interest has developed in the integration of these tunable oxide materials with existing semiconductor technologies.

The preparation of ceramic samples by solid-state reaction and the associated material properties are documented [3.44-3.48]. By way of comparison, Cann *et al.* studied a number of polycrystalline bismuth-based pyrochlores with the general form $Bi_2(B^{2+}{}_{2/3}B^{5+}{}_{4/3})O_7$ and $Bi_2(B^{3+}B^{5+})O_7$ where B^{2+} is the element Mg, Cu, Zn or Ni, B^{3+} is Sc or In, and B^{5+} is Nb or Ta [3.48]. Du *et al.* found that compositional changes through the substitution of Zn^{2+} ions by Sr^{2+} ions in the A site of $(Bi_{1.5}Zn_{0.5})(Zn_{0.5}Nb_{1.5})O_7$, that gave $(Bi_{1.5}Zn_{0.5-x}Sr_x)(Zn_{0.5}Nb_{1.5})O_7$ (x = 0.1-0.5), significantly affected the dielectric properties [3.46].

Little appears to have been published on thin-film BZN prepared by the sol-gel procedure [3.49, 3.50] or by the metallo-organic decomposition (MOD) method [3.51, 3.52]. Ren *et al.* described a sol-gel procedure using precursors bismuth acetate in acetic acid and pyridine, zinc acetate dehydrate, and niobium ethoxide in 2-methoxyethanol [3.49]. Films were deposited onto platinised silicon by spin-coating and crystallised by RTA at between 550^{o}C and 750^{o}C. This resulted in films of cubic pyrochlore structure with dielectric constants up to 150 and loss tan $\delta < 0.01$.

A number of references relate to BZN thin film samples prepared by RF magnetron sputtering [3.53-3.62] and this would seem the preferred route. Lu *et al.* described a sputter system operating at a base pressure of $1x10^{-8}$ Torr and incorporating a stoichiometric 75 mm diameter $Bi_{1.5}Zn_{1.0}Nb_{1.5}O_7$ target [3.59]. Substrate material selected was Pt/Al_2O_3 and platinised silicon. Typical deposition system parameters chosen were an Ar/O_2 sputter gas mixture flow ratio of 85/15, gas pressure of 50 mTorr and a sputter power of 150 W. During deposition the substrate temperature was maintained at 300^oC. A final *ex situ* anneal to crystallize the film was performed at 750^oC for 5 minutes in air. The film thickness was of the order of 160 nm according to TEM measurement. Dielectric measurements of films on Si substrate (figure 3.8) measured at a frequency of 1 MHz showed very low losses ($\sim 5x10^{-4}$), high dielectric constant of ~220 and tunability of about 40% at an applied field of 1.2 MV/cm. The results in figure 3.8 demonstrates that films on platinised Si have higher zero bias dielectric constant, and therefore have a larger tunability, than films on platinised Al_2O_3. Although the tunability of BZN on Pt/Al_2O_3 was only ~28%, this was increased to ~55% by applying a maximum bias field of 2.4 MV/cm. It was found that the properties of BZN films were very close to those of bulk ceramics. This is in stark contrast with ferroelectric materials such as BZT where thin films have a significantly reduced dielectric constant compared to bulk material.

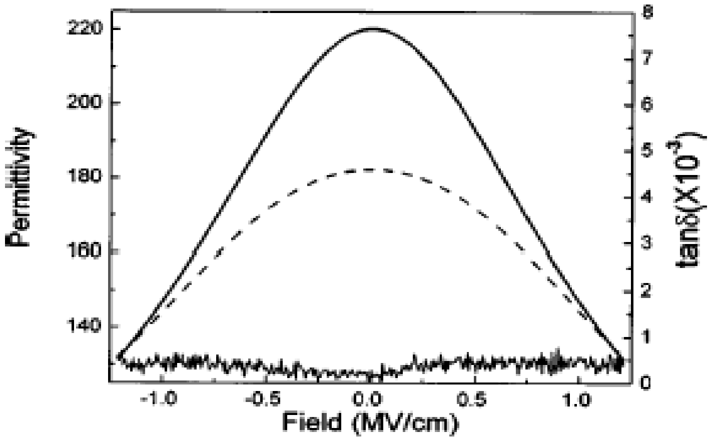

Figure 3.8 Permittivity and loss tangent as a function of DC bias field for BZN thin film on $Pt/SiO_2/Si$ (solid line) and Pt/Al_2O_3 (dashed line), measured at 1 MHz [3.59].

One of the main advantages of using sputtering over chemical solution deposition methods is that films can grow with a preferential orientation. Compared to BZN thin films deposited by RF magnetron sputtering, sol-gel derived BZN films have inferior dielectric properties. The peak zero bias dielectric constant for sputtered BZN films is higher than that achieved for films deposited by sol-gel, i.e., room temperature dielectric constants and loss for sol-gel deposited BZN typically <150 and ~0.01, respectively. Lu *et al.* also looked at the effect of varying the Pt thickness from 30 nm to 100 nm on the dielectric loss over the frequency range 10 kHz to 100 MHz [3.59]. Above 1 MHz the losses increased with frequency and with decreasing Pt thickness.

In order to grow material characterised by good dielectric properties it is essential to achieve good crystallinity. Interestingly, unlike perovskite structures such as BZT, which require higher temperature (600-800^{o}C) annealing to achieve good crystallinity, BZN films require much lower temperatures (>400^{o}C) to crystallise. These annealing conditions influence film stress. The effect of film stress on dielectric properties due to the thermal mismatch between BZN and the substrate has been investigated by sputter depositing BZN material onto a range of metal coated substrates including, silicon, vycor glass, magnesium oxide (MgO) and sapphire (Al_2O_3) [3.53]. By selecting appropriate substrate material the dielectric properties of the thin BZN films can be optimised.

BZN is an attractive material for tunable, voltage controlled, microwave device applications and for frequency agile devices such as the distributed phase shifter described by Park *et al.* [3.58].

3.4 Ferroelectric Thin Films and Ferroelectric Domains

The majority of ferroelectric materials, including BZT used in this study, are subjected to a structural phase transition from a high temperature non-ferroelectric (or paraelectric) phase to a lower temperature ferroelectric phase (see figure 3.3). Ferroelectric materials possess a unique polar axis and are characterised by spontaneous electric polarisation P whose orientation can be switched by an external electric field. Useful properties exhibited by material in the ferroelectric phase include polarisation hysteresis and high dielectric permittivities. The spontaneous polarisation of a ferroelectric is zero when the material is used in the paraelectric phase and this can have the advantage of smaller overall losses and the temperature coefficient of the permittivity is small. However, by applying a DC bias field to the paraelectric material, a polarisation can be induced. Small dielectric losses due to the disappearance of ferroelectric hysteresis can result in enhanced performance of microwave tunable devices.

Associated with the paraelectric-ferroelectric phase transition is a change in the dimensions of the crystal unit cell giving rise to a spontaneous strain x_S.

Material can be formed as crystals, bulk ceramics, thick layers or thin films. Single crystals are only used in applications where there is likely to be a significant advantage due to the higher associated cost. The research detailed in this thesis will focus specifically on polycrystalline ferroelectric thin film (i.e. BZT) made up of different sized grains. It is the random nucleation in the pyrolysed gel films that results in the characteristic polycrystalline, granular microstructure of BZT. The spontaneous polarisation in a grain in a ferroelectric film is unlikely to be uniformly aligned throughout the grain. Regions that do have polarisation alignment (all dipoles aligned in the same pole direction) are referred to as ferroelectric domains. These domains form to minimise the elastic energy created as the film becomes constrained by the substrate during a phase transition from paraelectric to ferroelectric (i.e. when cooled to below the Curie point T_C). Individual domains are separated one from another by domain walls of dimension one to ten nanometres in thin films. Between domains the polarisation orientation changes from one direction to another. The polarisation direction is determined by the crystallographic properties of the material and may be controlled by making compositional changes. By applying an external electric field it is possible to displace the domain walls which can affect the dielectric properties of the ferroelectric material. If the bias field is sufficiently large, domains may switch in direction. Switching dynamics in ferroelectric thin films based on the nucleation, growth and propagation of domains is discussed by Jung *et al*. [3.63]. The domain formation process is illustrated in figure 3.9.

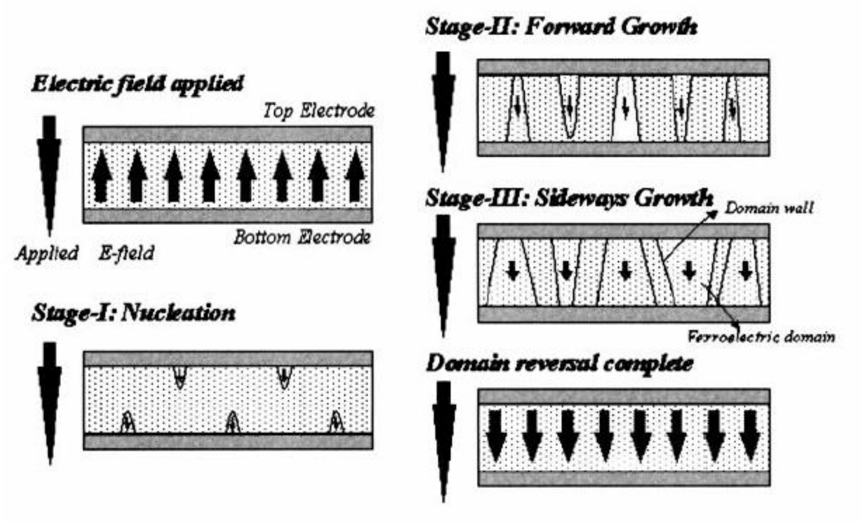

Figure 3.9 Domain formation in a ferroelectric thin film [3.63].

Non-ferroelectric dielectrics show a linear relationship between polarisation and applied electric field. By contrast, ferroelectric hysteresis is observed when a cyclic external field is applied to a ferroelectric film and is characterised by the coercive field E_c, remnant polarisation P_r, and saturated polarisation P_s as shown in figure 3.10 [3.64]. A good ferroelectric material has a large P_r value and a low E_c value. The schematic diagram (figure 3.10) also shows the orientation of dipoles in the ferroelectric layer at various stages in the hysteretic cycle. It is evident that all dipoles are orientated parallel to the field when the bias field is higher than or equal to the saturation polarisation electric field, and that the dipoles are randomly aligned at zero polarisation.

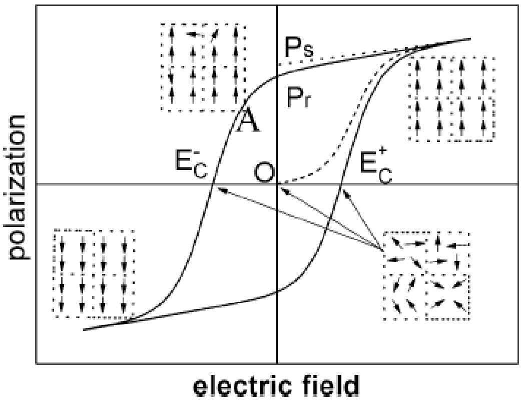

Figure 3.10 Hysteresis polarisation curve of a ferroelectric material showing relative dipole orientations [3.64].

It is recognised that in general ferroelectric thin films display a smaller permittivity than for bulk materials due to a range of factors including dielectric inhomogeneities, growth imperfections, materials composition changes at the interfaces, and residual stress caused by lattice constant and thermal expansion coefficient mismatch between film and substrate. Other research has shown that a thin non-ferroelectric interfacial layer ('dead' layer) of lower permittivity exists between film and electrodes as shown in figure 3.11 [3.64]. See section 3.9 for further discussion.

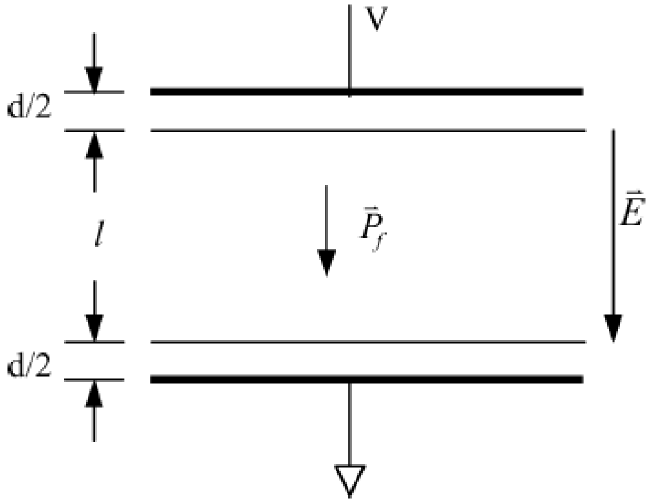

Figure 3.11 Schematic of a ferroelectric capacitor showing central ferroelectric layer separated from electrodes by thin non-ferroelectric ('dead') layers [3.64].

3.5 Thin-Film Dielectrics

Thin-film dielectric materials play a vital role in the development of a range of technologies from integrated circuit manufacture including CMOS transistor technology to dielectric materials for microwave applications. To accommodate this broad range of technologies there is a requirement for dielectric materials that have low to high dielectric constant (k). Also, it is often necessary to mix integrated capacitor technologies on a single substrate so that at one end paraelectric materials such as SiO_2 provide small capacitance while at the other end high-k ferroelectric materials such as PZT provide much larger capacitance, so that a total capacitance range fF to µF can be established [3.65, 3.66].

With advances in silicon and gallium arsenide (GaAs) integrated circuit (IC) manufacture and the requirement for ever smaller circuit geometries, there is a demand placed on the properties (physical, chemical and electrical) of the dielectric (insulating) material and associated metallisation. Reduced feature sizes in microelectronic circuits lead to improved circuit performance, however, signal runtime issues can result due to higher RC delays and crosstalk. Higher interconnect performance (lower line-to-line capacitance) can be achieved by the use of lower dielectric constant (low-k) insulators. In the vast majority of silicon processes, SiO_2 with a dielectric constant of ~4.0 has been used as the dielectric. However, in order to reduce device capacitance there is a need for a further reduction in dielectric constant to as close to 1.0 as possible, the lowest attainable k, that of a vacuum. A range of materials have been investigated for low-k dielectrics and include organic polymers such as benzocyclobutene (BCB) with k below 3.0 or ultra low-k (<2.0) materials like porous polymers and polytetrafluoroethylene (PTFE) (k=1.9) which can be spin coated [3.67]. Fabrication processes that use chemical vapour deposition (CVD) or spin coating techniques to deposit dielectric layers are preferred since these tend to produce higher quality films with excellent uniformity.

The chosen dielectric must also perform reliably when integrated with standard IC manufacturing (assembly and packaging) processes and may be required to exhibit thermal stability to >400^{o}C as well as mechanical and chemical stability (i.e. compatibility with cleaning, etching and polishing processes). Because a material has a low dielectric constant does not necessarily make it ideal for the intended application. If a material is to supersede another such as SiO_2 then properties such as low leakage, low thermal coefficient of expansion (<10 ppm/^{o}C), high dielectric breakdown voltage (2-3 MV/cm), low film stress, good adhesion to other materials and a thermal conductivity suitable for dissipating heat must be sought. General requirements for low-k dielectric materials and the integration challenges are discussed by Treichel *et al.* [3.68]. Some reliability issues and failure mechanisms associated with low-k dielectrics are presented by Scansen *et al.* [3.69].

For dielectric materials used in low to high frequency (RF and microwave) applications the important material properties are generally high dielectric constant, low dielectric loss, low temperature dependence of dielectric constant, and good tunability if required. In the case of the parallel-plate capacitor and other integrated capacitor devices, the larger the dielectric constant the smaller the component needed. High-k dielectrics are therefore important for the miniaturisation of components in, for example, hand-held and portable communications products. Ferroelectric thin films provide much higher dielectric constants than paraelectric material. Ulrich *et al*. investigated dielectrics in integrated capacitors for the use in microelectronic assemblies, and compared the dielectric constants for paraelectric and ferroelectric dielectrics [3.65].

Integration of ferroelectrics into electronic devices demands their use in the form of thin films. Thin dielectric films (typical thickness <1.0 μm) have been deposited by means of dry and wet processes including RF magnetron sputtering, pulsed laser deposition (PLD), chemical vapour deposition (CVD), electron beam evaporation, and sol-gel technique combined with spin coating. By contrast, thick dielectric films (>10 μm) are generally fabricated by ceramic processing such as screen printing, tape casting and transfer printing. With sol-gel deposited films, a single layer is typically 50 nm thick and films are built up to the required thickness by depositing several layers in succession. In multi-layer deposition residual tensile stress is a critical issue and is more significant for thicker films. Tensile stresses result from substrate clamping as the material crystallises. Thin film compositions have been developed that have greatly reduced processing temperatures (500-700^{o}C) in comparison to standard bulk ceramic sintering (1100-1400^{o}C).

The microstructure and properties of thin dielectric films can be modified in any of the following ways:

- Changing the composition (e.g. varying the Zr and Ti content in BZT)
- Doping and varying the percentage doping

- Depositing film on different materials (metal layers, conductive oxides, seed and buffer layers)
- Thermal treatments (hotplate, furnace and rapid thermal annealing)

3.6 The Sol-Gel Technique

3.6.1 Sol-Gel Process

The sol-gel method is a liquid phase process for the preparation of ceramic and thin film materials [3.70, 3.71]. Process steps involve the preparation of a sol (colloid), gelation of the sol, and removal of the solvent. The sol is produced from either inorganic or organic precursors (starting materials) such as metal organic compounds (e.g., metal alkoxides). The precursors consist of a metal element to which is attached an organic ligand (e.g., alkyl, alkoxy). Titanium (IV) isopropoxide [$Ti(OC_3H_7)_4$] is an example of a metal alkoxide precursor commonly used in preparing dielectric material. Although the chemistry of the sol-gel synthesis utilising metal alkoxide precursors is not well understood, it is hoped that new research will improve our understanding [3.72, 3.73]. Kessler *et al.* present new experimental data on the mechanisms of chemical modification of the alkoxides with application to new classes of materials [3.72].

A sol is a colloidal suspension of solid particles in a liquid either in the form of a particulate sol containing non-polymeric solid particles (particle size >1 nm), or a polymeric sol (particles no larger than 1 nm). Of most interest and relevance to this investigation are particulate sols which contain dense particles of the order of nanometres and larger. A gel is formed from a particulate sol when particles stick together in such a way as to form a network extending throughout the solution. The solution loses its fluidity and takes on the appearance of an elastic solid. Film formation from the fluid sol (or solution) prior to gelation can be achieved by dip coating, spraying or spinning.

Sol-gel processing has been used successfully for the preparation of many ceramics and thin films and has distinct advantages over conventional solid-state ceramic processing. Chemical routes such as sol-gel enable good control of stoichiometry due to atomic scale mixing of the starting compounds. Also, the processes are relatively simple and economical. The ability to control precisely the microstructure (e.g., porosity, densification) and to deposit films of controllable thickness over large area substrates is a distinct advantage compared to other routes such as PLD, and requires considerably less equipment. By the sol-gel route it is also possible to crystallise the material at much lower temperatures than would be achievable using other preparations based on solid-state reactions. This makes the sol-gel process particularly compatible with silicon IC technology.

3.6.2 Thin Film Formation

During spinning of the sol on the wafer, gelation and partial drying of the film occurs in a relatively short time (seconds) and generally results in more compact structures. The film thickness attained by spin coating is a balance between centrifugal force and solvent evaporation both of which increase with spin speed. Stress within the film during formation is created by dimensional constraints. The two competing mechanisms are, evaporation which compacts the film, and condensation reactions which stiffen the film and slows compaction. The relative rates of evaporation and condensation have a significant effect on the porosity of the film. A shear stress within the film develops due to fluid flow and precursor attachment to the substrate. Shrinkage due to drying and condensation reactions creates a tensile stress within the film.

An important stage in thin film formation after spinning the sol is the process of drying the film. This is a complex process of shrinkage due to deformation of the solid forming structure or network, liquid transport through the pores of the material, and the evaporation of liquid from the surface of the film (at the film-air interface) and from within the material resulting in diffusion of vapour to the film surface. As a consequence, stresses and strains develop in the shrinking film. These relate to the drying rate, volume and properties of the sol-gel film. For example, stresses build up due to pressure gradients in the pores of the film.

Also, diffusion of volatile components from the body (interior) to the surface causes a rise in tension within the material. The difference in the shrinkage rate between the drying surface and the body of the material giving rise to pressure gradients is the primary cause of drying stress. Factors affecting this include sol concentration and the deposition parameters such as spin frequency. For a detailed explanation of drying stress refer to Brinker and Scherer [3.70].

There is an obvious connection between stress and fracture of the material. Cracking of the film occurs when the stress in the material is greater than its strength. How to reduce or eliminate cracking in the film is an important issue. Chemical additives such as ethylene glycol are introduced to the sol in order to control cracking of the films. Crack growth can also propagate from inclusions in the film (e.g., from particulate contamination of the surface onto which the film is deposited). The cause of cracks in this case is due to the thermal expansion mismatch between inclusion and surrounding film, and is very much dependent on the size of the inclusion. The energy required to initiate crack growth originates from stress relief in the film around the inclusion. A little more detail on stress induced cracking will be given in section 3.7.

After drying, the film is amorphous (non-crystalline), but with sufficient heating will crystallise. For thicker films (>1 µm), it may be necessary to heat the material to even higher temperatures (sintering) to produce a pore free ceramic and so increase the densification of the film.

3.7 Stress and Defects in Thin Films

The complex issues and behaviour associated with stress, fatigue cracks and dislocation in solid films and its modelling has been addressed by a number of researchers [3.74-3.80]. Total film stress (σ_{film}) is given by.

$$\sigma_{film} = \sigma_{intrinsic} + \sigma_{extrinsic} \tag{3.1}$$

a combination of intrinsic stress ($\sigma_{\mathrm{intrinsic}}$) and extrinsic stress ($\sigma_{\mathrm{extrinsic}}$).

Stresses in polycrystalline thin films can be intrinsic as a result of growth stress or extrinsic due to thermal expansion mismatch between film and substrate. Extrinsic or thermal stress ($\sigma_{thermal}$) is defined as:

$$\sigma_{thermal} = \int_{T_1}^{T_2} \frac{(\alpha_{film} - \alpha_{substrate})E_{film}}{1 - \nu_{film}} dT \tag{3.2}$$

where E, α, and ν represent the elastic modulus, thermal expansion coefficient, and Poisson's ratio, respectively. Some typical values for the thermal expansion coefficients of substrate and thin film materials are given in appendix 1.

Stress is introduced into the crystal lattice of the film during cooling after the annealing (crystallisation) process. For BZT of ferroelectric composition, this occurs when transitions from cubic to other phases are encountered below the Curie temperature. Induced stress in thin ferroelectric films affects the dielectric and ferroelectric properties of the material. Lu *et al.* discuss phase transition related stress in ferroelectric thin films [3.74]. Contributing factors that give rise to stress include: thermal expansion and lattice parameter mismatch between film and substrate [3.76]; structural phase transformation (e.g., paraelectric to ferroelectric) of films when cooled from high temperature to room temperature; and formation and disappearance of grain boundary during film growth. All of this can result in an uneven distribution of stress through the film. The stress can take the form of either compressive or tensile and influences the Curie temperature (T_c) by increasing T_c for compressive stress and decreasing T_c for tensile stress. Film stress is force per unit area in Pa units for which positive values are assigned to tensile and negative values to compressive stresses. Stress can therefore vary from large tensile through zero to large compressive values dependent on the deposition method, materials and conditions chosen. Film stress can be a real issue reducing the dielectric constant, increasing the dielectric loss and limiting the tunability. As a consequence of stress in piezoelectric material used in actuators, a study of fracture behaviour is essential to address performance and reliability issues. On the other hand, stress in films can be a positive attribute as in the operation of the cantilever.

Defects in sol-gel deposited films can arise at the spin coating stage with the formation of striations and ‘comets’ similar to the defects observed in photoresist when spin coated. Striations are the result of inhomogeneities of the film thickness and can be reduced by using high spin speeds. The comet shaped regions are thinly coated areas which start from particles on the substrate or from air bubbles in the sol. Air bubbles can arise when dispensing the sol. Particulate contamination of the substrate surface is the most likely cause of defects due to inadequate substrate cleaning prior to spin coating.

Oxides that are porous can absorb water which tends to make films compressive, whereas oxide films devoid of water are tensile.

Virtually all vacuum deposited coatings including metallic and inorganic compound films are in a state of stress. The total film stress is composed of a thermal or extrinsic stress and intrinsic stress. The thermal stress is due to the difference in the thermal expansion coefficients of the film and the substrate material. Defects such as holes and hillocks form in films as a result of diffusion processes arising from temperature changes during deposition and annealing. Thornton *et al*. showed that intrinsic stress is due to crystallographic flaws that are built into the film during deposition [3.81]. Intrinsic stresses in thin films can be a real issue since tensile or compressive stresses can lead to film cracking or buckling. The origin of intrinsic stresses in evaporated and sputtered films is discussed in a paper by d’Heurle *et al*. [3.82].

In sputtering processes, both tensile and compressive stresses are possible depending upon the deposition conditions. Sputtering power and gas pressure both influence the sputter rate which has an effect on film stress. Chinmulgund *et al.* showed that for sputtered Ti there is a thickness dependency of stress. Below a film thickness of ~300 nm the as-deposited Ti is compressive and for films >300 nm the Ti is tensile [3.83]. After annealing the Ti film at 400^{o}C for 1 hour, the room temperature stress became more tensile due to the increased densification of the Ti film. At low argon pressure (<2 mTorr) sputtered metal films tend to yield compressive stress. As the pressure is increased the stress changes from compressive to tensile. Also, tensile stress is increased with film thickness but decreased with power. Tokura *et al*. showed that sputtered Pt films have compressive stress due to bombardment of the growing film by energetic argon atoms and inclusion of argon gas in the film [3.84]. Compressive stress is generated when energetic particles (atoms and ions) from the sputtering plasma hit the metal surface in accordance with the atomic peening model. The peening effect is when surface atoms are knocked into voids and grain boundaries within the film.

In evaporated high melting point metals (e.g. Cr) stresses are tensile since films usually exhibit a porous structure, whereas in low melting point metals (e.g. Au) comparatively small tensile as well as compressive stresses are built up due to increased densification of films. Abermann showed that stress correlates with growth mechanisms (columnar grain growth or island growth) caused by differences in the material mobility [3.85]. Thin film growth of gold by the generation of charged clusters during thermal evaporation is discussed by Barnes *et al*. [3.86]. They showed that the evaporated film quality is dependent on evaporation rate which affects the charging behaviour. Higher evaporation rates result in smooth, dense, good quality films due to the generation of larger, more easily charged clusters. By comparison, low evaporation rates generate small, neutral clusters that tend to result in a rough film of poor quality. Stress related effects in thin films are discussed by Thornton *et al*. and showed that electroplated films tend to produce tensile intrinsic-type stresses similar to those seen in evaporated coatings [3.81]. Porous structures also yield tensile stress.

Buehler *et al.* reported on the study of grain boundary diffusion and associated dislocation mechanisms in polycrystalline thin films on substrates [3.77]. Stresses in the film are relaxed by inelastic deformation mechanisms when material is transported from the surface into the grain boundary. The material defect called a diffusion wedge is formed as material accumulates in the grain boundary. This promotes dislocation activity within the grains.

Figure 3.12 shows the stages relating to the formation of a diffusion wedge along a grain boundary as a result of mass diffusion from the surface. This results in lattice distortion around the diffusion wedge with a concentration of stress in the vicinity of the film-substrate interface. This then gives rise to inelastic deformation and the formation of crack-like dislocations parallel to the plane of the film which subsequently causes the stress to be relaxed. Buehler *et al.* developed a model (atomistic simulation) to study deformation mechanisms in sub-micron polycrystalline thin films. A similar study was undertaken by Gao *et al.* that looked at diffusional deformation (i.e. grain boundary diffusion wedges) in thin metal films [3.78].

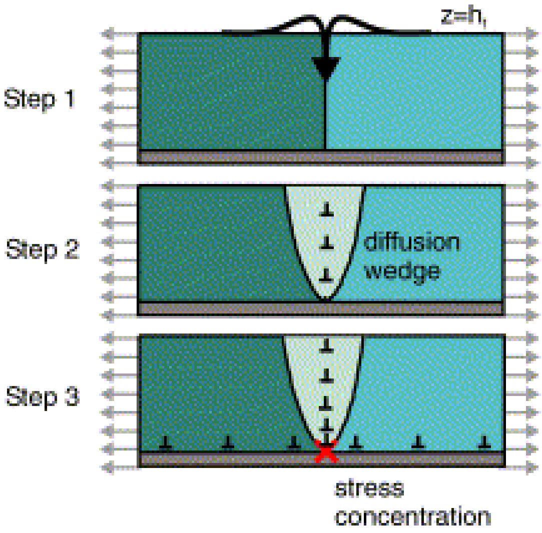

Figure 3.12 Formation of a diffusion wedge. Step 1 shows material being transported from the surface into the grain boundary. Step 2 displays formation of the diffusion wedge due to material accumulating in the grain boundary. Step 3 shows the stress concentration at the film-substrate interface causing dislocations parallel to the plane of the film [3.77].

Materials that develop stresses in grain boundaries can spontaneously crack depending on the size of the grains. Fatigue crack growth in ferroelectric material is exacerbated under mechanical and electrical loads [3.79]. It was pointed out that non-uniform domain switching in ferroelectrics can also produce internal stresses, that if sufficiently high, can result in crack growth.

Understanding deformation mechanisms in polycrystalline thin films and other ultrathin material layers are essential for the development of material systems and the miniaturisation of devices in areas such as integrated microelectronics, optoelectronics, nanotechnology and biotechnology (e.g. lab-on-a-chip).

Several authors have reported on the thermal stability of Pt, titanium diffusion and the stress dependence of platinum hillock formation; they also discuss ways of alleviating these problems [3.87-3.98]. Metal electrodes such as platinum play a significant role in determining the material and device properties and performance. Stress in Pt/Ti bottom electrode can be varied from tensile to compressive by modifying the sputtering conditions. Deformation of the Pt electrode due to the formation of defects (hillocks) can cause stress cracks to appear in the film and at worst lead to capacitor shorts. The problem arises during both sample preparation and post-annealing, and manifests itself when the Ti used as an adhesion layer diffuses into the Pt along the Pt grain boundaries. Hillocks form on the surface of the Pt film to relieve the compressive stress generated by the Ti diffusion and oxidation [3.87]. Although hillocks can affect leakage current, they can also serve as nucleation sites for growth of thin film. Cha *et al.* investigated the effects of Ti thickness on the orientation, stability, and electrical characteristics of Pt bottom electrodes and found that problems such as interdiffusion and surface roughness could be improved when Ti layers 3-5 nm thick were used [3.97]. To stabilise the Pt electrode others suggest using TiO_x in place of Ti as the adhesion layer [3.90, 3.91, 3.94].

3.8 Strain Layers

Large strain on thin films can be imposed by the substrate due to lattice mismatch so that films are subjected to in-plane deformation.

The thermal strain ($\varepsilon_{thermal}$) is given by:

$$\varepsilon_{thermal} = \int_{T_1}^{T_2} \left(\alpha_{film} - \alpha_{substrate}\right) dT \qquad (3.3)$$

where α_{film} and $\alpha_{substrate}$ are the thermal expansion coefficients of film and substrate. Films under tensile strain have positive values whereas films under compressive strain have negative values.

When using a Pt/Ti bottom electrode, Ti diffusion into the film can result in increased surface roughness and leakage. A thin (~10 nm) strain or buffer layer can be introduced to control the stress in the main layer and act as a barrier to interdiffusion between main layer and substrate. Similar problems with diffusion and stress fractures were encountered when growing a thin BZT film on Au/Cr coated silicon as part of the work of this thesis. These difficulties were overcome when a thin (25 nm) BZN buffer layer was introduced between the BZT main layer and metallised substrate. In this case the sputtered BZN buffer layer was under compressive stress whereas sol-gel deposited BZT was under tensile stress. Further details of this work can be found in sub-section 7.3.6. A more detailed account of buffer layers is given in section 3.10.

3.9 Interfacial Layers

Interfacial layers are very thin (typically ~6 nm), low dielectric constant layers near an interface which have different properties to those of the main film. A Schottky barrier exists at the metal/dielectric interface which results in band-bending and a depletion layer. The height of this barrier can be affected by factors such as the structure and composition of the film in the interface region (e.g. the change in oxygen vacancy concentration). A high concentration of oxygen vacancies can be generated by out diffusion of oxygen from the film into the Pt electrode especially at elevated processing temperatures. This can be counteracted through use of conductive oxides such as $LaNiO_3$. However, oxide electrodes are not suitable for voltage tunable microwave capacitors since they are too resistive. The interface between electrode and dielectric material has influence on the leakage current and breakdown electric field of thin films and can result in poor dielectric properties. For example, the dielectric constant of the interfacial layer does not change with applied bias voltage thus reducing the tunability of the main film. The interfacial layer also contributes to a decrease in device quality factor with increase in frequency. Electrode conductor losses (contact resistance and finite sheet resistance of the bottom and top electrodes) also influence the device quality factor at higher frequencies. This can be reduced by using thicker electrodes with a higher conductivity.

3.10 Seed and Buffer Layers

The effect of seed and buffer layers on the microstructure and electrical properties of a range of dielectric materials has been investigated including BZT [3.99-3.103], but not BZN. Researchers have demonstrated that improvements in dielectric properties of thin films can be achieved through the use of seed and buffer layers primarily by changing and controlling the crystallographic orientation and microstructure of the films. For example, Zhai *et al*. showed that films deposited onto Pt/Ti/SiO_2/Si substrates have a preferred (110) crystallographic orientation whereas films deposited on $LaNiO_3$/Pt/Ti/SiO_2/Si substrates display a (100) preferred orientation [3.100].

Methods adopted include:

- Annealing the bottom electrode. Observing the effect of heat treatment conditions on microstructure and dielectric behaviour.
- The selection of different bottom electrodes (e.g. $LaNiO_3$).
- Seed layers inserted between the dielectric thin film and the bottom electrode having the same composition as the dielectric main layer.
- Seed layers that have a different composition to that of the main layer.

Gao *et al.* looked at the effect of seed layers on the dielectric properties of BZT thin films [3.101]. Seed layers having the same composition as the BZT main layer were deposited on Pt/Ti/SiO_2/Si substrates. These seed layers were dried and annealed differently to the main layer and deposited in a range of thicknesses. According to Gao *et al*. it is the optimisation of seed layer thickness that determines the most favourable dielectric properties of BZT thin films. Morphology, including grain size of the BZT films, is affected by the seed layer thickness. High dielectric constants (>400) with moderate tunability (~37%) were achieved for seed layer and BZT film thicknesses of 20 nm and 380 nm, respectively. Figure 3.13 displays the room temperature dielectric constant and loss of BZT thin films as a function of frequency for different seed layer thicknesses [3.99]. Figure 3.14 shows how dielectric constant, loss and tunability vary with seed layer thickness at the measurement frequency of 100 kHz. [3.100].

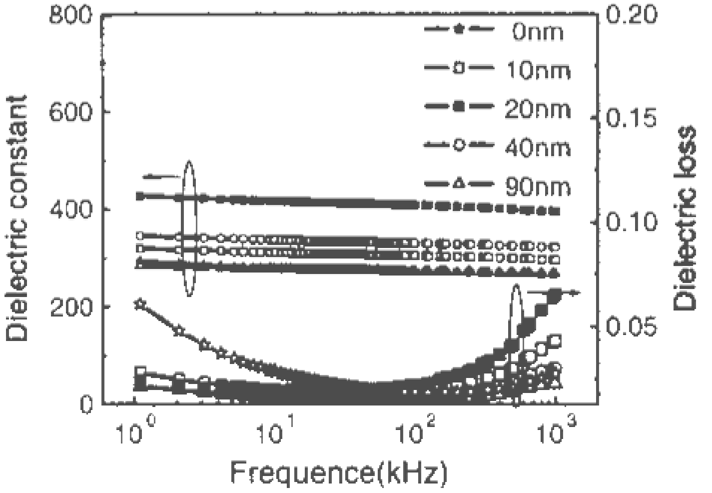

Figure 3.13 Room temperature dielectric constant and dielectric loss of BZT thin films as a function of the measuring frequency and BZT (same composition) seed layer thickness [3.99].

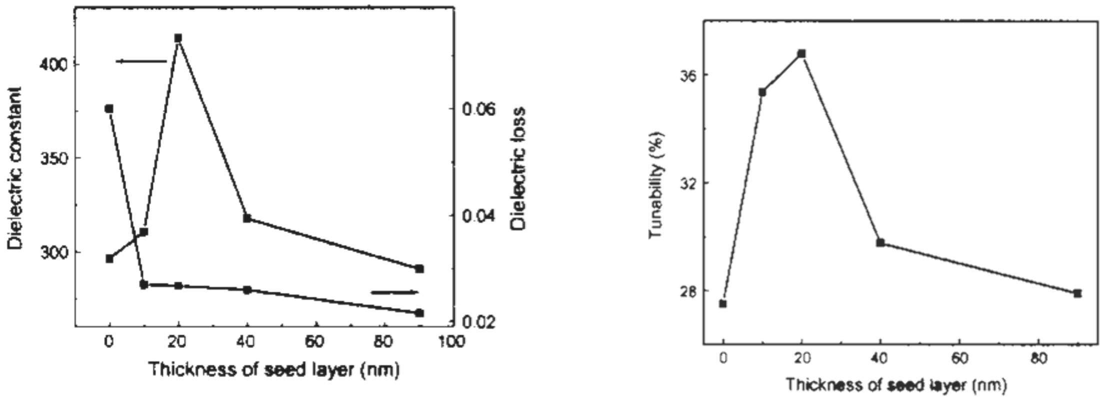

Figure 3.14 Room temperature dielectric constant, dielectric loss and tunability of BZT thin films as a function of BZT seed layer thickness at the measurement frequency of 100 kHz [3.100].

Gao *et al*. investigated the effect of buffer layers on the orientation, microstructure and dielectric properties of BZT thin films [3.102]. It was shown that the dielectric properties of ferroelectric thin films, including dielectric constant and tunability, are sensitive to the crystallographic orientation of the film. Hence, electrical properties could be improved by controlling the preferential orientation. Efforts have also been made to improve the dielectric properties by adding dopants and using conductive oxide electrodes such as $LaNiO_3$ [3.101]. Gao *et al*. have investigated the use of dopants and buffer layers to simultaneously lower the dielectric loss and enhance the dielectric tunability of BZT thin films. They also explain that interfaces between the thin ferroelectric films and the electrodes affect the measured dielectric properties [3.101]. There is an association between the existence of a so called interfacial “dead layer” at one or both metal electrodes and poor dielectric properties, in particular, a reduction of dielectric constant in ferroelectric thin films. Gao *et al*. say that this may arise from the oxygen interdiffusion, chemical reaction, structural defects, or Schottky barriers at the interfaces [3.101]. The thickness of this dead layer can be decreased through the use of conductive oxide electrodes ($LaNiO_3$). As a result, the dielectric constant and tunability of the ferroelectric thin films were enhanced. It was recognised that high tunability was attributed to the (100) orientation of the films and larger grain size. Buffer layers also prevent material diffusion from one layer to another.

3.11 Multilayer (Composite) Structures

Multilayer or composite structures incorporating ferroelectric and dielectric material, including BZT and BZN [1.28-1.35], have been investigated by a number of researchers. Films incorporating multilayer structures are composed of alternate layers of either different material or the same material but of a different composition. These composite structures are very promising for improving dielectric properties such as the figure of merit (FOM) for microwave tunable device applications. The FOM is a measure of the quality (high tunability and low dielectric loss) of the films.

Qin *et al*. looked at enhancing the electrical properties of multilayer $Ba(Zr_{0.2}Ti_{0.8})O_3/Ba_{0.6}Sr_{0.4}TiO_3/Ba(Zr_{0.2}Ti_{0.8})O_3$ (BZT/BST/BZT) thin films [1.29]. The pulsed laser deposition (PLD) technique was used to deposit BST and BZT/BST/BZT composite thin films on $LaNiO_3$ (LNO) coated lanthanum aluminate $LaAlO_3$ (LAO) substrates. Results indicated that there was little difference in the tunability between the two materials. Although the dielectric constant was suppressed in the BZT/BST/BZT sample compared to BST, the dielectric loss of the BZT/BST/BZT multilayer thin film (0.8%) was significantly lower than that of BST (2.1%) at applied electric fields of up to 300 kV/cm. As a consequence, the FOM of the BZT/BST/BZT composite film was 76.98 compared to a FOM of 31.08 for the BST thin film. Gao *et al*. investigated the dielectric properties of Ba($Zr_{0.2}Ti_{0.8}$)O_3/$MgTiO_3$ (BZT/MT) heterostructured thin films (~520 nm thick) prepared by sol-gel and deposited on Al_2O_3 substrates [1.28]. As can be seen in figure 3.15 the dielectric loss in the BZT/MT heterostructured films (~0.2%) was considerably lower compared to that of BZT (>1.0%). The FOM of the BZT/MT heterostructured thin film was 44.6, which was much better than that of BZT (16.9).

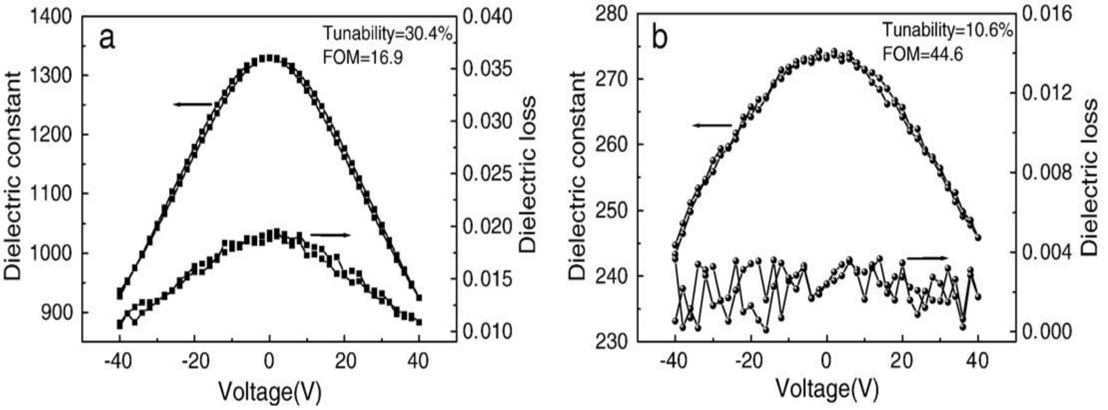

Figure 3.15 Dielectric constant and dielectric loss as a function of applied DC voltage for (a) BZT thin film and (b) BZT/MT heterostructured thin film [1.28].

Within the work of Zhai *et al*. details of a compositionally graded multilayer structure is presented [3.100]. The thin films formed on LNO/Pt/Ti/SiO_2/Si substrate comprised Ba($Zr_{0.35}Ti_{0.65}$)O_3, Ba($Zr_{0.18}Ti_{0.82}$)O_3, Ba($Zr_{0.09}Ti_{0.91}$)O_3, and $BaTiO_3$. The tunability of these composite structures was about 46% at a bias field of 400 kV/cm. The dielectric loss was less than 2%.

Fu *et al*. suggest that dielectric/ferroelectric composite films with well defined layered structure should behave like that of a ferroelectric film but with lower Curie-Weiss temperature [1.34]. For BZN/Mn-BST the tunability was 60% at

570 kV/cm and the dielectric loss was below 0.005 (figure 3.16). This gave a FOM of 120, one of the best results achieved for tunable material.

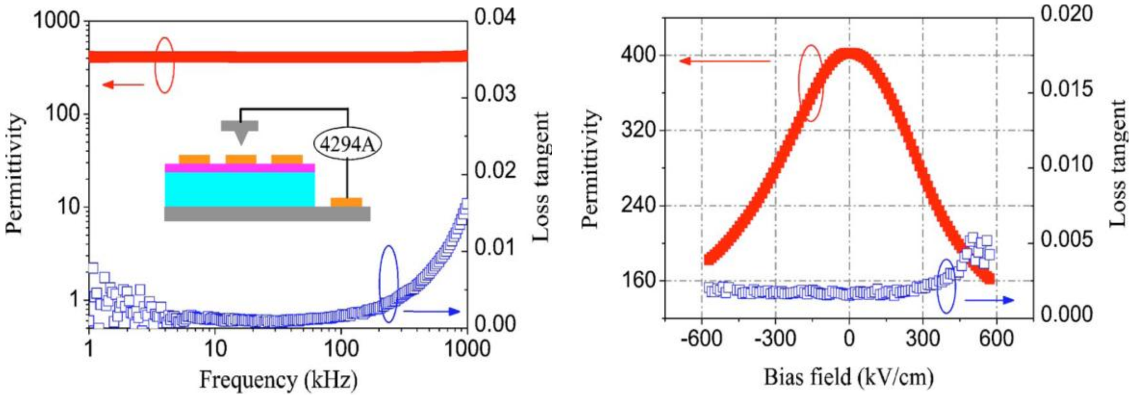

Figure 3.16 Permittivity and dielectric loss of BZN/Mn-BST heterolayered thin films as a function of frequency and electric field. The bias field results were obtained at a measurement frequency of 100 kHz [1.34].

Wang *et al*. reported on $Bi_{1.5}Zn_{1.0}Nb_{1.5}O_7/Ba_{0.6}Sr_{0.4}TiO_3/Bi_{1.5}Zn_{1.0}Nb_{1.5}O_7$ (BZN/BST/BZN) sandwich films deposited on platinised silicon substrates by RF magnetron sputtering [1.32]. These composite films are not ferroelectric at room temperature. They boast the high dielectric constant of BST films (~200-250) and the low dielectric loss of BZN films (<0.008 at 1 MHz). Yan *et al*. prepared $Ba_{0.5}Sr_{0.5}TiO_3/Bi_{1.5}Zn_{1.0}Nb_{1.5}O_7$ (BST/BZN) multilayer thin films on Pt/Al_2O_3 substrates by sol-gel method [1.30]. $Ba_{0.5}Sr_{0.5}TiO_3/Bi_{1.5}Zn_{1.0}Nb_{1.5}O_7$ (BST/BZN) comprises a cubic BST perovskite phase and a cubic BZN pyrochlore phase. The objective of combining BZN with BST films to form BST/BZN multilayer thin films was to reduce dielectric loss while maintaining high tunability. The figure of merit (FOM) result confirmed this showing that BST/BZN had a FOM twice that of BST and considerably higher compared to BZN.

Consequently, there is justification for exploring BZT/BZN composite structures based on the foregoing, in particular, the demonstration that BST/BZN composite films have good dielectric properties. A BZN/BZT/BZN sandwich film will combine the high dielectric constant (~250) and tunability (>50%) of BZT with the low dielectric loss (0.008) of BZN. In fact, BZT demonstrates lower dielectric loss than that of BST.

3.12 Dry Etching of BZN – A Constituent Chemical Analysis

To date there has been no evidence of previous research relating to the dry etching of BZN. However, there has been work published on other materials that contain bismuth, zinc or niobium, and it is the volatile species of these when interacting with hydrochlorofluorocarbon gas plasmas that is of interest so that an etching mechanism for thin-film BZN can be established.

Kim *et al*. looked at the etching of strontium bismuth tantalate $SrBi_2Ta_2O_9$ (SBT) thin films in $Cl_2/CF_4/Ar$ plasma and compared the volatile species of bismuth chloride ($BiCl_3$) with bismuth fluoride (BiF_3). They found that bismuth chloride was removed easily due to the relatively lower boiling point (440^oC) compared to that of bismuth fluoride (900^oC) [3.104]. In a more recent paper, Kim *et al*. confirmed that bismuth etching tends to favour chlorine chemistry [3.105].

Lee *et al*. demonstrated the etching of indium zinc oxide thin films in a C_2F_6/Ar gas which involved the chemical reaction of Zn element with fluorine radicals [3.106]. The formation of ZnF_2 compound on the etched surface due to the chemical reaction with fluorine radicals was confirmed using XPS analysis. It was also noted that Zn compound containing F element had a higher melting and boiling point than those containing Cl and Br resulting in a slower desorption process from the etched surface. The bombardment of energetic Ar ions assisted in the removal of volatile species. Other researchers demonstrated the etching of zinc oxide (ZnO) using C_2F_6 and NF_3 based gas mixtures by inductively coupled plasma reactive ion etching [3.107]. Lee *et al.* showed that the volatility of ZnF_2 is due to its low vapour pressure (1 Torr at 1243^oC) [3.107]. The chemical reaction of CH radicals with the Zn atoms in ZnO has been used to form Zn organic compound, $Zn(CH_x)_y$, from which volatile products such as dimethylzinc (CH_3-Zn-CH_3) with a low boiling point of 46^oC was produced [3.108]. Also, the etching rate was expected to increase due to Ar ion enhanced removal of the $Zn(CH_x)_y$ etch products.

The etching behaviour of niobium in pure SF_6 plasma was studied by Zijlstra *et al*. [3.109]. This fluorine based chemistry resulted in volatile NbF_5 reaction product. However, non-volatile $NbF_{x(<5)}$ products also build up during etching. Formation and removal of the volatile NbF_5 and non-volatile niobium-fluorine reaction products was accelerated by ion bombardment and thermal heat. Oxygen enhanced plasmas used to etch niobium include CF_4/O_2 [3.110] and SF_6/O_2 [3.111]. Foxe *et al*. used reactive gases $CBrF_3$ and CF_4, both found to be effective in the reactive ion etching of niobium [3.112]. Fabrication of nanostructures in thin niobium films was developed by Piotrowski *et al*. using a pattern transfer by reactive ion etching in CCl_2F_2/H_2 plasma [3.113]. In the etching of lithium niobate ($LiNbO_3$), Jackel *et al*. made use of gas mixtures based on gases CF_4, CHF_3 and CCl_2F_2 in combination with O_2 and Ar [3.114]. In this process the niobium tends to form the volatile compound with the fluorine in CF_4 and CHF_3 since the lithium reacts with the halogens to produce high melting point salts. Other lithium compounds formed (e.g. oxides and halides) are also non-volatile and can only be removed by sputtering. A CF_4/O_2 gas plasma was also employed to etch $LiNbO_3$ through work by Darbyshire *et al*. [3.115]. The work of Boucher *et al*. looked at the dry etching of Nb_2O_5 among other materials, using a combination of gases including CHF_3, CF_4 and SF_6 with O_2 and Ar [3.116]. In this case niobium pentafluoride (NbF_5) is the volatile etch product sublimed at a temperature of 230^oC. Hence, by heating the sample the etching rate can be increased. In previous work by Darbyshire, Nb_2O_5 was reactively ion etched using fluorine and chlorine compound plasmas and the results compared [3.117]. The etch rate of Nb_2O_5 using fluorine chemistry at a power density of 0.2 W/cm^2 was up to five times faster than when using chlorine based gas etchants under the same process conditions.

3.13 Zipping Varactor: Cantilever-Based Tunable Capacitor

In the early 1990s the first MEMS varactor was designed specifically for high frequency (HF) applications. For some time the development of MEMS variable capacitors was limited due to the small capacitance ratio (1.2-2.5) achievable compared to solid-state (silicon and GaAs) varactors which have capacitance ratios typically 4-6. However, in recent years MEMS varactors with capacitance ratios greater than 10 have been fabricated. The zipping varactor is a miniature device that uses a mechanical movement to achieve a variation in capacitance. MEMS varactors move several micrometers when actuated.

Various actuation mechanisms have been employed including electrostatic [3.118], piezoelectric [3.119] and thermal [3.120] actuations. Of these, electrostatic actuation has been the most researched. The cantilever interconnect structure is at the heart of the MEMS tunable component. Ketterl *et al*. described the design of a novel tunable microwave resonator using a coplanar waveguide (CPW) spiral inductor imbedded in a pyrex substrate with a cantilever interconnect structure (figure 3.17) [3.121].

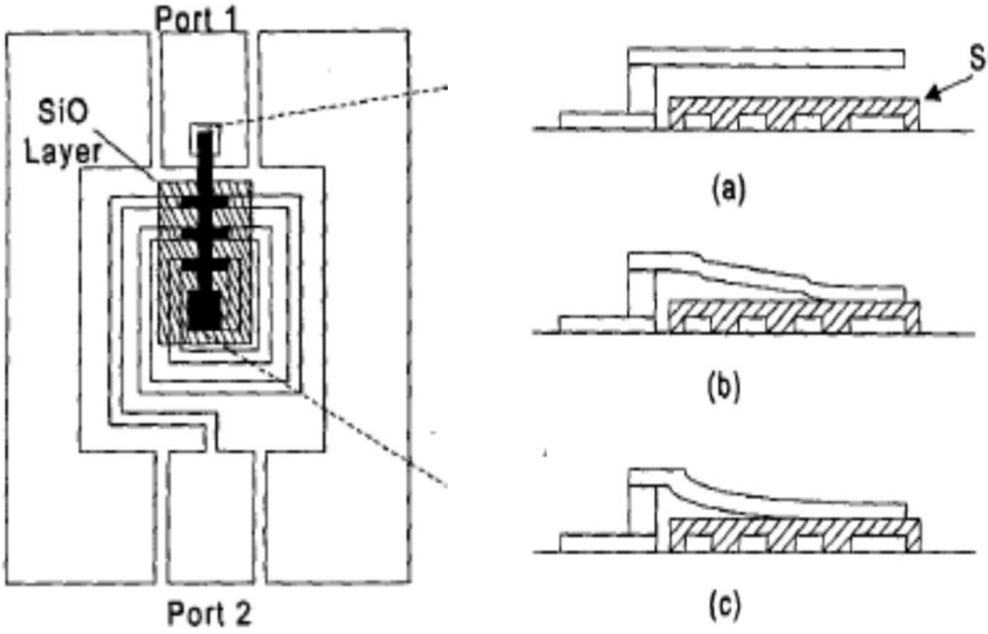

Figure 3.17 Fabricated tunable spiral resonator showing cantilever at (a) 0 V bias and (b) (c) in stages of actuation [3.121].

Resonance tuning between 3 and 7 GHz and Q-factors between 17 and 20 was achieved when a bias voltage between 0 and 40 V was applied. The device operates electrostatically when a bias is applied between the input and the output of the inductor. The tip of the cantilever beam makes contact with an insulator, silicon monoxide (SiO), deposited on the centre pad of the spiral inductor. By increasing the bias the beam deflects toward the inductor providing additional tuning.

Rebeiz highlights some examples of tunable electrostatic parallel-plate capacitors in a section (chapter 11) dedicated to MEMS varactors and tunable oscillators [1.7]. A summary is given of a paper by Hung and Senturia who had developed a cantilever-based tunable capacitor using a polysilicon process [3.122]. The paper describes the “zipping motion” of the cantilever as it is progressively pulled down over the bottom electrode when a voltage between the bottom electrode and cantilever is increased. The dielectric is an air gap between cantilever and bottom electrode. Dimple spacers are employed to fix the air gap in the down-state position. The width and position of the cantilever have been designed for a specific C-V characteristic. For a 40 V bias voltage the capacitance was tuned from 0.55 pF to 1.0 pF. The only drawback was the 1 GHz limit to the operating frequency due to inductance of 15-20 nH.

Ionis *et al*. described a differential multi-fingered MEMS tunable capacitor based on the zipper actuation principle for use in RF IC applications such as filters and voltage controlled oscillators (VCOs) [3.123]. The simplified structure is shown in figure 3.18 which displays dimples on the top plate with corresponding holes or trenches in the bottom plate; contact between the two plates is prevented. The top plate of the zipper is made of two materials, a gold layer over polysilicon.

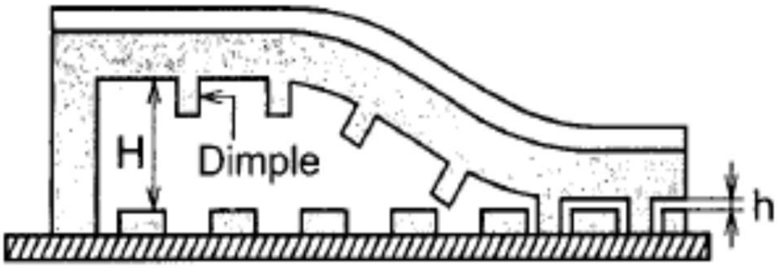

Figure 3.18 Schematic cross-section of the cantilever top plate with dimples and the polysilicon bottom plate with holes on insulating substrate [3.123].

The tuning range of this device is calculated from the parallel-plate capacitor formula $C_{max}/C_{min} \leq H/h$, where H and h are the maximum and minimum vertical distances between the two plates, respectively. For H=2.75 μm and h=0.75 μm the theoretical maximum tuning range for the device is 3.67. In practice the tuning range is smaller since one side of the top plate is fixed. The capacitance was tunable from 3.1 pF to 4.6 pF (46%) with a 35 V tuning bias. This device enabled a CMOS VCO to be tuned from 1.47 GHz to 1.54 GHz (4.8%).

Electrostatic actuators were developed by Gray *et al*. which used in-plane stress gradients along the length of a triangular shaped bimetallic Au cantilever beam to significantly improve the tuning range of the device for application to RF tuning [3.118]. A diagram of the bimetallic structure is shown in figure 3.19.

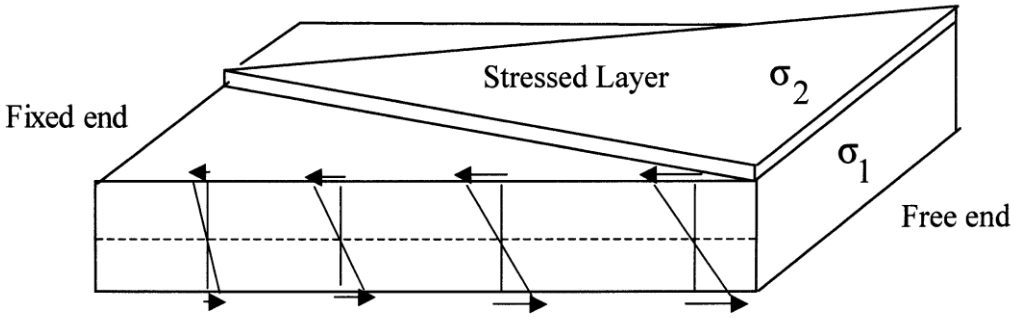

Figure 3.19 Illustration of bimetallic gold beam with patterned stressed hard gold. Bimetallic structure composed of a highly stressed layer of stress σ_2 and a bottom substrate of stress σ_1 [3.118].

The pull-down characteristics of four actuator variants were analysed with a peak tuning range of 70% achieved for a device which had a pull-down voltage of 280 V. Triangular cantilever dimensions are typically 500 μm x 1000 μm. The tuning range of this device is limited by the snap-down instability that occurs early in the movement of the cantilever. Balance between an attractive electrostatic force and a mechanical restoring force controls the position of the top electrode. A 1.5 μm thick patterned layer of benzocyclobutene (BCB) polymer was chosen for the dielectric material needed to insulate the bottom electrode. Figure 3.20 shows an SEM image of the fabricated device.

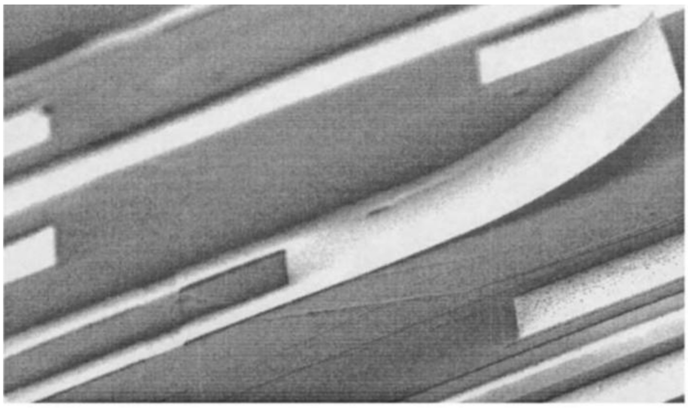

Figure 3.20 SEM image of device displaying the curved cantilever beam [3.118].

An interesting structure was demonstrated by Lee *et al*. which showed a rectangular plate (top plate of a parallel-plate tunable capacitor) supported on two ZnO piezoelectrically actuated cantilevers formed on a silicon substrate [3.124]. The cantilever-type, surface-micromachined tunable capacitor can be seen in figure 3.21. A DC voltage pulls down the movable top capacitor electrode reducing the air gap between this and a fixed bottom electrode attached to the substrate. Large capacitance tuning was achieved with a minimum capacitance of 1.82 pF at 40 V resulting in a capacitance tuning ratio of 14 to 1 (1,400%).

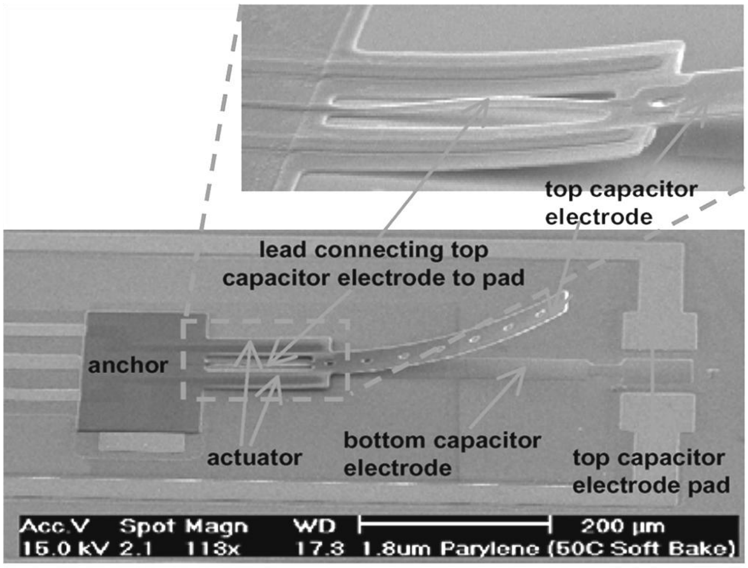

Figure 3.21 SEM image of surface-micromachined tunable capacitor showing the lead connecting top electrode to pad [3.124].

The development of a continuously variable MEMS capacitor is described by Pu *et al*. [3.125]. This zipping varactor has a movable top electrode actuated by application of a DC bias voltage between top and bottom electrodes. The device can be tuned continuously between the minimum and maximum capacitance thus eliminating the pull-down instability usually associated with electrostatic switches or actuators. Simulation results are presented for varactors with SiO_2 and PZT 30/70 dielectrics. Modelled results with high-k PZT dielectric gave continuous capacitance tuning of >60 compared to low-k SiO_2 dielectric of 11.5. Early prototypes of varactors have been fabricated on coplanar waveguide (CPW) transmission lines. In a second paper by Pu *et al.* based on earlier modelling, zipping varactor devices with large capacitance tuning range were fabricated and characterised [3.126]. A measured capacitance ratio of 16.5 was achieved for a series-mounted varactor operating at bias voltages to 46 V. The tuning range in this case was limited due to instability at 32 V bias as a result of fabrication issues. Pu *et al.* also looked at the design and simulation of zipping devices with shaped top and bottom electrodes (figure 3.22) to achieve continuously variable capacitance and controlled zipping [3.127].

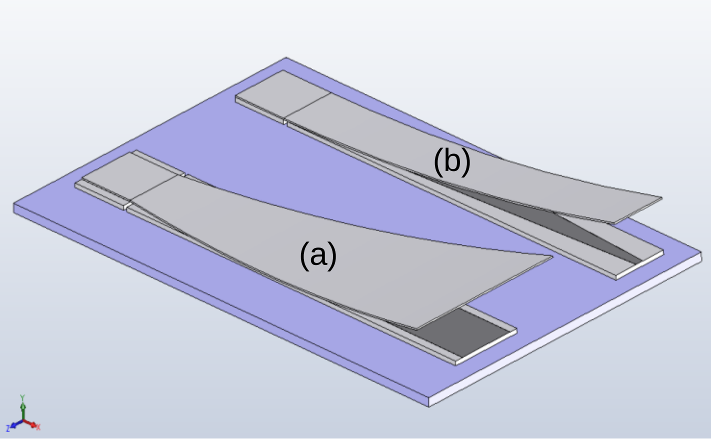

Figure 3.22 Two methods of achieving controlled zipping by use of (a) shaped top electrode and (b) shaped bottom electrode [3.127].

4 Experimental Methods

This chapter will outline the methods adopted and devised to fabricate and test a range of capacitor structures and their associated thin-film dielectric materials.

4.1 Chemical Synthesis of BZT Sol

Sol-gel compositions investigated included $Ba(Zr_{0.05}Ti_{0.95})O_3$, $Ba(Zr_{0.20}Ti_{0.80})O_3$ and $Ba(Zr_{0.35}Ti_{0.65})O_3$. For each composition the weight of the starting materials was calculated, the detail given in appendix 2. A BZT composition with very high Zr content, i.e. $Ba(Zr_{0.95}Ti_{0.05})O_3$, was also investigated but failed after a few attempts due to precipitation forming in the sol after synthesis. Such synthesis problems tended to worsen as a function of increasing Zr content. By way of an example, consider the chemical synthesis of $Ba(Zr_{0.05}Ti_{0.95})O_3$.

In order to grow the first $Ba(Zr_{0.05}Ti_{0.95})O_3$ compositional thin film, a 0.3 M concentration sol was prepared using the precursors barium acetate [$Ba(CH_3COO)_2$], zirconium (lV) propoxide [$Zr(O(CH_2)_2CH_3)_4$] and titanium (lV) butoxide [$Ti(O(CH_2)_3CH_3)_4$]. Acetic acid (CH_3COOH) was used as a solvent. Barium acetate powder was weighed and dissolved in 20 ml of acetic acid, heated gently to ~70^oC and refluxed for 1 hour. Zirconium propoxide and titanium butoxide liquids were weighed and mixed in a mole ratio Zr:Ti of 5:95 in a glove box. Upon removal from the glove box this solution was combined with 10 ml of acetic acid while stirring. After cooling the barium acetate solution to room temperature it was mixed with the combined zirconium propoxide and titanium butoxide solution. Next, 5 ml of ethylene glycol (CH_2OHCH_2OH) was added to the composite solution and stirred at room temperature overnight. Efficient mixing was essential since separate regions of $BaTiO_3$ and $BaZrO_3$ must be avoided. The concentration of the final solution was adjusted to 0.3 M by the further addition of acetic acid to make a 50 ml sol. To reduce the problem of cracking in the films, the concentration was later changed to 0.25 M by the addition of a further 10 ml of acetic acid. The addition of the ethylene glycol had the dual function of controlling the viscosity and stabilising the solution against hydrolysis. This original route adopted for BZT sol synthesis is displayed in the process flowchart of figure 4.1 and is based on, although not identical to, a sol produced by Zhai *et al*. [3.103]. This 50 ml, 0.25 M concentration solution was extremely stable and no precipitation formed over an 18 month period of use.

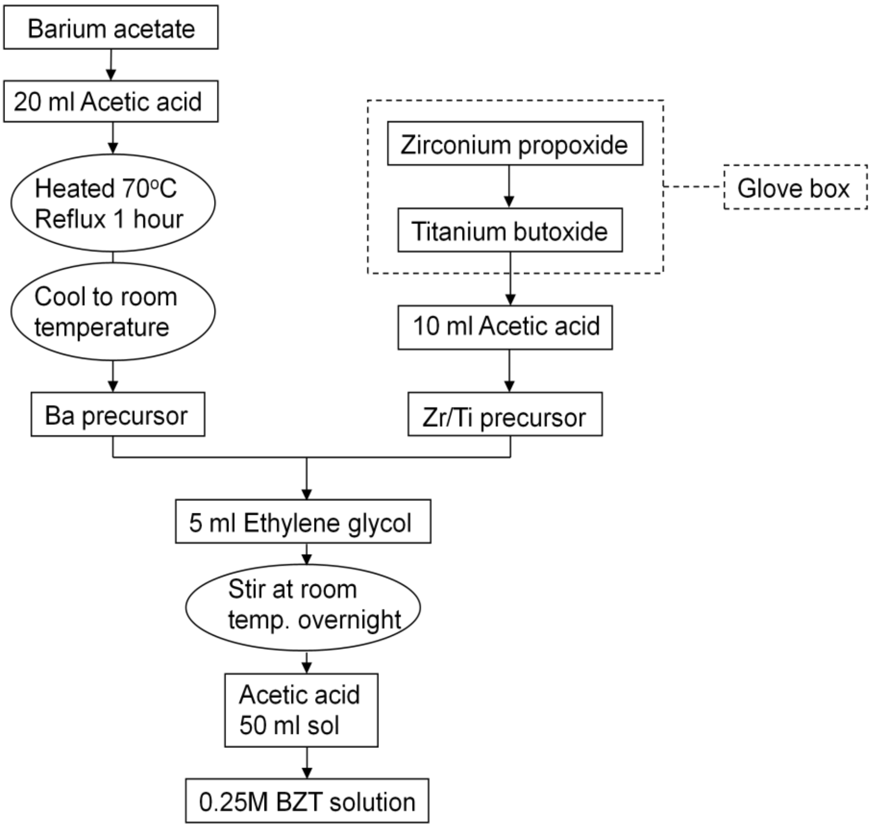

Figure 4.1 A flowchart that details the initial synthesis of BZT sol.

BZT thin films with good dielectric properties were produced from this sol (BZT1). However, some difficulty in replicating the process for this and other compositions persisted, resulting in films with inferior electrical performance. Following the synthesis routes formulated by other researchers (appendix 3) was to be avoided in some cases since 2-methoxyethanol ($CH_3OCH_2CH_2OH$), which is extremely toxic, was used as solvent or to adjust the viscosity of the final solution. Sol batch variants BZT2 to BZT6 (highlighted in table 4.1) using modified syntheses were trialled with only moderate success. After making further modifications to the sol synthesis vastly improved results were achieved for batches BZT7 to BZT9. A summary of batches processed is presented in table 4.1 and a process summary for each batch is given in appendix 4.

Table 4.1 Processed sol batches.

Sol Batch	Date Produced	Composition (Zr/Ti)	Concentration
BZT1	07/03/2007	5/95	0.3M - 0.25M
BZT2	21/11/2007	20/80	0.25M
BZT3	12/11/2008	5/95	0.25M
BZT4	01/12/2008	35/65	0.25M
BZT5	10/12/2008	35/65	0.25M
BZT6	18/12/2008	35/65	0.25M - 0.125M
BZT7	16/07/2009	5/95	0.25M
BZT8	27/07/2009	20/80	0.25M
BZT9	29/07/2009	35/65	0.25M
BZT10	04/08/2009	95/5	Failed

4.1.1 Modified and Improved BZT Sol Synthesis

Sol Batches BZT7 (5/95), BZT8 (20/80) and BZT9 (35/65).

Final modifications made to the sol synthesis recipe to achieve a clear, precipitation free and stable sol included the following.

To the barium acetate was added 30 ml of glacial acetic acid. This was then heated to 70^{o}C and refluxed for two hours. To the zirconium-titanium mixture 3 ml of acetylacetone (AcAc $CH_3COCH_2COCH_3$) was added while continually stirring. The solution continued to be stirred for 30 minutes. Once the barium acetate and acetic acid solution had cooled to room temperature the Zr-Ti precursor solution was added slowly while continuing to stir. To the combined Ba and Zr-Ti precursor solutions 5 ml of anhydrous ethylene glycol was mixed. The final solution was stirred overnight at room temperature then heated to 70^{o}C and refluxed for two hours. The only exception was batch BZT9 which required a second, additional reflux at 70^{o}C for three hours before the sol was precipitation free and remained clear. This resulted in sols with no precipitation and that remained clear for several months of use with only a small increase in the sol particle size. The films produced were of excellent microstructural quality with good dielectric properties. Examples of thin films produced from these sols and their associated characteristics are presented in the results sections.

4.1.2 BZT Sol Stability

It is important that sols remain clear and free from precipitation which can occur as the solution ages. If this is going to occur it is usually within the first few hours or days from when the sol was made. Some issues with precipitation were encountered with some of the sol batches due to problematic synthesis as highlighted in appendix 4. This was rectified by tweaking the process as detailed in sub-section 4.1.1 for sol batches BZT7, BZT8 and BZT9 which have a composition of $Ba(Zr_{0.05}Ti_{0.95})O_3$, $Ba(Zr_{0.20}Ti_{0.80})O_3$ and $Ba(Zr_{0.35}Ti_{0.65})O_3$, respectively. The three sols remained clear, free from precipitation and usable even after a period of several months. The particle size was measured using photon correlation spectroscopy (PCS), a technique described in sub-section 4.6.8. Over a period of four months measurements were made and the average particle size increased by only 3 nm from 12 nm to 15 nm. According to size distribution data obtained using PCS, particle sizes within the sol ranged from the order of 3 nm to a few hundreds of nm.

4.2 Sample Cleaning

Wafers and samples with deposited layers can become easily contaminated with grease or particulates while handling and being transported, and require cleaning before further layers of metallisation or dielectrics can be deposited, otherwise adhesion of one layer upon another may be compromised. In a cleanroom environment the particle count can be maintained low, however, in a semi-clean area such as the coatings laboratory there may be some issues with contamination. Virgin metal or dielectric layers are ideal for further processing without the need for additional cleaning. If samples become contaminated, a solvent clean with acetone and IPA (rinsed with deionised (DI) water) is preferred followed by a blow dry with filtered nitrogen. When solvent drying stains are present the samples can be further cleaned in an Ar/O_2 or pure O_2 plasma using either a barrel asher or deep reactive ion etching (DRIE) system, respectively. For stubborn contamination (e.g. inorganic contaminants) acid cleaning in weak sulphuric (H_2SO_4) solution for about 2 minutes followed by a rinse with DI water is recommended. A note of caution, a weak acid clean is generally to be avoided since this may result in microetching and an increase in the surface roughness.

The barrel etcher used for sample cleaning was a bench mounted Polaron PT7160 RF Plasma Barrel Etcher. The cylindrical chamber is designed to accommodate a 100 mm diameter wafer positioned centrally. Therefore, smaller samples had to be mounted on a blank 100 mm wafer. Samples were ashed using Ar/20%O_2 fed into the reactor from a single gas line through a vertical tube flowmeter. Gas is fed in automatically when a critical vacuum pressure is reached. For a routine cleaning operation the power is normally set to ~10 W although higher powers have been used to remove persistent contamination, typically 20 W to 30 W. The standard etching duration of either 30 or 60 minutes was used, dependent on the type of contamination and its persistence. The DRIE machine is a Surface Technology System (STS) Multiplex Advanced Silicon Etcher (ASE) and was used to etch a polymer skin left behind after photoresist mask removal. This equipment uses pure oxygen as the reactive gas as opposed to the Ar/O_2 mix employed on other etching machines.

4.3 Material Deposition Techniques

Techniques for depositing metal layers and complex oxide dielectric (ferroelectric and non-ferroelectric) thin films employ either physical or chemical methods. Physical processes can be primarily divided into thermal evaporation and sputtering; chemical methods divided into vapour phase (e.g. CVD) and liquid phase (e.g. CSD) processes. Some of the film preparation methods are presented in figure 4.2 with those currently employed as part of this research highlighted in red.

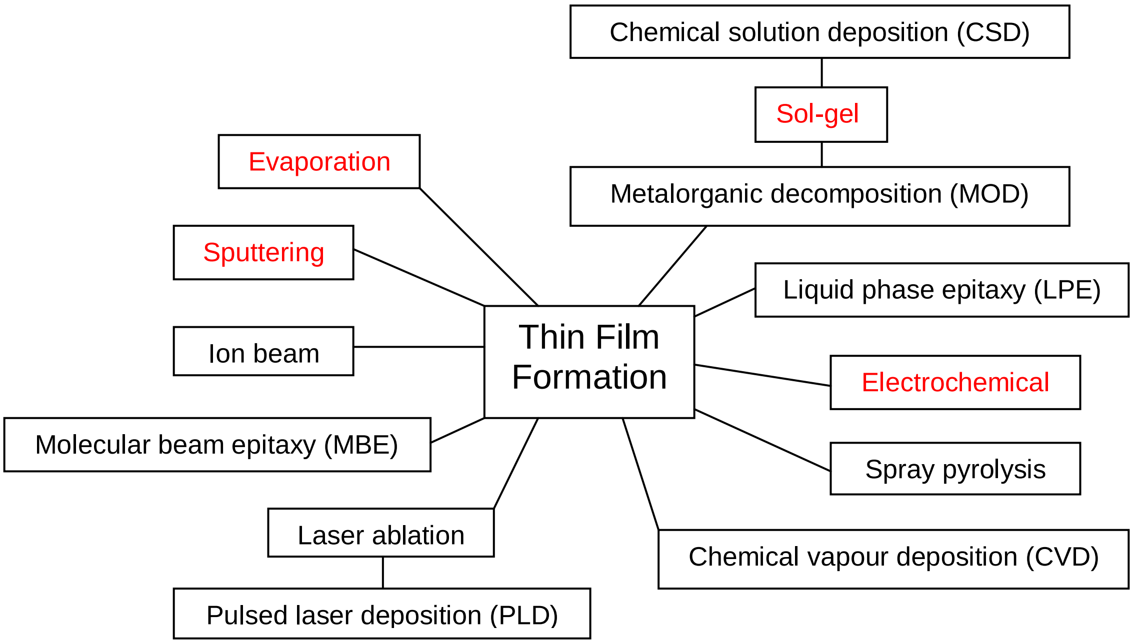

Figure 4.2 Thin film deposition methods with those in use for this work highlighted in red.

4.3.1 Substrate Metallisation (Sputtering)

Substrate used for the bulk of the research was platinised silicon (111) prepared by sputter depositing *circa* 10 nm thick Ti and 100 nm thick Pt onto 100 mm diameter SiO_2/Si wafers. The SiO_2 was thermally grown commercially to a thickness of 200 nm to prevent the formation of platinum-silicide at elevated temperatures. Platinum films show poor adhesion to semiconductor and dielectric substrates. Hence, a thin layer of titanium is deposited as an adhesion promoter between the Pt film and the substrate. The thin Ti layer and Pt were sputtered using a Nordiko 2000 sputtering system equipped with RF and DC magnetrons. The Ti was RF sputtered in argon at an RF power of 300 W and an argon pressure of 5 mTorr resulting in a deposition rate 0.33 nm/s. The Pt was DC sputtered in argon using a sputtering current of 0.7 A and voltage 420 V. The argon pressure was 5 mTorr and the deposition rate ~2.0 nm/s. Due to the low sputter yield of Pt, DC sputtering was preferred. Much higher deposition rates can be achieved for a given power density compared to the rates obtained by RF sputtering. Also, DC power can be applied since metallic targets such as

Pt are electrically conductive and hence don't suffer from charge accumulation and arcing issues associated with targets of insulating materials.

Other substrate metallisation used for the parallel-plate capacitor experiments were Pt(150nm)/Ti(10nm), Au(100nm)/Ti(10nm), Au(200nm)/Ti(10nm), Pt(100nm)/Au(200nm)/Ti(10nm), Au(100nm)/Cr(10nm), Au(800nm)/Cr(10nm), and also trialled to a limited extent was sputtered Pt(100nm)/Ti(10nm) onto which Au(100nm)/Cr(10nm) was evaporated. For the zipping varactor the metallisation on 100 mm diameter glass wafers was Pt(100nm)/Ti(10nm) and Pt(100nm)/Au(200nm)/Ti(10nm). Further details of this are provided in the results section for high-k zipping varactor (chapter 8). For the LCP investigation evaporated and sputtered Au(100nm)/Cr(10nm) was used.

4.3.2 Top Electrode Metallisation (Thermal Evaporation)

For fixed value and voltage tunable parallel-plate capacitors an array of circular Au/Cr top electrodes each ~0.73 mm in diameter was thermally evaporated onto the thin film through a shadow mask using an Edwards E480 machine. A 40 amp rated tungsten spiral filament was used to evaporate Cr and a 25 amp rated molybdenum boat used to evaporate the Au. The foil mask plate was suspended above the tungsten filament and molybdenum boat using the circular frame shown in figure 4.3. A vacuum base pressure of *circa* 3×10^{-6} mbar ($\sim2.25\times10^{-6}$ Torr) was reached prior to evaporation using a diffusion and rotary pump combination. Also, the appropriate material parameters including density were preset using the thickness measuring meter. An *in situ* crystal sensor was used for real-time monitoring of the metal layer thickness. Electrical current used to evaporate the Cr was 28 A and for Au 25 A. The target thickness for Cr and Au was 10 nm and 100 nm, respectively.

Figure 4.3 shows the inside of the evaporation chamber (stainless steel bell jar). Samples were positioned on the mask plate and secured with Kapton tape. Five small (~2 cm^2) Si pieces can be seen mounted on the metal foil plate that is divided into nine square recesses for processing multiple samples. However, using this mask plate resulted in a significant misalignment of the Cr and Au layers primarily due to a small gap between the metal foil mask and samples. Alternatively, a smaller square electrode array could be deposited by thermal evaporation through a shadow mask utilising an etched silicon FBAR structure. In this case the sample made improved contact with the rigid silicon mask plate to the extent that no misalignment between the Au and Cr layers could be observed. The silicon mask plates (not visible in figure 4.3) were attached to the underside of the metal foil mask plate with Kapton tape.

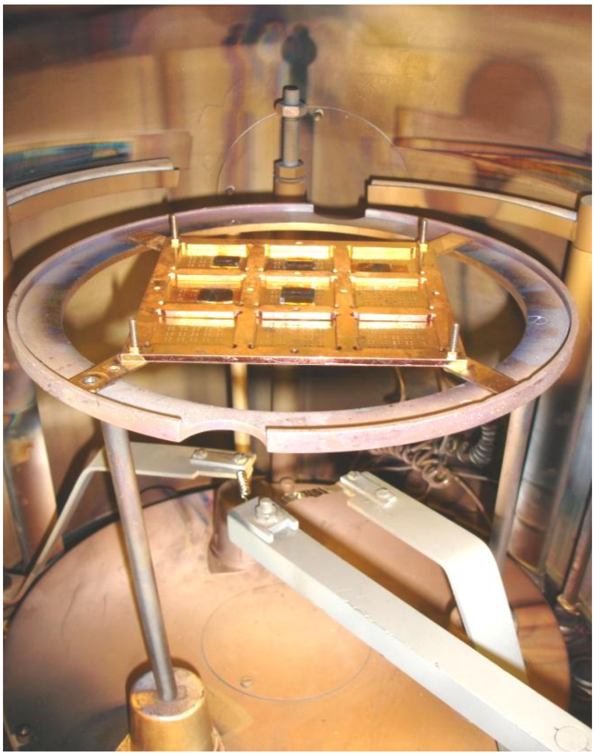

Figure 4.3 View inside the vacuum chamber of the Edwards E480 thermal evaporator showing the position of the metal mask plate relative to the tungsten spiral filament and molybdenum boat.

4.3.3 Sol-Gel Deposition of BZT

A single 100 mm metallised SiO_2/Si wafer was hand cleaved into ~2 cm^2 pieces for ease of handling. The sol-gel was deposited onto the substrate using a syringe fitted with a 0.2 μm Whatman filter to avoid particulate contamination, then spun at an optimum speed of 3000 rpm for 30 seconds. Subsequent pyrolysis heat treatment to remove residual organics and annealing of films was initially performed using three varied approaches. (1) Each layer dried at 350°C for 10 minutes and annealed at 700°C for 15 minutes by hotplate. (2) Each layer dried at 350°C for 10 minutes with a final anneal of all layers at 700°C by either hotplate or RTA. (3) Each layer dried at 350°C for 5 minutes and at 550°C for 5 minutes by hotplate and a final anneal of all layers by RTA at temperatures between 550°C and 700°C. Typically six to eight layers in total were deposited. The preferred route for the BZT sol-gel coating process is shown in figure 4.4.

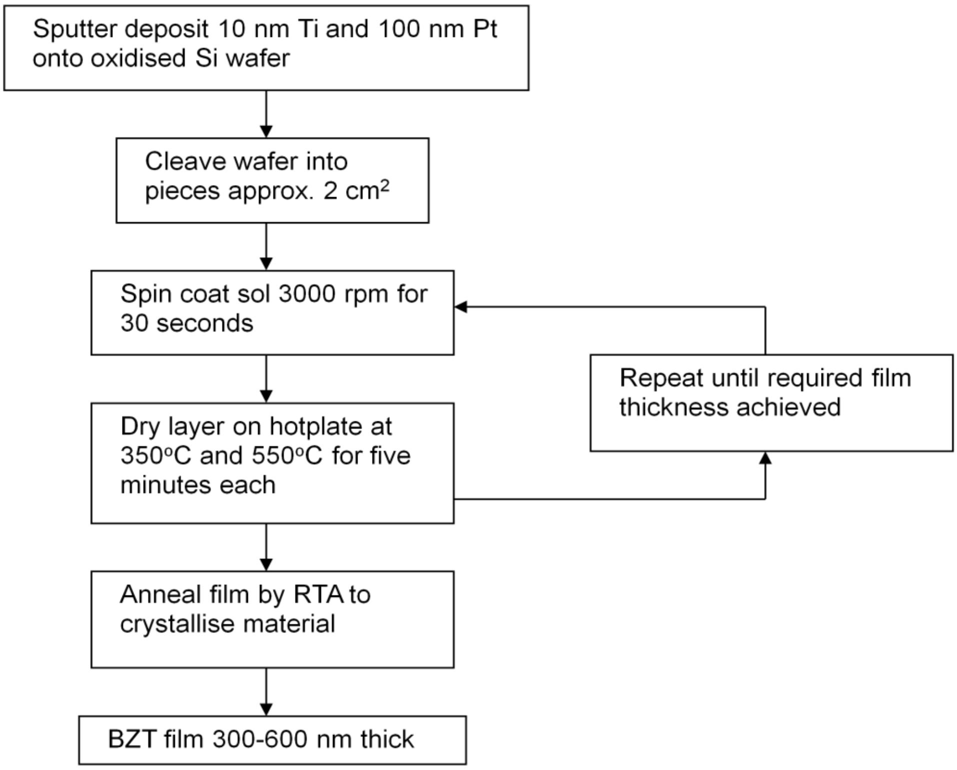

Figure 4.4 BZT thin film fabrication process flow.

Having deposited and crystallised the thin film, a small area of the film was etched in a 10% HF solution to expose the Pt bottom contact so that film thickness and electrical measurements could be taken. Film thickness was measured on the Dektak surface profile measuring instrument and compared to cross-sectional SEM measurements. For eight layers spun, films typically 600 nm thick were deposited from the 0.3 M solution (75 nm per layer) and 400 nm thick from the 0.25 M sol (50 nm per layer).

Experimental trials were conducted to determine the effect of varying the spin speed of BZT(20/80) sol on resultant film thickness and microstructure. Six layers in each case were spun onto platinised silicon substrates and heat treated; a final crystallisation anneal was performed at 700°C for 15 minutes on the hotplate. Spin speeds used varied from 1500 rpm to 4000 rpm. A graph of BZT film thickness and dielectric constant as a function of spin speed was plotted from thicknesses measured by Dektak surface profilometer and SEM, and from dielectric constants calculated using MIM capacitor measurements (figure 4.5).

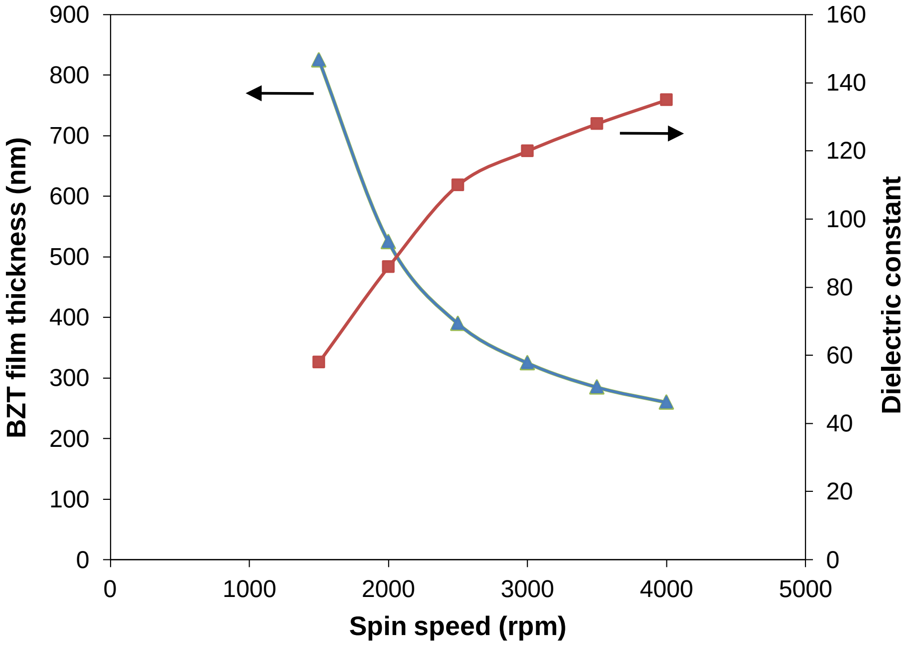

.

Figure 4.5 The effect of spin speed on BZT film thickness and dielectric constant for six layers spun. Thickness measured after final annealing.

From figure 4.5 it can be seen that there was initially a rapid reduction in film thickness as the spin speed was increased from 1500 rpm which then reduced more slowly above 2500 rpm. Film uniformity improved as the spin speed was increased (figure 4.6). The greatest variation in BZT film thickness was ±50 nm for a sample piece (of area 2 cm^2) that had been spin coated at 1500 rpm. Also, as the spin speed was increased and the films became dense, the dielectric constant of the material increased. The nonlinear relationship between spin speed, thickness and dielectric constant was partly due to the degree of solvent evaporation while spinning the sol, which also impacted on the film microstructure after the crystallisation anneal. The effect of spin speed on the BZT thin film microstructure can be seen in the SEM micrographs of figure 4.6.

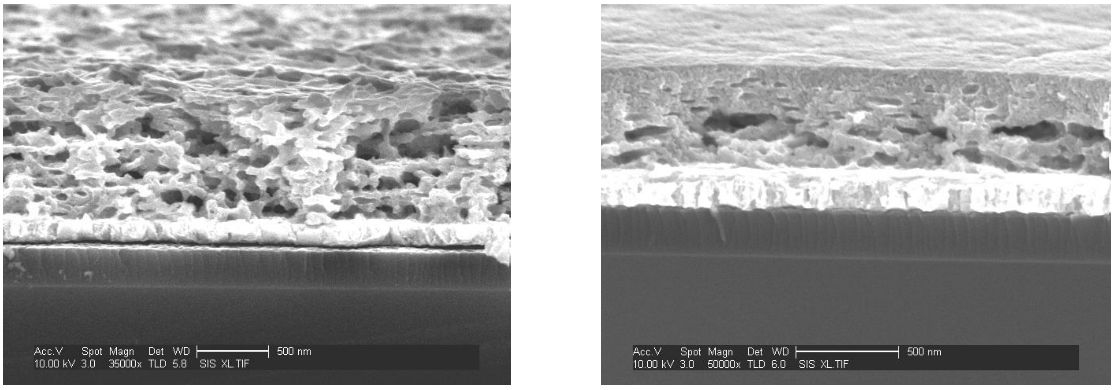

1500 rpm 2000 rpm

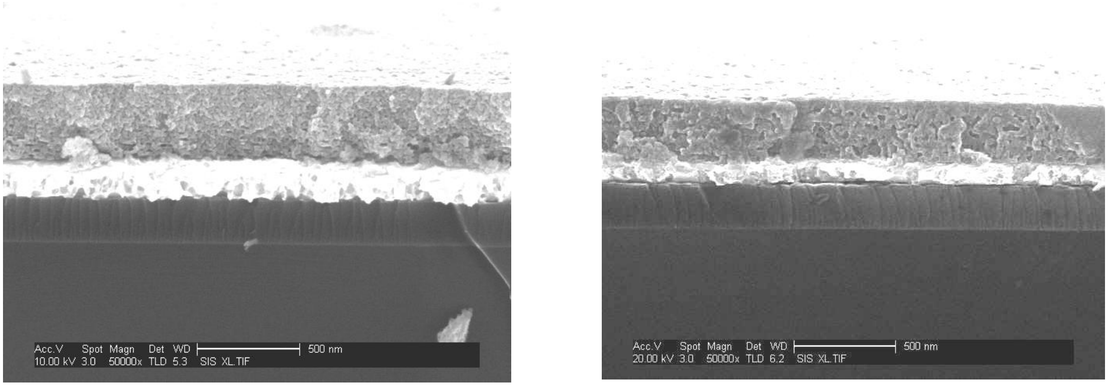

2500 rpm 3000 rpm

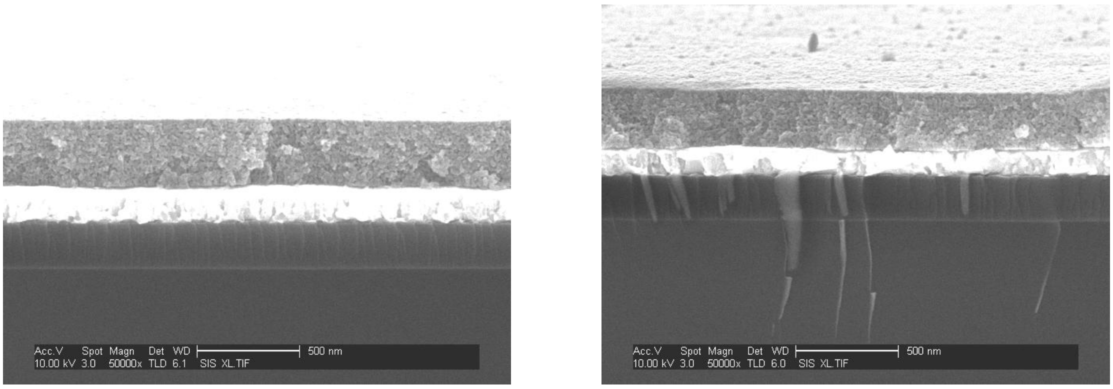

3500 rpm 4000 rpm

Figure 4.6 SEM micrographs of BZT thin films deposited on platinised silicon substrates by spin coating sol-gel at the speeds indicated.

It is evident from the SEM sectional images (figure 4.6) that as the spin speed was increased the films became dense and more uniform after annealing. At the slowest spin speed of 1500 rpm the film was interspersed with very large voids created by larger volumes of solvent and air bubbles being driven off when heat treated. To a lesser extent voids can also be seen in the film spun at 2000 rpm. The incorporation of voids into the films also had a noticeable effect on reducing the dielectric constant at spin speeds below 2500 rpm. The use of porous material is a way of fabricating low-k dielectric thin films. The dielectric loss of the material in each case was measured and found to be ~0.02 for films which had been spun at 2500 rpm and above, and 0.03 and 0.04 for films spun at 2000 rpm and 1500 rpm, respectively. For completeness the XRD scans of the polycrystalline films spun at each extreme of 1500 rpm and 4000 rpm can be seen in figure 4.7.

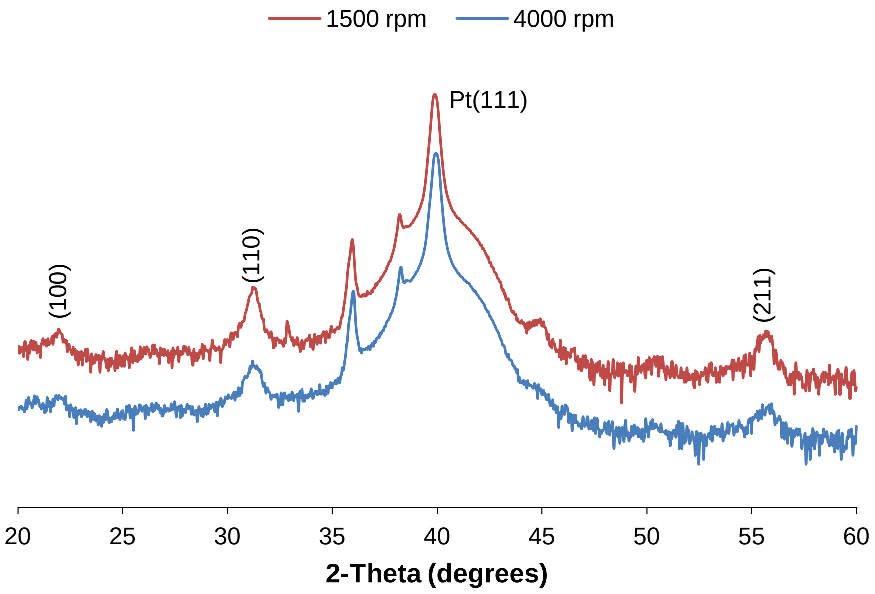

Figure 4.7 XRD diffractograms of BZT thin films spin coated at 1500 rpm and 4000 rpm and annealed on the hotplate at 700^{o}C for 15 minutes.

The XRD scans show good crystallisation of BZT thin films with the main crystallographic peak at (110). Similar spectra were observed for the other films spin coated at speeds between 1500 rpm and 4000 rpm.

4.3.4 RF Magnetron Sputtering of BZN

RF magnetron sputtering was the preferred deposition method for growing thin BZN films with fixed stoichiometry. One of the main advantages of using sputtering over chemical solution deposition methods is that films can grow with a preferential orientation. Compared to BZN thin films deposited by RF magnetron sputtering, sol-gel derived BZN films have inferior dielectric properties, i.e., room temperature dielectric constants typically <150, and higher dielectric loss (~0.01).

BZN thin films (~300 nm thick) were deposited on platinised and Au coated silicon wafer pieces by RF magnetron sputtering using a 200 mm diameter stoichiometric target supplied by Pi-Kem Limited and specified as Bi(1.5)Zn(1.0)Nb(1.5) oxide, 99% purity raw material of density 6.86 g/cc. The sputtering system (Scientific Vacuum Systems (SVS) V2400) has a target to substrate separation of 100 mm. Power levels can be set at up to 1250 W. However, to avoid damage to the ceramic target due to thermal shock, power levels were set to a maximum of 400 W. *In situ* substrate heating to 760^{o}C, and gas pressure to 50 mTorr, are attainable. With an overnight pump-down using the rotary and cryo pump (temperature typically 15K) a base pressure of ~$3x10^{-7}$ Torr can be achieved. The sophisticated control system of the sputtering equipment has a human machine interface (HMI) operator panel (main control and status display) which is connected to a programmable controller (PLC). The HMI allows control of the machine, the editing of processes and the setting up of parameters, among other things. Under programmable control the SVS will automatically perform all stages of the process including substrate heating, gas handling, substrate rotation and oscillation, pre-sputter target clean, and the main sputtering operation.

Cross-wafer uniformity of deposition over a 100 mm Si wafer was investigated for variations in substrate table oscillation. BZN sputtering parameters were: RF power 400 W, *in situ* substrate temperature 300^{o}C, working gas pressure 40 mTorr and an Ar/O_2 gas ratio 85/15. A rotational speed of 2 rpm was maintained for the substrate table throughout. The deposition duration was 200 minutes. Kapton tape was used to mask off a narrow area along the diameter of the wafer. From the measured thickness (using Dektak) at regular intervals across the diameter of the wafer, the extent of cross-wafer uniformity was established (figure 4.8). By determining the deposition rate empirically in this way, the sputtered BZN film thickness could be controlled with reasonable precision.

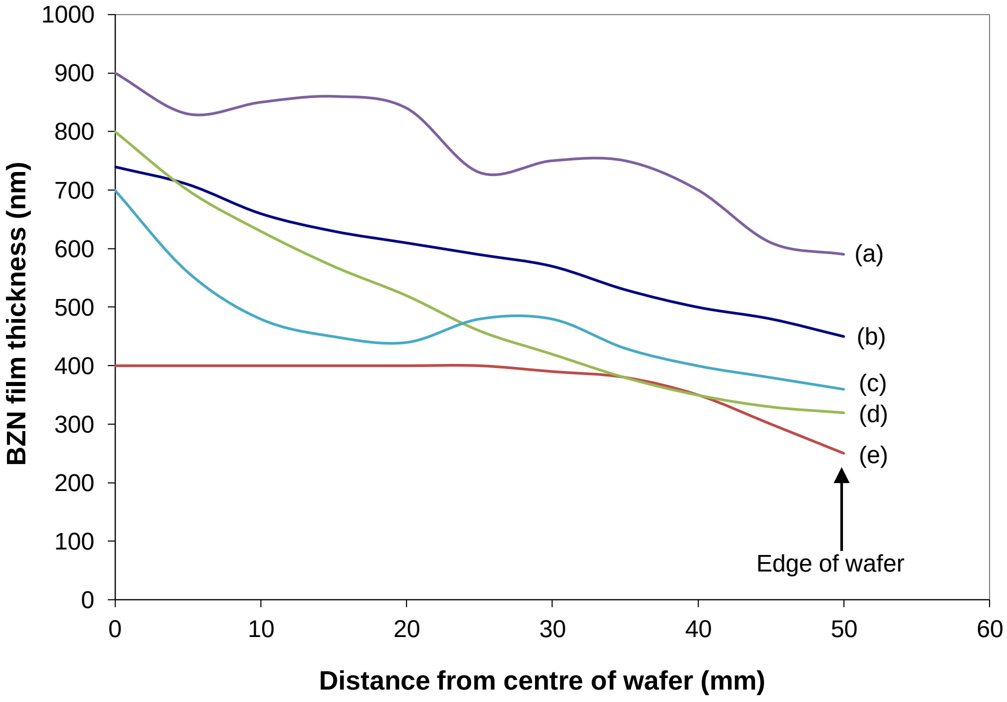

Figure 4.8 Variation in BZN film thickness from centre to edge of 100 mm diameter wafer for different oscillation settings (a) 0^o (fixed centrally), (b) 15^o-20^o, (c) 20^o-25^o (d) 25^o (fixed) and (e) 20^o-30^o.

In figure 4.8 significant differences in the BZN deposition rate and uniformity can be seen as the oscillation settings are changed. Curve (a) displays the thickness variation for no oscillation and the substrate table positioned centrally below the target. Curve (d) shows the variation for no oscillation but the substrate table position fixed at 25^o with respect to the central position. Curve (b) shows the variation for oscillation between 15^o and 20^o, curve (c) the oscillation between 20^o and 25^o, and curve (e) the oscillation between 20^o and 30^o. The best uniformity was achieved for the maximum oscillation from 20^o to

30^o (curve e), although the BZN deposition rate (2 nm/min) was somewhat suppressed. Cross-wafer thickness non-uniformity is not necessarily seen as an issue at this stage since it enables devices (e.g. zipping varactor) to be tested and characterised with different dielectric thicknesses. For this purpose a gradual, uniform variation in thickness across the wafer should be chosen (e.g. the smaller oscillation angle between 15^o and 20^o as in curve b of figure 4.8).

4.3.5 Nickel Plating

Nickel electroplating was developed as a hard masking process for the reactive ion etching of zipping varactor features in thin BZN films. The apparatus for the plating is shown in figure 4.9.

Figure 4.9 Nickel electroplating facility (plating bath, heater/stirrer unit, and multimeter). The DC current supply unit is not shown.

The plating operation was performed in a large (3 litre) glass beaker containing a solution (electrolyte) of nickel sulphamate [$Ni(NH_2SO_3)_2$], nickel chloride ($NiCl_26H_2O$) and boric acid (H_3BO_3). Pure nickel balls were used as the anode during nickel plating. The temperature of the plating solution was maintained at

50^{o}C. The wafer to be plated was attached to the cathode by means of a crocodile clip and immersed into the solution. A current supply to the plating cell was provided by a DC current calibrator type 132 unit. A hand-held multimeter placed in series with the current supply and anode was used to measure the current in mA. The solution was continually agitated using a magnetic stirrer at the rate of 500 rpm. After a set plating time to give the desired plating thickness based on Faraday’s equation, the wafer was removed from the electrolyte and rinsed in flowing water, and then blow dried with nitrogen.

4.4 Thermal Processing Procedures

The thermal processing of materials is a critical stage in the development of good quality thin-film dielectrics for capacitor applications, and has a significant influence on the growth characteristics and crystallisation (columnar, granular). This can affect such things as residual stress, film densification, porosity and surface roughness. In this investigation two thermal processing methods were adopted, hotplate and rapid thermal annealing (RTA). There is a noticeable difference between hotplate annealing and rapid thermal processing in the way that some dielectric materials grow. In some complex oxide materials a columnar grain structure is encouraged to grow by thermal annealing the sample on a hotplate where heat is directed through the substrate to the thin film. With RTA the heating of the sample is by radiant thermal energy using halogen lamps so that the substrate and film are heated simultaneously and more rapidly than by hotplate. This can influence grain growth and crystallisation of the material in ways different to that achieved by hotplate annealing, and may encourage the growth of a granular structure as opposed to a columnar structure.

4.4.1 Hotplate Thermal Treatment and Annealing

Two hotplates were used in this work for the thermal processing of BZT and BZN dielectric thin films and multilayer structures. For lower temperature ($\leq 350^{o}$C) processing a Thermolyne Cimarec 3 hotplate with manual temperature control was employed. This hotplate was used either at a fixed temperature preheated to 350°C (e.g. to pyrolyse the sol-gel BZT thin films) or it was ramped up from room temperature to 350°C to facilitate a more gentle heating of the sample. The heating characteristic of this hotplate can be seen in figure 4.10. For higher temperature processing (500°C-700°C) a Sawatec HP-160/700 programmable hotplate was employed which also allows for manual loading and hand timed processing.

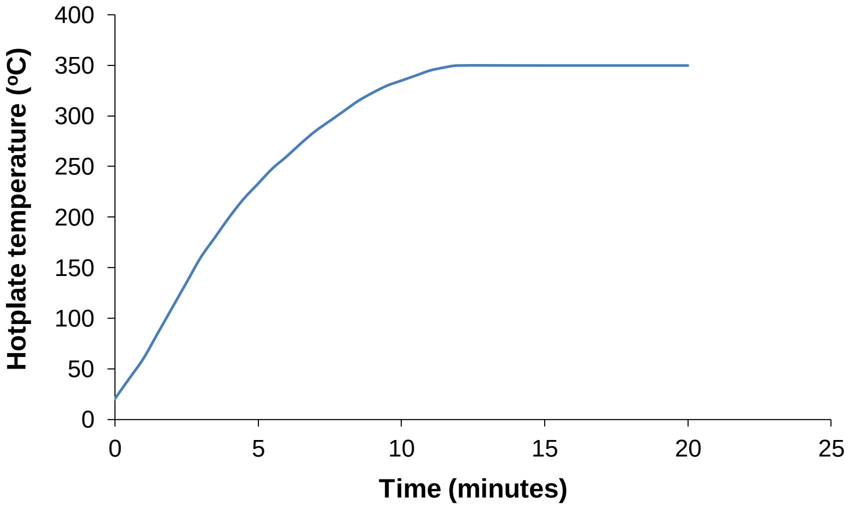

Figure 4.10 Hotplate (Cimarec) temperature ramp from room temperature to 350°C.

A Raytek noncontact infrared thermometer was used to measure the surface temperature. The unit's optics sense emitted, reflected and transmitted energy which are collected and focused onto a detector. Electronics in the unit translates the thermal radiation into a temperature reading. A built in laser is used to aim the thermometer. The accuracy of the temperature reading is: ±1°C error in the reading for temperatures ≤100°C and ±1% error in the reading for temperatures >100°C.

4.4.2 Rapid Thermal Annealing (RTA)

Rapid thermal processing was used for higher temperature annealing and crystallisation of dielectric thin films. The equipment used in this investigation was an AG Associates Heatpulse 210 system that can operate to a maximum working temperature of 800°C. A quartz sample holder is designed to take a

100 mm diameter wafer so that smaller samples (~2 cm^2), such as those used in this study, must be mounted on a blank 100 mm mechanical silicon wafer. The temperature of the process is measured by a thermocouple attached to the quartz sample holder tray. This thermocouple is not configured to operate at temperatures above 800^{o}C as it will not survive repeated processing. The RTA is fitted with a supply of nitrogen, argon and air for providing annealing atmospheres. Each gas can be used independently or in combination with others and is controlled by a manual flow meter. A flow rate of 30 L/min for air was selected. Radiant energy from tungsten-halogen lamps surrounding the sample chamber provides the heating and is cooled by the flow of compressed air. Samples are heated radiatively at their top surface and conductively at their bottom surface. Control of the equipment is menu driven from a computer by selecting a recipe file. Recipes can be edited and thermal processes changed. After processing and before removing the sample, the RTA is cooled to below 250^{o}C by heat dissipation to the surroundings and by the gas flow. Typical thermal ramp profiles of two developed recipes can be seen in figure 4.11. This shows the minimum RTA temperature (200^{o}C plateau) for BZN annealing and the maximum temperature (750^{o}C plateau) for BZN and BZT annealing.

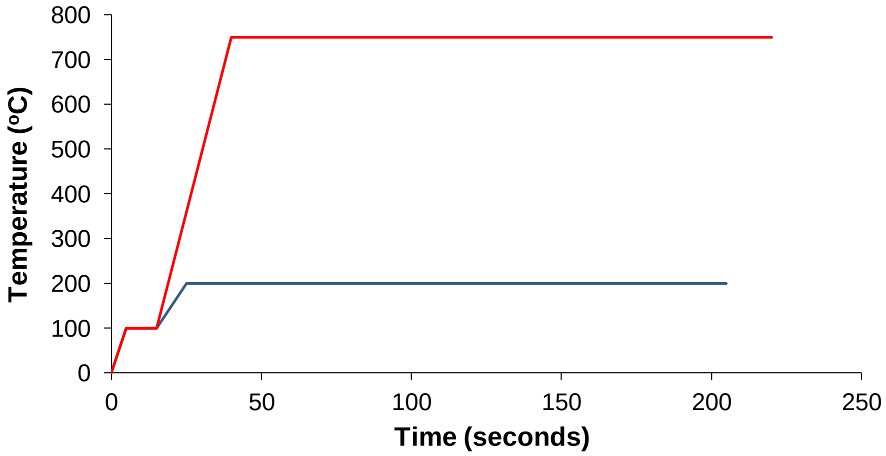

Figure 4.11 RTA ramp profiles for the lowest and highest processing temperatures.

For the lowest RTA temperature (200^{o}C) used, the profile ramped from room temperature to 100^{o}C in 5 seconds, was held at 100^{o}C for 10 seconds, and then ramped to the annealing temperature of 200^oC in10 seconds. This equated to a 10$^oC/s$ heating ramp. For the highest RTA temperature (750^oC), the ramp time from 100^oC to the annealing temperature of 750^oC was 25 seconds equating to a 26$^oC/s$ heating ramp. The 100^oC plateau at the start was introduced to avoid an initial temperature overshoot. The duration of the main temperature plateau for these experiments ranged from 60 to 180 seconds.

4.5 Etching of Materials

The etching of metal and complex oxide dielectric layers can be performed by either wet chemical etching or dry etching. Various dry etching techniques can be employed including reactive ion etching (RIE), plasma etching, ion beam milling, reactive ion beam etching (RIBE) and chemically assisted ion beam etching (CAIBE). The method chosen for etching BZT was a wet chemical process and for BZN was RIE. Masking of BZT and BZN thin films was performed using either photoresist or metal layers.

4.5.1 Wet Chemical Etching

Wet chemical etching was performed on metal and dielectric films. Metals such as gold, chromium, and nickel were etched using standard etchants. Gold was etched in a solution of iodine and potassium iodide [I_2(16g)/KI(42g)/H_2O(142g)]; chromium was etched with a solution of ceric ammonium nitrate and acetic acid [$Ce(NH_4)_2(NO_3)_6$(16%)/CH_3COOH(3%)/H_2O(81%) percentage by weight]; nickel was etched in ferric chloride ($FeCl_3$). The etching of BZT used a 5% HF solution which gave an etching rate of ~300 nm/min. Attempts were made by Lu *et al*. to wet etch BZN [4.1]. They found that as-deposited BZN could be etched with 1:10 buffered HF solution whereas fully crystallised BZN required a much stronger 40% HF solution. Based on the literature review conducted and reported on in section 3.10 of this thesis, it was decided to use a combination of fluorine and chlorine chemistry in the wet etching process. Hence, for crystalline BZN an etching solution containing 0.5% HF, 4.5% HCl and 95% H_2O was used resulting in an etch rate of 60 nm/min. Both the fluorine and chlorine in the solution formed volatile species with the elemental components of the BZN.

4.5.2 Dry Etching

The etching was performed in a Plasma Technology RIE80 planar etching system of the type shown schematically in figure 4.12. The excitation frequency is 13.56 MHz with impedance tuning to achieve reflected power levels below 1% of the forward operating power. The top plate of the vacuum chamber is the grounded electrode of a parallel-plate arrangement. The substrate platform is water cooled via a chiller unit and the temperature maintained at about 16^{o}C. For the etching trials a graphite cover plate was positioned over the cathode, since a carbon cathode yields a very smooth and much cleaner etched surface than a stainless steel or anodised aluminium cathode. In the case of stainless steel or anodised Al cathodes, surface roughness of films is caused by micromasking from the deposition of contaminants such as Fe and Al.

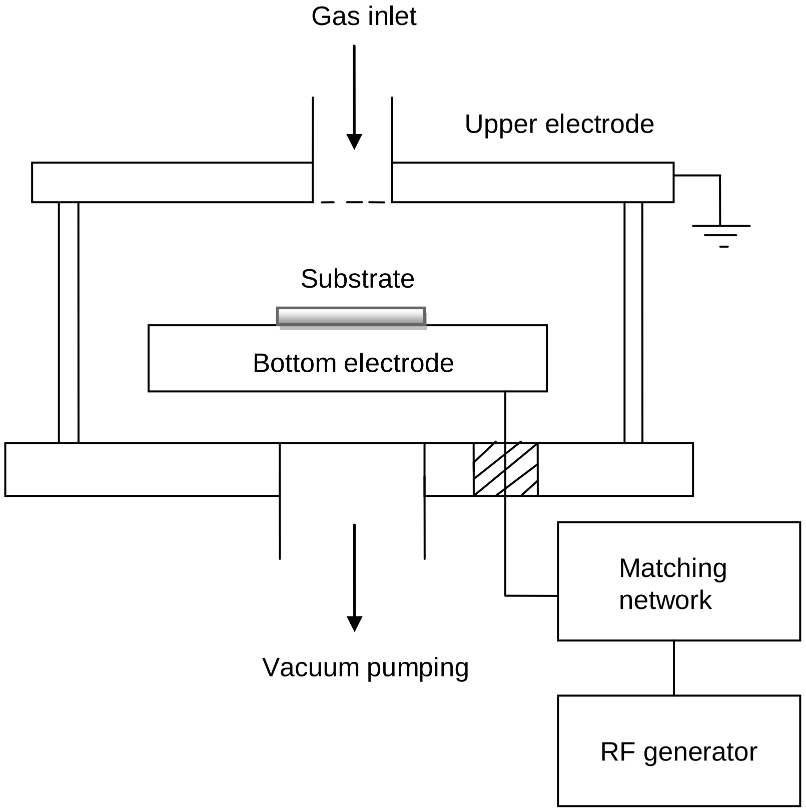

Figure 4.12 Schematic of the planar reactive ion etching system.

A rotary and mechanical booster pump maintains a vacuum base pressure down to $1x10^{-4}$ torr. Mass flow controllers and a variable conductance valve between the pumps and the chamber control the flow of gas into and out of the reactor and the chamber pressure, respectively. The gases used were Ar, $20\%O_2/80\%Ar$ and CHF_3 fed into the chamber on three separate gas lines through a gas showerhead in the centre of the top plate. Argon was used primarily for etching metal layers, Cr, Au, Ti and Pt. In some cases the Ti can become oxidised forming TiO_x. If a TiO_2 film is present then this can be etched using a CHF_3 plasma. A combination of CHF_3 and Ar gases were used for etching dielectric layers such as BZN.

4.6 Materials Characterisation

Various analytical techniques were employed to examine the microstructure and composition of the metallic and dielectric thin films used in this investigation including, scanning electron microscopy (SEM), energy-dispersive x-ray (EDX), focused ion beam (FIB)-SEM, optical microscopy, x-ray diffraction (XRD), x-ray photoelectron spectroscopy (XPS), atomic force microscopy (AFM), inductively coupled plasma-mass spectrometry (ICP-MS), photon correlation spectroscopy (PCS) and Dektak profilometer. This section will present a brief overview of these methods.

4.6.1 SEM and EDX Analysis

Scanning electron microscopy (SEM) with built-in capability of energy-dispersive x-ray (EDX) analysis of the elements was used for the inspection of various thin film materials in this study. SEM has been used to examine the detailed surface morphology and cross-sectional structure of as-deposited and subsequent heat treated metal and dielectric films.

The scanning electron microscope uses a focused beam of electrons to impact on the surface of the sample to be imaged or analysed. The signals generated can originate from relatively low energy (few tens of eV) secondary electrons, high energy backscattered electrons (energies up to 40 keV) and characteristic x-rays.

Two systems were used, a Sirion XL30 Schottky Field Emission Gun (SFEG) SEM and an Environmental SEM (ESEM). The ESEM is a specialised form of electron microscopy that enables analysis of insulating materials. The presence of a gas or “environment” in the specimen chamber, resulting in a low vacuum, acts as an electrical charge conductor avoiding sample charging and facilitating signal detection. However, the ESEM is limited in resolving the feature sizes typically associated with samples in this study and would generally be used only at times when the SFEG-SEM was nonoperational. Therefore, for the bulk of the work, the SFEG-SEM was used with its ability to image at 250,000 times magnification, resolving to the order of nanometres. To achieve this, the SFEG-SEM utilises a sharp tungsten tip from which electrons are emitted by means of a quantum mechanical tunnelling process when in close proximity to a positively biased extraction electrode. Acceleration voltages used ranged from 5 kV to 20 kV. The SFEG employed here was one of two possible types of field emission source, a thermal field emission source as opposed to a cold field emission source. The main advantage of the field emission source is a higher brightness giving higher resolution compared to a purely thermionic gun.

To minimise the effect of charging, samples were prepared by attaching the substrate to the holder using conductive carbon tape. For highly insulating samples, a very thin (few nm) layer of carbon or gold was sputter deposited onto the surface using a SEM-prep coater. The coating provided a conducting path to ground so that surface charging during examination was avoided. This was particularly useful for enhancing the contrast between photoresist and the substrate material.

Energy-dispersive x-ray (EDX) was used for the compositional analysis of the BZT and BZN thin films typically 300 nm to 400 nm thick. A cobalt standard was used to calibrate the EDX signal prior to measuring the actual sample. Analysis originates from within the film in contrast to surface analysis methods. This technique therefore provided no information about film composition in the surface atomic layers. Also, depth-profiling analysis is not possible with this technique. Other disadvantages are insensitivity to light elements and poor detection sensitivity of ~1% atomic. However, it does give relative atomic percentages of constituents so that the stoichiometry of the various BZT compositions could be verified. An acceleration voltage of 10 kV was used in the analysis. For each element present the weight and atomic percentages were recorded.

4.6.2 Focused Ion Beam (FIB)-SEM

The simple and fast method of viewing a sample in section by SEM is to fracture cleave the substrate. Generally this method is satisfactory. However, this does not always produce a clean, regular surface for imaging by SEM, and it can be difficult to distinguish between different layers. This can be resolved by FIB-SEM whereby a focused ion beam is used to cut a very small slot into the material under investigation so that the sample can be viewed in section. The FEI FIB 200 instrument has a gallium (Ga) ion source which is heated to melt the gallium. The liquid Ga flows along a wire and Ga ions are emitted by a high electric field (i.e. column voltage) up to 30 kV. A variable beam current from 1 pA to 1150 pA can be used for imaging (70 pA), course milling (1000+ pA) and to cut trenches or lines. The equipment also has a platinum source that can be used to deposit Pt as a protective coating or for making conductive paths.

4.6.3 Optical Microscopy

The optical microscope used to image thin film surface features was a Polyvar microscope fitted with a digital camera for large area imaging (~70 mm diameter). The camera is attached to a desk top computer. The microscope has been calibrated and software developed so that measurements can be made on the images captured using the 5x, 10x, 20x and 50x objective lenses. The captured images are stored on computer or via a USB port to an external storage device.

4.6.4 X-Ray Diffraction (XRD)

X-ray diffraction (XRD) is a technique used to characterise the amorphous and crystallisation states of the dielectric thin films before and after annealing, respectively. The various crystalline forms known as phases of the compound can be identified and quantified for powders and solid samples. Identification is achieved by comparing the XRD pattern or diffractogram obtained from an unknown sample with an internationally recognised database (International Centre for Diffraction Data) containing reference patterns. Reference intensity values are accessible from data provided by the Joint Committee on Powder Diffraction Standards (JCPDS). An example of the JCPDS data for $Ba(Zr_{0.20}Ti_{0.80})O_3$ is shown in table 4.2. For completeness, a comparison can also be made against diffractograms published in other reference works by established researchers.

Table 4.2 JCPDS data for $Ba(Zr_{0.20}Ti_{0.80})O_3$ using Cu K_α radiation with Ni filter.

2θ (Deg.)	Intensity	hkl
21.917	8	100
31.193	100	110
38.455	22	111
44.692	25	200
50.314	7	210
55.512	45	211
65.031	25	220

The equipment used in this study was a Siemens D5005 x-ray diffractometer with Cu K_α radiation source (λ = 0.154 nm). X-ray diffractograms for BZT and BZN thin films show the x-ray intensity (in arbitrary units) as a function of 2θ in degrees from 20^o to 60^o in increments of 0.04^o. The lattice spacing d for which a peak appears can be calculated from the Bragg equation $n\lambda = 2d\sin\theta$, where λ is the wavelength of the radiation, n is an integer number, and θ is the angle between the lattice planes and the incident beam. The diffractogram shows phases present as peak positions, phase concentrations as peak heights, and crystallite size/strain as indicated by peak widths. Table 4.2 data shows that the maximum phase concentration (peak intensity) for BZT occurs at a peak position of $2\theta=31.193^{o}$ for the (110) plane.

The widths of the peaks in a particular phase pattern provide an indication of the average crystallite or grain size. Large crystallites or grains give rise to sharp, narrow peaks, while the peak width increases as the crystallite or grain size reduces. However, peak broadening also occurs as a result of variations in d-spacing caused by micro-strain but can be differentiated from that of crystallite size effect. The crystallite/grain size can be compared to the average grain size as measured by SEM and atomic force microscopy (AFM).

4.6.5 X-Ray Photoelectron Spectroscopy (XPS)

XPS has become one of the key non-destructive surface characterisation techniques. It is a surface sensitive technique ideal for application to thin film studies since surface properties are different to bulk properties and critical to interfacial interactions. It is also a highly sensitive technique for the analysis of surface contaminations.

The XPS equipment used in these studies was a VG ESCALAB Mk2 with magnesium source and Al anode. An acceleration voltage of 14 kV produces monochromatic x-ray radiation which irradiates the surface of the sample under investigation. This results in the ejection of photoelectrons from the surface of the substrate. The depth of analysis in XPS is determined by the inelastic mean free path λ of the ejected electrons, and is generally of the order 10-40 Å. The x-ray photoelectron energy (kinetic energy) is calculated from $KE=h\nu-BE-\phi$ where $h\nu$ is the x-ray energy, BE is the binding energy of the electron and ϕ is the work function of the material, a constant for a given material. An electron analyser counts electrons of a given energy and the spectrometer scans across an energy range resulting in an x-ray photoelectron spectrum of counts as a function of either KE or BE in electron volts. Values of BE are tabulated for all elements. From the energy data, qualitative information (elements) and quantitative information (concentrations) are derived.

This technique can also be used to access composition-depth information by sputter eroding the thin film. The profile is obtained by sequential ion beam etching and surface analysis. An inert argon ion beam from a cold-cathode ion source of energy a few keV is scanned electrostatically across the surface of the sample to produce a rectangular crater. Using inert argon avoids chemical interaction at the surface. Spectroscopy is performed before etching and following each etch cycle to build up a depth profile. Multi-element depth profiles are plotted composition (atomic %) as a function of depth.

4.6.6 Atomic Force Microscopy (AFM)

Scanning probe microscopy (SPM) is a technique whereby a sharp probe is scanned across the surface of a sample and the tip sample interaction monitored. SPM consists of two primary forms, scanning tunnelling microscopy (STM) and atomic force microscopy (AFM) of which the latter has three distinct modes of operation, contact mode, noncontact mode or tapping mode AFM. In this study tapping mode AFM was used, the equipment being a Digital Instruments Dimension 3000 AFM. Silicon probes comprised of 125 μm long single beam cantilever and tip integrated assembly with a nominal tip radius of curvature 5-10 nm. Other characteristics of the etched silicon probes are spring constant 20-100 N/m and resonant frequency 200-400 kHz. Tapping mode AFM operates by scanning a tip attached to the end of an oscillating cantilever across the sample surface. The tip lightly “taps” on the sample surface during scanning contacting the surface at the bottom of its swing. The topography of the sample surface is obtained by recording the vertical position z of the scanner for each x, y data point provided constant oscillation amplitude and hence tip-sample interaction is maintained. Advantages of tapping mode AFM include higher lateral (x, y) resolution (1 nm to 5 nm), lower forces and less damage to soft samples (no scraping). The disadvantage is a slightly slower scan speed compared to contact mode AFM. Section and roughness analysis can be performed in addition to three-dimensional imaging.

4.6.7 Inductively Coupled Plasma – Mass Spectrometry (ICP-MS)

A Perkin Elmer Sciex-Elan 9000 ICP-MS was used to analyse the chemical composition of BZT sols. The ICP-MS is a technique for determining the elemental composition of samples generally in liquid or gaseous form. However, solid samples can be analysed using laser ablation or heated cells to vaporise the sample. Gas samples can be measured directly. The BZT sols used in this study were relatively viscous liquids that required additional dilution. To prepare the sample it was diluted 100,000 times to bring the expected concentration in the part per billion (ppb) range. This resulted in lower background levels that led to lower limits of detection and higher sensitivities. Dilution of liquids and the decomposition of solid samples are usually achieved by the use of some acids, such as nitric, hydrochloric, hydrofluoric, perchloric and sulphuric acid. Nitric acid is often used as a high-purity reagent for the sensitive determination of metals at concentrations of ppb levels in sample solutions, and to utilise its oxidising ability.

For this work the resultant solution was acidified to 3% HCl and 1% HNO_3. This helped to reduce the amount of zirconium that stuck to and contaminated the ICP-MS equipment. The diluted solution was introduced into a nebuliser which converts the liquid sample into an aerosol of very small droplets. These droplets are carried through a spray chamber into the tube or injector. The liquid mist is injected into the plasma formed by ionising argon using an RF coil. The plasma at a temperature of ~6000^{o}C ionises the elements present in the droplets by drying to a solid and then heating to a gas. These ions exit the plasma and are then focused by the ion lens, separated by their mass-to-charge ratio in the quadrupole mass spectrometer, and measured by the detector. The measured signal intensities are then converted into concentrations (μg/L) of each element.

The sols for each of the three BZT compositions (5/95, 20/80 and 35/65) used in the fabrication of thin-film capacitors were analysed using this method, and the results for the diluted solutions are presented in table 4.3. Each result is the mean of three replicate readings in μg/L.

Table 4.3 Concentration values in µg/L of each element in the three BZT sols used. Atomic number adjusted data shown in parenthesis.

	$Ba(Zr_{0.05}Ti_{0.95})O_3$	$Ba(Zr_{0.20}Ti_{0.80})O_3$	$Ba(Zr_{0.35}Ti_{0.65})O_3$
Barium	348	420	457
Zirconium	13.4(0.046)	64(0.193)	127(0.335)
Titanium	153(0.954)	147(0.807)	139(0.665)

After factoring in the atomic numbers for Zr (40) and Ti (22) the actual Zr/Ti ratio values could be calculated from the data displayed in parenthesis in table 4.3.

4.6.8 Photon Correlation Spectroscopy (PCS)

PCS is a method used to measure particle size in liquids, typically below 1 µm, and so is ideal for analysing the aging characteristics of samples such as the BZT sols used in this investigation. Essentially, PCS measures Brownian motion and relates this to the size of the particles, i.e. the random movement of particles bombarded by the solvent molecules that surround them. The technique works on the basis of scattered light from a focused monochromatic coherent He-Ne laser of fixed wavelength 633 nm, and detected by a photomultiplier. A correlator or signal comparator calculates the correlation function from the electrical pulses received from the photomultiplier. The PCS software then performs the data analysis.

The PCS equipment used in this study was a Malvern Instruments Zetasizer 3000. The sol sample under investigation was dispensed into a 10 mm square glass cuvette which was placed into a housing kept at a constant temperature within the PCS. A constant temperature is necessary in order to maintain a stable viscosity and to avoid convection currents in the sample which would distort the measurement due to non-random movements. If a low count is recorded the laser power can be increased. If the solution is too viscous it can be diluted with an appropriate supporting solution. Water was not appropriate. Use of an alcohol based solution such as IPA was tried but reacted with the sol which precipitated out. Acetic acid was the only suitable solvent for reducing the solution concentration.

4.6.9 Dektak Profilometer

The Dektak^3 ST Surface Profiler was used to measure film thicknesses and film surface roughness. The Dektak provides measurement of both the mean roughness (Ra) and the maximum value of roughness (Max Ra) over a pre-selected scan range. For this work Dektak measurements of film thickness and surface roughness were generally checked against measurements obtained using the SEM and AFM, respectively.

4.7 Electrical Characterisation

4.7.1 Electrode Configurations

To perform electrical measurements a standard parallel-plate, metal-insulator-metal (MIM) [MFM for BZT(5/95)] capacitor was fabricated. A schematic cross-section of the MIM capacitor structure on silicon is shown in figure 4.13.

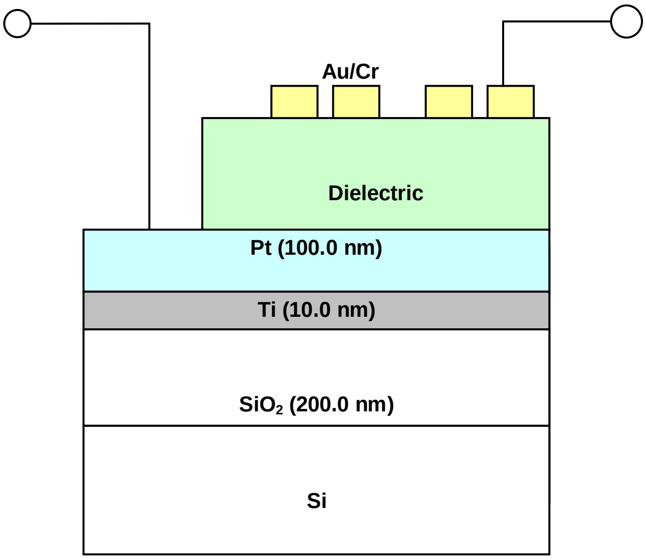

Figure 4.13 Schematic cross-section of the MIM thin-film capacitor with electrical connection to common Pt/Ti bottom electrode and Au/Cr top electrode.

The structure consisted of a SiO_2/Si substrate with a blanket metallisation coverage which constituted the bottom electrode in the MIM structure. The dielectric thin film (e.g. BZT) was of the order of 300 nm to 400 nm thick. To measure electrical properties over the entire area of the substrate an array of circular Au/Cr top electrodes each ~0.73 mm in diameter was thermally evaporated onto the thin film through a shadow mask. These dots comprised 100 nm thick Au over 10 nm thick Cr. By masking the sample with photoresist and etching a small area of the BZT film in a 10% HF solution the ground plane (bottom electrode) of the structure was exposed. Each individual capacitor was connected electrically one at a time using needle probes.

The parallel-plate MIM configuration was chosen for the following reasons:

- Can be probed directly from above.
- Used to minimise the effect of parasitics (reduced series resistance and inductance) on measurements.
- Allows for greater tunability at lower bias voltages.
- Eliminates frequency dispersion for measured capacitance and loss tangent (i.e. the defect concentration inside the bulk of the capacitor is much lower compared to the surface of the film).

The bottom electrode plays a crucial role in the performance and characterisation of dielectric thin films in MIM capacitors. The choice of metallisation initially made was Pt(100nm)/Ti(10nm) since Pt is chemically stable and has the ability to withstand the high temperatures and oxidising conditions during dielectric deposition, including the crystallisation temperature. Other bottom electrode metallisation layers used in the MIM structure are listed in sub-section 4.3.1 (substrate metallisation).

The top electrode deposition was the final stage in the MIM capacitor fabrication process and so was not required to withstand high temperatures. Therefore, thermally evaporated Au/Cr was used as opposed to sputtered metals.

For the zipping varactor the base metallisation was Pt(100nm)/Ti(10nm) and Pt(100nm)/Au(200nm)/Ti(10nm) deposited on two 100 mm glass substrates.

4.7.2 Low Frequency Dielectric Properties and Measurements

The dielectric constant (ε_r) of thin-film BZT and BZN at low frequency (≤300 kHz) for a parallel-plate, metal-insulator-metal (MIM) type structure was calculated from the equation:

$$\varepsilon_r = \frac{Cd}{\varepsilon_o A} \tag{4.1}$$

where C is the capacitance, d is the thickness of the film, ε_o is the permittivity of free space, $8.85\text{x}10^{-12}$ F m^{-1}, and A is the capacitor (top electrode) area.

To characterise material in terms of its dielectric properties it was necessary to accurately determine the thickness of the film and the area of the capacitor (i.e. area under the top electrode). One simple, fast way that the film thickness could be found was by etching a via in the film and measuring the step height using the Dektak profilometer. Error in height and surface roughness measurement was 300nm ±5nm and 5.0nm ±0.2nm, respectively. Alternatively, a small piece of the substrate could be fracture cleaved and examined in section on the SEM.

To determine the area of the capacitor, accurate measurements (accuracy ±0.1µm at 5x optical magnification) were taken of the diameter of the Au/Cr top contact using the Polyvar optical microscope with digital camera attachment. This top electrode was formed by thermal evaporation through a 0.75 mm diameter circular shadow mask. Due to a small gap between the mask and sample, and the position of the Cr and Au filaments in the evaporation system relative to the sample position, there was a misalignment between the deposited Cr and Au (figure 4.14). The effective area of the capacitor was determined from the electrical breakdown patterns as displayed in figure 4.14. Crescent shaped areas at the edge of the electrode were either Cr or Au, not both. In these peripheral areas the Cr was very thin (10 nm) and the Au may not have had good electrical contact with the dielectric due to inadequate adhesion.

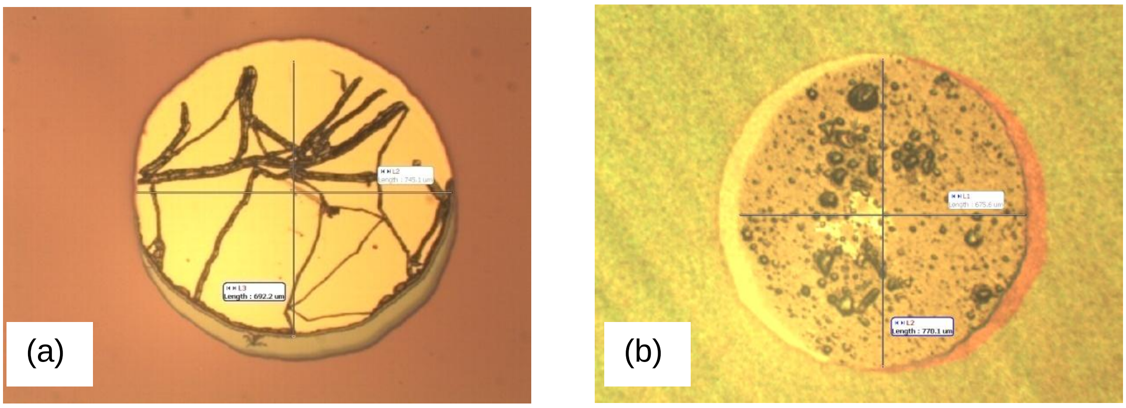

Figure 4.14 Examples of Au/Cr top electrodes displaying the misalignment between evaporated Cr and Au together with areas subject to electrical breakdown. Dimensions marked (a) 692.2µmx745.1µm and (b) 675.5µmx770.1µm.

Electrical breakdown occurred where there was both Cr and Au deposited (figure 4.14). The full extent of the damage caused by electrical breakdown and subsequent thermal runaway is shown in the SEM micrographs of figure 4.15.

The diameter of the Au/Cr region of the capacitor was measured for six samples by optical microscope and the average diameter calculated to be 0.73 mm (7.3×10^{-4} m). The error in the measurement of the diameter was ±0.002 mm. Hence, the average radius (r) was 3.65×10^{-4} m, the area (A) was 4.19×10^{-7} m^2 and $\varepsilon_o A = 3.7 \times 10^{-18}$ Fm. For example, with a film of thickness 500 nm (5×10^{-7} m) and a capacitance of 1 nF (10^{-9} F), the dielectric constant (ε_r) is 135.

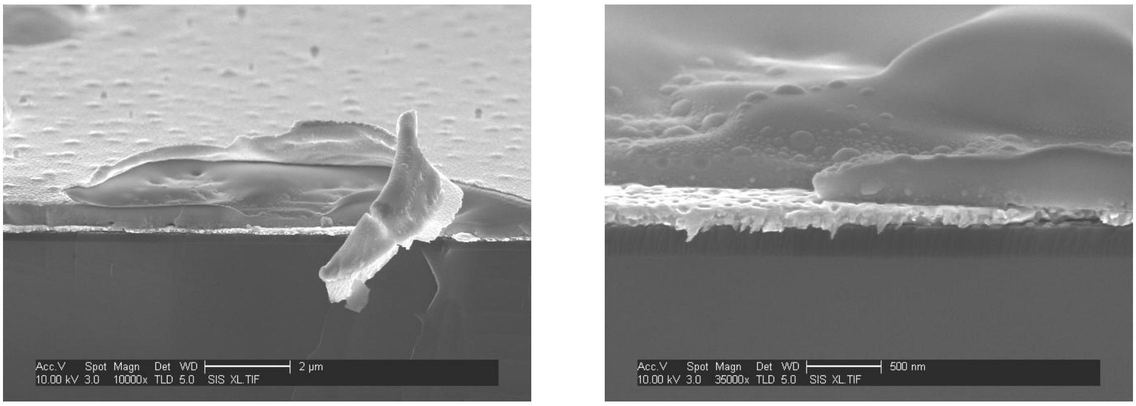

Figure 4.15 SEM micrographs showing evidence of extensive damage to BZN thin film and Au top electrode after electrical breakdown.

The dielectric loss for frequency dependent dielectric material can be derived from the complex permittivity [3.2]. For a capacitor C_o with an ideal (lossless) dielectric (vacuum) subject to an alternating electric field the current I leads the voltage V by 90^o so that:

$$I = j\omega C_o V \tag{4.2}$$

The effect of a lossy dielectric can be described by the complex relative permittivity.

$$\varepsilon_r = \varepsilon'_r - j\varepsilon''_r \tag{4.3}$$

where ε'_r and ε''_r are the real and imaginary parts of the relative permittivity, respectively. The imaginary part ε''_r represents the losses in the dielectric.

It follows that:

$$I = j\omega\varepsilon_r C_o V = j\omega\varepsilon'_r C_o V + \omega\varepsilon''_r C_o V \tag{4.4}$$

When a capacitor contains a lossy dielectric a component of the current is in phase with the voltage V as represented by the phasor diagram of figure 4.16.

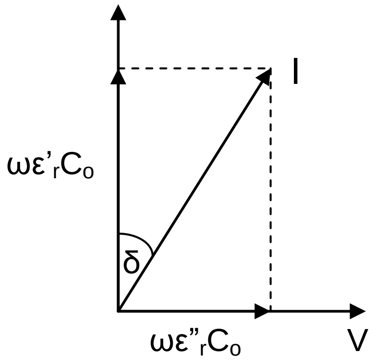

Figure 4.16 Phasor diagram for a lossy capacitor.

From the phasor diagram:

$$tan\delta = \frac{\omega\varepsilon''_r C_o V}{\omega\varepsilon'_r C_o V} = \frac{\varepsilon''_r}{\varepsilon'_r} \tag{4.5}$$

where tanδ is a measure of the losses in the dielectric.

A Wayne Kerr Precision Component Analyser 6425B and probe station (see figure 4.18) were used to connect to the top and common bottom electrodes so that dielectric properties of capacitance and loss tangent (tanδ) could be measured over the frequency range 1 kHz to 300 kHz. The advantage was that at low frequencies electrical characteristics could be obtained using relatively large area MIM capacitors to estimate the dielectric properties of the film. A simplified fabrication process could therefore be implemented. To measure the tunability, a DC bias voltage of up to 50 V was applied at a fixed frequency of 100 kHz and 300 kHz. From the low frequency capacitance and dielectric loss measurements, the dielectric constant (ε_r), relative tunability (n_r), quality factor (Q) and figure of merit (FOM) were calculated using equation 4.1 above together with the following equations 4.6 to 4.9:

$$n_r = \frac{\varepsilon(0) - \varepsilon(E)}{\varepsilon(0)}\ x\ 100\% \tag{4.6}$$

where ε(0) and ε(E) are the dielectric constants at zero and maximum applied DC voltage, respectively.

Since ε_r is proportional to C for a given film thickness, then:

$$n_r = \frac{C(0) - C(E)}{C(0)}\ x\ 100\% \tag{4.7}$$

where C(0) and C(E) are the measured capacitances at zero and maximum applied DC voltage, respectively.

$$Q = \frac{1}{tan\,\delta} \tag{4.8}$$

$$FOM = \frac{Tunability\ (\%)}{tan\,\delta\ \ (\%)} \tag{4.9}$$

From equation 4.6 it is evident that material with higher dielectric constant ε(0) possess larger tunability for a given bias field E. A combination of high tunability with either larger or smaller dielectric constant is very application dependent. For example, for tunable microwave applications ideally require a decrease in dielectric constant and loss without seriously affecting the tunability. A high value of dielectric constant of ferroelectrics is not particularly desirable for devices operating at high frequency since device dimensions can be prohibitively small. Because of the interdependency of dielectric constant, dielectric loss and tunability, controlling the material properties by process optimisation is essential.

The Wayne-Kerr component analyser has a programmable internal supply that is limited to providing a 20 V DC bias across the capacitor under test. The voltage range of this instrument was extended to 50 V by connecting an external power supply (Keithly Digital Voltage Source) between the bias link terminals, the total voltage being a sum of the internal and external voltages. Two probe needles attached to micromanipulators were connected to the four terminals of the instrument. This provided continuous correction for losses occurring in measurement leads or fixtures and ensured the resolution and accuracy over the entire measurement range. When first connecting the capacitor to the component analyser via the probes and four terminal connections, open and short circuit trimming is necessary. This procedure compensates for stray capacitance and series impedance of the test leads/fixtures. They are applied automatically at all frequencies, levels and ranges. No re-trimming should be necessary unless the test connections are changed. The equipment was operated in the parallel C and R equivalent circuit mode with an AC drive level of 100 mV ±2 mV. Repetitive measurements were made at a normal rate (~300 ms/measurement).

System error measurements in capacitance, dissipation factor and frequency:

- Capacitance (C) accuracy at 1 kHz was ±0.05%; the resolution 0.002pF at 1 kHz, 0.0002pF at 10 kHz, 0.002pF at 50 kHz and 0.01pF at 100 kHz.
- Dissipation factor (D) accuracy at 1 kHz was ±0.002 and the resolution 0.00005 up to 10 kHz, 0.0005 at 100 kHz and 0.002 at 300 kHz.
- The frequency accuracy was ±0.01%.

4.7.3 Sheet Resistance Measurements

The sheet resistance of the bottom electrode metallisation significantly affects the dielectric properties, such as loss and tunability, of a dielectric thin film, and therefore has a direct bearing on device performance. The sheet resistance of combinations of metal layers incorporating Pt and Au deposited on SiO_2/Si substrate as listed in sub-section 4.3.1 was measured.

A simple, non-destructive way of measuring the sheet resistance of the metal layers utilised the Karl Suss four-point probe shown schematically in figure 4.17. There are two possible probe configurations, a linear probe arrangement, and a square probe array that can be used on small specimens to improve accuracy. For these measurements the linear array of probes was chosen. Four equally spaced tungsten needles were brought into contact with the surface of the plate to be measured. The needles are spring mounted to minimise sample damage during probing. A known test current was passed between the outer needles using a DC Current Calibrator Type 132 and the resultant potential difference between the inner needles was measured using a Keithly 195A Digital Multimeter. Since very little current flows through the voltage sensing probes, there are no errors introduced due to the contacts.

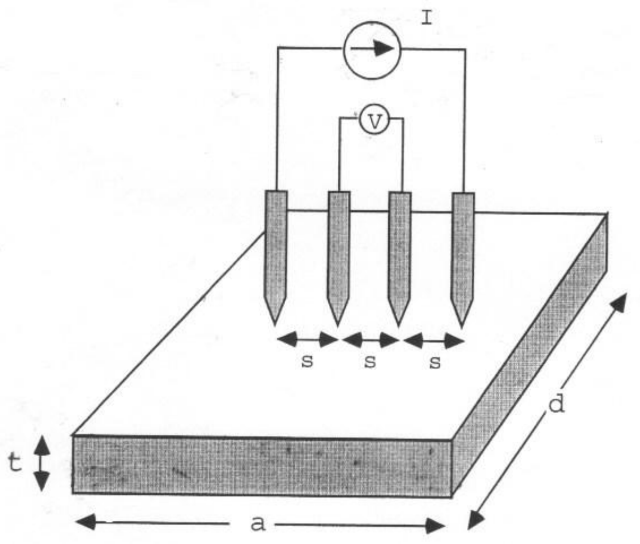

Figure 4.17 Four-point probe (linear configuration) on rectangular sample.

With the probes centred on a very wide (lateral dimension d»s) and a very thin (thickness t«s) sample, where s is the probe spacing of ~1 mm, the resistivity is given by:

$$\rho = \frac{\pi}{ln2} t \left(\frac{V}{I}\right) \ \Omega\text{cm} \tag{4.10}$$

Sheet resistance (R_s) is therefore:

$$R_s = \frac{\rho}{t} = \frac{\pi}{ln2}\left(\frac{V}{I}\right) \tag{4.11}$$

$$= 4.53\left(\frac{V}{I}\right) \ \Omega/\text{sq} \tag{4.12}$$

In general, R_s=C(V/I) where C is a geometric correction factor. Provided the sample size (lateral dimension) d to probe spacing s is d/s>40, then C=4.53. A table of correction factors C can be referenced in an early paper by Smits [4.2]. If we therefore set the current in the outer probes to a value of 4.53 mA, the sheet resistance is simply the voltage reading in mV. The error in the voltage measurement and hence sheet resistance was ±0.03 Ω/sq. All samples were of the same size (2cm x 3cm) and shape (rectangular) so that a direct comparison could be made between the sheet resistances for the various metal layers, rather than focusing on the absolute values of each. The correction factor C for the sample size used according to Smits [4.2] is 4.48.

4.7.4 Measurement of Hysteresis (P-E) Loops

An essential property of ferroelectrics is the ability to reverse or change the orientation of the polarisation direction by an electric field. This key property is exhibited pictorially in a hysteresis or polarisation vs electric field (P-E) loop (figure 3.10). A Radiant Technologies RT-66A Standardised Ferroelectric Test System was used to measure the ferroelectric hysteresis. This can be used in two set-up configurations depending on the coercive field required for the test sample. The RT-66A module can operate to maximum applied voltage of ±20 V for the testing of thin samples (<1 µm). For thicker samples, the RT-66A High

Voltage Interface (HVI) is connected, where voltages up to ±4000 V can be applied. In this study film thicknesses of ~300 nm were typical and so only the lower voltage (to ±20 V) configuration was required for loop measurements. The sample was connected to the RT-66A by means of a probe station (figure 4.18) which made contact to the top and bottom electrodes of the individual capacitors under test.

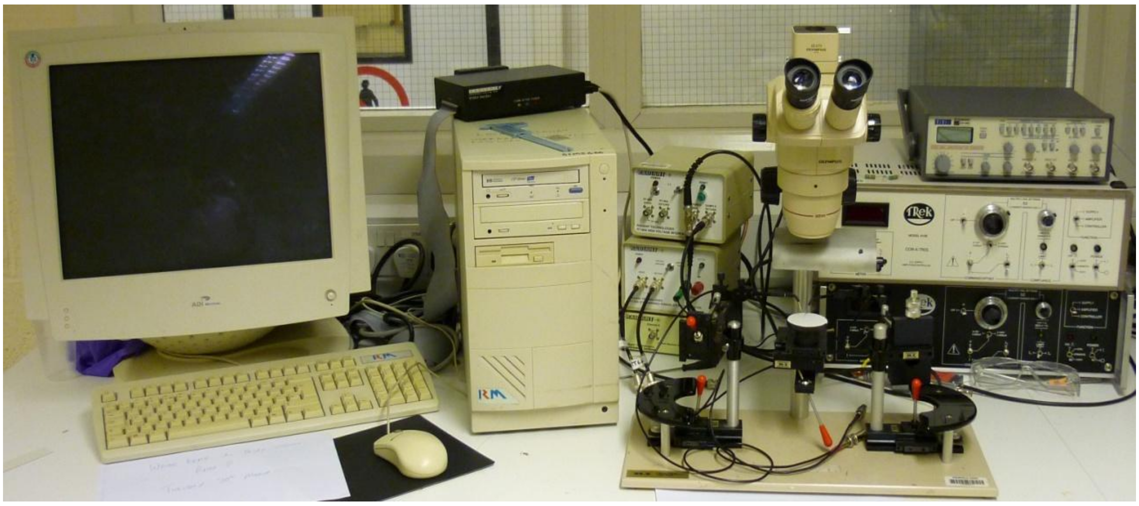

Figure 4.18 Experimental apparatus for measuring ferroelectric hysteresis with probe station in the foreground.

The main input parameters included applied voltage V_{max}, hysteresis period in ms, area of capacitor in cm^2, thickness of dielectric film in μm, and the plot option of either polarisation as a function of voltage or field. From the resulting hysteresis loop the maximum or saturation polarisation (P_{max}), the remnant polarisation ($\pm P_r$) in $\mu C/cm^2$ and the coercive field ($\pm E_c$) in kV/cm could be extracted.

4.7.5 Poling of Ferroelectrics

Thin film material in the ferroelectric phase possess spontaneous electric polarisation. Polarisation induced by the application of a sufficiently strong external electric field is manifest as a P-E hysteresis loop. At first this hysteresis may not be well developed due to the initial quasi-random orientation of ferroelectric domains, the most thermodynamically stable configuration. Poling of the material is required to align the domains and “freeze” the polarisation state. Electrical poling can be performed by cooling the material from the paraelectric phase into the ferroelectric phase while maintaining the applied electric field. This was achieved for BZT by firstly heating the sample on a hotplate to ~120^{o}C just above the Curie temperature and at the same time applying an electric field of the order of 100s kV/cm. These conditions were held for 10 to 20 minutes. The reorientation of dipoles is made easier under these conditions. The application of the electric field was maintained until the temperature of the sample dropped below 80^{o}C. This was undertaken since internal film stress with temperature can change the dipole orientation back to the initial thermodynamically stable quasi-random state. The equipment comprised of a hotplate with thermocouple and automated heater control to accurately set and maintain the temperature. Two spring mounted probes connected the DC power supply to the top and bottom electrodes of the parallel-plate capacitor to be poled. A voltage of up to 10 V (200 kV/cm) was applied. Although spring mounted probes are designed to minimise sample damage, there was some deterioration to the top electrode resulting in failure of some of the components. An alternative approach was to apply the electric field using the probe station shown in figure 4.18, with the sample mounted on a manually controlled hotplate with attached thermocouple.

5 Modelling of Bilayers and Multilayer Structures of Two Components

The modelling of bilayer, and by extension multilayer structures, was based on work carried out by Sherman *et al*. and Astafiev *et al*. on the dilution of tunable ferroelectric with linear dielectric material (ferroelectric-dielectric composites) [5.1-5.4]. They described four component distribution models, the columnar composite model (parallel connection of two capacitors), the layered composite model (series connection of two capacitors), the spherical inclusion model, and the effective medium approximation which involves the random distribution of components. The four models are represented schematically in figure 5.1.

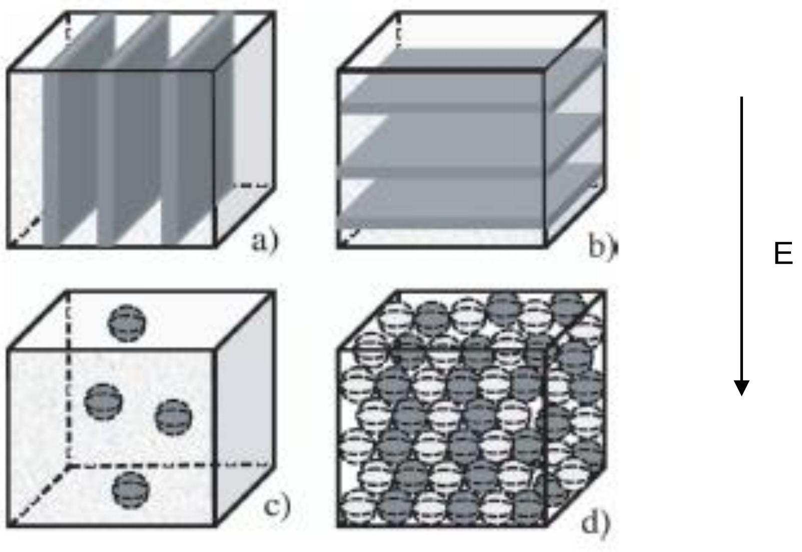

Figure 5.1 Four model representations (a) columnar composite, (b) layered composite, (c) spherical inclusion and (d) effective medium. The dark and light regions are the linear dielectric and ferroelectric material, respectively [5.2].

For the work on BZT/BZN bilayer structures the layered composite model (figure 5.1b) was used in which layers are oriented perpendicular to the direction of the applied electric field. The bilayer consisting of two electrically tunable (nonlinear) dielectric layers (one ferroelectric layer in the paraelectric phase and one non-ferroelectric layer) can be represented by the series connection of two capacitors. Excel was used to model the layered composites.

5.1 Dielectric Constant of Layered Composite

The effective dielectric constant or relative permittivity, ε_{eff} of the BZT/BZN layered composite (BZN buffer layer and BZT main film) is given by [5.2, 5.3]:

$$\frac{1}{\varepsilon_{eff}(V_f)} = \frac{(1 - V_f)}{\varepsilon_{BZT}} + \frac{V_f}{\varepsilon_{BZN}} \tag{5.1}$$

where V_f is the volume fraction or concentration of the BZN dielectric layer, and ε_{eff}, ε_{BZT} and ε_{BZN} are the dielectric constants of the composite film (effective), BZT and BZN, respectively.

The equation can be rearranged to give:

$$\varepsilon_{eff}(V_f) = \frac{\varepsilon_{BZT}\varepsilon_{BZN}}{\varepsilon_{BZN}(1 - V_f) + \varepsilon_{BZT}V_f} \tag{5.2}$$

Since the surface area of both layers is the same, the volume fraction V_f can be replaced by d_f, the thickness fraction.

When $V_f = 0$, then $\varepsilon_{eff}(V_f) = \varepsilon_{BZT}$ and when $V_f = 1$, $\varepsilon_{eff}(V_f) = \varepsilon_{BZN}$.

The results of the modelling of dielectric constant for the layered composite are displayed in figures 5.2-5.4. After inputting a typical value for the dielectric constant of BZT (ε_{BZT}=200) and three well spaced values for BZN (ε_{BZN}=20, 80, 140), the effective dielectric constant was plotted as a function of V_f, the volume fraction of BZN (figure 5.2). When the BZN buffer layer has low dielectric constant (<80) it is preferable to maintain the volume fraction of BZN also low (<0.1), otherwise a significant reduction in the effective or composite dielectric constant will be realised. This is illustrated well in figures 5.3 and 5.4 which both show the effect of varying the dielectric constant of BZT and BZN on the composite dielectric constant, ε_{eff}, for a BZN volume fraction V_f of 0.08 and 0.16, respectively. For a *circa* 300 nm thick BZT film, the BZN volume fraction of 0.08 and 0.16 represents a BZN buffer layer thickness of 25 nm and 50 nm, respectively.

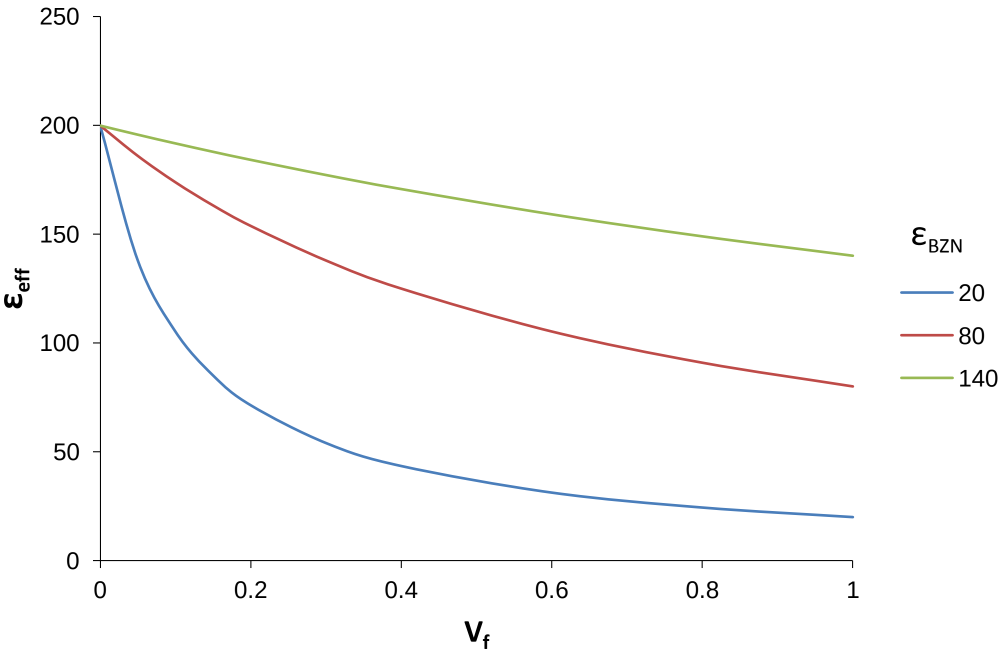

Figure 5.2 Modelled effective dielectric constant as a function of the volume fraction V_f of BZN. The modelling was performed for BZT thin film with dielectric constant ε_{BZT}=200.

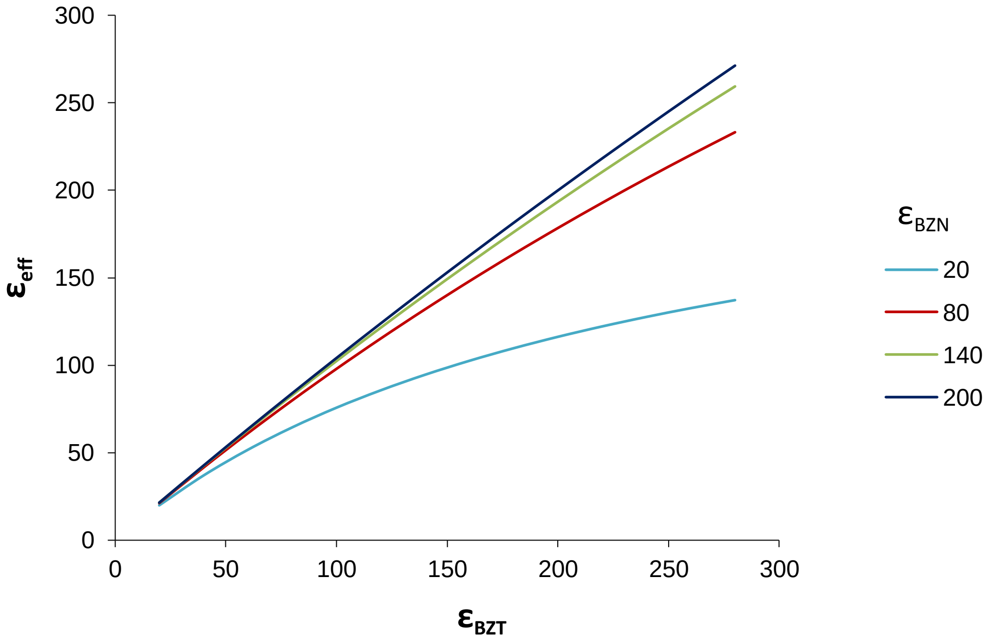

Figure 5.3 Influence of varying the BZT and BZN dielectric constant on the effective or composite dielectric constant for a BZN volume fraction of 0.08.

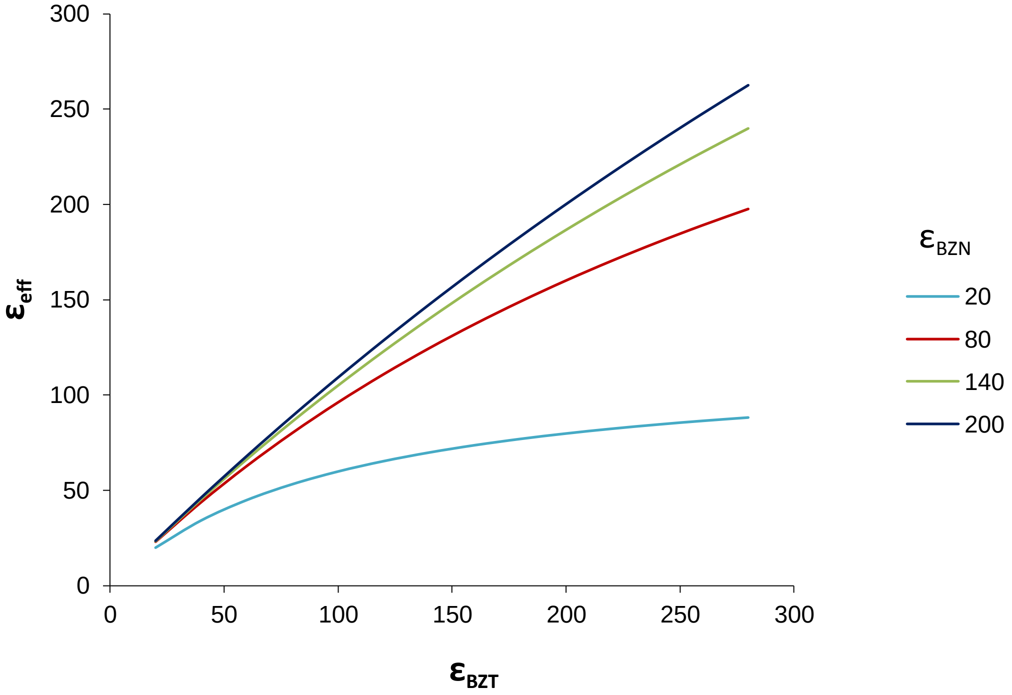

Figure 5.4 Influence of varying the BZT and BZN dielectric constant on the effective or composite dielectric constant for a BZN volume fraction of 0.16.

Using the data presented in figures 5.2-5.4 it is possible to tailor the dielectric constant of the composite thin film by varying the volume fraction of BZN compared to that of BZT (i.e. by increasing or decreasing the buffer layer thickness relative to the thickness of the BZT thin film).

5.2 Dielectric Loss of Layered Composite

Astafiev *et al*. developed an equation for the effective loss tangent of a composite consisting of two lossy capacitors connected in series [5.3]. This has been used and adapted for the BZT/BZN bilayer modelling.

$$tan\delta_{eff}(V_f) = \frac{tan\delta_{BZT}\varepsilon_{BZN}(1-V_f) + tan\delta_{BZN}\varepsilon_{BZT}V_f}{\varepsilon_{BZN}(1-V_f) + \varepsilon_{BZT}V_f} \qquad (5.3)$$

When $V_f = 0$, $\tan\delta_{eff}(V_f) = \tan\delta_{BZT}$ and when $V_f = 1$, $\tan\delta_{eff}(V_f) = \tan\delta_{BZN}$.

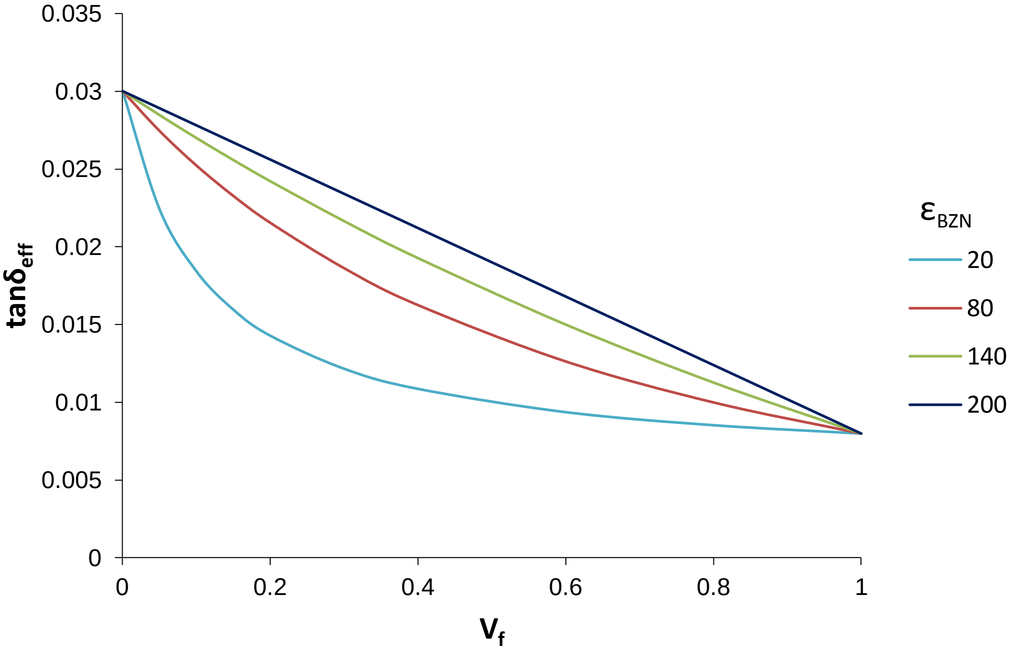

Figure 5.5 Dielectric loss of composite as a function of the BZN volume fraction V$_f$ for range of BZN dielectric constant values. The dielectric loss of BZN was chosen to be 0.008.

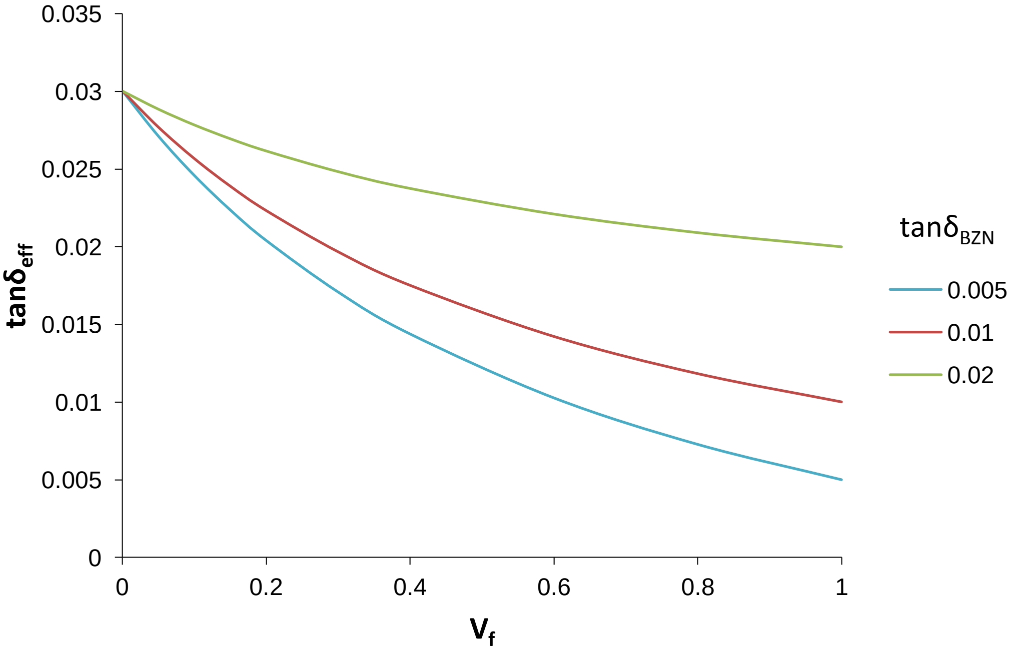

Figure 5.6 Variation in the composite dielectric loss with the BZN concentration for three values of BZN loss. The modelling was performed using a BZT thin film loss of 0.03.

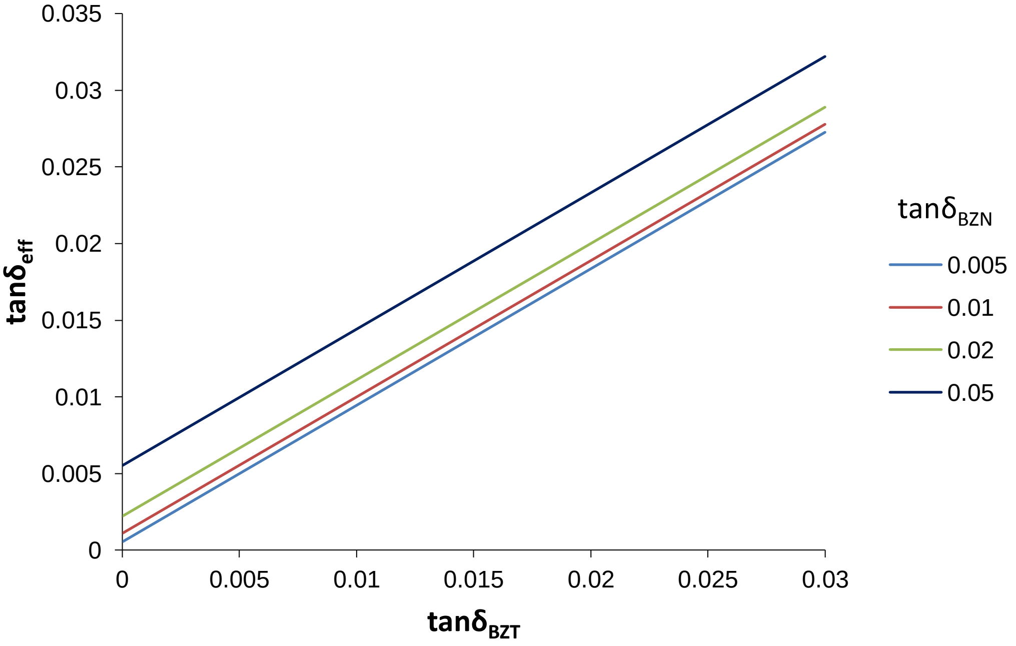

Figure 5.7 The effect of varying the individual BZT and BZN dielectric loss on the composite thin film loss. BZN volume fraction is 0.08.

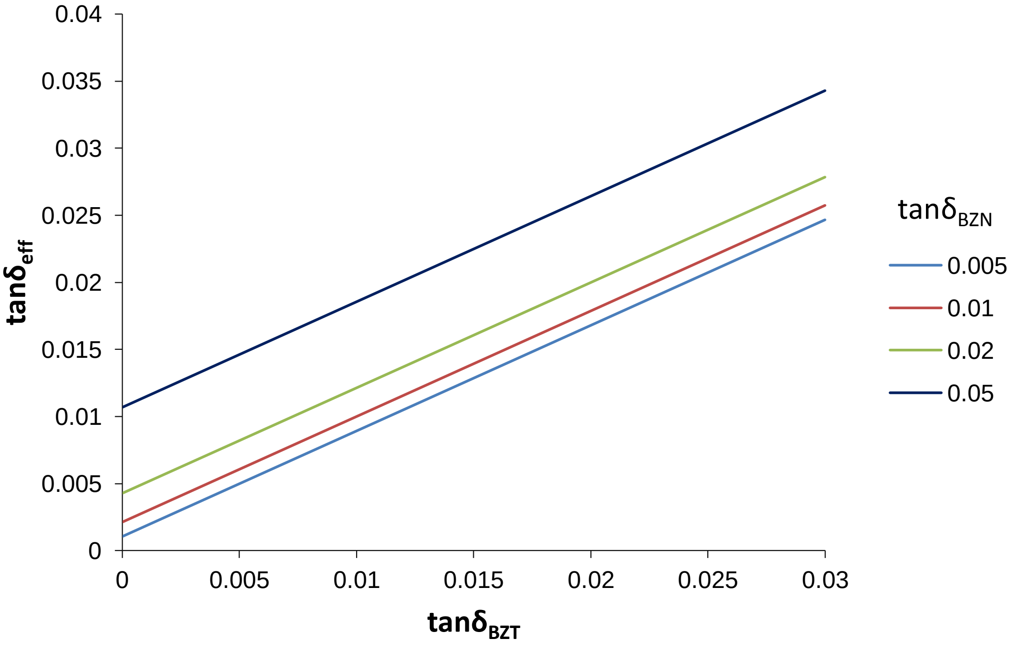

Figure 5.8 The influence of changing the BZT and BZN dielectric loss on the composite thin film loss. BZN concentration is 0.16.

Figures 5.5 and 5.6 show how the dielectric loss of the bilayer can be influenced by changes in the volume fraction of BZN for different values of BZN dielectric constant and loss. According to the result in figure 5.5, it is preferable to use a BZN buffer layer with lower dielectric constant if the volume fraction of BZN is maintained low (i.e. a thinner buffer layer). If the dielectric constant of the BZN is low, a thinner buffer layer will also result in an improved bilayer dielectric constant compared to the dielectric constant obtained using a thicker BZN layer (figure 5.2). By depositing a thinner buffer layer the effective dielectric loss of the composite can be kept lower (compare the graphs in figures 5.7 and 5.8).

5.3 Tunability of Layered Composite

Using the equation for the dielectric constant of the layered composite given in section 5.1 an equation for the absolute and relative tunability can be derived.

Effective absolute tunability n_{eff} is:

$$n_{eff} = \frac{\varepsilon_{eff}(0)}{\varepsilon_{eff}(E)} = \frac{\dfrac{\varepsilon_{BZT}(0)\varepsilon_{BZN}(0)}{\varepsilon_{BZN}(0)\left(1-V_f\right)+\varepsilon_{BZT}(0)V_f}}{\dfrac{\varepsilon_{BZT}(E)\varepsilon_{BZN}(E)}{\varepsilon_{BZN}(E)\left(1-V_f\right)+\varepsilon_{BZT}(E)V_f}} \tag{5.4}$$

$$n_{eff} = \frac{\varepsilon_{BZT}(0)\varepsilon_{BZN}(0)(\varepsilon_{BZN}(E)\left(1-V_f\right)+\varepsilon_{BZT}(E)V_f)}{\varepsilon_{BZT}(E)\varepsilon_{BZN}(E)(\varepsilon_{BZN}(0)\left(1-V_f\right)+\varepsilon_{BZT}(0)V_f)} \tag{5.5}$$

The absolute tunability can now be used to determine the relative tunability which commonly characterises the thin film material reported on in this thesis.

The effective relative tunability $n_{r,eff}$ is:

$$n_{r,eff} = 1 - \frac{1}{n_{eff}} = \frac{\varepsilon_{eff}(0)-\varepsilon_{eff}(E)}{\varepsilon_{eff}(0)} \tag{5.6}$$

$$n_{r,eff} = \frac{\varepsilon_{BZT}(0)\varepsilon_{BZN}(0)\left(\varepsilon_{BZN}(E)\left(1-V_f\right)+\varepsilon_{BZT}(E)V_f\right)-\varepsilon_{BZT}(E)\varepsilon_{BZN}(E)(\varepsilon_{BZN}(0)\left(1-V_f\right)+\varepsilon_{BZT}(0)V_f)}{\varepsilon_{BZT}(0)\varepsilon_{BZN}(0)(\varepsilon_{BZN}(E)\left(1-V_f\right)+\varepsilon_{BZT}(E)V_f)} \tag{5.7}$$

When $V_f = 0$

$$n_{r,eff} = \frac{\varepsilon_{BZT}(0) - \varepsilon_{BZT}(E)}{\varepsilon_{BZT}(0)} = n_{BZT} \tag{5.8}$$

When $V_f = 1$

$$n_{r,eff} = \frac{\varepsilon_{BZN}(0) - \varepsilon_{BZN}(E)}{\varepsilon_{BZN}(0)} = n_{BZN} \tag{5.9}$$

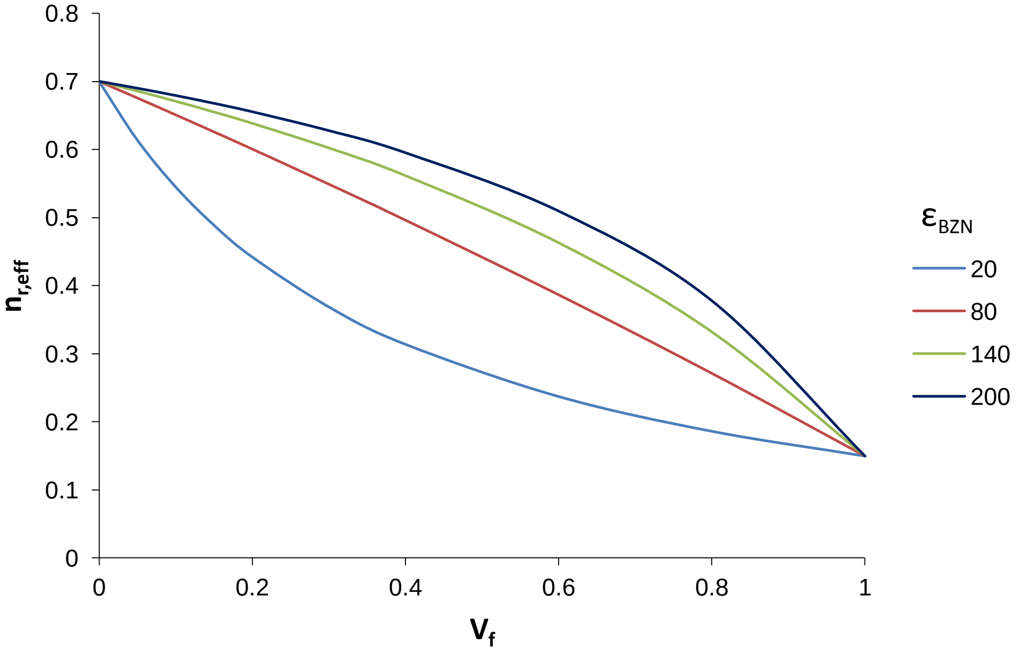

Figure 5.9 Relative tunability of the layered composite as a function of the BZN volume fraction V_f with variation in the dielectric constant of BZN. The dielectric constant of BZT is 200.

The set of curves in figure 5.9 show the effect that varying the BZN dielectric constant has on the composite tunability for BZN concentrations in the range 0 to 1. Empirical data for $\varepsilon_{BZT}(0)$, $\varepsilon_{BZT}(E)$, $\varepsilon_{BZN}(0)$ and $\varepsilon_{BZT}(E)$ was input into equation 5.7 to compute $n_{r,eff}$. It is evident that the maximum tunability is achieved for a very thin ($V_f<0.1$) BZN buffer layer if the dielectric constant of BZN is low. For high (>100) BZN dielectric constant, the BZN layer thickness can be increased without a significant reduction in the composite tunability, even though the BZN tunability is only ~15% compared to that of BZT (70%).

5.4 Figure of Merit (FOM) of Layered Composite

The figure of merit K is defined as:

$$K = \frac{Tunability}{Loss} = \frac{n_{r,eff}}{tan\delta_{eff}(V_f)} \tag{5.10}$$

The FOM (K) can be modelled as a function of the BZN concentration (V_f) by using the tunability data displayed in figure 5.9 and dividing it by the loss data from the graph of figure 5.5. The resultant plot is presented in figure 5.10.

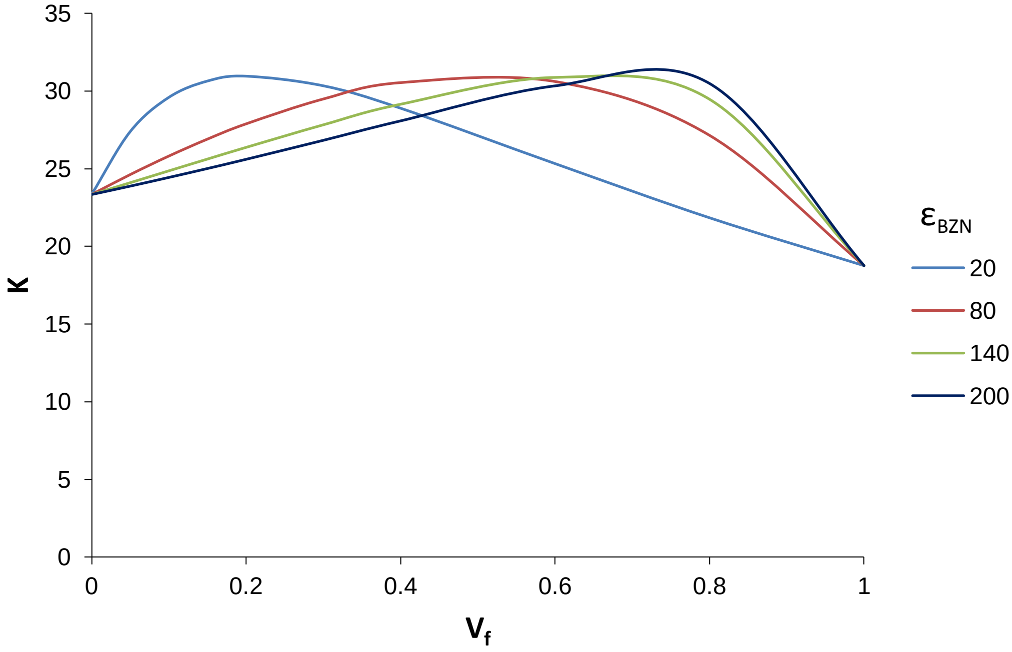

Figure 5.10 Figure of merit K of the layered composite as a function of the BZN volume fraction V_f with variation in the dielectric constant of BZN.

As shown in figure 5.10, the FOM varies generally between 20 and 30 over the range of BZN concentrations and dielectric constants indicated. For BZN with a low dielectric constant (20) it is preferable to use a thin BZN buffer layer to grow a thicker BZT main layer, whereas the FOM data indicates a preference for a thicker BZN buffer layer when the BZN dielectric constant is high. Hence, the buffer layer thickness selected is determined by the requirement for either good tunability or low loss, or some compromise between tunability and loss.

5.5 Conclusions of Modelling

The dielectric properties (dielectric constant, loss, tunability and figure of merit) of a film containing two separate dielectrics in a layered composite have been modelled using empirical data from single layer films. The modelling package has specific application to a very thin BZN buffer layer and a thicker BZT main layer and is an aid to determining the required buffer layer thickness in relation to the thickness of the main layer. It shows the influence that varying the buffer layer thickness has on the dielectric properties of the tunable thin-film capacitor at low frequency (at or below 300 kHz). Although the maximum dielectric constant achieved for BZT thin film experimentally was 450, a more typical value of 200 was chosen for the computation.

As determined by experiment, the dielectric loss of BZN thin films tend to be slightly lower than that of BZT thin films. In this case, as the thickness of the BZN layer increases the overall loss of the composite film decreases, implying that it is possible to accommodate a thicker buffer layer without compromising the loss figure. However, the modelling also shows that for a thin BZN buffer layer of lower dielectric constant than that of the thicker main BZT layer, the composite dielectric constant can be maximised by keeping the BZN buffer layer as thin as is practicable. By varying the thickness of the buffer layer the dielectric constant of the layered composite can be reduced or increased. Similarly, by experiment, the tunability of BZN thin film has been shown to be much lower than that of BZT thin film under the same measurement conditions. To maximise the tunability of the composite film it is therefore preferable to use the thinnest possible BZN buffer layer.

Overall, the modelled data shows that a very thin (~25 nm) BZN buffer layer is required if the dielectric constant and tunability of a 300 nm thick BZT film is to be maximised while the dielectric loss is maintained low.

The demonstrated modelling of dielectric properties for the BZT/BZN bilayer structure can also be used for modelling other multilayer structures of two components.

6 Fixed Value, Linear Dielectric Capacitor

6.1 Introduction

Fixed value capacitors with low-k (<10), medium-k (15-30) and high-k (>30) dielectric materials find application primarily with silicon technologies. Applications include small area decoupling capacitors, information storage components such as dynamic random-access memories (DRAMs), and as the transistor gate dielectric in complementary metal-oxide semiconductor (CMOS) field-effect transistor (FET) logic devices, requiring insulators with excellent mechanical, electrical and dielectric properties. Moderate dielectric constant materials are preferred for gate dielectrics. Silicon dioxide (SiO_2) is a linear dielectric (permittivity is independent of field) that has traditionally been used as the insulator. However, it has been reported that the silicon dioxide gate dielectric of transistors in CMOS has become so thin (1.4 nm) that its leakage current is too large. Considerable efforts have been made to develop replacement dielectrics. By investigating alternative insulators with a higher dielectric constant, the thickness of the dielectric can be increased. Some alternative higher permittivity dielectrics to replace SiO_2 include Ta_2O_5, TiO_2, Al_2O_3, ZrO_2, HfO_2, La_2O_3, $SrTiO_3$, $SrZrO_3$ and $(Ba_xSr_{1-x})TiO_3$ (BST) [3.65, 3.66]. For example, intermediate permittivity, amorphous and crystalline Ta_2O_5 was developed for DRAM technology. Also, crystalline BST was previously selected as one of the dielectric materials for high permittivity DRAM applications. In contrast to SiO_2, BST is strongly nonlinear (permittivity decreases with increasing field). Other complex oxide materials could be investigated for similar applications, including amorphous and crystalline BZT and BZN.

Fixed value capacitors are also used in GaAs monolithic microwave integrated circuits (MMICs), e.g. for low impedance DC blocking. These capacitors contain layers of silicon nitride or polyimide between metal (Pt/Au/Ti) electrodes in a MIM configuration. Silicon nitride layers are thin (~120 nm) and so make high value capacitors in the range 0.5 to 60 pF, whereas thicker (1.5 μm) polyimide layers make lower value capacitors ranging from 0.06 to 2.5 pF. The capacitance of MIM capacitors is clearly a strong function of the insulator (dielectric) thickness. To achieve higher capacitance it is therefore necessary to either decrease the film thickness or to increase the capacitor area. However, caution must be exercised to avoid a low breakdown strength or high leakage current density due to defects.

Another area of interest includes capacitors fabricated on flexible polymer substrate such as liquid crystal polymer (LCP) laminate (or sheet). Commercial LCP material is supplied in thin film form with thicknesses ranging from 25 μm to 3.0 mm. One or both sides of the LCP film may have a thick copper cladding. LCP has a coefficient of thermal expansion 8.0-17.0 ppm/^{o}C and a melting temperature ~320^{o}C. Since LCP films are not perfectly planar there can be issues with material deposition, spin coating of photoresist and lithography. This also makes the sol-gel spin-coating process problematic on unclad LCP. Sputtering is therefore the preferred deposition technique. There are also challenges with the use of analytical techniques such as SEM and AFM on flexible substrates.

6.2 Capacitor Configurations

One capacitor structure commonly used incorporates a SiO_2 dielectric grown directly onto silicon (one capacitor electrode) and covered with a metallic layer (the second or top electrode) in a configuration known as a metal-insulator-semiconductor (MIS) capacitor. This structure is impracticable using sol-gel derived BZT thin film due to processing issues. Hence, a structure was used in which the BZT (and BZN) was deposited on a metallic bottom electrode in a metal-insulator-metal (MIM) [MFM for ferroelectric BZT] configuration. The MIM capacitor was fabricated to characterise the fundamental electrical properties of the dielectric films. Generally, complex oxide dielectrics are processed at relatively high temperatures so that the electrodes must be stable against oxidation (noble metals or conductive oxides routinely used).

In this study a simple parallel-plate capacitor was fabricated using BZT and BZN dielectrics with a blanket bottom metal electrode on oxidised silicon and

LCP substrate. The BZT sol-gel films were deposited using multiple spin and bake cycles; the BZN films were RF magnetron sputtered at an elevated temperature of up to 300^{o}C. The different bottom electrode metallisations used are discussed in sub-section 4.3.1 (substrate metallisation). The top metal was thermally evaporated Au/Cr (~0.73 mm diameter circular dots). This MIM capacitor configuration was chosen so that it could be easily probed from above. Measurements were taken on these small area (~4.2x10^{-3} cm^2) capacitors which showed, in the majority of cases, a high yield (90%) and relatively low loss (0.01). An optical image of the top electrode metallisation, which shows significant misalignment of the Cr and Au layers, can be seen in figure 6.1.

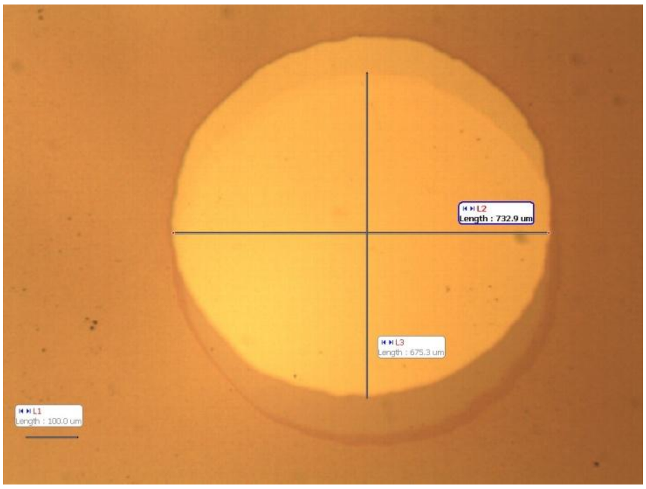

Figure 6.1 Optical image of a ~0.73 mm (730 μm) diameter Au/Cr top electrode showing Au dot displaced from Cr contact. The Cr only area can be seen as a crescent shaped region at the bottom of the image whereas the Au only area is a crescent at the top. The Au/Cr area is the elliptical region in the centre bounding the measurement cross-hairs (dimensions 733 μm and 675 μm).

In addition to the circular top contacts, smaller square shaped electrodes were deposited by thermal evaporation through a shadow mask utilising an etched silicon FBAR structure. The mask consisted of an array of ten square shaped holes arranged in pairs of equal size. These holes ranged in size from 135 μm x 135 μm (~1.8x10^{-4} cm^2) to 375 μm x 375 μm (~1.4x10^{-3} cm^2). Figure 6.2 is an SEM photomicrograph of the smallest of the Au/Cr top contacts deposited on

BZN thin film. On samples which used the circular top electrode and where it had been difficult to achieve a high working yield of capacitors due to defects, the smaller square electrodes were also deposited to improve yield. However, the smallest area electrode can be difficult to probe when taking measurements.

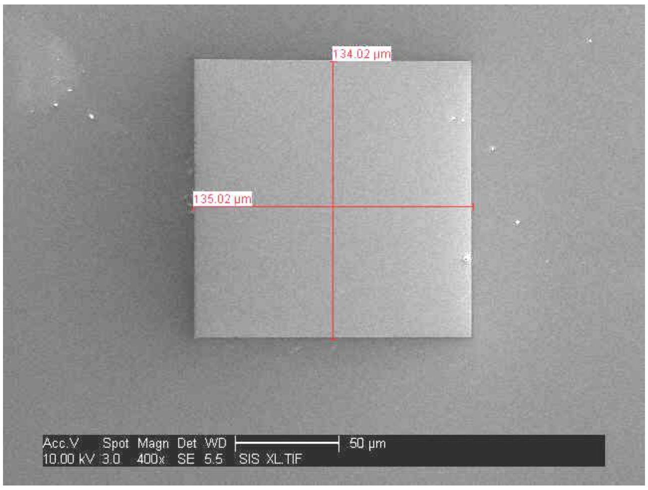

Figure 6.2 SEM micrograph showing the smallest (135 µm^2) of the square shaped Au/Cr top electrodes deposited by thermal evaporation on BZN thin film.

Unlike the circular top electrode (shown in figure 6.1), for the square contact there is an imperceptible misalignment between the Au and the Cr adhesion layer indicating much reduced separation between mask and substrate. This better defined electrode feature resulted in more accurate dielectric measurements. Under these smaller area capacitors the reduced defect density due to cracks, dislocations, impurities and porosity can also result in a significant increase in the measured breakdown strength of the material.

6.3 Results and Discussion

6.3.1 Amorphous or Nanocrystalline BZN Thin Films Deposited on Platinum Electrode

It has been demonstrated by Lu *et al*. that the maximum tunability of the dielectric constant of ~40% was achieved for BZN sputter deposited on Pt coated silicon at a bias field of 1.0 MV/cm, and ~55% for a BZN film sputter deposited on Pt/Al_2O_3 at an applied bias field of 2.4 MV/cm [3.59]. Other researchers, including Thayer *et al*., reported that BZN generally has a modest tunability of ~10% for an applied bias ±830 kV/cm [3.51]. For a thin BZN film deposited on platinised silicon by the metalorganic decomposition (MOD) method, Thayer *et al.* found that a high bias field of 1.8 MV/cm induced 30% tunability at room temperature. Measurements were repeated after cooling the sample to 77 K which decreased the electronic conductivity. This enabled higher field to be applied without dielectric breakdown. At 77 K Thayer *et al.* had increased the tunability to 45% [3.51]. However, there was a trade-off associated with increased loss due to relaxation. It was not possible to perform low temperature measurements on BZN material due to inadequate test facility.

Even though researchers report quite significant tunability (55%) for BZN thin-film capacitors, it has not been possible to replicate these results even using similar processing conditions for the RF magnetron sputter deposition of BZN and the subsequent thermal treatment. Peak tunabilities for BZN deposited on platinised silicon of the order of only 15% were achieved. Rather than focus all of the effort on using BZN as a tunable material, it was decided to give more attention to its use in fixed value capacitors, the zipping varactor, and as a buffer layer for BZT thin film growth on Au bottom electrode. An investigation into the use of amorphous and crystalline BZN thin films deposited on Pt and Au bottom electrodes was instituted. In particular, there appears to be no reported investigation of amorphous or nanocrystalline thin-film BZN by other researchers.

The microstructure of amorphous or nanocrystalline BZN material grown on Pt and Au was compared. The XRD diffractogram in figure 6.3 shows the amorphous nature of the BZN film sputter deposited at 300^{o}C onto a platinised silicon wafer piece. There is no evidence of the characteristic crystallographic peaks usually associated with the polycrystalline structure of BZN after annealing. The strongest peak (222) would normally be positioned at ~29^{o} but here we see only a broad hump indicative of an amorphous type structure. The SEM image of the BZN surface for the same sample showed a nanocrystalline microstructure.

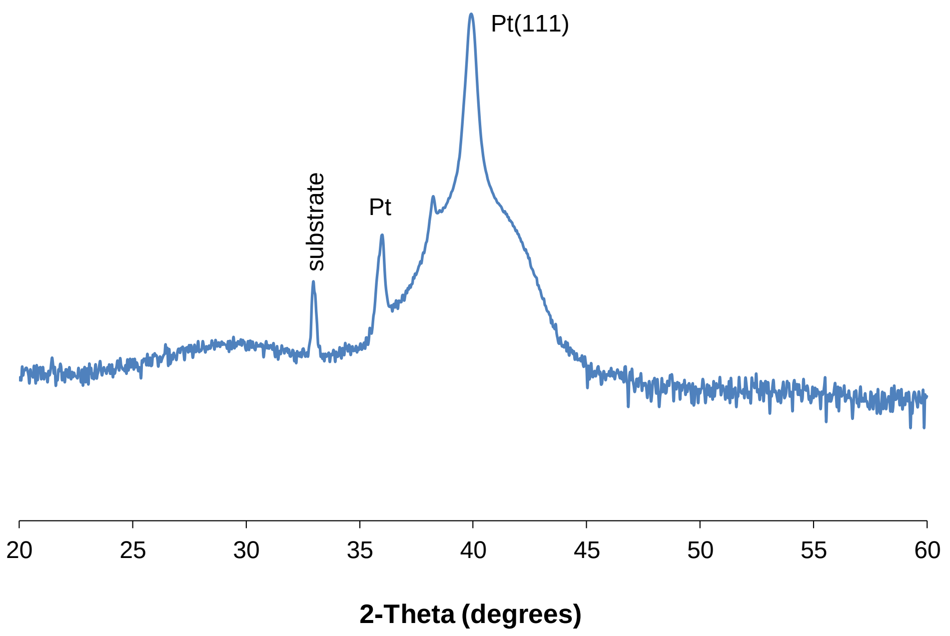

Figure 6.3 Typical XRD pattern showing the amorphous or nanocrystalline nature of the BZN thin film when sputter deposited on Pt coated silicon substrate at 300°C.

EDX analysis was also performed on the as-sputtered BZN thin film so that the deposited thin film composition (atomic %) could be compared to that of the target material in the sputtering machine which is $Bi_{1.5}Zn_{1.0}Nb_{1.5}O_7$. A cobalt standard was used as calibration. Figure 6.4 shows the EDX spectrum for the as-sputtered BZN thin film with distinctive peaks representing Bi, Zn and Nb. The corresponding weight and atomic percentages associated with each of the elements as displayed in figure 6.4 are listed in table 6.1. The atomic percentage data is required to determine the stoichiometry of the deposited thin film. To achieve the best measurement accuracy the film thickness should be of the order of 500 nm or greater. The data in figure 6.4 and table 6.1 is representative of a BZN film typically 350 nm thick and indicates slightly low zinc content of 0.8, i.e. $(Bi_{1.5}Zn_{0.3})(Zn_{0.5}Nb_{1.5})O_6O'_{0.7}$. This may account for the reduced tunability.

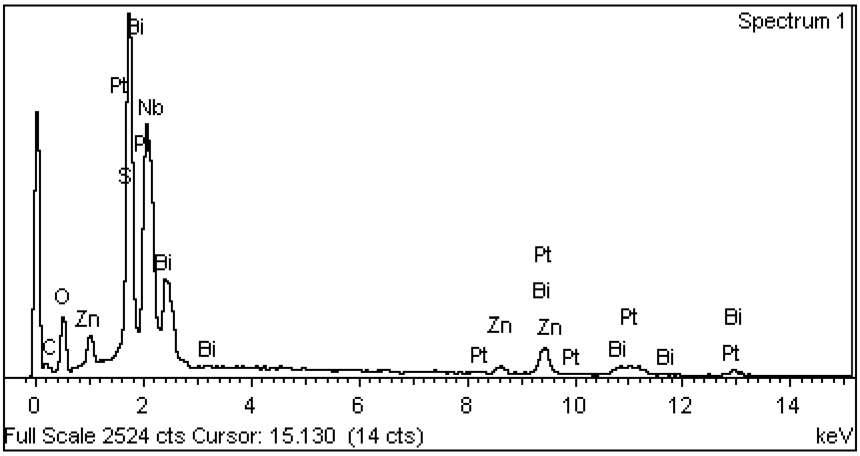

Figure 6.4 EDX spectrum of as-sputtered BZN thin film at 15 keV showing Bi, Zn and Nb peaks.

Table 6.1 EDX analysis of as-sputtered $Bi_{1.5}Zn_{1.0}Nb_{1.5}O_7$ thin film displaying weight and atomic percentages of each element detected.

$Bi_{1.5}Zn_{1.0}Nb_{1.5}O_7$

Element	Weight%	Atomic%
C K	1.17	4.78
O K	15.82	48.53
Si K	14.85	25.95
Zn K	3.01	2.26
Nb L	8.74	4.62
Pt M	36.76	9.25
Bi M	19.66	4.62
Totals	100.00	

Analysis of the microstructure of the as-deposited BZN thin films was performed using SEM. Typical photomicrographs of the surface and in section can be seen in figure 6.5. The SEM of the BZN surface clearly shows the nanocrystalline structure that develops when a 350 nm thick BZN film is grown on platinised silicon at 300°C. In section the 350nm BZN film can be seen on the 100nm thick Pt bottom electrode below which is the 200 nm thick SiO_2 buffer layer on silicon.

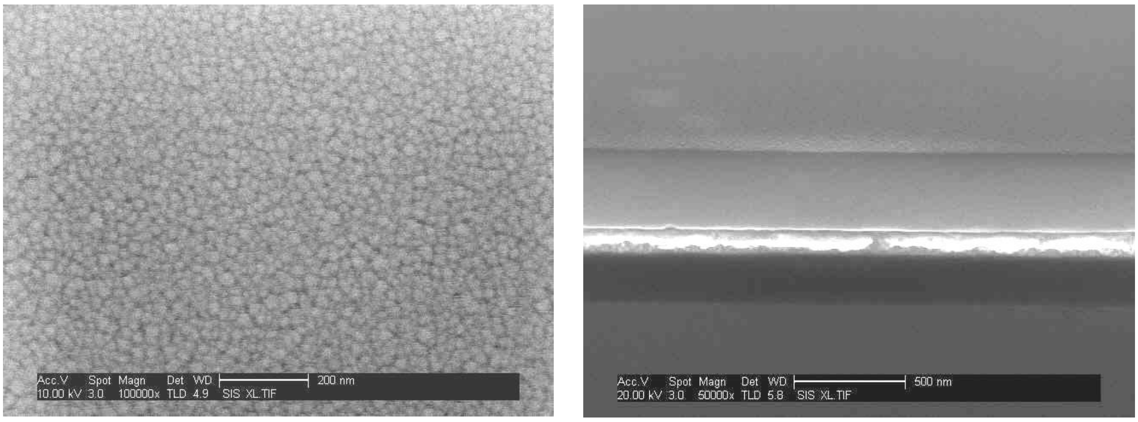

Figure 6.5 SEM micrographs of the surface and section of an as-sputtered BZN film on a Pt/Ti lower electrode.

From the SEM micrograph of the layered section, the BZN film is seen to be uniform, dense and free of defects such as cracks, hillocks and pinholes. There is no delaminating of film from substrate.

Electrical measurements were performed on the nanocrystalline BZN films at low frequency (to 300 kHz) using a MIM capacitor structure employing a sputtered Pt/Ti bottom electrode and thermally evaporated Au/Cr top electrode. The results are presented in figure 6.6 which shows the variation in dielectric constant and loss with frequency. There is little variation in either dielectric constant or loss across the frequency range with a dielectric constant very close to 50 and loss 0.02 or lower. The amorphous BZN dielectric thin-film capacitors were not tunable. The main disappointing outcome was the low dielectric strength (250 kV/cm) of this material considering the films appear dense and free from defects. It is generally recognised, by using statistical analysis and applying the Weibull function, that small grained samples have larger dielectric strength compared to large grained specimens. Also, the maximum temperature seen by the BZN film and Pt/Ti layer was 300^{o}C (i.e., when the BZN was sputtered down). The sample would therefore be unlikely to see substantial diffusion of Ti or Pt into the BZN film causing an electrical pathway. There is nothing in the SEM micrographs to suggest this. Other amorphous materials including BZT have shown much higher breakdown strength compared to their crystalline films even when heated to a similar temperature (300^{o}C) and above.

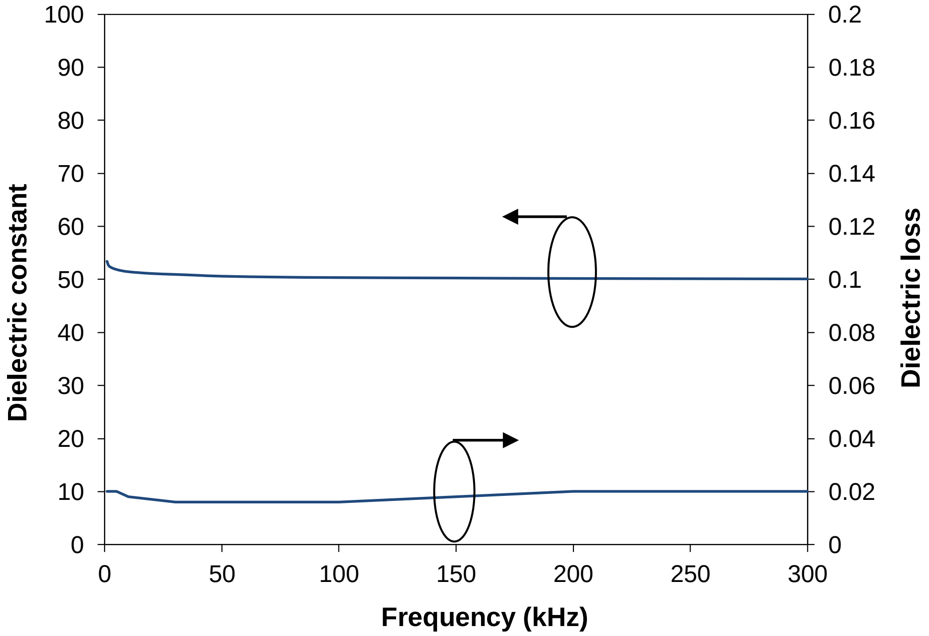

Figure 6.6 Dielectric properties of nanocrystalline BZN thin film as a function of frequency.

6.3.2 Nanocrystalline BZN Thin Film Growth using Seed Layers

One way to increase the dielectric strength of the nanocrystalline BZN thin film was to deposit a seed layer on the Pt/Ti electrode prior to growing the BZN. By way of an experiment the primary seed material chosen was BZT deposited using the sol-gel process. BZT was selected since this material had already been well characterised on platinised silicon for three different compositions. A single layer of BZT(20/80) was spun onto the platinised silicon sample to a thickness of ~30 nm. This very thin layer was annealed and crystallised at 650^{o}C on the hotplate for 15 minutes followed by RTA at 700^{o}C for 1 minute. Onto this seed layer was deposited a 350 nm thick BZN film by RF magnetron sputtering; the substrate temperature was maintained at 300^{o}C. Other seed layer materials trialled were barium strontium titanate (BST) and lead strontium titanate (PST) also deposited using the sol-gel technique under the same processing condition as used for BZT. However, these materials had not been well characterised. It must be noted that the use of PST as a seed layer was for comparison purposes only, since this work is dedicated to developing lead-free dielectric thin-film capacitors. The XRD plot of BZN thin film on BZT seed layer is shown in figure 6.7. The BZT crystalline (110) peak can be just seen at about 32^{o} on the XRD spectrum which contains no BZN crystallisation peaks.

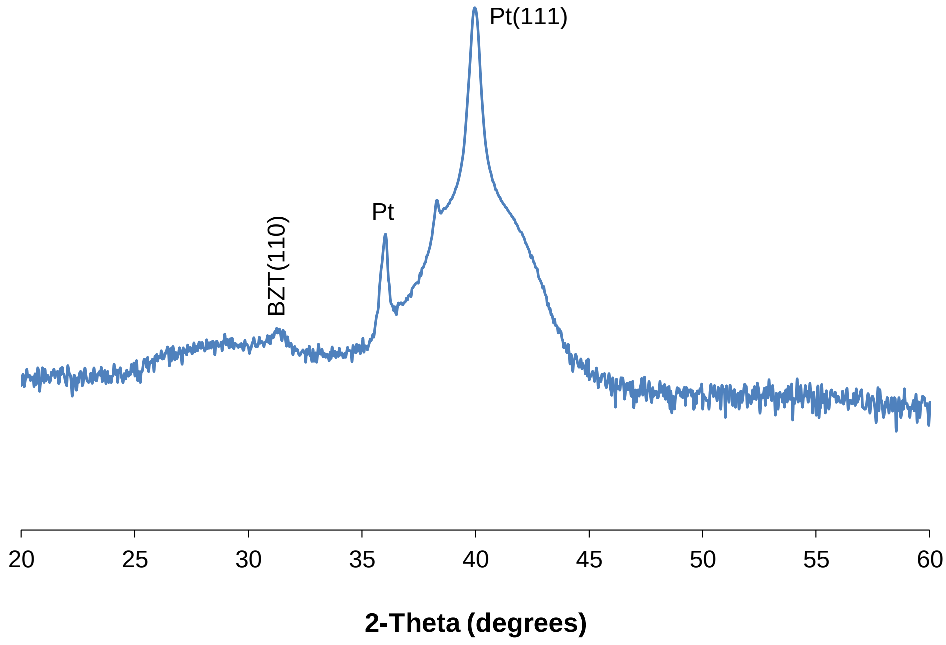

Figure 6.7 XRD plot of BZN thin film grown on platinised silicon with intermediate BZT(20/80) seed layer.

Figure 6.8 shows the surface and sectional microstructure of the BZN thin film sputter deposited on BZT(20/80) seed layer on platinised silicon substrate. In section the BZT layer can be seen above the bright Pt layer and has a granular microstructure. From the surface image of the BZN thin film it is evident that very small grains are arranged in much larger clusters with well defined grain boundaries. These clusters vary in size over the surface of the film. The structure of BZN grown on this seed layer is clearly columnar (straight grain boundaries that run through the film) and is very different to the microstructure of BZN grown directly on Pt (figure 6.5). The very small grains observed in the BZT seed layer act as nucleation centres for columnar growth in the much thicker BZN film. The BZN film grown on BZT seed layer is also dense and uniform with no obvious defects. A similar dense, columnar microstructure was observed for BZN films grown on very thin (~30 nm) BST and PST seed layers.

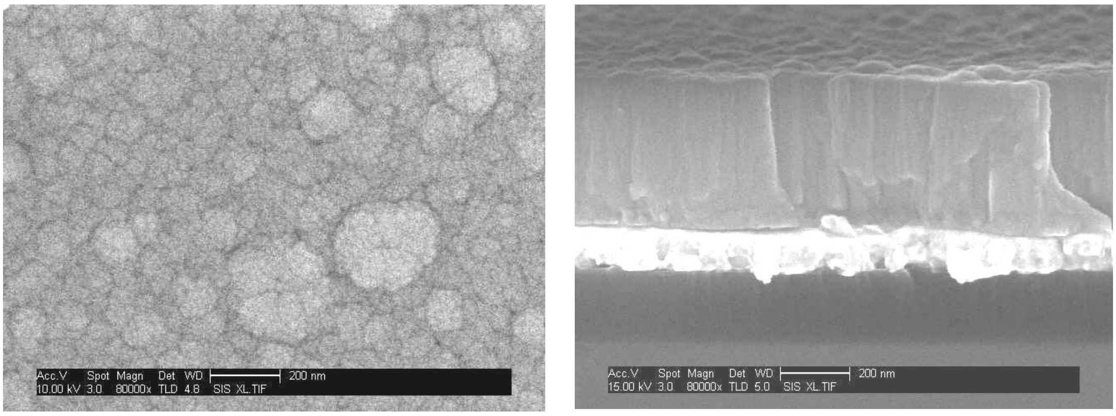

Figure 6.8 SEM micrographs showing the surface and section of as-sputtered BZN thin film on BZT seed layer.

Low frequency electrical characterisation of BZN using three different seed layers BZT, BST and PST each 30 nm thick was also performed and the results are displayed in figure 6.9.

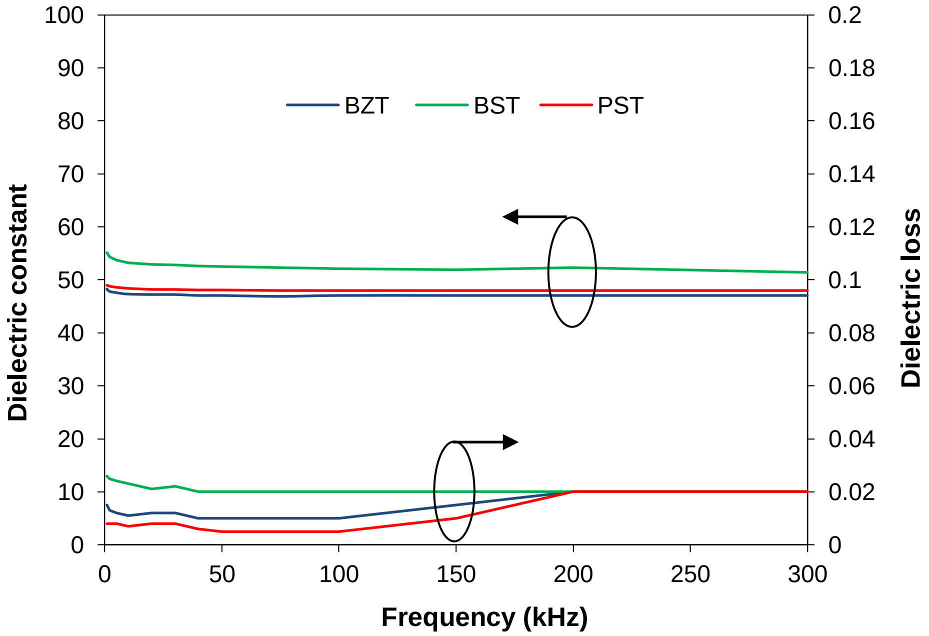

Figure 6.9 Dielectric constant and loss as a function of frequency for BZN thin film with BZT, BST and PST seed layers.

As we have seen, the deployment of a seed layer can significantly influence the microstructure of BZN. The electrical measurements on the other hand indicate the influence, if any, that the seed layer has on the dielectric properties of the

BZN film. It is interesting to compare these results in figure 6.9 with the data presented in figure 6.6 for BZN grown directly on Pt. The dielectric constant and loss had changed very little from that recorded for BZN deposited on Pt, surprisingly close to 50 for all samples with seed layers. It was expected that the higher dielectric constant seed material compared to BZN would have resulted in a further increase in the combined permittivity according to the equation for the dielectric constant of layered composites given in section 5.1. The reason for this could be Pt/Ti diffusion into the very thin (~30 nm) seed layer when annealed at high temperature (700^{o}C) causing the layer to become conductive prior to depositing the BZN film. The dielectric loss was generally similar for all samples. However, below a frequency of 200 kHz a reduced loss for BZN film on BZT and PST seed layer was realised. The most significant advantage of employing a seed layer for nanocrystalline BZN growth was the improved dielectric strength that this gave compared to the strength (250 kV/cm) achieved when growing amorphous BZN directly on Pt. The breakdown strength of nanocrystalline BZN grown on BZT, BST and PST seed layers was 560 kV/cm, 530 kV/cm and 470 kV/cm, respectively. Increased strength resulted in part from the change in microstructure of the BZN film (i.e., a dense film of columnar structure), but also dependent to a large extent on the dielectric seed layer material selected (e.g., BZT resulted in the highest strength).

6.3.3 Crystalline BZN Thin Film Growth on Platinised Silicon

We now turn attention to fully crystallised BZN material. The method by which the BZN thin film samples were annealed directly influenced the crystallisation and resultant microstructure of the BZN. We start by comparing samples annealed by hotplate and rapid thermal annealing (RTA). The XRD plots of the as-sputtered material and that annealed on the hotplate and by RTA are shown in figure 6.10. Clearly the as-sputtered material deposited onto the heated (300^{o}C) substrate had not fully crystallised but has a nanocrystalline structure (figure 6.5). There was also a significant difference between material annealed on the hotplate and material crystallised using RTA. The lower intensity and wider diffraction peaks of the hotplate annealed sample indicate a smaller grain size whereas, material annealed by RTA with high intensity, narrow peaks suggest a larger grain size. This was borne out by SEM analysis of the thin film surfaces as shown in figure 6.11.

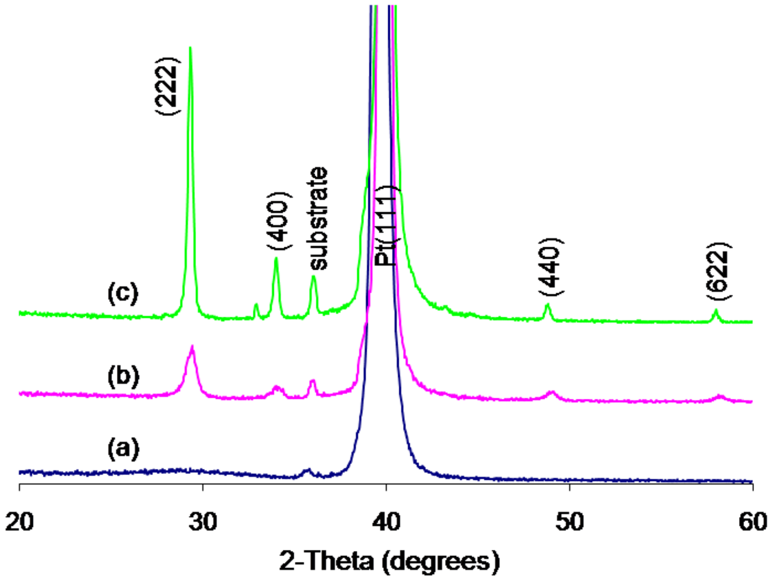

Figure 6.10 XRD diffractogram of thin-film BZN (a) as-sputtered, (b) after annealing on hotplate at 600°C for 10 minutes and (c) after annealing by RTA at 600°C for 3 minutes.

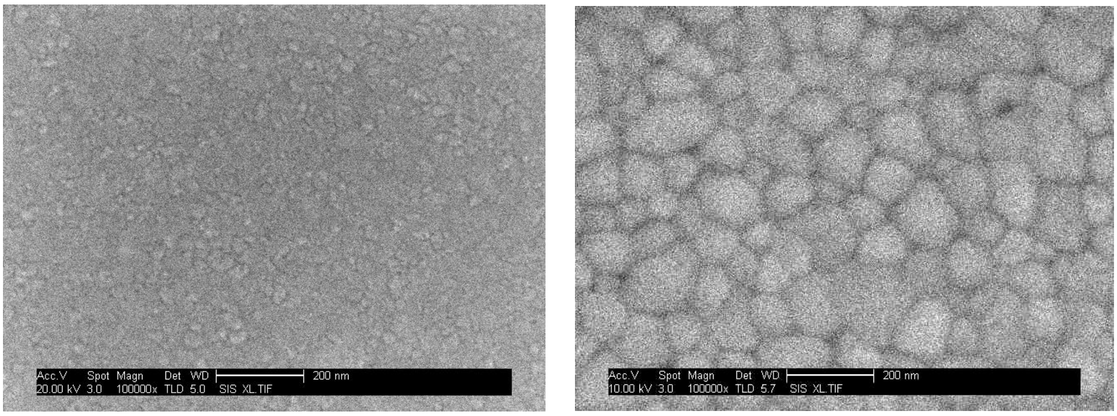

(a) (b)

Figure 6.11 SEM micrographs of BZN thin film surfaces after annealing (a) at 600°C for 10 minutes on the hotplate and (b) at 600°C for 3 minutes by RTA.

BZN thin film samples annealed by RTA at 600°C and 700°C for 3 minutes crystallised particularly well as seen in the polycrystalline XRD pattern of figure 6.12. The sharp crystallographic major peak (222) indicates a large grain size similar to the grain size displayed in the SEM micrograph in figure 6.11b.

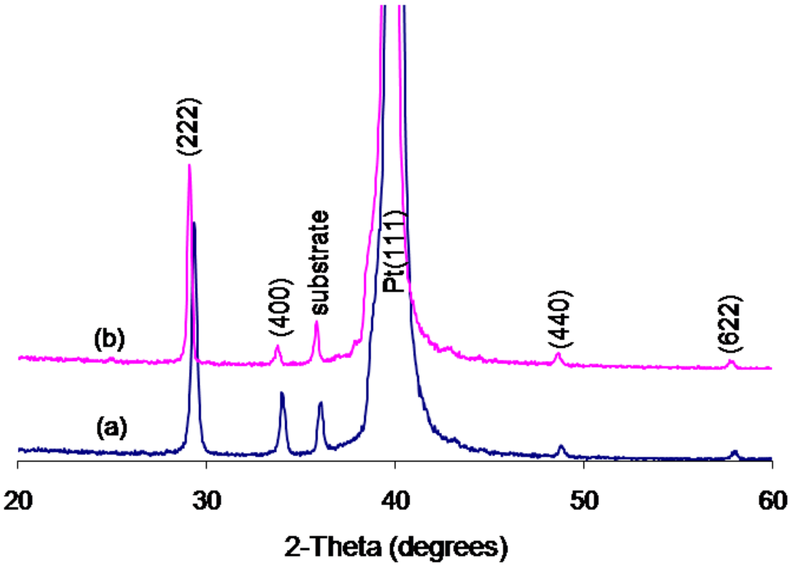

Figure 6.12 XRD patterns of BZN thin films annealed by RTA at (a) 600°C and (b) 700°C.

Dielectric properties of BZN deposited on platinised silicon as a function of frequency to 300 kHz are shown in figure 6.13. The dielectric constant was significantly higher for thin-film BZN annealed by RTA at the elevated temperature of 700°C. Below 100 kHz the dielectric loss was very low (~0.003) for both samples rising to 0.01 and 0.02 at 300 kHz for BZN annealed at 600°C and 700°C, respectively. There was very little or no tuning of dielectric constant with applied electric field for thin-film BZN. At lower bias fields no tuning was observed, with only rapid tuning occurring at higher bias fields close to the breakdown threshold of the material (figure 6.14). These findings are at odds with the results presented by other researchers for thin BZN films deposited on platinised silicon and processed under similar conditions. For BZN annealed by RTA at 700°C the dielectric strength was somewhat reduced (~150 kV/cm) when compared to material annealed at 600°C (~350 kV/cm).

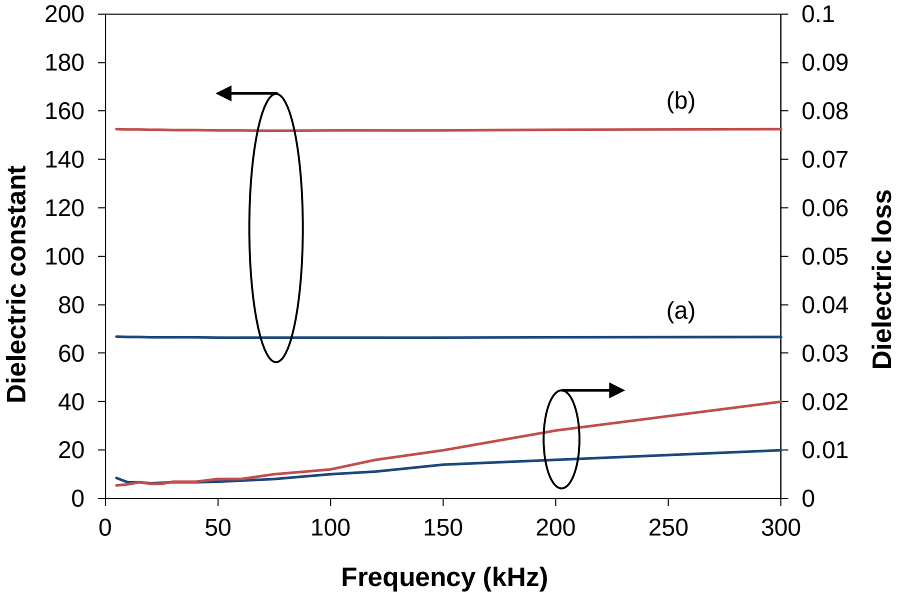

Figure 6.13 Dielectric properties as a function of frequency for thin-film BZN annealed by RTA at (a) 600°C and (b) 700°C.

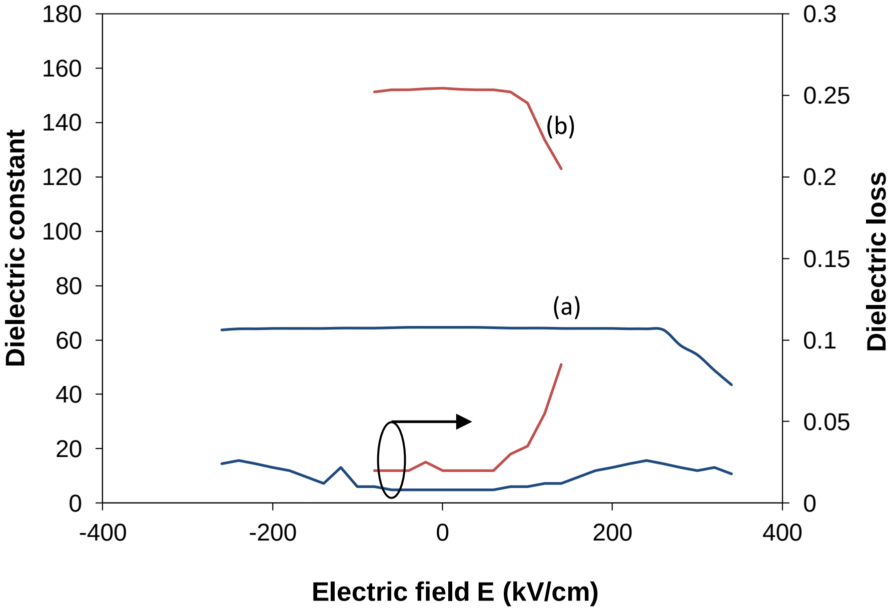

Figure 6.14 Dielectric properties of thin-film BZN as a function of DC bias field after RTA at (a) 600°C and (b) 700°C.

Due to the lack of tuning, the crystalline BZN thin film dielectric material may be a suitable candidate for use in fixed value capacitors. However, the low dielectric strength may be a limiting factor in certain applications. Some material and process refinements implemented to increase the breakdown strength of BZN thin films for application to the zipping varactor will be discussed in chapter 8 of this thesis.

6.3.4 Two-Step Sputtering Deposition Method (BZN/BZN Bilayer)

It has been shown that the microstructure and dielectric properties of crystalline BZN can be altered by a process known as the two-step sputtering deposition method. This was based on work carried out by Chen *et al.* who were specifically looking at this technique as a means of decreasing the interfacial transition layer (dead layer) between BST film and platinum electrode [6.1]. Since the dielectric constant of the interfacial layer is lower than that of the bulk film, reducing the thickness of the interfacial layer results in a higher overall dielectric constant. Experiments have shown that the BZN microstructure and permittivity can be changed using a modified two-step process by varying the thickness of the two sputtered layers and by judicious *ex situ* annealing.

A modified two-layer process has been developed where the first BZN layer is sputter deposited on platinised silicon, the sample removed from the sputtering chamber and annealed by hotplate or RTA to crystallise the material. The sample then has a second film sputter deposited onto the first. This is then *ex situ* annealed either in the same way or differently.

For the initial experiments the two sputtered layers were each annealed by hotplate at 650^{o}C for 10 minutes. Of the two samples processed, one was given an additional, final annealing by RTA at 650^{o}C for 3 minutes. The crystallisation and microstructure of the samples were examined by XRD and SEM, respectively. The XRD patterns of figure 6.15 displays the crystallisation behaviour of the two samples. It can be clearly seen by observing the dominant peak at (222) that the sample final annealed by RTA shows improved crystallisation over the sample annealed by hotplate. The narrow peak of the

RTA processed sample also indicates a larger grain structure which has been characteristic throughout.

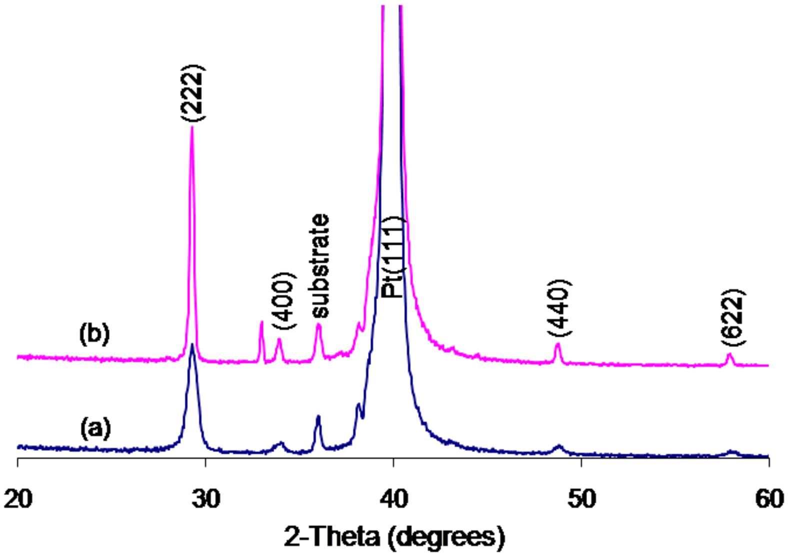

Figure 6.15 XRD patterns of two-layer samples where (a) both layers annealed by hotplate at 650°C for 10 minutes and (b) both BZN layers annealed by hotplate at 650°C for 10 minutes followed by a final annealing by RTA at 650°C for 3 minutes.

The cross-sectional microstructure of the two samples is shown in figure 6.16.

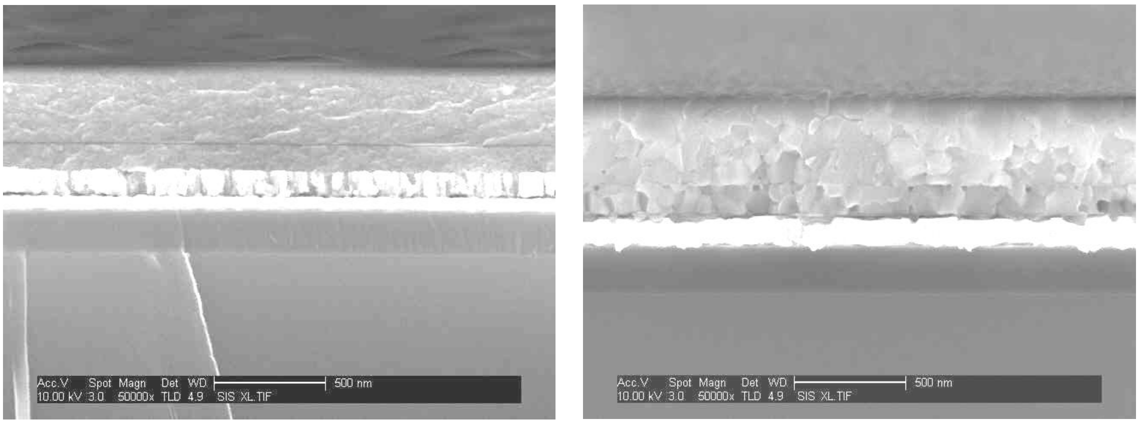

(a) (b)

Figure 6.16 SEM sections of BZN/BZN bilayers showing (a) both layers annealed by hotplate at 650°C for 10 minutes and (b) both layers annealed by hotplate at 650°C for 10 minutes and a final annealing by RTA at 650°C for 3 minutes.

As expected, the sectional microstructure of the two layers within each sample was identical. However, there were observable differences in the microstructure between the sample hotplate annealed and the sample final annealed by RTA as indicated by the XRD results (figure 6.15). The difference in microstructure did have a bearing on the dielectric properties of the composite film as shown in figure 6.17. This was particularly so in the case of the dielectric constant.

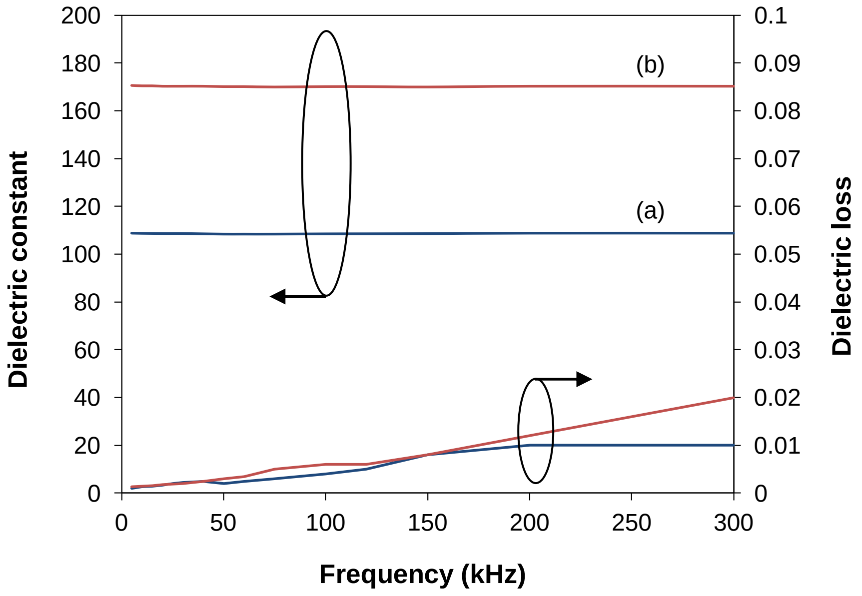

Figure 6.17 Dielectric properties of BZN/BZN bilayers as a function of frequency for (a) both layers annealed by hotplate at 650°C for 10 minutes and (b) both layers annealed by hotplate at 650°C for 10 minutes and a final annealing by RTA at 650°C for 3 minutes.

There were distinct advantages to annealing BZN thin films (including bilayers) by RTA rather than by hotplate since RTA annealed material resulted in a higher dielectric constant and with only a modest increase in the dielectric loss. This is demonstrated in figure 6.18 which shows a graph of dielectric constant and loss as a function of annealing method for the two sputtered BZN layers. The data for three different annealing strategies are displayed including the annealing of each of the two sputtered layers by hotplate, the annealing of both sputtered layers by RTA, and the annealing of both layers by hotplate with a final annealing of the composite film by RTA. The dielectric constant of ~170 for the two layers annealed by hotplate with a final annealing by RTA was a similar result to that of a single layered film annealed by RTA. A low dielectric loss of between 0.004 and 0.006 was measured at a frequency of 100 kHz and 0 V bias for the samples processed.

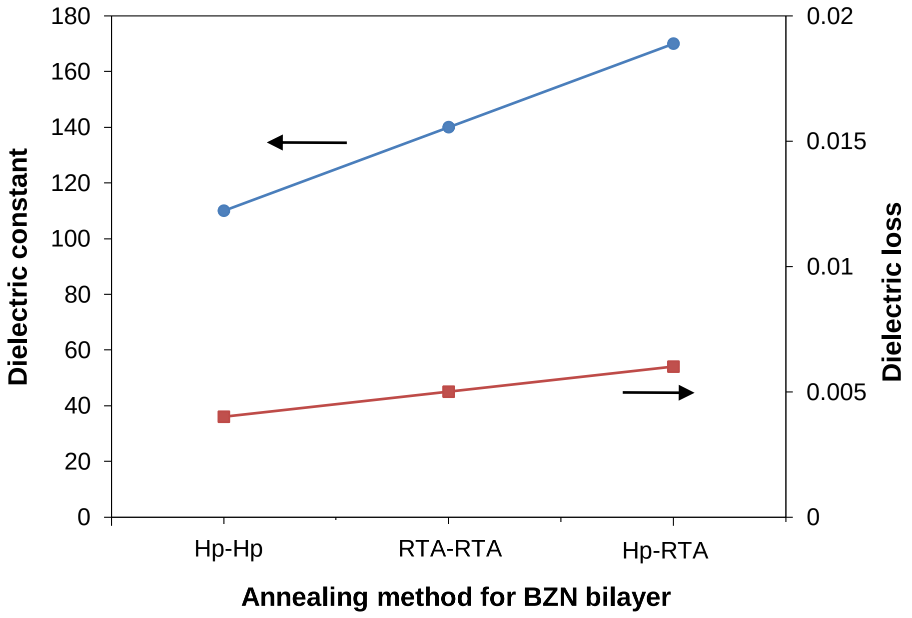

Figure 6.18 Variation in dielectric constant and loss with annealing method used to crystallise the two BZN layers in the bilayer sputtering process.

Based on the improved dielectric constant achieved when annealing by RTA as opposed to hotplate annealing, further experiments were conducted using the two-step process by *ex situ* annealing each sputtered BZN layer by RTA. When the two sputtered BZN layers were first annealed and crystallised by RTA, a very different and useful result was obtained.

An XRD scan was performed on both layers after sputter deposition and subsequent *ex situ* annealing. These XRD results are displayed in figure 6.19. The XRD patterns of the two layers both annealed at 650^{o}C by RTA for 3 minutes are near to identical indicating good crystallisation of the material. The composite film is clearly polycrystalline with the major peak at (222), as has been the case with sputtered single-layer films annealed under the same conditions.

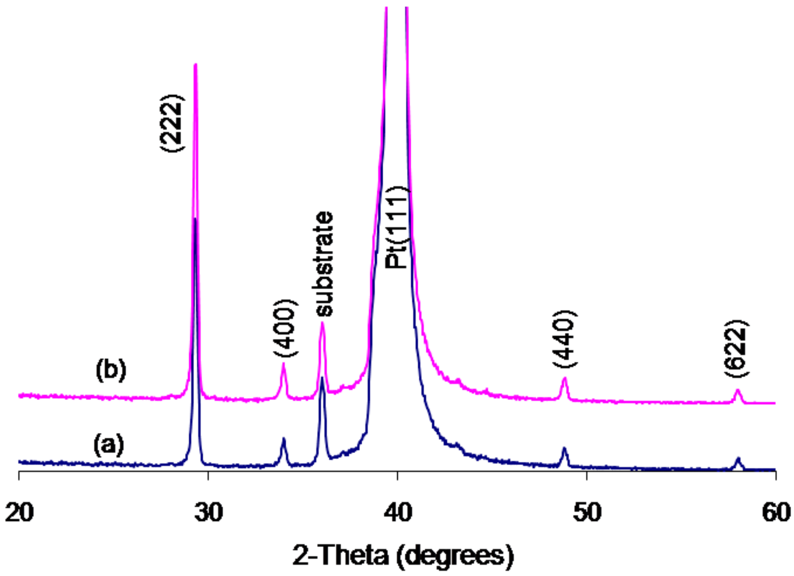

Figure 6.19 XRD patterns for (a) first sputtered BZN thin film annealed at 650°C by RTA for 3 minutes and (b) second sputter deposited BZN thin film annealed at 650°C by RTA for 3 minutes.

Although the XRD patterns are near identical, the microstructure of the two layers are dissimilar as can be seen in the SEM section of figure 6.20. A comparable result was obtained for a second sample (figure 6.21) annealed in the same way, although the second sputter deposited or top layer thickness was much thinner (i.e. 120 nm thick compared to 400 nm thick in figure 6.20).

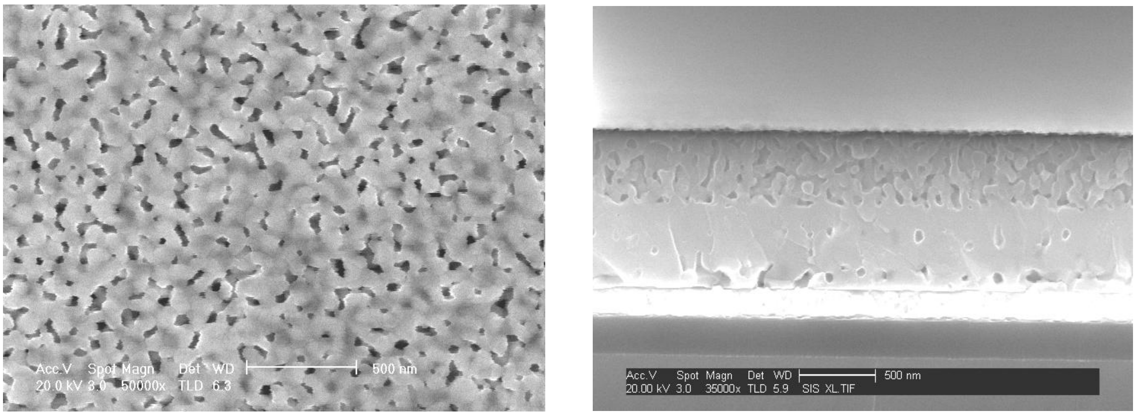

Figure 6.20 SEM micrograph of the surface and section of a two layer BZN thin film after *ex situ* annealing both layers by RTA at 650°C for 3 minutes.

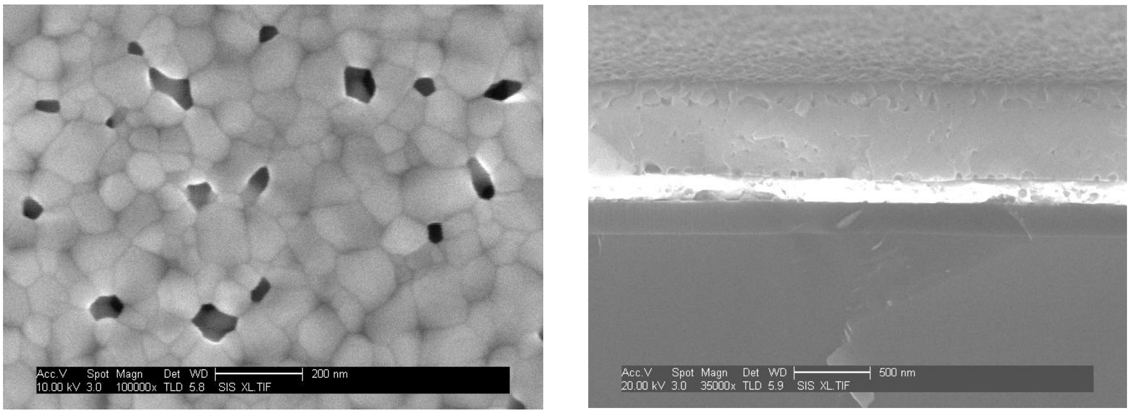

Figure 6.21 SEM micrograph of the surface and section of a bilayer BZN thin film after annealing both layers by RTA at 650°C for 3 minutes. A much thinner (~120 nm) top layer can be seen in section.

An interesting transition in the microstructure from the first sputtered BZN layer to the second, top BZN layer is displayed in figures 6.20 and 6.21. The first layer appears dense whereas the second layer is very porous. The microstructure of this porous layer is a consequence of nucleation and crystallisation growth from an existing large grain structure associated with the first crystallised BZN layer and is very similar to that of a BZN single layer sputter deposited and crystallised directly on silicon as shown in figure 6.22.

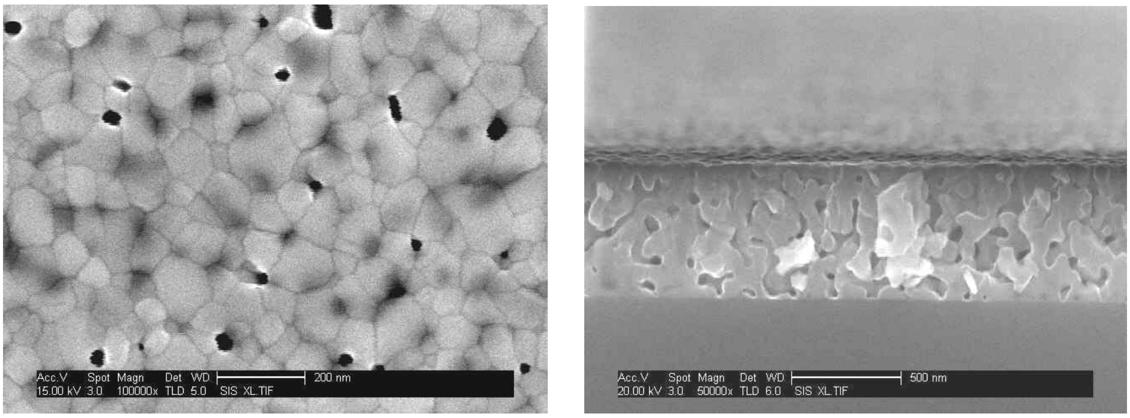

Figure 6.22 SEM images of the surface and in section of a BZN thin film sputter deposited on silicon and annealed by RTA at 650°C for 3 minutes.

It is generally acknowledged that a porous layer has reduced dielectric constant compared to a dense layer, and so by varying the thickness of the porous layer it was possible to vary the dielectric constant. For example, lower values of dielectric constant were achieved by depositing a thinner first sputtered BZN layer, annealing that layer by RTA, and then growing a much thicker second layer which was also subsequently annealed by RTA. Higher values of dielectric constant were therefore achieved when a thinner second or top layer was annealed by RTA compared to the thickness of the first sputtered layer. Using the two-step sputtering deposition method in this way it has been possible to control the dielectric constant of 500 nm thick BZN thin films grown on platinised silicon over the range 70 to 170 as shown in figure 6.23.

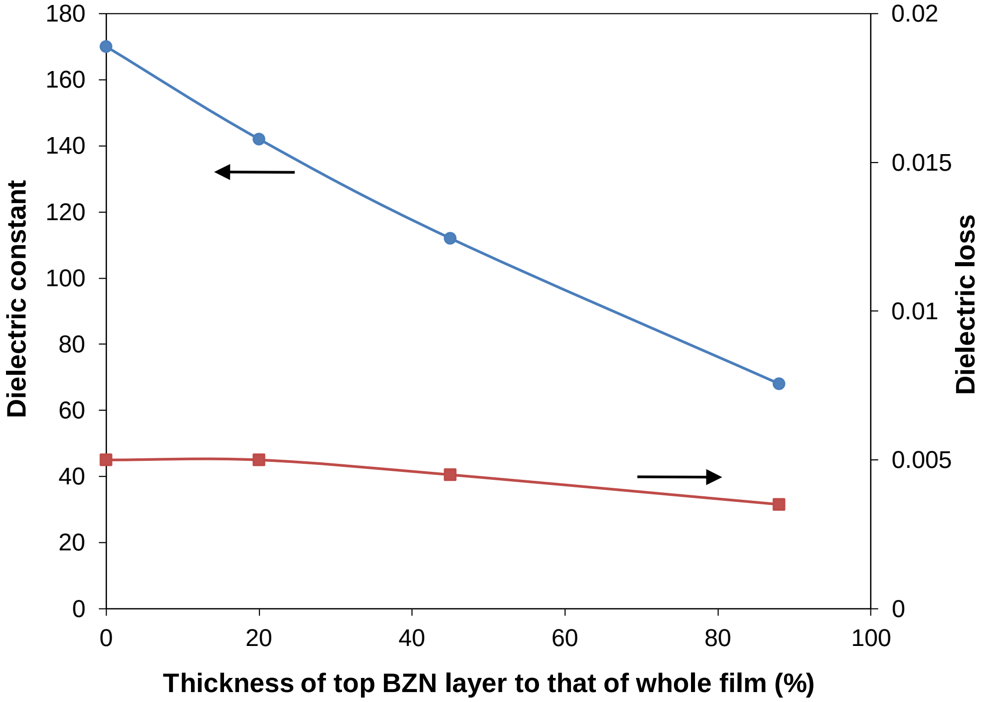

Figure 6.23 Dielectric constant as a function of the variation in the thickness of the top BZN layer as a percentage of the thickness of the composite BZN film.

The near linear relationship between dielectric constant and the variation in the thickness of the top BZN layer relative to the thickness of the film shows a substantial decrease in dielectric constant as the thickness of the top sputtered layer is increased. The maximum dielectric constant of 170 was achieved for a single sputtered layer annealed by RTA at 650°C for 3 minutes with no second layer (i.e. 0%). In this work, the minimum dielectric constant was 70 for a top BZN layer that was 88% of the thickness of the composite BZN film. To accomplish this, both sputtered BZN layers were *ex situ* annealed and crystallised by RTA at 650^{o}C for 3 minutes. It should be possible to reduce the dielectric constant below 70 by further increasing the top layer thickness relative to the thickness of the whole film, i.e. closer to 100%. The loss was maintained at or below 0.005. Both dielectric constant and loss were measured at 100 kHz and 0 V bias.

6.3.5 Nanocrystalline BZN Thin Film Growth on Liquid Crystal Polymer (LCP) Substrate: A Trial Investigation

Feasibility studies were conducted which looked at the potential growth of nanocrystalline BZN thin films on Au/Cr coated LCP. The RF magnetron sputter deposition of BZN could not be performed at 300^{o}C, as is the case for deposition on other substrate materials, since this was rather close to the melting temperature (~320^{o}C) of the LCP. Deposition temperatures chosen were 25^{o}C, 100^{o}C and 200^{o}C. Initial trials looked at depositing ~300 nm thick BZN films on thermally evaporated and sputtered Au(100nm)/Cr(10nm) coated flexible LCP substrates with and without copper cladding. Evaporated Au/Cr circular top electrodes completed the parallel-plate structure from which electrical measurements could be made. The surface morphology of the BZN films deposited on LCP were examined by optical microscope to 50x magnification since an examination by SEM or AFM proved problematic due to substrate expansion and deformation.

Deposition of a thin BZN film onto an LCP substrate held at a temperature of 200^{o}C caused the LCP substrate to expand and buckle. This resulted from a softening of the LCP together with growth stresses in the sputtered BZN film which tend to be compressive. When tested electrically none of the capacitors were found to be working. Although material deposited onto Au coated LCP at a substrate temperature of 25^{o}C displayed the least expansion and deformation, dielectric measurements showed that none of the capacitors functioned.

At a substrate temperature of 100^{o}C there was expansion and distortion of the LCP but somewhat reduced compared to that seen at 200^{o}C. BZN films appeared smooth following the surface contours of the LCP, crack free, and without defects such as hillocks and pinholes associated with a compressive film. The capacitors were tested and found to be working on LCP without copper cladding, but not working on LCP with cladding. The measured dielectric properties as a function of frequency for a thin BZN film grown on Au coated LCP are shown in figure 6.24. Data for the two capacitor structures, one with thermally evaporated Au/Cr bottom electrode and the other with sputtered Au/Cr bottom electrode, are displayed.

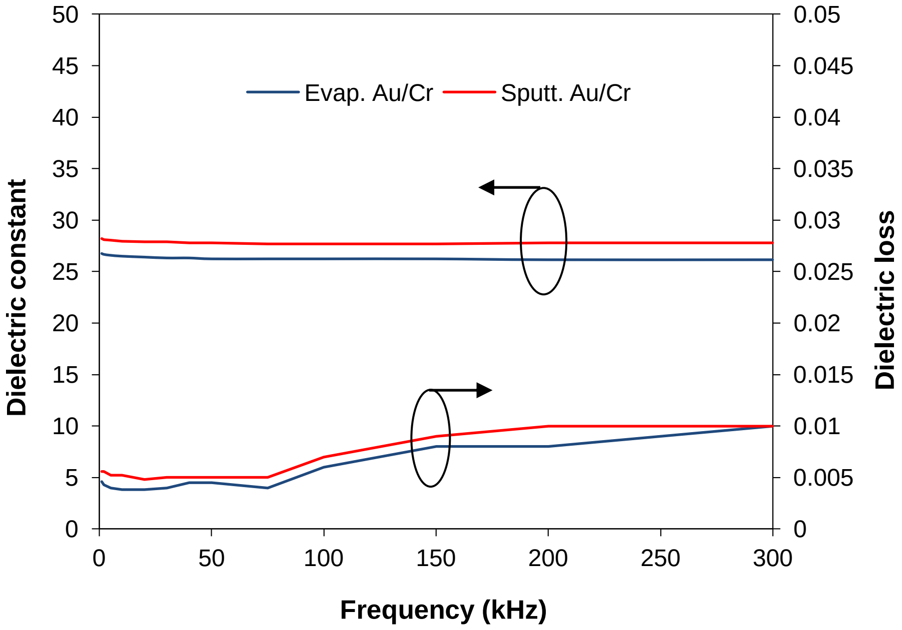

Figure 6.24 Dielectric constant and loss variation with frequency for BZN thin film sputter deposited on Au coated LCP.

For a 300 nm thick BZN film on LCP with evaporated Au/Cr bottom and top electrodes a dielectric constant and loss of 26 and 0.004 was achieved, respectively. When the sputtered Au/Cr bottom electrode was used, the dielectric constant was 28 and the loss 0.005, similar to the results obtained when using evaporated Au/Cr electrode. However, the breakdown strength of the capacitors with sputtered bottom electrode (650 kV/cm) was much higher than those with the evaporated electrode (250 kV/cm). This was mainly due to the inferior quality of the thermally evaporated Au/Cr compared to the sputtered metals. Evaporated films tend to display thickness uniformity variations and can have a higher defect density than their sputtered counterparts. Rough and disordered surfaces generate localised electric field intensities which for thin dielectric films result in premature electrical breakdown.

Although the progress of this work has been limited, the initial feasibility study has demonstrated that growth of a thin BZN film on flexible substrates is possible, with a potential application to fixed value capacitors.

6.3.6 Low-K Amorphous BZT Thin Films on Pt and Au Electrode

Much effort has been invested in researching alternative low-k dielectrics to SiO_2 which have good insulating properties. The dielectric constant value can be varied by altering the density of the film (e.g. lowering the dielectric constant by introducing porosity). Ultra low-k dielectric layers are likely achievable using porous films. The material to replace SiO_2 (permittivity ~4) needs to have a higher dielectric constant so that thicker films result in a comparable or improved electrical performance. These films therefore require materials with increased density. Thin-film amorphous barium zirconate titanate (BZT) is one possible material candidate. Work on the material and electrical properties of amorphous BZT thin films have not been previously reported on by other researchers. This again is a preliminary material characterisation exercise, not about finding a material that will fulfil all the requirements for specific practical applications. The work programme will then be expanded at a later date to incorporate applications subject to satisfactory early outcomes.

Amorphous BZT thin films were deposited on $Pt/Ti/SiO_2/Si$ and $Au/Cr/SiO_2/Si$ substrates by the sol-gel technique. Following spin coating, the thin BZT films underwent a pyrolysis hotplate bake at 350^oC for 5 minutes, immediately followed by a bake at 550^oC for 5 minutes, both in air. The 550^oC bake was probably close to the highest temperature possible without crystallising the film. For the BZT film to remain amorphous there would be no final crystallisation anneal. X-ray diffraction patterns of BZT thin film on Pt and Au coated SiO_2/Si substrate are shown in figure 6.25. Clearly there are none of the characteristic crystallographic peaks displayed, the principle one for BZT being (110) at $\sim 31^o$.

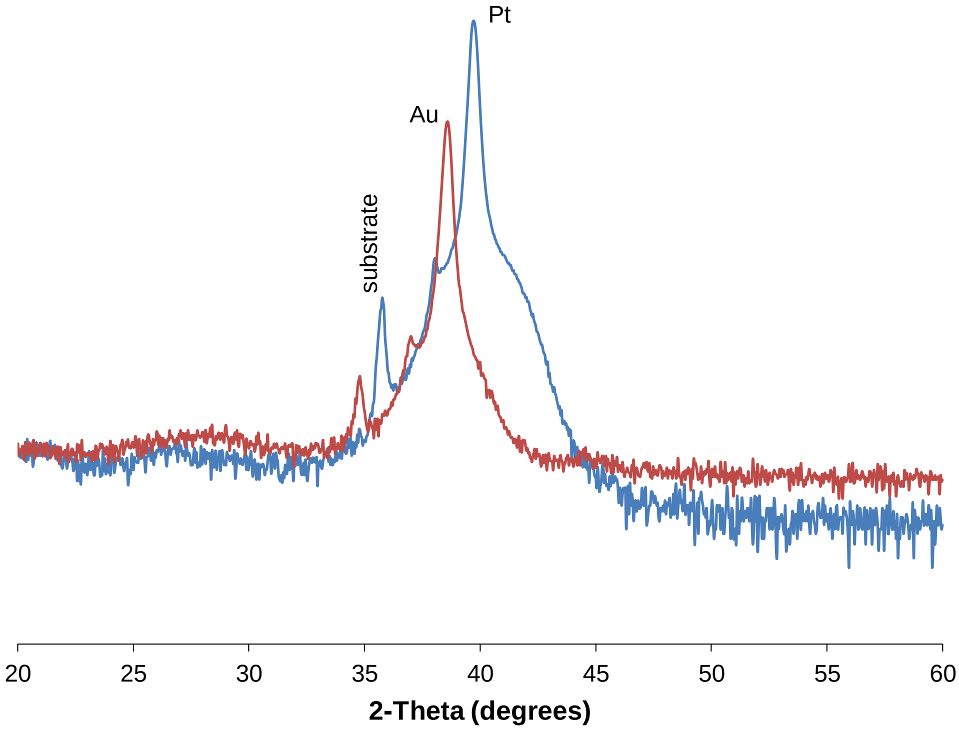

Figure 6.25 XRD patterns of BZT thin film deposited on Pt (blue) and Au (red) bottom electrodes.

The amorphous nature of the material was confirmed by examining the surface morphology using SEM which gave no evidence of a nanocrystalline phase as can be seen in figure 6.26. Films appear extremely dense and uniform with no observable defects (cracks, pinholes, hillocks, etc).

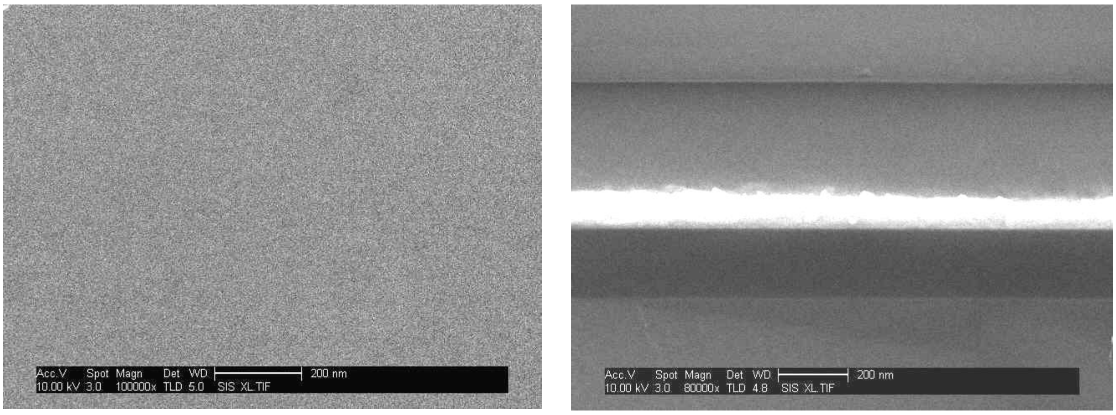

Figure 6.26 SEM micrographs of the surface and section of an amorphous BZT(5/95) thin film grown on Au bottom electrode (bright layer in section).

From the SEM images it is also evident that a 300 nm thick amorphous BZT film can be grown directly on Au layer without the need for an intermediate buffer, unlike crystalline BZT which requires a buffer layer. Charge-electric field (C-E) measurements of the capacitors (0.73 mm diameter disc) provided additional proof that the BZT films were in the amorphous phase. The C-E measurement in figure 6.27 shows a linear relationship between charge and field indicating a lack of ferroelectric domains and grain microstructure in the thin amorphous BZT(5/95) film.

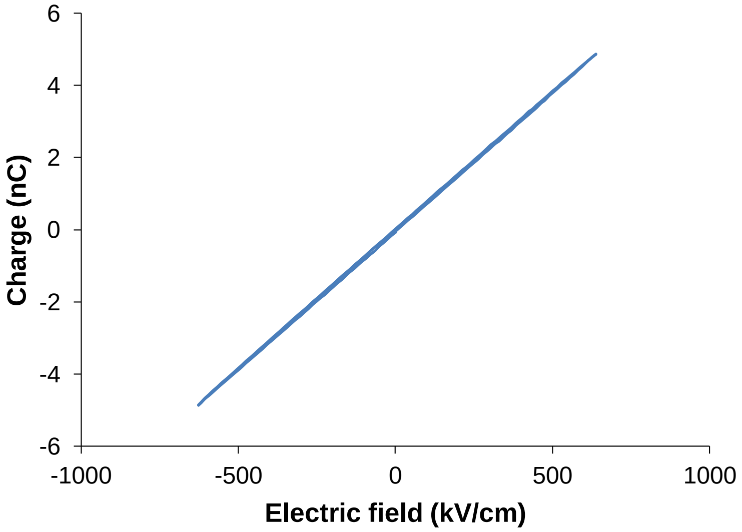

Figure 6.27 C-E measurement of BZT(5/95) thin film on Au/Cr bottom electrode.

The surface morphology images and a measurement of surface roughness of these films were obtained using AFM. The AFM images in figure 6.28 show a plan view and three dimensional projection of the surface over an area of 5 μm^2. These are surface images of the amorphous BZT thin film that had been grown on Au coated SiO_2/Si substrate. In the three dimensional projection of the surface the height dimension is 25.0 nm per division. The mean surface roughness R_a taken from the AFM image statistics was 0.758 nm. The surface roughness measured by Dektak surface profilometer over a much longer scan distance (5 mm) compared to AFM was 3.5 nm. The Dektak method resulted in a coarser measurement due to the size of the stylus. Either way it shows the BZT surface to be smooth with few discernible features (defects).

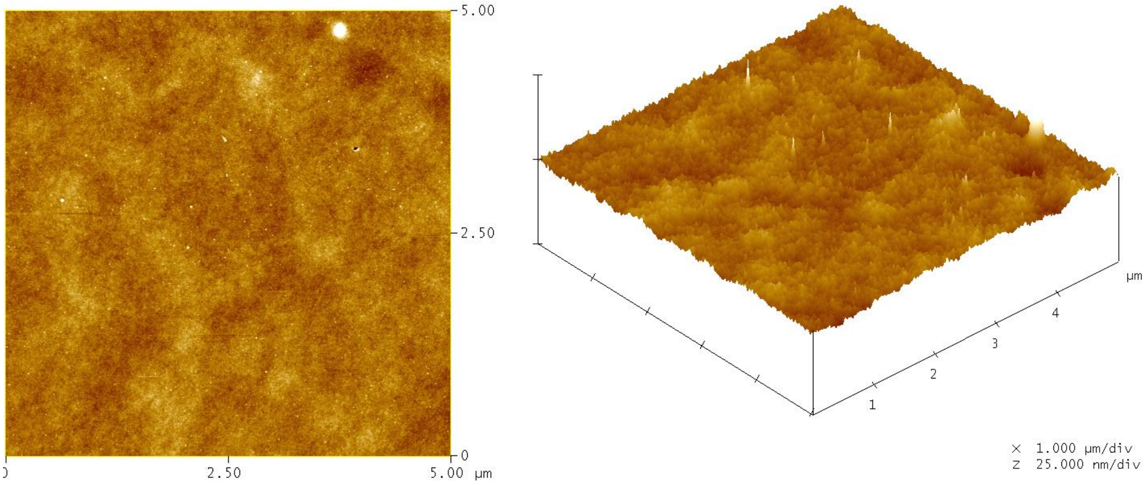

Figure 6.28 Surface AFM images of the amorphous BZT(5/95) film on Au electrode. Same sample as imaged by SEM in figure 6.26.

Low frequency electrical measurements were performed on the MIM capacitors with sputtered Pt/Ti and Au/Cr bottom electrodes and evaporated Au/Cr top electrodes. Three BZT compositions, 5/95, 20/80 and 35/65 were used as amorphous dielectric layer in the MIM configuration and the results compared.

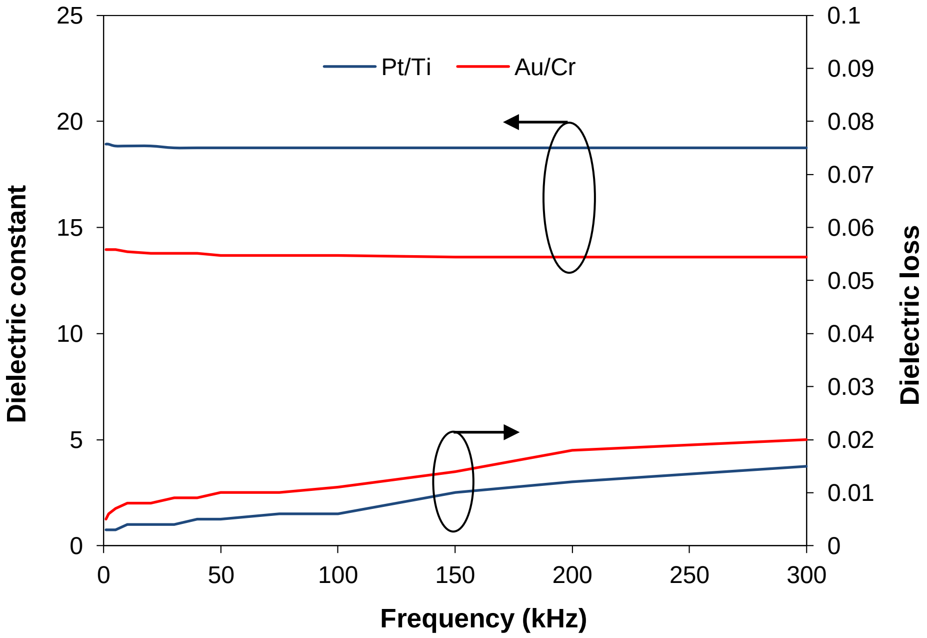

Figure 6.29 Dielectric measurements as a function of frequency representative of all three BZT compositions 5/95, 20/80 and 35/65 deposited on Pt/Ti and Au/Cr.

Figure 6.29 above shows the variation in dielectric constant and loss for amorphous BZT thin films grown on Pt/Ti and Au/Cr bottom electrodes. The variation in dielectric constant and loss with frequency was extremely similar for the three BZT compositions investigated and so only one set of curves are displayed in figure 6.29. The dielectric constant for BZT films of all compositions deposited on Pt/Ti was ~19. When deposited on Au/Cr bottom electrode the dielectric constant was reduced to ~14. This was accompanied by a slightly higher dielectric loss for BZT on Au/Cr compared to BZT material grown on Pt/Ti. Where films were more porous there was a substantial reduction in the dielectric constant as expected. However, the surface of these films tended to be significantly rougher. Figure 6.30 shows the AFM surface image of the porous BZT(20/80) and BZT(35/65) thin films deposited on Au/Cr electrode.

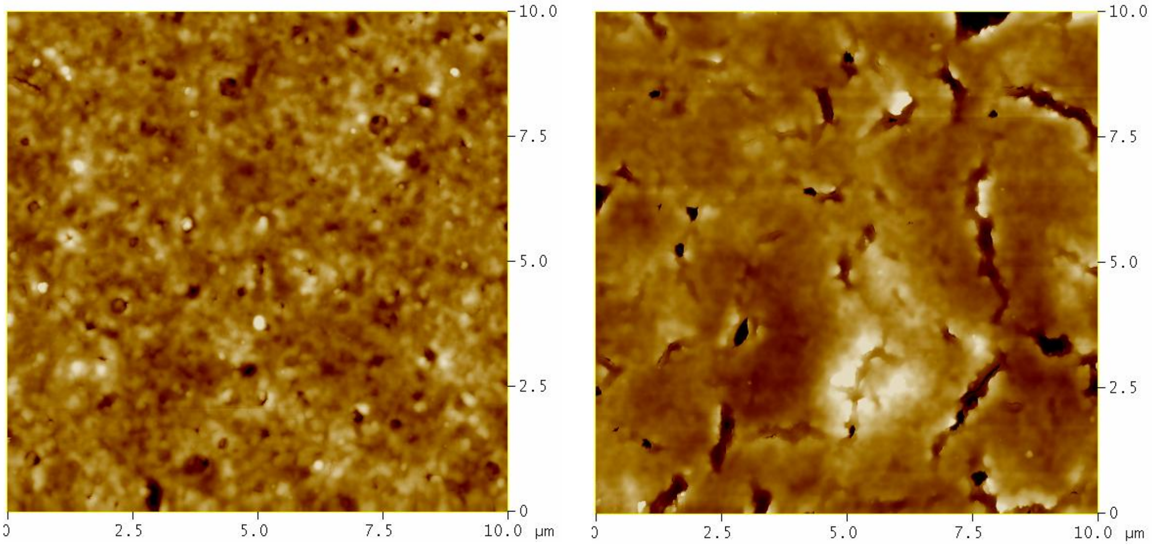

(a) (b)

Figure 6.30 AFM surface images of (a) BZT(20/80) and (b) BZT(35/65) thin films grown on Au/Cr/SiO_2/Si substrate.

The mean surface roughness R_a of BZT(20/80) and BZT(35/65) taken from the AFM image statistics was 11.0 nm and 27.5 nm, respectively. The Dektak surface roughness measurement over a much longer linear scan was 8.2 nm and 8.6 nm. Dielectric properties as a function of frequency for these films are displayed in figure 6.31. The lowering of the dielectric constant of the two BZT compositions to the values displayed in figure 6.31 from those presented in figure 6.29 resulted primarily from the introduction of porosity. Although the dielectric breakdown strength generally decreases with the increase of porosity, the strength of porous BZT(20/80) and BZT(35/65) was ~1.3 MV/cm, similar to that of nonporous BZT thin film material of the same composition. One way that porosity can be introduced is by reducing the sol spin speed as demonstrated in the SEM micrographs of figure 4.6 (sub-section 4.3.3). By simply increasing the thickness of a single spun layer, pores were incorporated. However, reducing the spin speed below ~2500 rpm resulted in a variation in film thickness across the sample which increased with decreasing spin speed. Alternatively, porosity can be introduced by increasing the thickness through changes to the solution concentration [6.2]. In the case of BZT, the concentration can be reduced by the addition of a solvent such as acetic acid, and increased by distillation. A further investigation should form part of the future work programme.

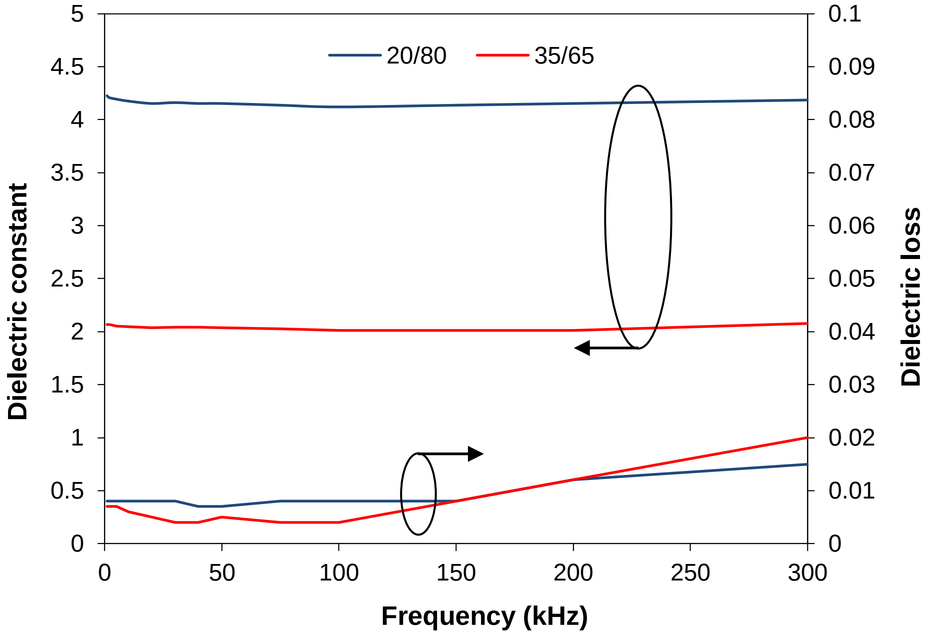

Figure 6.31 Variation of dielectric constant and loss with frequency for amorphous BZT(20/80) and BZT(35/65) thin films on Au/Cr electrode.

With the application of a positive electric bias field there was no observed change in the capacitance for all samples tested up to and including the breakdown voltage. Each of the capacitors was therefore tested to destruction so that the dielectric strength of the material could be accurately determined. The dielectric strength was measured for thin film material deposited on Pt/Ti and Au/Cr using the three BZT(Zr/Ti) compositions 5/95, 20/80 and 35/65. As can be seen in figure 6.32 the breakdown strength of amorphous BZT thin film grown on Au/Cr electrode decreases gradually as the Zr content in the BZT is increased, whereas, for amorphous BZT grown on Pt/Ti there is considerable variability in the dielectric strength as a function of composition compared to amorphous BZT deposited on Au/Cr. The highest dielectric strength achieved was 1.83 MV/cm for amorphous BZT(5/95) grown on Pt/Ti/SiO_2/Si substrate. In both capacitor configurations (Pt/Ti and Au/Cr bottom electrode) there appeared to be a trend toward higher dielectric strength for BZT material with lower Zr content, accentuated when BZT was grown on Pt/Ti. Generally, for all compositions the dielectric breakdown strength was significantly higher (50% or more) for amorphous BZT thin films compared to fully crystallised BZT material. Consequently, amorphous BZT performs much better as an insulator.

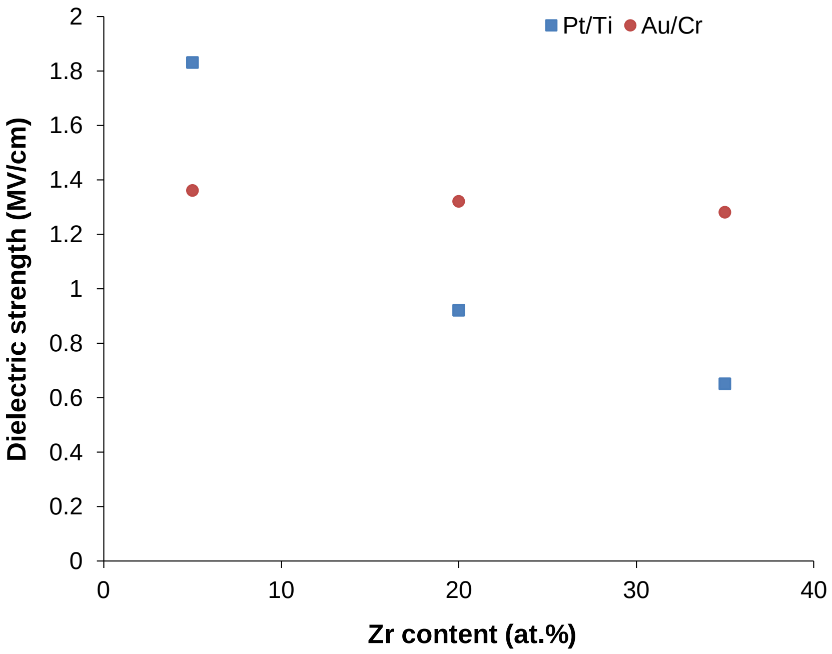

Figure 6.32 Scatter diagram of dielectric strength variation with BZT composition for amorphous BZT films grown on Pt/Ti and Au/Cr bottom electrodes.

6.4 Summary of Main Features and Achievements

The difficulty of achieving a medium to high tunability for BZN thin film grown on platinised silicon by RF magnetron sputtering led to its use in the fixed value, linear dielectric capacitor. Parallel-plate capacitors were fabricated and tested using BZN thin film material in both the amorphous (nanocrystalline) phase and the crystalline phase. The low tunability was primarily attributable to a deficiency of zinc in the sputtered thin films, specifically at the A site in the pyrochlore structure of BZN.

As-sputtered amorphous BZN thin films grown on Pt coated silicon have a granular microstructure and display a low dielectric strength (250 kV/cm). By introducing a very thin (30 nm) seed layer such as BZT, BST or PST between the as-deposited film and bottom electrode a columnar grain structure was encouraged to grow, substantially increasing the breakdown strength (560 kV/cm for a BZT seed layer). A moderate dielectric constant of ~50 and a low dielectric loss of <0.01 at 100 kHz operating frequency and 0 V bias was achieved for amorphous BZN thin film with seed layer. There was no significant advantage of using a PST seed layer compared to BZT, therefore maintaining the lead-free approach. A lower dielectric constant of 28, very low loss (0.005) and a breakdown strength of 650 kV/cm was recorded for amorphous BZN thin film grown directly on Au coated LCP at a deposition temperature of 100^{o}C.

It has been shown that the microstructure and dielectric constant of crystalline BZN thin film can be altered through use of an adapted technique termed the two-step sputtering deposition method. Using this method it was possible to vary the dielectric constant dependent on the thickness of the two sputtered layers both *ex situ* annealed by RTA. By introducing porosity into the second or top sputtered layer and changing its thickness relative to the first sputtered layer, the dielectric constant of the composite film was varied between 70 and 170. Although in this case a total film thickness of 500 nm was chosen, there is scope for extending the range to higher and lower values of dielectric constant by varying the top porous layer thickness and the overall film thickness (combined porous and nonporous layers). The use of the two-step sputtering deposition method for varying and controlling the dielectric constant in this way is seen as a significant achievement.

A high strength, low-k dielectric material was realised when amorphous BZT thin films were deposited on Pt/Ti and Au/Cr coated silicon substrates and characterised. A particularly low dielectric constant of 14 for films without porosity and as low as ~2 for films with a porous structure was achieved when BZT thin films with the higher Zr content (0.20 and 0.35) were grown on Au coated silicon and pyrolysis heat treated at 350^{o}C and 550^{o}C consecutively. At frequencies <150 kHz the dielectric loss of amorphous BZT grown on Pt/Ti and Au/Cr electrodes was <0.01 and the dielectric strength was between 1.0 MV/cm and 2.0 MV/cm. This work has not been previously reported on and so is also viewed as a significant achievement and contribution to knowledge.

7 The Voltage Tunable Capacitor

7.1 Introduction

Dielectric materials including ferroelectrics used in voltage tunable applications are characterised by a high dielectric nonlinearity (i.e. the dependence of dielectric constant on electric field) together with low dielectric loss. Researchers have continually looked for ways to enhance the dielectric properties of these materials by increasing tunability while reducing the loss. The figure of merit (FOM) is a measure of this. Other investigators have demonstrated success in using BZT and BZN as tunable dielectric material. However, results obtained for BZN in this work were particularly disappointing and did not reflect the outcomes of others. The best result was for a 300 nm BZN thin film deposited on Au coated SiO_2/Si substrate and crystallised by RTA at 400^{o}C for 3 minutes. A peak tunability of 25% was achieved with a dielectric strength of 2.0 MV/cm. At 300 kHz the dielectric constant and loss for this material was 90 and 0.07, respectively. As a consequence of the poor performance relating to the use of BZN, the focus of attention has been toward BZT as a thin film tunable material in both the paraelectric and ferroelectric phases. In this work various methods have been adopted and devised to improve the dielectric properties of BZT. These include, changes to the BZT composition (from ferroelectric to paraelectric at room temperature), control of film stress through thermal processing, use of a BZN buffer layer, and growth of multilayer structures containing layers of different BZT composition. This chapter will discuss the methods used for enhancing the performance of the voltage tunable capacitor in terms of the material and dielectric properties. The analytical and electrical measurements will also be presented and discussed.

7.2 Capacitor Fabrication

Thin-film BZT, BZT/BZN bilayers and BZT multilayer thin films were deposited on a range of metallised SiO_2/Si substrates, by the sol-gel method in the case of BZT, and by RF magnetron sputtering in the case of BZN. The growth of predominantly (110) oriented BZT and (222) oriented BZN polycrystalline films were achieved using appropriate heat treatment. Sample heating was carried out on either a hotplate or in a rapid thermal annealing (RTA) furnace in atmospheric environment. The individual sol-gel deposited BZT layers were pyrolysed at 350^{o}C then 550^{o}C on separate hotplates for 10 minutes. The BZT thin films were exposed to a final crystallisation anneal between 550^{o}C and 750^{o}C using RTA or a combination of hotplate and RTA. A hybrid processing technique was adopted for the growth of BZT/BZN bilayers using sol-gel and sputtering procedures. This hybrid approach has been used by researchers to deposit other combinations of materials [7.1]. The metal-insulator-metal (MIM), parallel-plate capacitor was chosen to achieve high dielectric constant tunabilities at lower bias voltages. This structure can also be used to minimise the effect of parasitics (i.e. reduced series resistance and inductance) on measurements. In all samples the top electrodes were thermally evaporated Au/Cr deposited through a shadow mask. Some issues have been encountered with thermal deterioration of the top electrode when using higher field strengths. Overheating and blistering of Au resulted in some cases. The dielectric breakdown and thermal runaway was primarily dependent on the microstructure of the dielectric material. Further details of the experimental arrangement and a full list of metals used for the bottom electrode can be found in chapter 4.

7.3 Results and Discussion

7.3.1 Annealing of Pt/Ti and Hillock Formation

A Pt/Ti metal layer is commonly used as the electrode material in the MIM capacitor for reasons discussed in chapter 4. As already mentioned, Pt cannot be deposited directly on oxidised silicon; a Ti adhesion layer is required. Many of the dielectric materials used in the voltage tunable capacitor such as complex metal oxides require high processing temperatures. At high temperature the Ti adhesion layer can migrate predominantly along grain boundaries through the Pt thin film. In air Ti is oxidised resulting in hillock formation at the Pt surface. The diffusion and oxidation of Ti also increases the compressive stress due to the associated volume expansion. The surface morphology of Pt films was examined by SEM and AFM.

Due to problems associated with stress and cracking of dielectric films, the effect of temperature on the microstructure of the Pt/Ti layer was investigated. In particular, stress in BZT thin films induced by morphological changes in the Pt/Ti layer can be a significant issue. The morphology of the Pt surface at different stages of heat treatment and annealing is presented. The surface texture of Pt can be seen in the SEM and AFM images of figures 7.1 and 7.2.

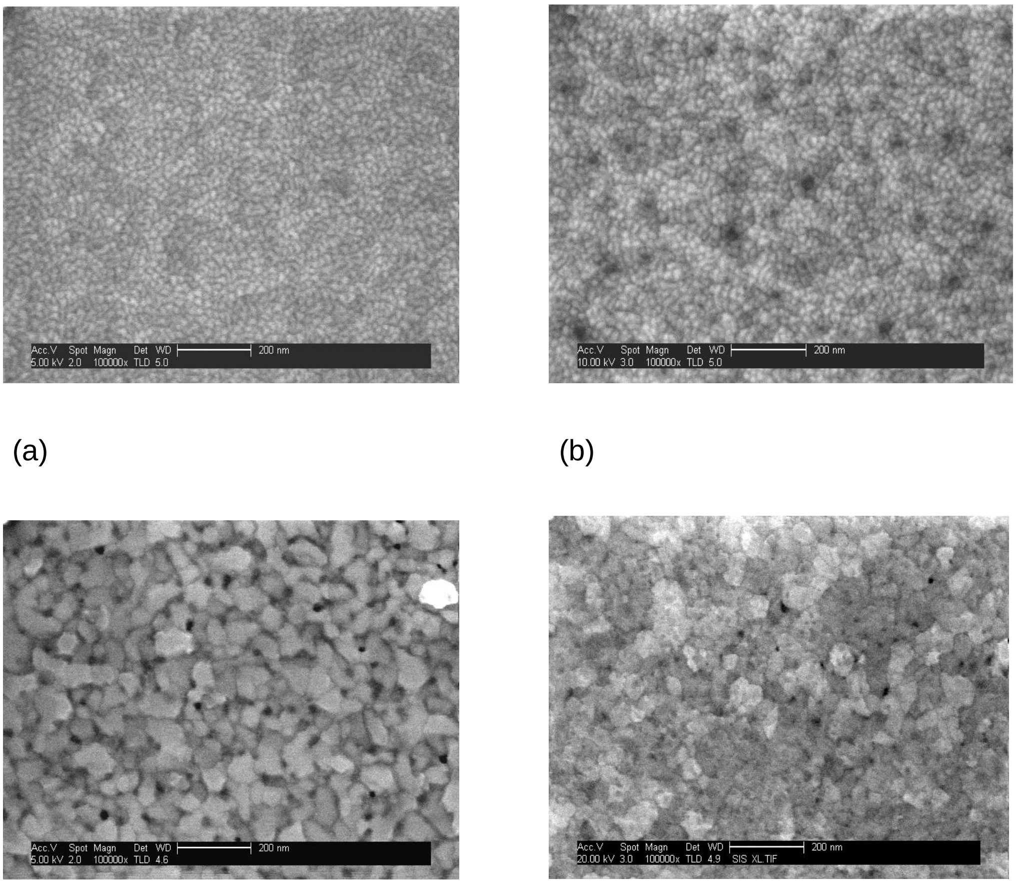

(a) (b)

(c) (d)

Figure 7.1 SEM micrographs of the platinum surface: (a) as-sputtered, (b) after heating to 350^{o}C on a hotplate for 10 minutes, (c) after heating to annealing temperature of 700^{o}C by RTA for 3 minutes, and (d) after removing a BZT thin film previously annealed at 700^{o}C.

The fine grained surface microstructure of the as-grown Pt is shown in figure 7.1(a). Figure 7.1(b-d) demonstrates the effect that the drying and annealing thermal processes had on the Pt surface. At 350^{o}C a slight increase in the Pt grain size is observed (figure 7.1b) compared to the as-grown film. However, the Pt grain size can be seen to have increased appreciably from *circa* 15 nm at room temperature (figure 7.1a) to *circa* 60 nm at 700^{o}C (figure 7.1c). Compare this to the SEM micrograph of the Pt surface after removal of a previously deposited BZT film annealed at 700^{o}C (figure 7.1d). Again, the grain size of the Pt can be seen to have increased substantially (to ~60 nm) when compared to the as-sputtered sample (figure 7.1a). The important observation is that the Pt grain size had increased significantly whether there was a film present or not. The dielectric film present on the Pt surface doesn't appear to have constrained the grain growth and volume expansion of the Pt film during thermal processing. Signs of porosity can also be observed at the surface of the heat treated Pt.

Further evidence of the effect of thermal treatment and annealing on the morphology of the Pt surface is presented in the AFM images of figure 7.2. Figure 7.2a shows the AFM surface image of Pt layer after heating to 350^{o}C on a hotplate for 10 minutes. Minor defects (white) at the surface can be seen although the film is generally smooth. Figure 7.2b is an AFM image of the Pt surface after annealing by RTA at 700^{o}C for 3 minutes and shows appreciably more defects resulting in a rougher surface. Both measurements were taken over a small sample area of 2.5 μm^2; the vertical scale in the three dimensional images is 50.0 nm/division. The AFM results for the sample annealed at 700^{o}C (figure 7.2b) indicate the presence of hillocks at the Pt surface to a height of ~50 nm in addition to the increased grain size observed in the SEM micrographs (figure 7.1). The higher the substrate temperature the larger the Pt grains which results in an increase in surface roughness. The change in morphology of the Pt electrode can cause stress in the BZT thin film and form microcracks or shorten the gap between upper and lower electrodes resulting in increased leakage current. By lowering the annealing temperature and reducing the surface roughness, fewer problems should be encountered at the interface between the electrodes and the dielectric material provided the crystallisation of the dielectric material is not seriously compromised. See chapter 5 for a more detailed explanation of stress and crack formation in thin films.

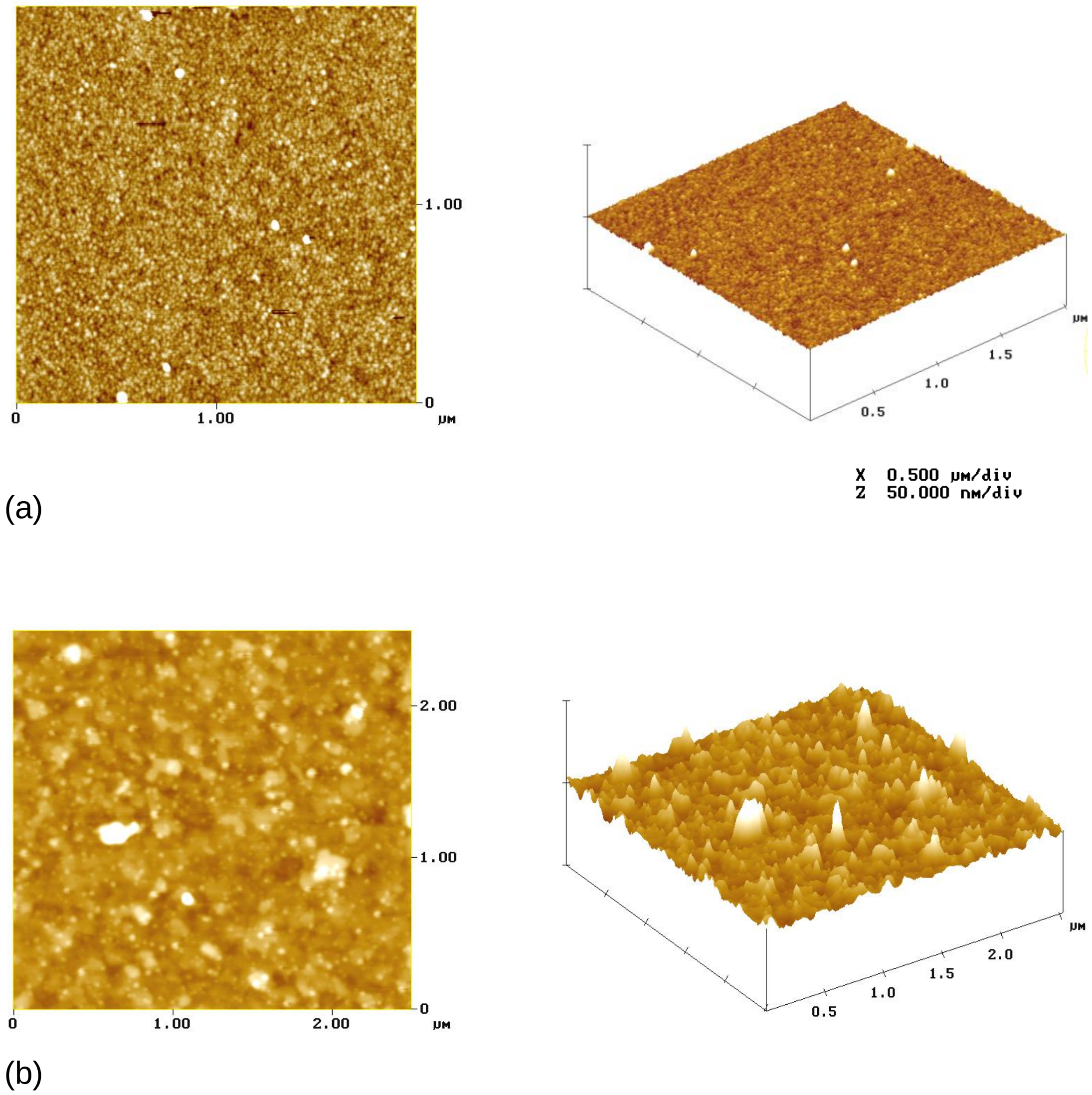

Figure 7.2 AFM images of the Pt surface: (a) after heating to 350°C on a hotplate for 10 minutes, and (b) after heating to annealing temperature of 700°C by RTA for 3 minutes.

X-ray photon spectroscopy (XPS) was used to analyse the composition of the Pt surface after annealing. The XPS analysis (figure 7.3) detected the presence of titanium and oxygen at the surface after the annealing process, also implying the existence of a TiO_2 phase. This indicated diffusion and oxidation of Ti through the Pt layer resulting in hillock formation of the surface. Carbon was also detected which implies some contamination of the Pt surface. The Pt and Ti detail scans shown in figures 7.4 and 7.5, respectively, allowed the relative amounts of the two elements to be calculated.

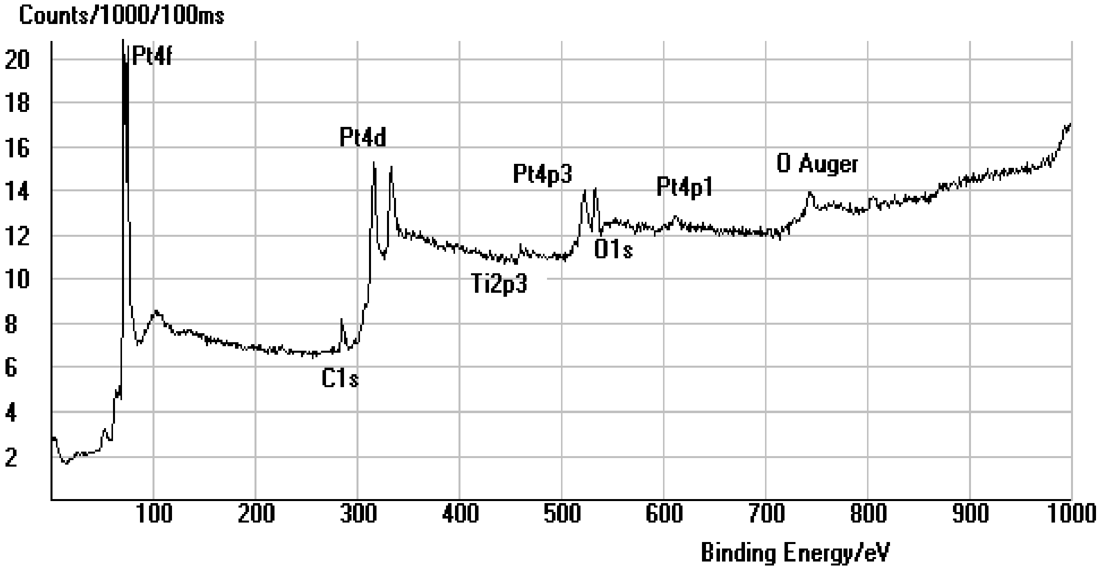

Figure 7.3 XPS survey scan of the Pt surface after annealing at 700°C by RTA showing the presence of Ti.

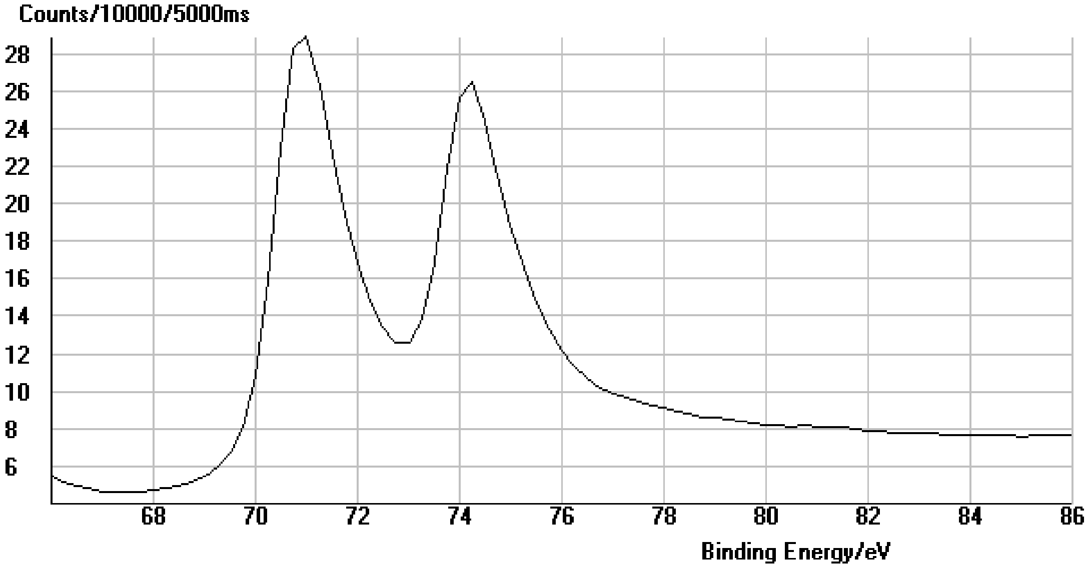

Figure 7.4 Pt details scan. The area under the 4f7/2 peak (left hand peak) is 54910.

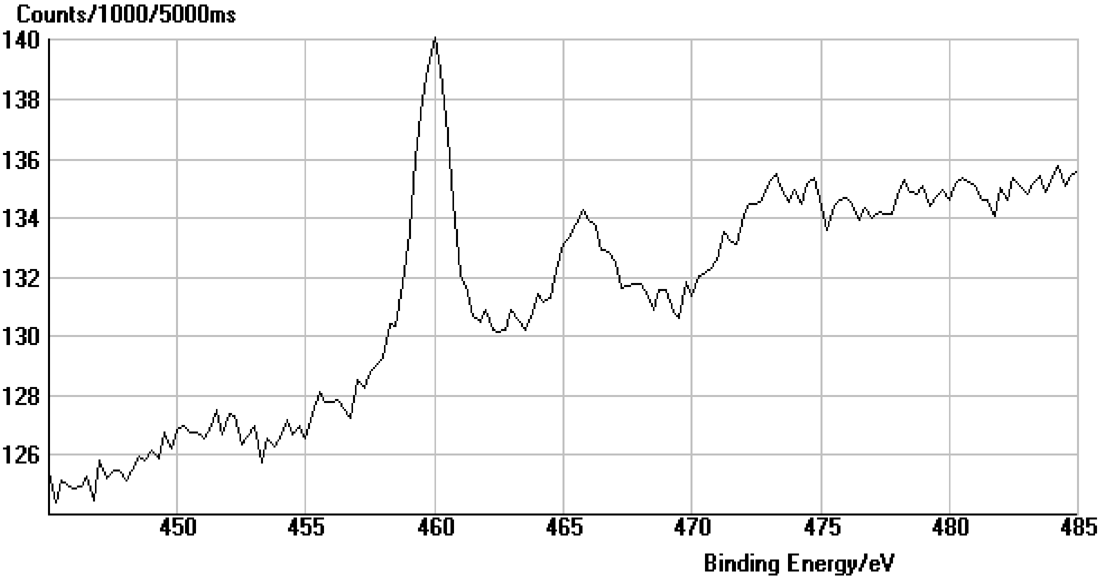

Figure 7.5 Ti details scan. The area under the Ti 2p3/2 peak (left hand peak) is 4395.

Using the area under the major peaks at 71 eV for Pt (figure 7.4) and 460 eV for Ti (figure 7.5) together with the atomic sensitivity factors, the relative amounts of the two elements were Pt:Ti, 31377:3995 (or approximately 8:1). This confirmed the presence of quite significant quantities of Ti (and by inference TiO_2) at the Pt surface after high temperature (700^{o}C) annealing. To alleviate the problem, it may be preferable to oxidise the Ti layer prior to depositing the Pt. A further investigation should be undertaken to look at the effects that a TiO_2 layer has on the adhesion and resistivity of the bottom electrode, and how this impacts on the MIM tunable capacitor performance. Alternatively, there may be an advantage to selecting other metals such as Au/Cr or Pt/Au/Ti. The next section will detail experiments that measure the sheet resistance of a range of metals suitable for use as electrodes in the tunable capacitor and zipping varactor.

7.3.2 Sheet Resistance Measurements of Metal Electrodes

The quality of the electrodes, and in particular the bottom electrode in the MIM structure, is contributory to achieving good dielectric properties in the dielectric thin film. Ohmic losses in the capacitor electrodes can mitigate the advantages of low dielectric loss film at high frequencies. The sheet resistance of various layered metal electrodes deposited on SiO_2/Si substrates were measured using the four-point probe technique which is described in section 4.7. Each sample was of the same size (2 cm x 3 cm) and shape to maintain measurement consistency. A comparison was then made between the different metal layers. Seven metal layer combinations were investigated, Pt(100nm)/Ti, Pt(150nm)/Ti, Au(100nm)/Ti, Au(100nm)/Cr, Au(800nm)/Cr, Pt(100nm)/Au(200nm)/Ti and Au(100nm)/Cr/Pt(100nm)/Ti. In all but the final combination the above metal layers were *in situ* sputter deposited, the Ti, Cr and Au being RF magnetron sputtered, and the Pt DC sputtered. For Au/Cr/Pt/Ti the Ti and Pt were sputtered, the Cr and Au were thermally evaporated.

For each metal layer the sheet resistance was measured over the temperature range 300^{o}C to 700^{o}C for durations of up to 60 minutes on a hotplate and 3 minutes by RTA. The sheet resistance of all samples recorded at a hotplate temperature of 300^{o}C and 700^{o}C as a function of duration is displayed in figures 7.6 and 7.7, respectively.

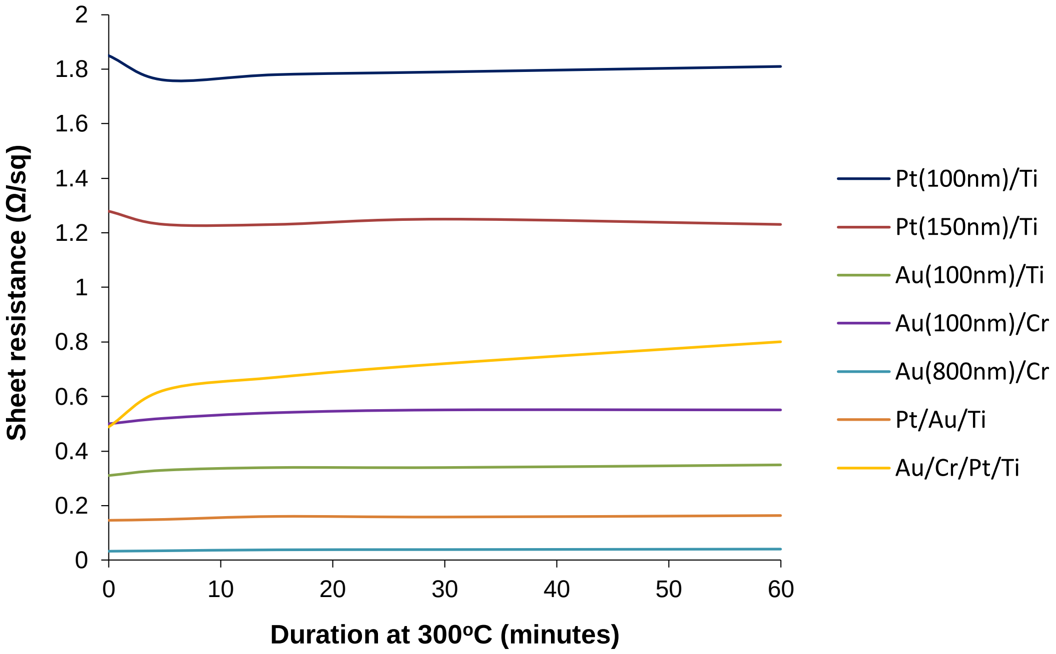

Figure 7.6 Variation in sheet resistance with time at a fixed hotplate temperature of 300^{o}C.

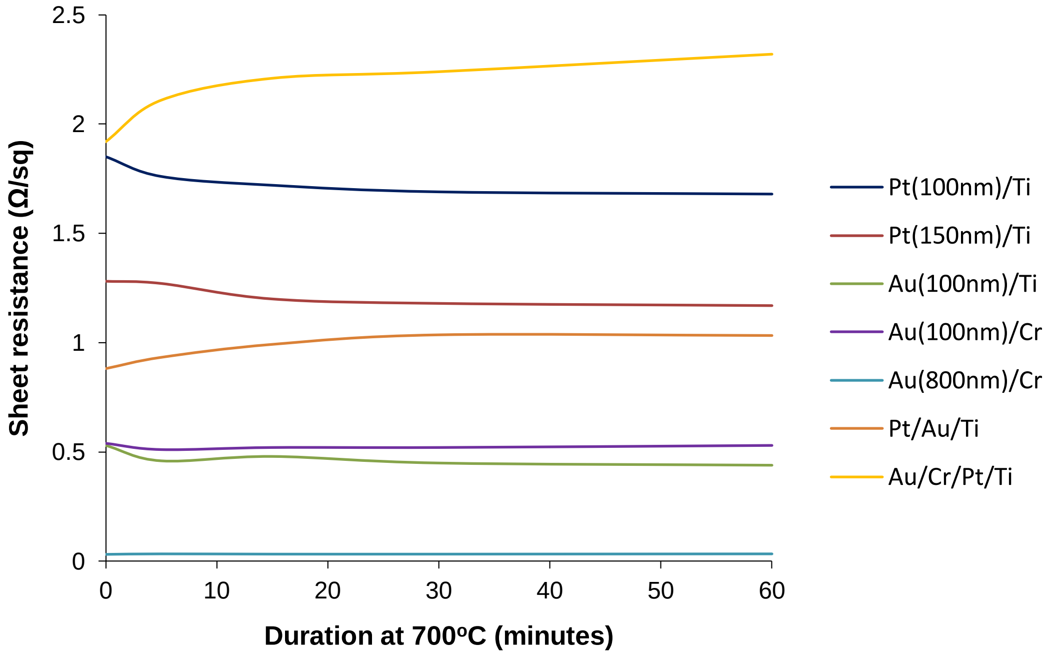

Figure 7.7 Change in sheet resistance with time at a fixed hotplate temperature of 700°C.

At hotplate temperatures between 300°C and 700°C the sheet resistance characteristics are similar to those displayed in figures 7.6 and 7.7, and so only data for the two extremes of temperature have been presented. Looking at both sets of data of sheet resistance measured at the fixed hotplate temperature of 300°C (figure 7.6) and 700°C (figures 7.7), there is little variation in the sheet resistance with time up to one hour. Consequently, there was no significant deterioration of the metal layers with time at any fixed hotplate temperature, although this did not preclude the diffusion of one metal into another at higher temperatures as can be the case with Ti diffusing into Pt along grain boundaries. The only metal layer to see a notable increase in sheet resistance with time was Au/Cr/Pt/Ti where the Pt/Ti had been sputter deposited on SiO_2/Si substrate and the Au/Cr thermally evaporated onto the Pt. This change with time was a consequence of inferior quality Au/Cr due to the thermal evaporation process. The hybrid deposition approach was initially chosen so that a comparison could be made to an all sputtered process, and to explore alternative solutions to lowering the sheet resistance. The lowest sheet resistance by far was recorded for sputtered Au(800nm)/Cr. The very thick (800 nm) Au layer was originally selected for use in the zipping varactor as a highly conductive bottom electrode. Details of this structure and the associated experimentation will be discussed in chapter 8.

For each of the seven metal layer combinations investigated, the sheet resistance was also plotted as a function of hotplate temperature (figure 7.8) and RTA temperature (figure 7.9) over the temperature range 300°C to 700°C.

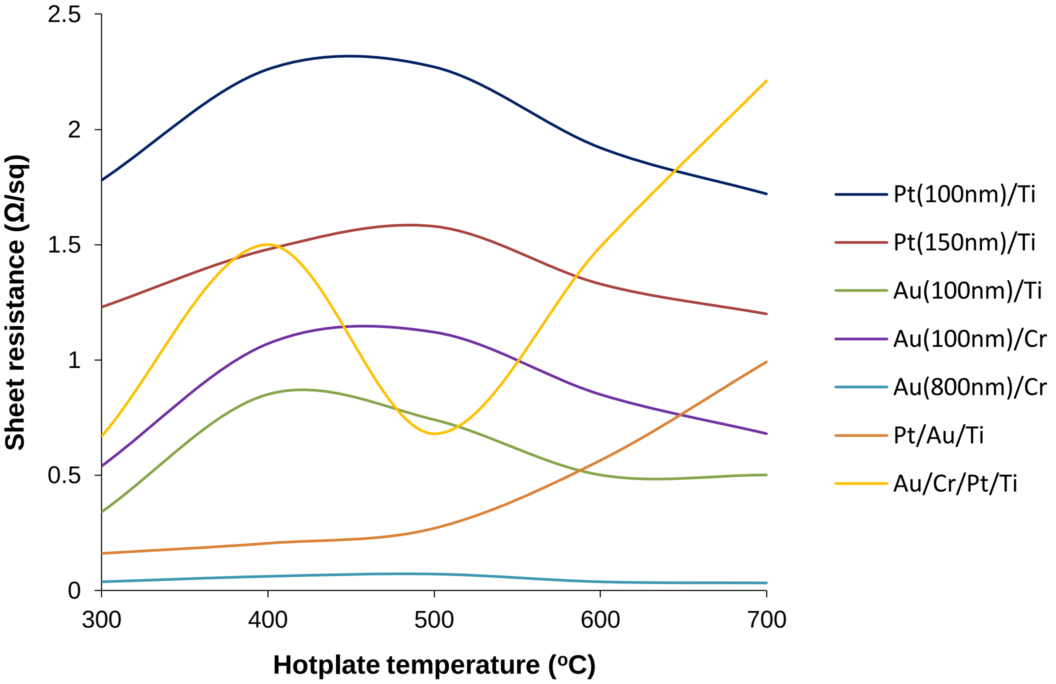

Figure 7.8 Sheet resistance as a function of hotplate temperature for seven different metal layer combinations.

Observing the data for the variation in sheet resistance with the hotplate temperature (figure 7.8) it is noticeable that the layers containing just two metal components follow a very similar contour. There is an increase in sheet resistance with temperature initially to a broad peak between 400°C and 500°C then a decrease in sheet resistance up to 700°C to a value which is close to the value at 300°C. Those layers with more than two metal components, as in the case of Pt/Au/Ti and Au/Cr/Pt/Ti, behave very differently. For example, the sputtered Pt/Au/Ti layer maintains a low sheet resistance to ~500^{o}C and then increases quite rapidly beyond 500^{o}C. The sheet resistance of Au/Cr/Pt/Ti follows a convoluted contour with temperature which is probably not surprising given the quality difference between evaporated Au/Cr and sputtered metal.

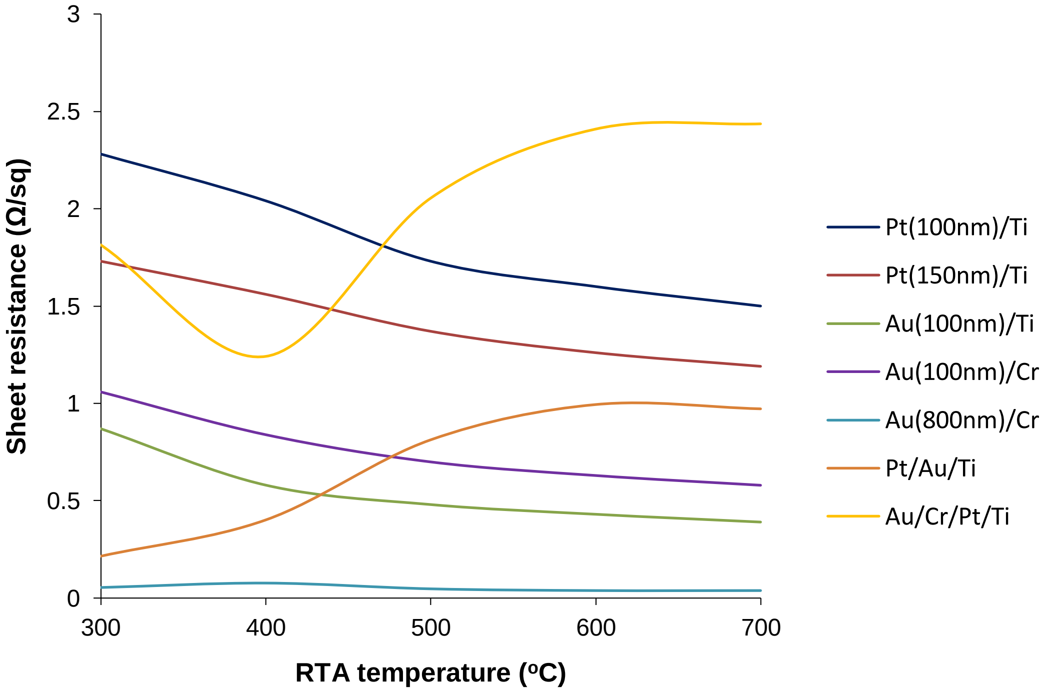

Figure 7.9 Variation in sheet resistance with RTA temperature for different metal layers.

A very different picture is evident when observing the data for the variation of sheet resistance as a function of RTA temperature as shown in figure 7.9. For all of the layers with two metal components there is a continual but gradual decrease in sheet resistance with increasing temperature. This is evidence that the resistivity of pre-annealed and stressed metallic films is higher than that of subsequently annealed material. This is important since residual stress in metal layers can lead to degradation of electrical characteristics in thin-film capacitors especially at high frequencies. For layers with three or more metal components, sheet resistance contours follow a more contorted path which cannot be very easily explained. The sheet resistance characteristic of multiple metal layers is therefore complex and requires an understanding of how the various individual metal components interact together with changes in temperature (e.g. diffusion of one metal into another). This study should be considered for future work.

Finally, some experiments were conducted to look at the change in sheet resistance of Pt(150nm)/Ti and Pt(100nm)/Au(200nm)/Ti metal layers on SiO_2/Si substrate when a sample of each was heated to 300°C on the hotplate for 5 minutes and then transferred hot to the RTA furnace for additional heat treatment at low temperature (300°C, 350°C and 400°C) for 3 minutes.

<ins>Pt/Ti</ins>

Hotplate 300°C, 5 minutes + RTA 300°C, 3 minutes:	1.43Ω/sq to 1.88Ω/sq
+Hotplate 300°C, 5 minutes + RTA 350°C, 3 minutes:	1.88Ω/sq to 1.63Ω/sq
+Hotplate 300°C, 5 minutes + RTA 400°C, 3 minutes:	1.63Ω/sq to 1.56Ω/sq
Hotplate 300°C, 5 minutes + RTA 400°C, 3 minutes:	1.25Ω/sq to 1.40Ω/sq

<ins>Pt/Au/Ti</ins>

Hotplate 300°C, 5 minutes + RTA 300°C, 3 minutes:	0.14Ω/sq to 0.23Ω/sq
+Hotplate 300°C, 5 minutes + RTA 350°C, 3 minutes:	0.23Ω/sq to 0.37Ω/sq

This novel heat treatment process was used to successfully anneal and crystallise thin BZN films at very low temperatures (300°C-400°C) for zipping varactor fabrication, and will be discussed in more detail in chapter 8.

7.3.3 Compositional Analysis of BZT Thin Film

Compositional analysis using EDX was performed on BZT thin films grown on Au coated silicon rather than platinised silicon; the Ti adhesion layer used to deposit Pt gives rise to a spurious reading. To grow and crystallise BZT on Au required a BZN buffer layer. The compositional analysis of $Ba(Zr_{0.05}Ti_{0.95})O_3$ and $Ba(Zr_{0.35}Ti_{0.65})O_3$ thin films as measured by EDX was compared to the compositional analysis on the sol performed using ICP-MS (sub-section 4.6.7).

The weight and atomic percentages of each of the elements detected are listed in table 7.1. It is the atomic percentage data that determines the stoichiometry.

Table 7.1 EDX analysis data for each element in $Ba(Zr_xTi_{1-x})O_3$ thin films grown on Au coated silicon with intermediate BZN buffer layer.

$Ba(Zr_{0.05}Ti_{0.95})O_3$

Element	Weight%	Atomic%
C K	1.11	4.10
O K	18.94	52.24
Si K	3.19	5.01
Ti K	12.91	11.90
Cr L	11.16	9.47
Co L	1.28	0.96
Zn L	1.25	0.84
Zr L	1.16	0.56
Nb L	2.31	1.10
Ba L	35.14	11.29
Au M	6.82	1.53
Bi M	4.74	1.00
Totals	100.00	

$Ba(Zr_{0.35}Ti_{0.65})O_3$

Element	Weight%	Atomic%
C K	2.01	7.58
O K	21.09	59.78
Si K	0.94	1.52
Ti K	9.80	9.28
Zn L	0.51	0.36
Zr L	8.64	4.30
Nb L	0.26	0.13
Ba L	40.20	13.27
Au M	13.86	3.19
Bi M	2.68	0.58
Totals	100.00	

From atomic percent data in table 7.1 the Zr and Ti content of $Ba(Zr_{0.05}Ti_{0.95})O_3$ film was calculated to be 0.045 and 0.955, respectively. These values are almost identical to those in table 4.3 obtained when using ICP-MS to analyse the $Ba(Zr_{0.05}Ti_{0.95})O_3$ sol, i.e. Zr(0.046) and Ti(0.954). The $Ba(Zr_{0.35}Ti_{0.65})O_3$ film composition was Zr(0.32) and Ti(0.68) compared to 0.335 and 0.665 for the sol.

7.3.4 Thin-Film BZT Grown on Pt and Au Bottom Electrodes

Improvements to the dielectric properties of BZT thin films have been achieved in several different ways, for example, by the appropriate selection of substrate material including bottom electrode metallisation, by use of the correct thermal treatment, through the incorporation of seed and buffer layers between dielectric film and bottom electrode, and by the growth of multilayer dielectric structures. In this chapter an answer to the question as to whether it is preferable to use the dielectric material (BZT) in the paraelectric or ferroelectric phase or at the phase boundary between the two will be sought. The use of Pt and Au coated SiO_2/Si substrates, appropriate thermal treatments, seed/buffer layers and multilayer structures will be addressed in the quest to further improve the low frequency (to 300 kHz) performance of the voltage tunable capacitor.

Consider firstly the growth of BZT on $Pt(111)/Ti/SiO_2/Si(100)$ substrate and the thermal treatments employed to improve the BZT crystallinity. Material crystallisation was performed using hotplate, rapid thermal annealing (RTA), and by a combination of hotplate and RTA. The XRD patterns in figure 7.10 clearly show crystallisation of $Ba(Zr_{0.05}Ti_{0.95})O_3$ thin film when annealed on the hotplate at 700°C for 15 minutes, whereas, crystallisation had not taken place when annealed at 650°C. It is evident that films annealed at 700°C have a distinctly polycrystalline structure with the appearance of (100), (110), (200), (210) and (211) peaks in the XRD spectra.

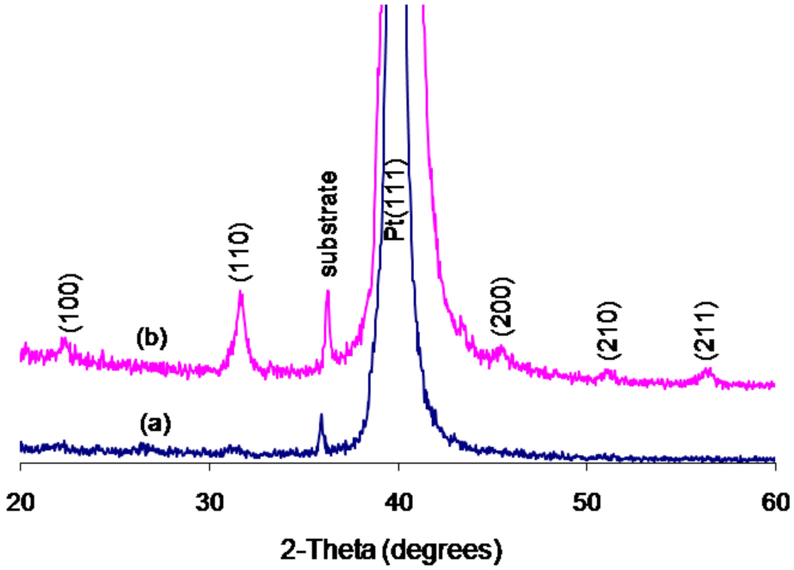

Figure 7.10 X-ray diffraction patterns of BZT(5/95) thin films annealed by hotplate at (a) 650°C for 15 minutes and (b) at 700°C for 15 minutes.

The diffractogram of thin-film BZT annealed at 700°C displays phases present (peak positions), phase concentrations (peak heights) and crystallite size/strain (peak widths). The peak width increases with decreasing crystallite size. The films annealed at 700°C in air by hotplate display a dominant polycrystalline perovskite peak at (110). This indicates a preferential (110) grain orientation for BZT thin film deposited on Pt(111)/Ti/SiO_2/Si(100) substrate. Since there was no crystallisation of the material when annealed at 650°C, higher temperature annealing was therefore required when processing BZT films on the hotplate for short durations. However, a significant reduction in the temperature of crystallisation could be achieved by using RTA. A comparison is now made between the XRD patterns of $Ba(Zr_{0.05}Ti_{0.95})O_3$ thin films after having been annealed by hotplate at 700°C and by RTA at 500°C and 700°C as shown in figure 7.11. At an annealing temperature of 500°C some of the peak heights are reduced. In all spectra the (110) crystallographic peak dominates. The polycrystalline nature of these thin films is due to a lattice mismatch between BZT thin film and substrate (Pt/Ti/SiO_2/Si).

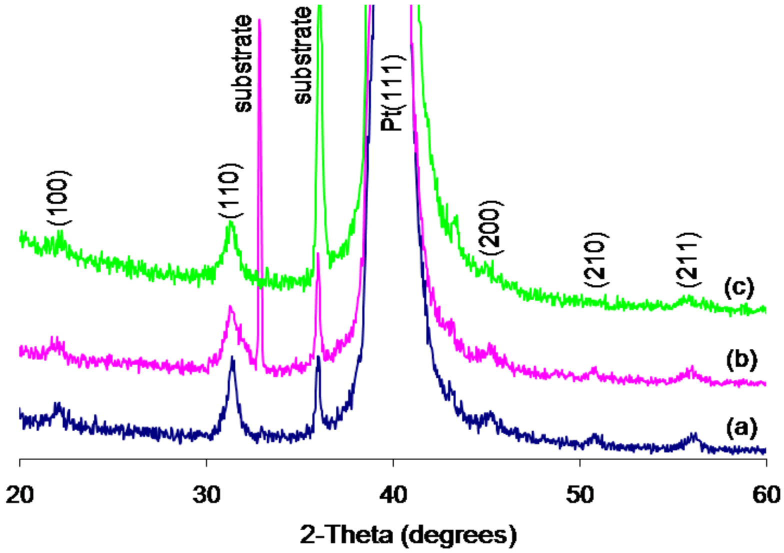

Figure 7.11 XRD patterns of BZT(5/95) thin film after annealing at (a) 700°C for 15 minutes by hotplate, (b) 700°C for 3 minutes by RTA and (c) 500°C for 3 minutes by RTA.

Figure 7.12 shows the XRD spectrum of BZT(5/95) thin film grown on Pt coated SiO_2/Si substrate and annealed by RTA at 450°C and 700°C. For the material annealed at 450°C a peak is visible at approximately 26.8° which indicates a second phase. Tang *et al*. suggest that this is an intermediate phase associated with the complex carbonate $Ba_2(Ti,Zr)_2O_5CO_3$ [3.16]. When annealed by RTA at 500°C the film fully crystallises (fig 7.11) and the intermediate phase disappears according to the following chemical decomposition.

$$Ba_2(Ti,Zr)_2O_5CO_3 \rightarrow 2Ba(Ti,Zr)O_3 + CO_2\uparrow$$

Improved crystallisation is seen as the RTA temperature is raised above 500°C.

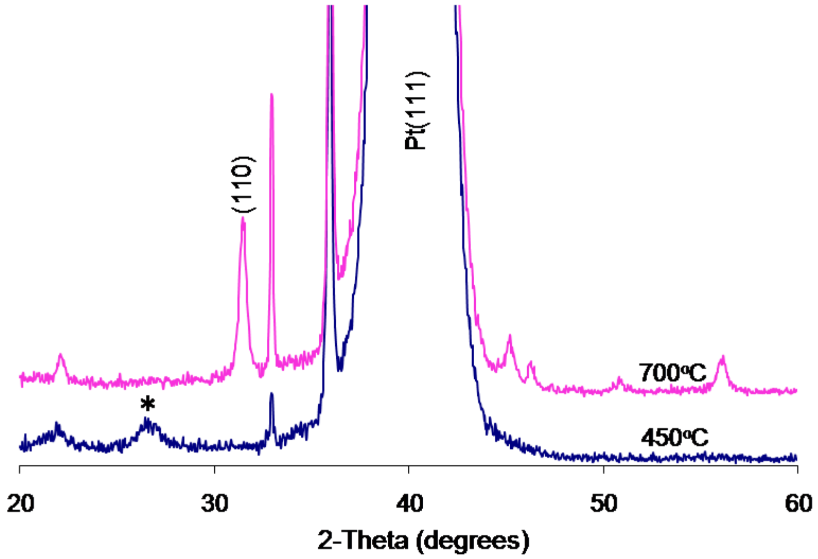

Figure 7.12 XRD plot of BZT(5/95) thin film deposited on platinised silicon and annealed by RTA showing intermediate phase * at 450°C.

The XRD spectrum of BZT annealed at 700°C (fig. 7.12) shows excellent crystallisation of film based on peak intensity corresponding to the (110) plane. Similar XRD patterns to that shown in figure 7.12 were generated for all three BZT compositions, BZT(5/95), BZT(20/80) and BZT(35/65), when annealed by RTA at the higher temperature of 700°C. A significant improvement in crystallisation was seen in raising the annealing temperature by just 50°C from 700°C to 750°C and this was reflected in the microstructure of the BZT thin film as shown in the SEM micrographs of figures 7.13 and 7.14.

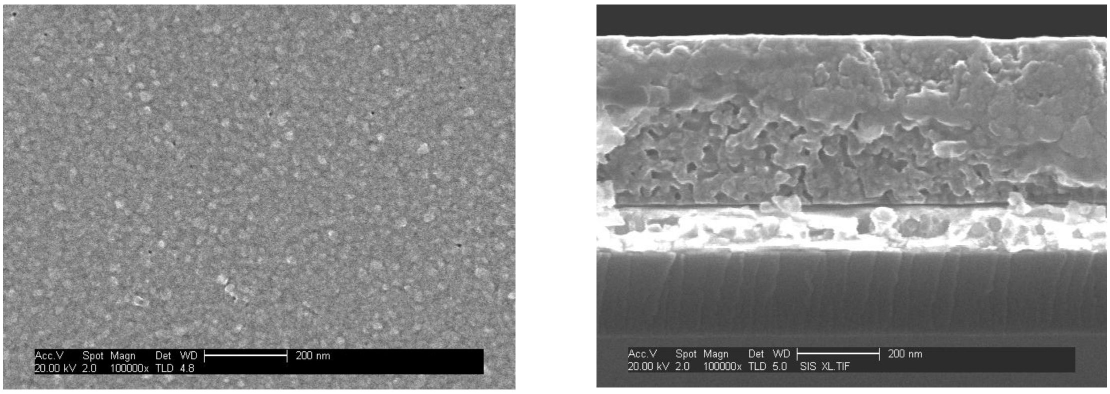

(a) (b)

Figure 7.13 SEM micrographs of thin-film BZT(5/95) annealed at 700°C by RTA showing (a) surface granular microstructure, and (b) fracture cross-section of BZT film on Pt layer (white).

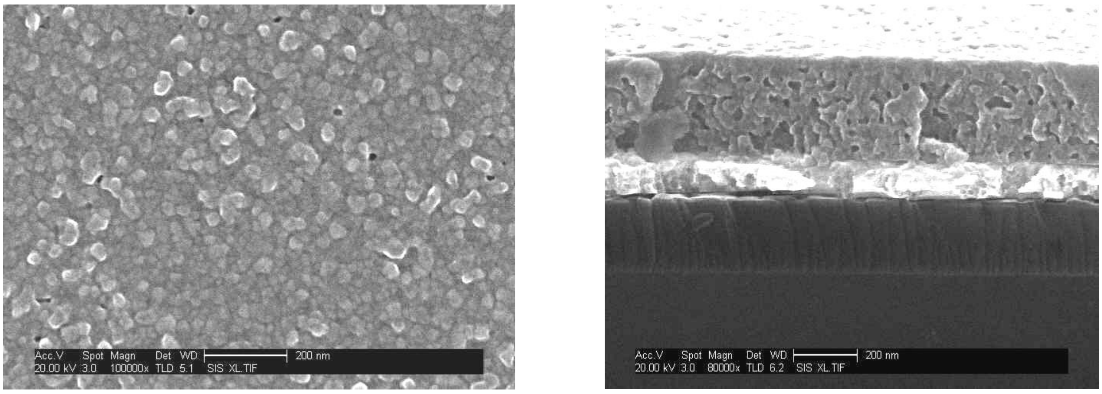

(a) (b)

Figure 7.14 SEM micrographs of thin-film BZT(5/95) annealed at 750°C by RTA showing (a) larger granular structure and (b) section of BZT film on Pt layer.

From the SEM images of the surface of the thin films (figures 7.13a and 7.14a) the grain size can be seen to have increased substantially on annealing at the higher temperature. Surprisingly, however, only a small increase in the surface roughness (R_a) was recorded, from 3.8 nm to 4.1 nm for the samples annealed at 700°C and 750°C, respectively. The advantage of having a larger grain size is that domain walls in larger grains are easier to switch under external field. Generally, though, BZT films have a relatively small grain size which reduces domain motion, so can make switching difficult. This ideally makes it necessary to anneal BZT films at the highest temperature possible in order to achieve material with the largest grain size for tunable applications. However, by increasing the temperature beyond 750°C, and with increased surface roughness, problems can be encountered at the interface between the electrode and dielectric material resulting in a decrease in dielectric constant. Alternatively, by lowering the annealing temperature in order to reduce the surface roughness the crystallisation of the material may be compromised. Based on these experiments, the RTA temperature chosen was 750^{o}C.

Samples were prepared by growing BZT thin films on platinised silicon using the sol-gel technique. Films with three different BZT compositions were deposited, one that is in the ferroelectric phase at room temperature, BZT(5/95), one in the paraelectric phase, BZT(35/65), and one at or around the morphotropic phase boundary between ferroelectric and paraelectric, BZT(20/80). The material was fully crystallised using RTA at 750^{o}C for 2 minutes in air.

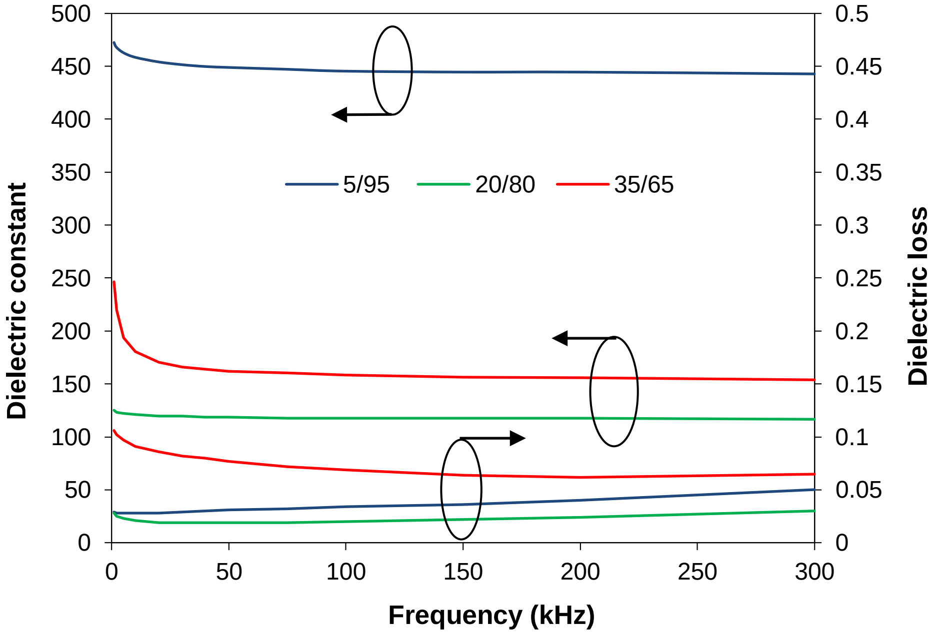

Figure 7.15 Frequency dependent dielectric properties of BZT for three different thin film compositions grown and crystallised on Pt/Ti/SiO$_2$/Si substrate.

Ferroelectric materials are characterised by polarisation hysteresis and high dielectric constant. These properties vary with grain size which is related to domain width. Average grain size decreases with the increase of the Zr content. It is thought that this is attributed to lower grain growth rates from the more slowly diffusing Zr^{4+} ion which has a larger ionic radius than Ti^{4+}. Due to the high dielectric constant (figure 7.15) and dielectric strength (figure 6.32) of thin-film $Ba(Zr_{0.05}Ti_{0.95})O_3$ which is ferroelectric at room temperature, the tunability was 75% compared to 66% for BZT(20/80) and 57% for BZT(35/65) when deposited on $Pt/Ti/SiO_2/Si$ substrate. The increase in tunability of BZT thin films with decreasing Zr content is shown in figure 7.16. Also, tunability decreased for films grown on Pt/Au/Ti compared to films deposited on Pt/Ti due in part to the increasing electrode sheet resistance at higher RTA temperatures (figure 7.9).

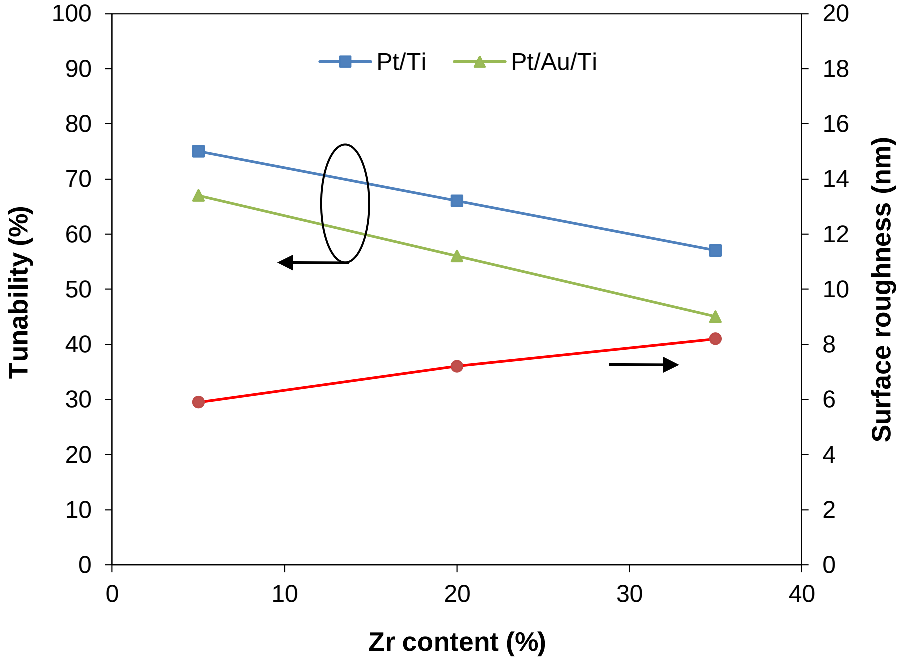

Figure 7.16 Tunability and surface roughness as a function of the Zr content in BZT thin films deposited on platinised silicon. Also, tunability of BZT on Pt/Au/Ti.

The surface roughness generally increases with the increase of grain size (i.e BZT films with lower Zr content). However, experimental results (figure 7.16) showed that surface roughness increased with increasing Zr due to a nanoporous structure in BZT films with the higher Zr content. Low roughness is contributory to high dielectric constant and tunability in BZT thin films mainly due to an improved interface between the electrodes and dielectric layer.

For low frequency applications, operating in the ferroelectric phase does appear to be advantageous. This may not be the case when operating at high frequency especially for ferroelectric material that is also piezoelectric. Higher dielectric losses in ferroelectric thin films due to hysteresis and fatigue degrade high frequency performance of tunable devices, so at microwave frequency it may be preferable to operate in the paraelectric phase.

BZT thin films were also deposited on Au/Cr/SiO_2/Si substrate using the sol-gel method. Earlier experimental results showed that it was possible to successfully grow amorphous BZT thin films with good insulating properties on Au electrode. Difficulty arises for all BZT compositions when attempting to anneal and crystallise the material on Au at the high temperatures required. XRD analysis showed that the films had fully crystallised. However, due to the thermal expansion mismatch between the BZT thin film (~6.3×10^{-6} K^{-1}) and Au layer (14.1×10^{-6} K^{-1}), deterioration of both the Au layer and BZT film resulted.

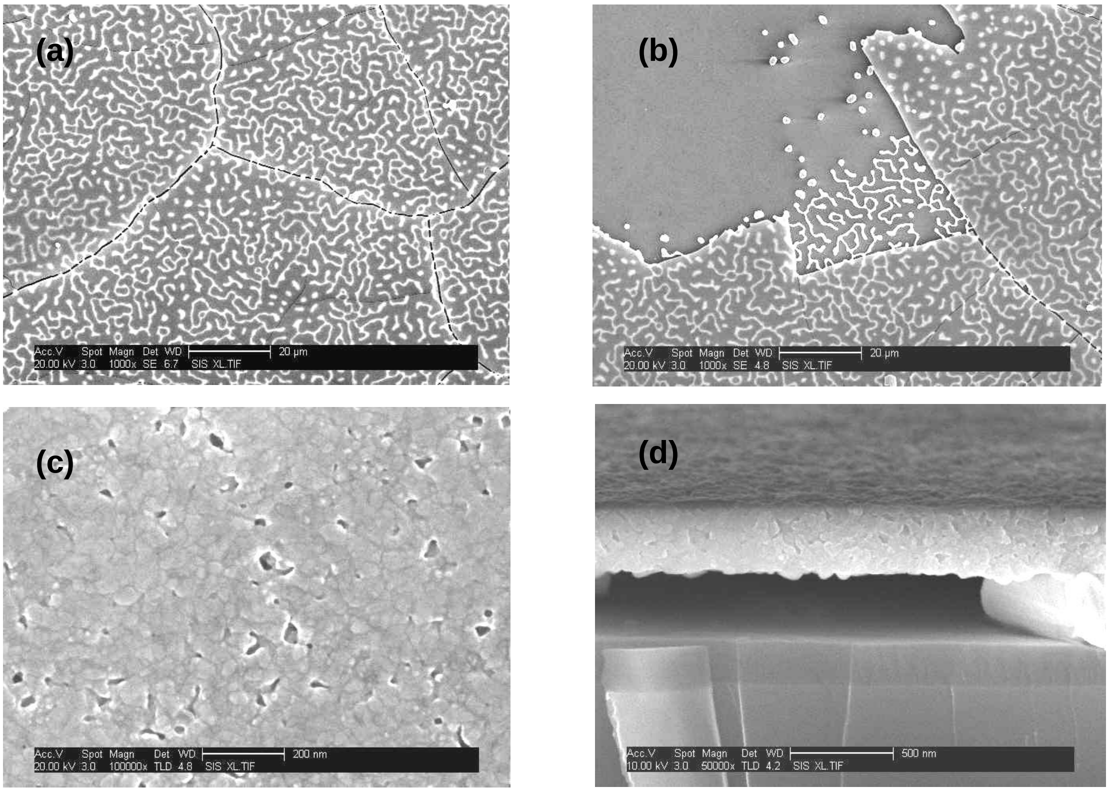

Figure 7.17 SEM micrographs displaying BZT(35/65) thin film on Au coated silicon after annealing by RTA at 750°C for 2 minutes. Images (a) and (b) show cracking and peeling of film above Au islands, (c) shows the BZT surface microstructure and (d) is a sectional image of film delaminated from substrate.

After annealing, gold islands of different shapes and sizes were formed beneath the BZT layer as can be seen from the SEM images in figure 7.17. The BZT film itself was cracked and peeling, and in the bottom right hand image of figure 7.17 the BZT film can be seen resting on one of the gold islands separating the film from the SiO_2/Si substrate. The formation of pores, cracks, and thickened layer regions brought about by surface diffusion of Au all contributed to the unsuccessful growth of BZT film directly on Au electrode. A solution to this problem has been devised, and the detail along with experimental evidence is presented in sub-sections 7.3.5 and 7.3.6.

7.3.5 Thin-Film BZN Growth on Au Coated Silicon

Consider BZN film growth and crystallisation on Au(100nm)/Cr(10nm)/SiO_2/Si substrate. A 320 nm thick film was sputter deposited onto an Au coated substrate at 300^{o}C, then *ex situ* annealed by RTA at 400^{o}C for 3 minutes to crystallise the film. Crystallisation at such a low temperature (figure 7.18) ensured successful growth of BZN on Au without defects (i.e. compared to BZT that required the much higher annealing temperature of 700^{o}C to 750^{o}C).

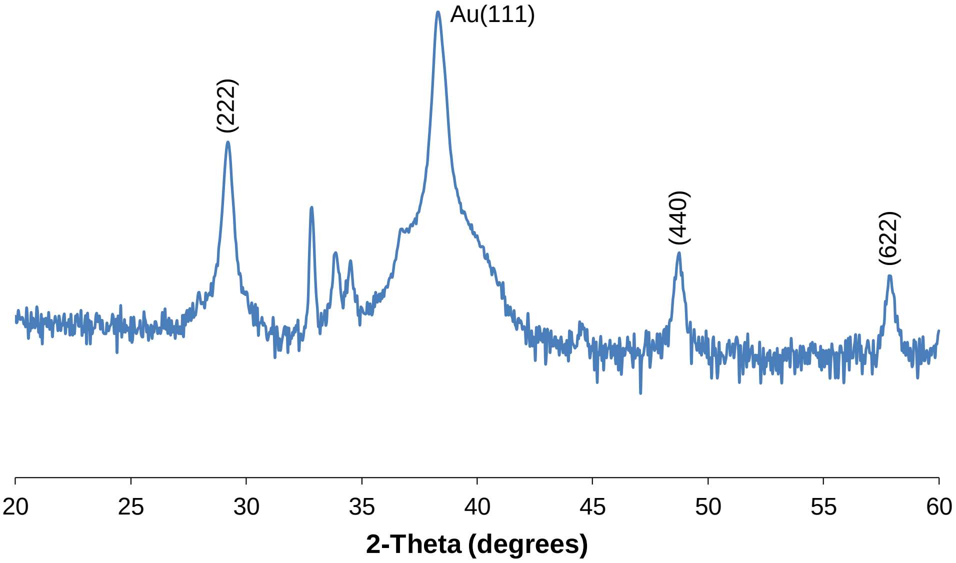

Figure 7.18 XRD spectrum of BZN thin film grown on Au coated silicon substrate and annealed by RTA at 400^{o}C.

The intensity of the XRD peaks in figure 7.18 indicates excellent crystallisation of material. Peak widths are narrow indicating a large grain structure for BZN. This was verified by SEM as can be seen in figure 7.19. The grain sizes range from *circa* 20 nm to 100 nm.

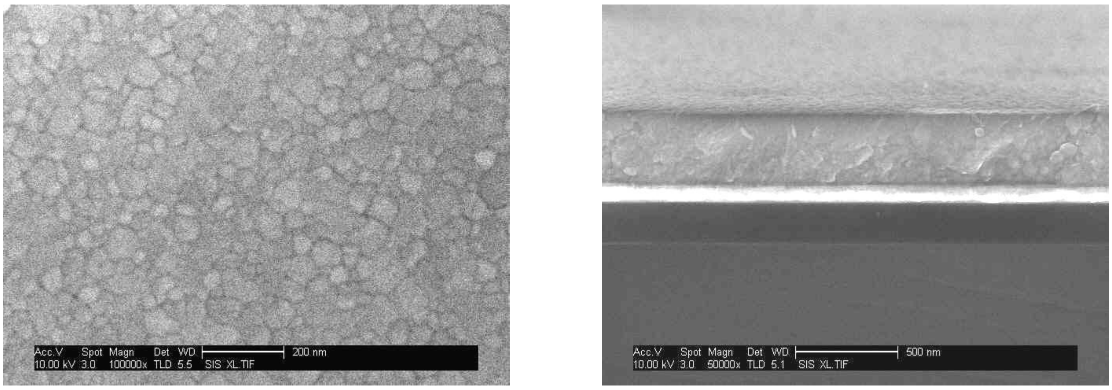

Figure 7.19 SEM images of the surface and in section showing a BZN thin film with large granular microstructure. In the fracture cleaved image the 320 nm thick BZN film can be seen on 100 nm thick Au layer (white).

Much improved tunability (25%) was recorded for BZN thin film on Au bottom electrode compared to that obtained for BZN grown on Pt (15%). This was mainly due to the high breakdown strength (~2.0 MV/cm) of the material. However, this was much lower than the typical tunabilities (up to 55%) for BZN recorded by other investigators, probably due to Zn deficiency. Other dielectric properties of BZN film on Au were a dielectric constant of 92 and loss of 0.065.

BZN is not ideally suitable as a tunable material based on current experimental evidence. The ability to successfully grow BZN on Au layer, and to crystallise the material at very low temperature, makes it suitable for other applications, including its use as a buffer layer for BZT growth on Au bottom electrode. This work will be discussed in the following sub-section.

7.3.6 Growth of BZT Thin Film on Au Using BZN Buffer Layer

It has been demonstrated that BZT thin film material grown on platinised silicon and operating in the ferroelectric phase gave the highest tunability at low frequency. However, in the paraelectric phase the tunability of BZT film was reduced. The use of a lower resistivity electrode material such as Au(100nm)/Cr compared to Pt(100nm)/Ti (see figure 7.9) resulted in improved dielectric properties for the growth of thin-film BZT in the paraelectric phase provided a buffer layer was inserted between the Au electrode and dielectric film. BZN was a good choice of material for the buffer layer since the thermal expansion coefficient of BZT (~$6.3x10^{-6}$ K^{-1}) is better matched to BZN ($7.92x10^{-6}$ K^{-1}) than to Au ($14.1x10^{-6}$ K^{-1}). A further rationale behind the use of BZN as buffer layer for BZT growth is that sputtered BZN thin film is characterised by compressive stress distinguished by blistering, hillock and pinhole formation whereas sol-gel deposited BZT is characterised by tensile stress distinguished by film cracking. Also, the growth of BZN on Au bottom electrode had already been demonstrated (sub-section 7.3.5). The higher tunability (25%) of BZN grown on Au compared to a maximum tunability of only 15% for BZN grown on Pt was a further argument for its suitability as a buffer material.

According to the work done on the modelling of bilayers in chapter 5 of this thesis, it is preferable to deposit a very thin BZN buffer layer on Au prior to the growth of BZT thin film. A range of BZN buffer layer thicknesses from 25 nm to 100 nm were trialled and experimental results indicate that bilayer dielectric properties can be optimised using a 25 nm thick buffer layer. With a very thin BZN buffer layer the dielectric properties of a *circa* 300 nm thick BZT film will be relatively unaffected by the BZN dielectric properties, whereas, there is likely a significant advantage in using the higher conductivity Au electrode compared to using Pt.

To examine the effect of the heat treatment and annealing temperatures on the microstructure of a very thin (25 nm) BZN film, a trial experiment was conducted which involved sputter depositing the film on Au coated silicon at an *in situ* substrate temperature of 300^0C. The 25 nm BZN film was then *ex situ* heat treated on separate hotplates at 350^oC for 5 minutes and at 550^oC for a further 5 minutes, with a final anneal by RTA at 750^oC for 2 minutes. This replicated the conditions normally used for pyrolysing and annealing the BZT thin film. An

XRD scan of the annealed 25 nm thick BZN film showed that the material had crystallised well as can be seen in figure 7.20.

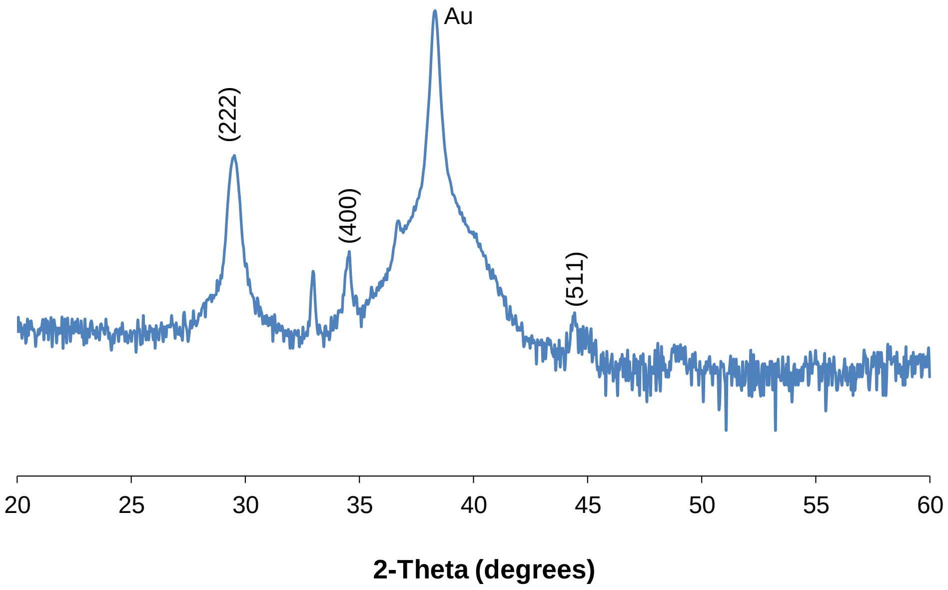

Figure 7.20 XRD diffractogram of 25 nm thick BZN film grown on Au coated silicon and annealed by RTA at 750°C for 2 minutes.

What is interesting about the XRD scan of the BZN film in figure 7.20 is that one dominant crystallographic peak has appeared at (222). Other strong peaks (440) at ~49° and (622) at ~58°, that are always visible when much thicker (~300 nm) BZN films are deposited and annealed even at low temperature, are no longer present. It is certainly difficult to resolve these peaks against the background noise. This implies that the BZN film was not thick enough to support these crystallographic orientations.

The surface and sectional SEM images of the 25 nm thick BZN film grown on Au coated silicon and crystallised by RTA at 750°C are shown in figure 7.21. The images show a large grain microstructure comparable to that displayed by thicker (300 nm) BZN films. Although the film surface appears rough due to the size of the grains in comparison to the thickness of the film, more importantly, there is no evidence of the BZN thin film delaminating from the Au layer. There is excellent adhesion of BZN film to Au layer even after annealing at the high temperature of 750°C. Also, there appears to be no serious defects in the film.

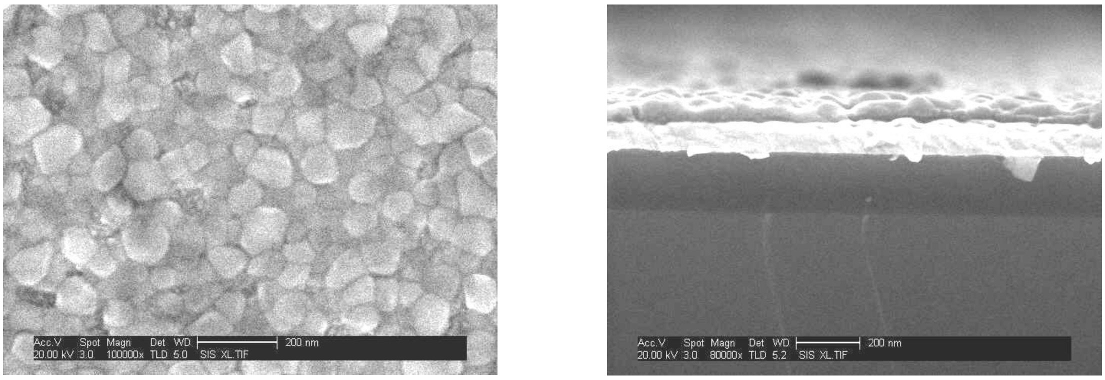

Figure 7.21 SEM images of the surface and in section of 25 nm thick BZN film on Au (bright layer in section) coated SiO_2/Si substrate.

Since BZN is a non-ferroelectric material, experiments were performed using BZT thin films that have, or near to, a room temperature paraelectric phase, as in the case of BZT(20/80) and BZT(35/65). The evidence that BZN thin film is non-ferroelectric came from polarisation hysteresis measurements on a 300 nm thick BZN film crystallisation annealed by RTA at 700°C (figure 7.22a).

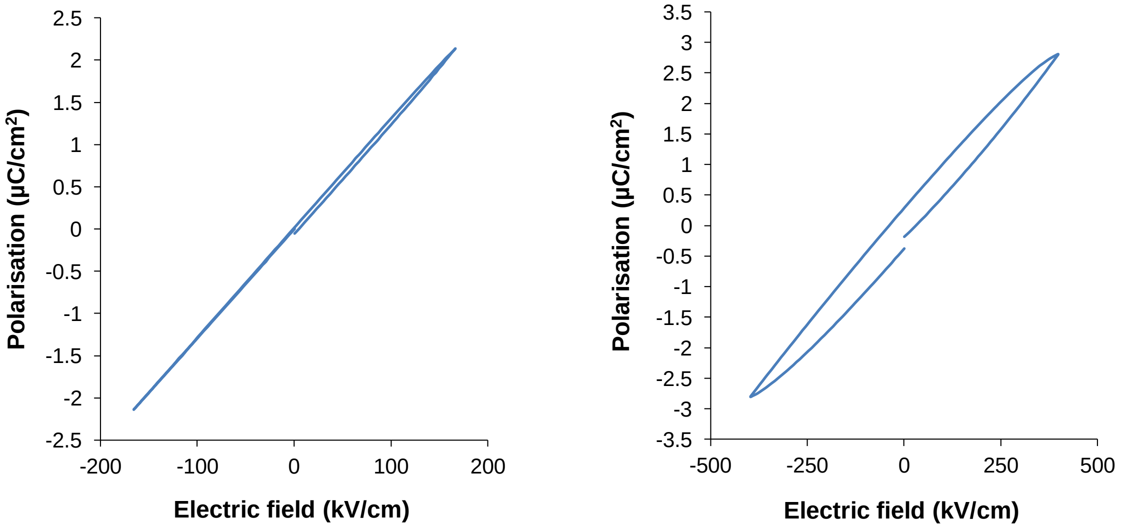

(a) (b)

Figure 7.22 P-E loop measurement for (a) BZN thin film deposited on platinised Si substrate showing no hysteresis and (b) BZT(20/80) thin film grown on Au coated Si with a 25 nm thick BZN buffer layer displaying some hysteresis.

BZN has a cubic pyrochlore crystal structure with no spontaneous polarisation as evidenced by the lack of a hysteresis loop in the polarisation versus electric field plot. The BZT(20/80) thin film grown on 25 nm BZN buffer layer showed ferroelectric behaviour. At room temperature the composition $Ba(Zr_{0.20}Ti_{0.80})O_3$ is near to a morphotropic phase boundary between the tetragonal, orthorhombic and rhombohedral ferroelectric phases and the paraelectric phase. At this temperature, which is near the Curie temperature, the P-E hysteresis loop is characteristically elliptic in shape as can be seen in figure 7.22b. A similar hysteresis loop was observed for $Ba(Zr_{0.35}Ti_{0.65})O_3$ thin film on BZN buffer layer, the BZT(35/65) film being paraelectric at room temperature. The BZN buffer layer had little influence on the P-E loop measurement of the BZT film.

Looking at the data for the variation in tunability with Zr content in BZT (figure 7.16), it is the BZT films with the higher Zr content that ideally require an increase in their tunability if they are to find application in tunable devices. A solution to this research problem was found.

The thin (25 nm) BZN buffer layers were prepared in exactly the same way for the actual samples as described above except a crystallisation anneal by RTA at 750^{o}C was not performed prior to depositing the BZT films. When growing the BZT thin film a total of six BZT layers were spin coated, each layer being pyrolysed on separate hotplates at 350^{o}C for 5 minutes and then at 550^{o}C for a further 5 minutes. After a 300 nm film had been grown a final crystallisation anneal was performed by RTA at 750^{o}C for 2 minutes.

Consider firstly the material properties of BZT thin films grown on Au bottom electrode with a 25 nm thick intermediate BZN buffer layer. The XRD patterns of BZT(20/80) and BZT(35/65) are displayed in figure 7.23 and show clearly that both the BZN and BZT films had crystallised. Characteristic, dominant peak intensities for BZN(222) and BZT(110) planes are distinctly visible. Even though the BZN buffer layer is very thin it shows good crystallisation. SEM images of the surface and in section for BZT(20/80) and BZT(35/65) thin films on BZN buffer layer on Au can be seen in figures 7.24 and 7.25, respectively.

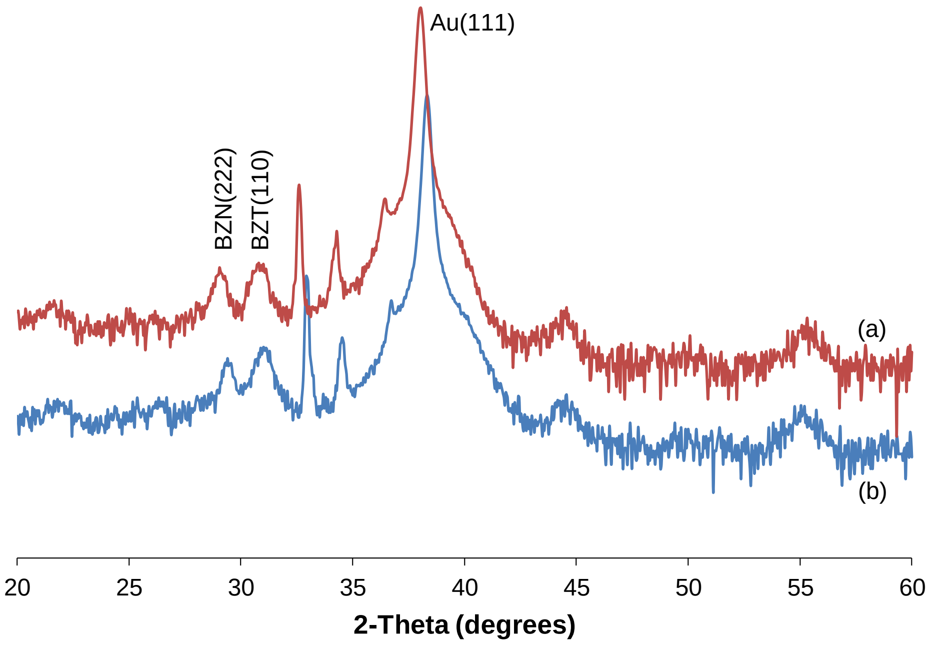

Figure 7.23 XRD spectra showing crystallisation of BZT thin film and BZN buffer layer on Au electrode for BZT compositions (a) 20/80 and (b) 35/65.

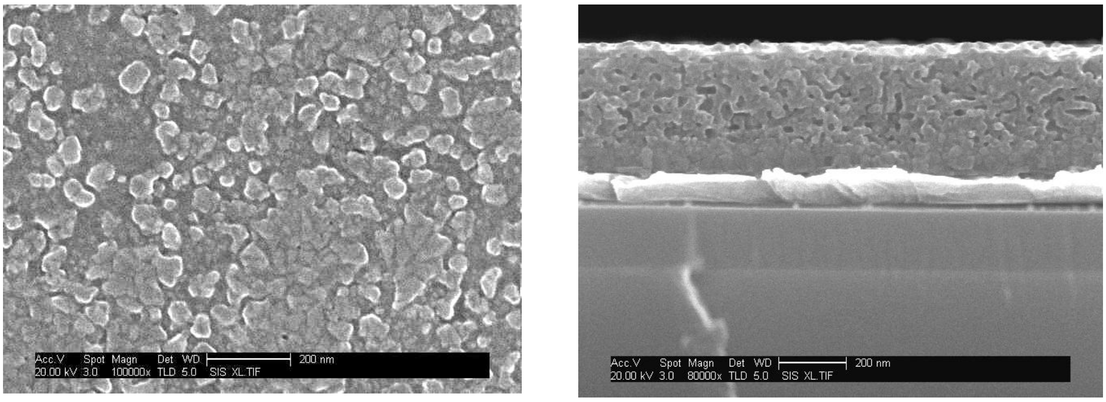

Figure 7.24 SEM images of the surface and in section showing the microstructure of BZT(20/80) thin film on BZN buffer layer.

In the fracture cleave image of figure 7.24 the dense granular microstructure (small grains) of the thin (~25 nm) BZN buffer layer can be seen just above the Au layer and produces growth in the BZT film which has a very different microstructure (larger grains) to BZN. The BZT film also appears to be nanoporous. The successful growth of BZT film on Au bottom electrode is likely due to the dense granular structure of the BZN layer and the reasonably well matched thermal expansion of BZT to BZN which prevents cracking of the film. The BZT(20/80)/BZN bilayer film is of uniform thickness.

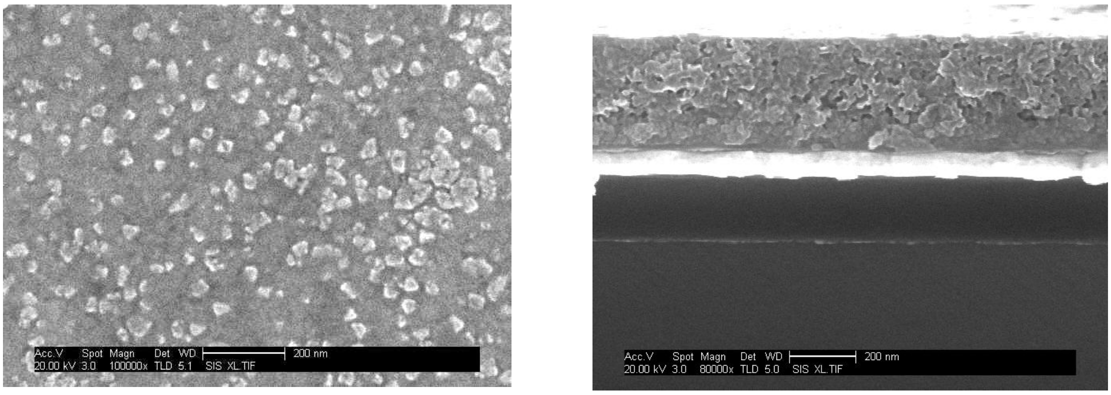

Figure 7.25 SEM images of the surface and in section showing the microstructure of BZT(35/65) thin film on BZN buffer layer on Au (bright layer).

The microstructure of BZT(35/65) thin film grown on BZN/Au/Cr/SiO_2/Si, as highlighted in the SEM micrographs of figure 7.25, has a smaller grain size and appears more dense compared to the microstructure of BZT(20/80) film grown on BZN/Au/Cr/SiO_2/Si substrate (figure 7.24). This is consistent with the work of others who found that the average grain size decreased and the microstructure became dense with increasing Zr content.

For comparison purposes a BZT(35/65) thin film was deposited on BZN buffer layer with Pt/Ti bottom electrode. The SEM images of the surface and sectioned microstructure can be seen in figure 7.26.

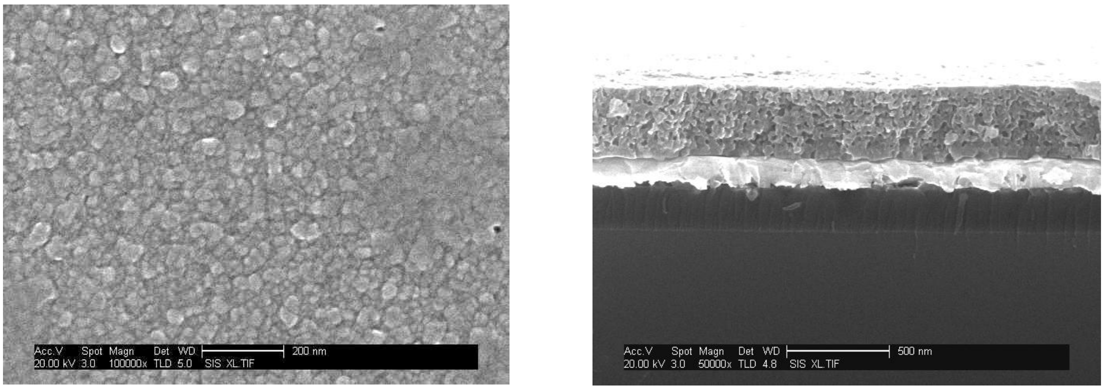

Figure 7.26 SEM micrographs of the surface and in section for BZT(35/65) grown on BZN/Pt/Ti/SiO_2/Si substrate.

XRD analysis showed excellent crystallisation of BZT and BZN. It is evident that BZT(35/65) thin film grown on BZN/Au/Cr/SiO_2/Si substrate (figure 7.25) has a different microstructure to that deposited on BZN/Pt/Ti/SiO_2/Si (figure 7.26), although the grain size is the same. The BZT film grown on Pt electrode with intermediate BZN buffer layer displays a nanoporous microstructure (sectional SEM image, figure 7.26), and has a very similar microstructure to that of BZT when deposited directly on Pt electrode without buffer layer (figure 7.27a).

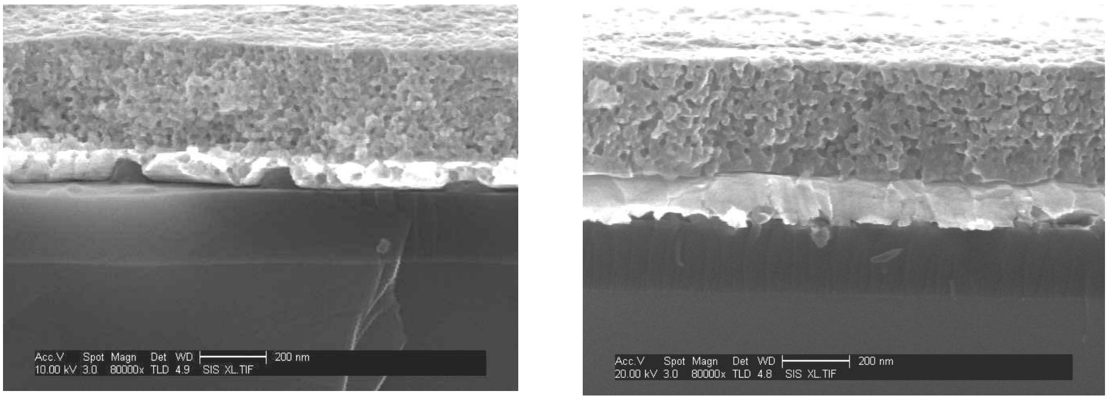

(a) (b)

Figure 7.27 SEM micrographs showing fracture cleave microstructures of (a) BZT thin film grown on Pt coated SiO_2/Si and (b) BZT film deposited on BZN buffer layer on Pt/Ti/SiO_2/Si substrate.

Electrical measurements were made and the results compared. Initially, a comparison was made of the dielectric properties of BZT(35/65) grown on Pt bottom electrode with and without a BZN buffer layer (figures 7.28 and 7.29). As the data suggests in figure 7.28, the introduction of a thin (25 nm) BZN buffer layer has had the effect of reducing the overall dielectric constant of the BZT/BZN bilayer, partly due to the lower permittivity of the BZN compared to BZT (refer to chapter 5 on modelling), but also due to a variation in the porosity of the BZT films in the two samples. Comparing the two cross-sectional SEM images, the BZT film deposited on Pt with an intermediate BZN buffer layer (figure 7.27b) appears to contain larger pores compared to the BZT film grown directly on Pt. The introduction of a BZN buffer layer between BZT(35/65) film and Pt bottom electrode had little effect on the tunability of the dielectric. Further electrical measurements and comparisons are presented in figures 7.30 to 7.33.

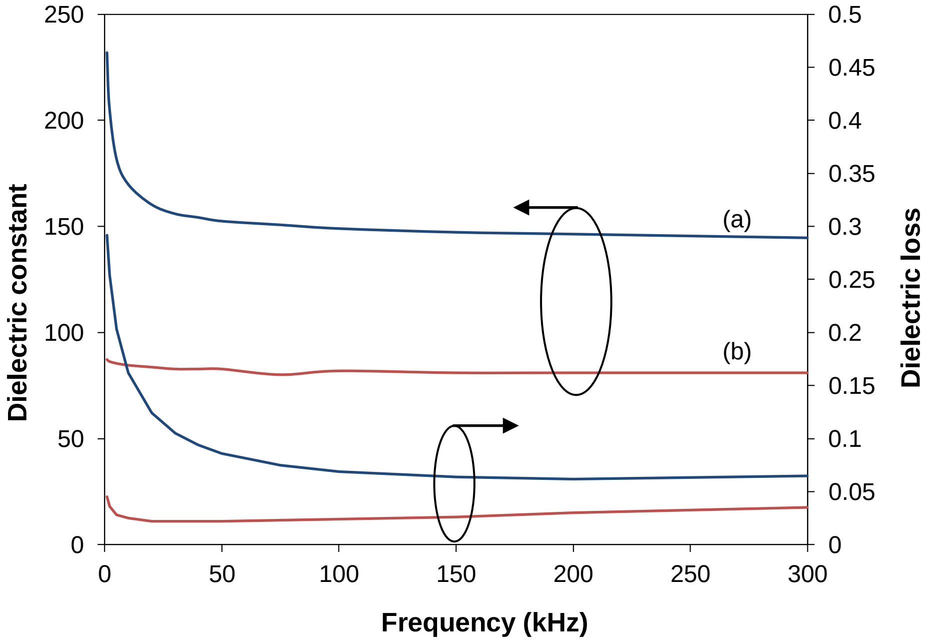

Figure 7.28 Dielectric properties as a function of frequency for (a) BZT(35/65) grown directly on Pt bottom electrode and (b) BZT(35/65) deposited on Pt electrode with an intermediate BZN buffer layer.

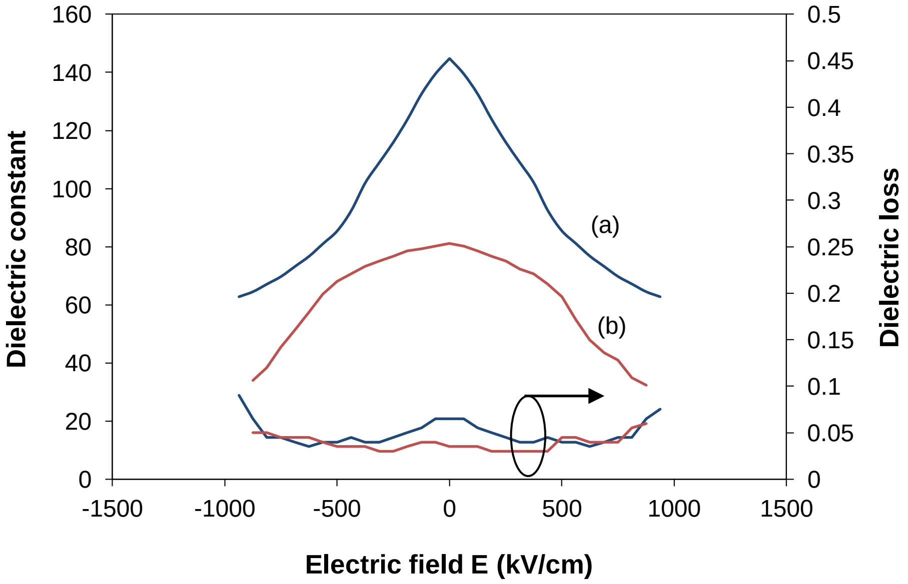

Figure 7.29 Dielectric properties as a function of electric field at a frequency of 300 kHz for (a) BZT(35/65) grown on Pt electrode and (b) BZT(35/65) deposited on Pt with a BZN buffer layer.

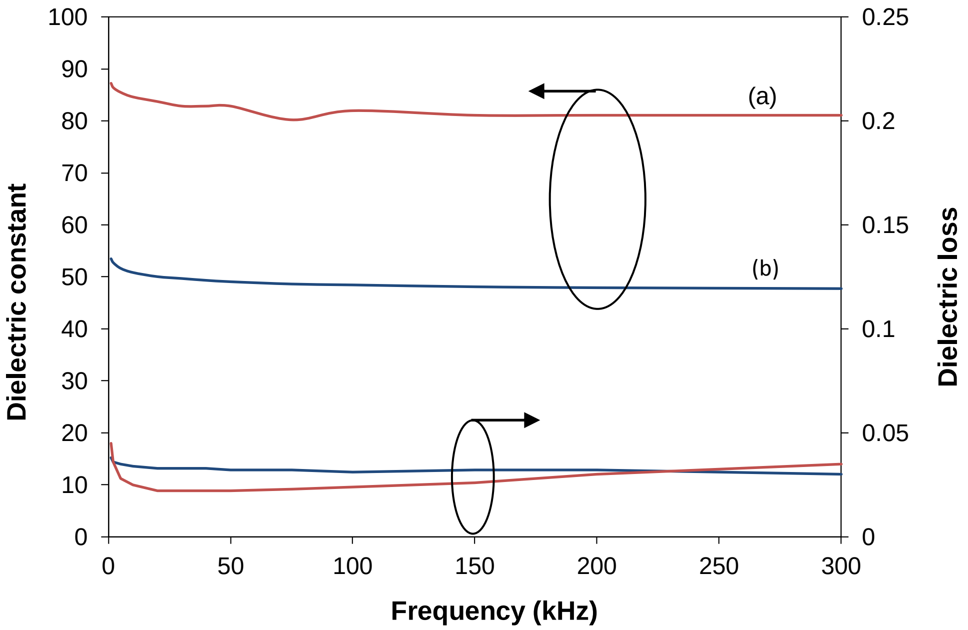

Figure 7.30 Variation in dielectric properties with frequency for: (a) BZT(35/65) grown on Pt electrode with an intermediate BZN buffer layer and (b) BZT(35/65) deposited on Au with a BZN buffer layer.

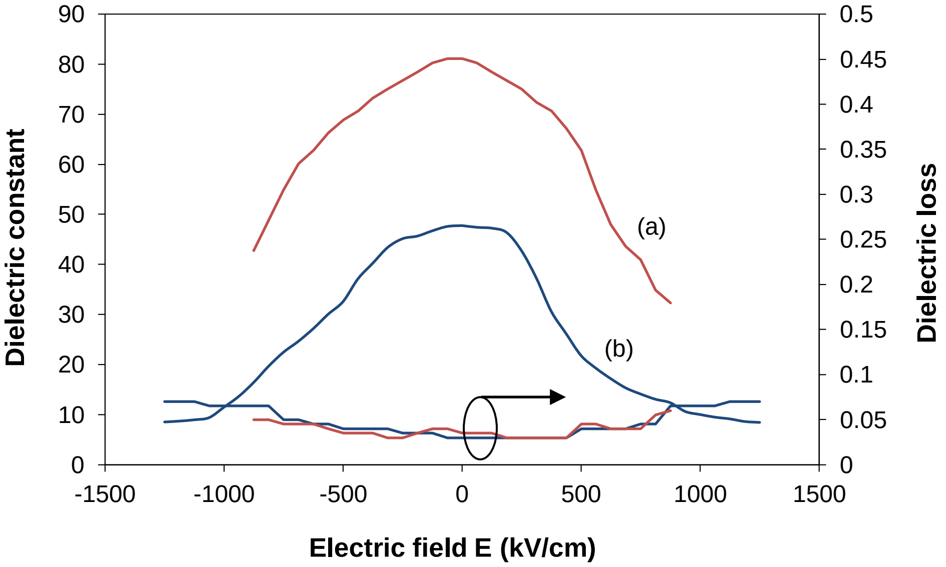

Figure 7.31 Dielectric properties as a function of electric field at a frequency of 300 kHz for: (a) BZT(35/65) grown on Pt with a BZN buffer layer and (b) BZT(35/65) deposited on Au with a BZN buffer layer.

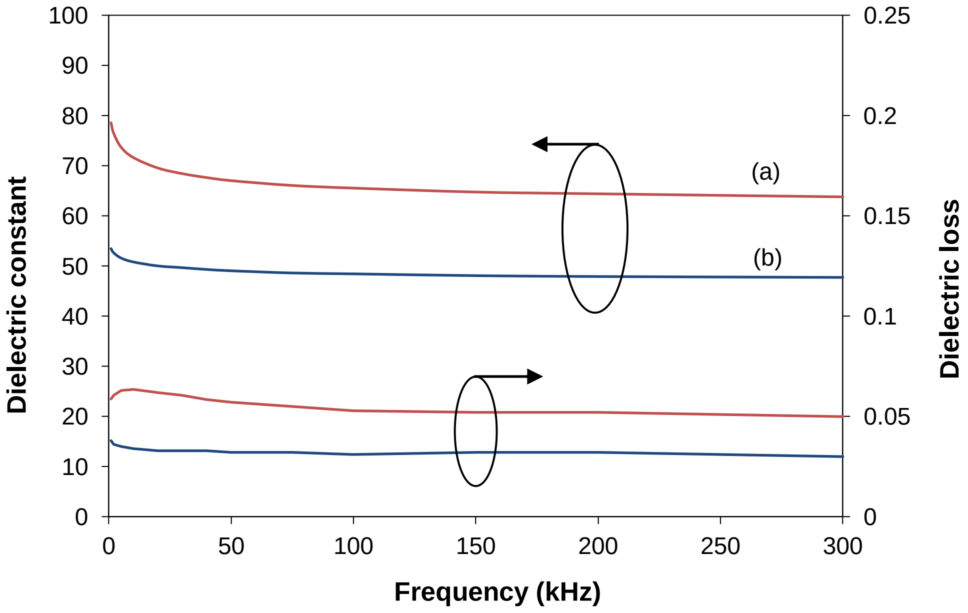

Figure 7.32 Variation in dielectric properties with frequency for: (a) BZT(20/80) thin film deposited on Au electrode with an intermediate BZN buffer layer and (b) BZT(35/65) film deposited on Au with a BZN buffer layer.

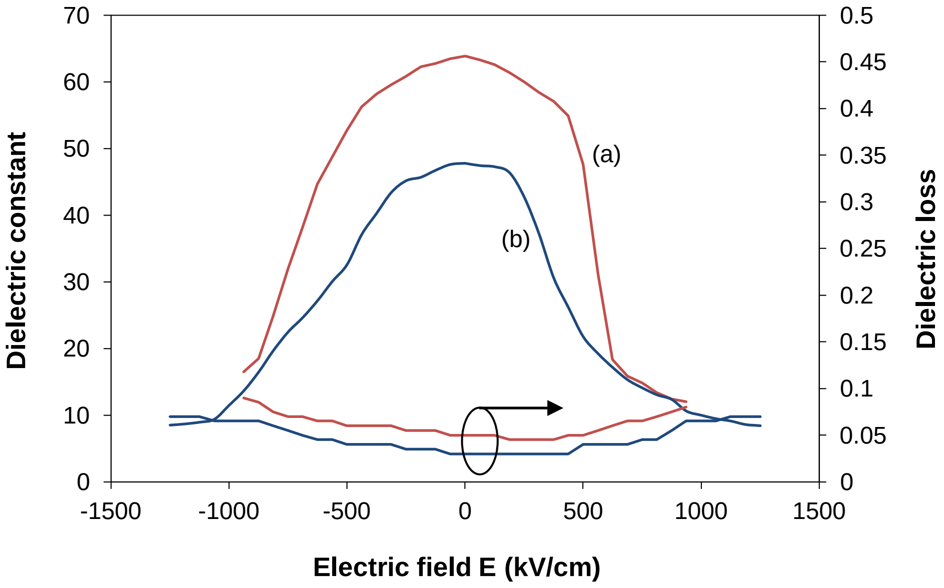

Figure 7.33 Dielectric properties as a function of electric field at a frequency of 300 kHz for: (a) BZT(20/80) deposited on Au with a BZN buffer layer and (b) BZT(35/65) deposited on Au with a BZN buffer layer.

The data presented in figures 7.30 and 7.31 make a comparison of the dielectric properties as a function of frequency and electric field for BZT(35/65) film grown on a very thin (25 nm) BZN buffer layer on Pt and Au electrodes. Although the sample with a BZT(35/65)/BZN bilayer deposited on Au rather than on Pt displayed a lower dielectric constant and similar dielectric loss, it did boast a significantly higher tunability (82% compared to 60% on Pt) which translated into a higher figure of merit (FOM) value (27 on Au compared to 20 on Pt). The reduced dielectric constant was partly due to increased BZT roughness (from 3.3 nm on Pt electrode to 11.7 nm on Au electrode) which created problems at the interface between the electrodes and dielectric material. Improved tunability was attributable to higher dielectric strength (1.25 MV/cm on Au, 0.87 MV/cm on Pt) and higher conductivity of Au compared to Pt, and is testimony to the fact that BZT can be grown on Au provided an intermediate buffer layer is deposited beforehand. Asymmetry of the dielectric constant vs electric field measurements when the polarity was switched was primarily due to different Schottky barrier heights (i.e. metal work functions) at top (Au/Cr) and bottom (Pt/Ti) electrodes.

A comparison was made of the dielectric properties with frequency and bias field for BZT(20/80) and BZT(35/65) thin films grown on BZN/Au/Cr/SiO_2/Si substrate as shown in figures 7.32 and 7.33. The film thicknesses of both samples were the same and so the reduced dielectric constant of BZT(35/65) was likely a consequence of slight differences in the microstructure and increased surface roughness. The tunability of the two samples BZT(20/80) and BZT(35/65) was very high, 81% and 82%, respectively. However, the dielectric constant of BZT(35/65) grown on BZN/Au/Cr/SiO_2/Si substrate was very low (48) especially when compared to BZT(35/65) thin film deposited directly on Pt coated Si (145), an order of magnitude difference. In order to achieve the higher tunability and dielectric strength of BZT thin film grown on Au with BZN buffer, there appears to be a compromise with lower dielectric constant, although for certain applications that require high tunability combined with lower permittivity this could be an advantage. When plotting the dielectric constant as a function of electric field for a given material it is not always easy to extract the tunability from the data. It is therefore useful to note how the tunability itself varies with the electric field. This has been plotted in figure 7.34 together with dielectric loss so as to be consistent with data previously presented in figures 7.28 to 7.33.

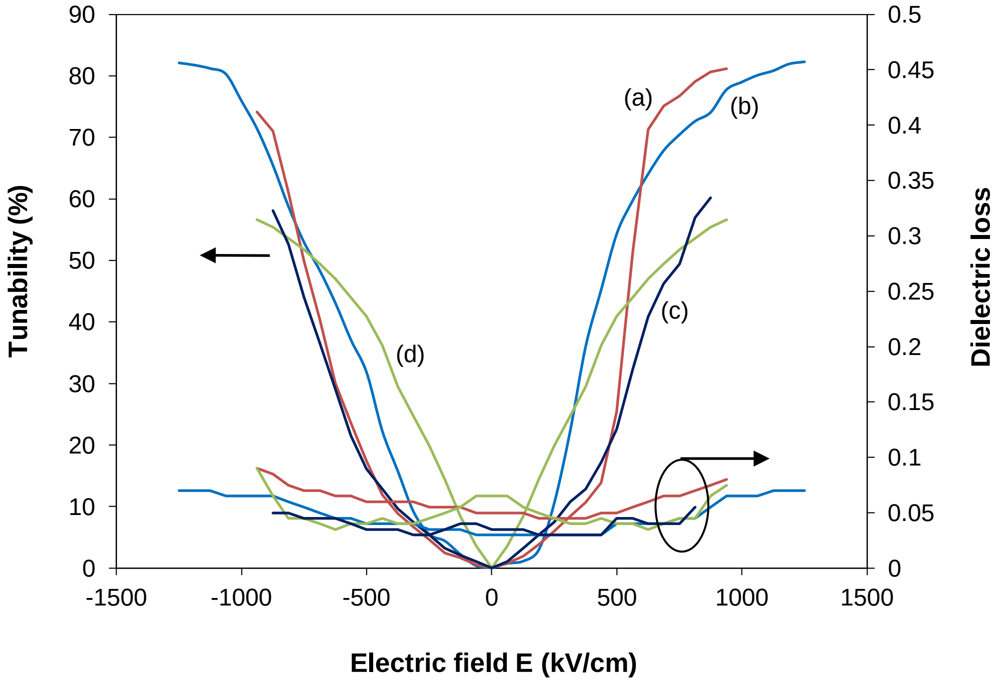

Figure 7.34 Variation of tunability and dielectric loss with electric field at a fixed frequency of 300 kHz for (a) BZT(20/80) grown on Au bottom electrode with intermediate BZN buffer layer, (b) BZT(35/65) deposited on Au with BZN buffer layer, (c) BZT(35/65) deposited on Pt with BZN buffer layer, and (d) BZT(35/65) grown directly on Pt bottom electrode.

From the graph of tunability as a function of electric field as displayed in figure 7.34, it is possible to quickly establish the rate of tuning with field and the maximum tunability for a given dielectric. The maximum tunability data for thin-film BZT grown on BZN buffer layer on Au and Pt electrodes has been added to the data presented in figure 7.16 and is shown in figure 7.35. Straightforward comparisons between materials can therefore be made. It is clear that maximum tunability for BZT(20/80) and BZT(35/65) compositions was achieved when a very thin (25 nm) BZN buffer layer was inserted between the BZT thin film and Au bottom electrode to form a BZT/BZN bilayer structure on Au.

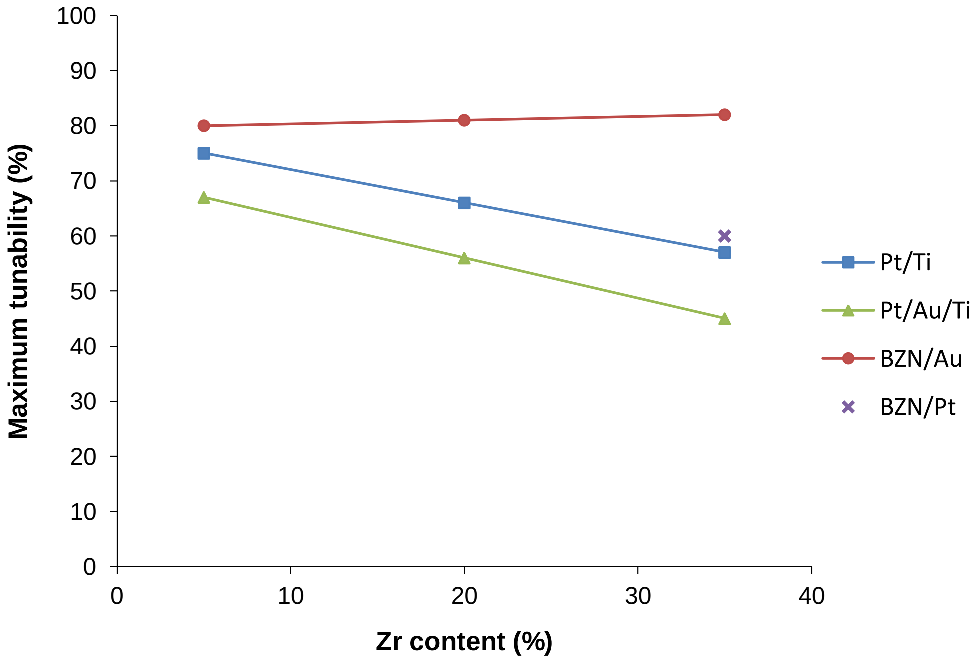

Figure 7.35 Maximum tunability as a function of the Zr content in BZT thin films deposited on metal electrode with and without an intermediate BZN buffer layer.

Interestingly, use of a BZN buffer layer between BZT(35/65) dielectric film and Pt electrode appears to have improved the tunability very little over that of BZT deposited directly on Pt/Ti/SiO_2/Si substrate.

7.3.7 BZT Multilayer Structures

Multilayer films are composed of alternating layers of different material or the same material of different compositions. The objective of the work on voltage tunable capacitors was to find dielectric materials with enhanced dielectric properties. Multilayer BZT thin films were studied with a view to maximising the tunability while maintaining reasonably low dielectric loss. Several BZT thin film multilayer compositions were investigated experimentally and the best results were obtained for a structure incorporating alternate layers of BZT(5/95) and BZT(35/65), each layer 50 nm thick. Films were prepared by sol-gel technique each layer deposited by spin-coating at 3000 rpm for 30 seconds. The layers were pyrolysed on separate hotplates at 350^{o}C for 5 minutes and at 550^{o}C for a further 5 minutes. After all six layers had been spun and heat treated, a final crystallisation anneal was performed by RTA at 750°C for 2 minutes. A schematic diagram of the structure can be seen in figure 7.36.

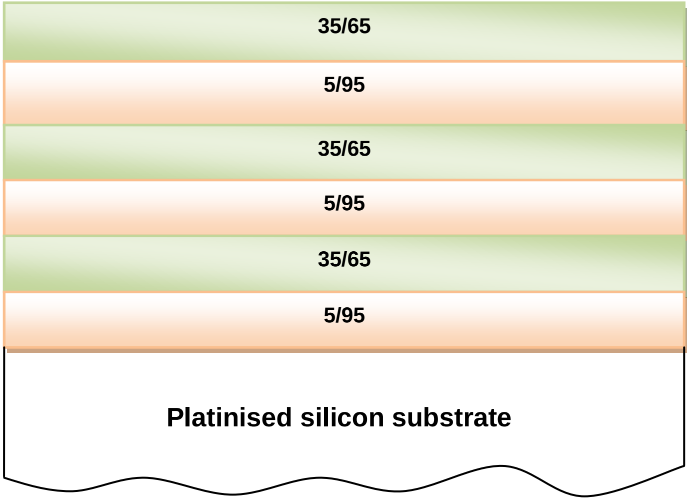

Figure 7.36 Schematic diagram of BZT multilayer structure deposited on Pt/Ti/SiO_2/Si substrate. Each BZT layer is 50 nm thick.

The multilayer BZT thin film on platinised silicon substrate showed excellent crystallisation with the most intense peak at (110) plane, as has previously been the case with BZT single compositional films grown on Pt bottom electrode. The microstructure of the composite film was examined by SEM and images of the surface and section can be seen in figure 7.37.

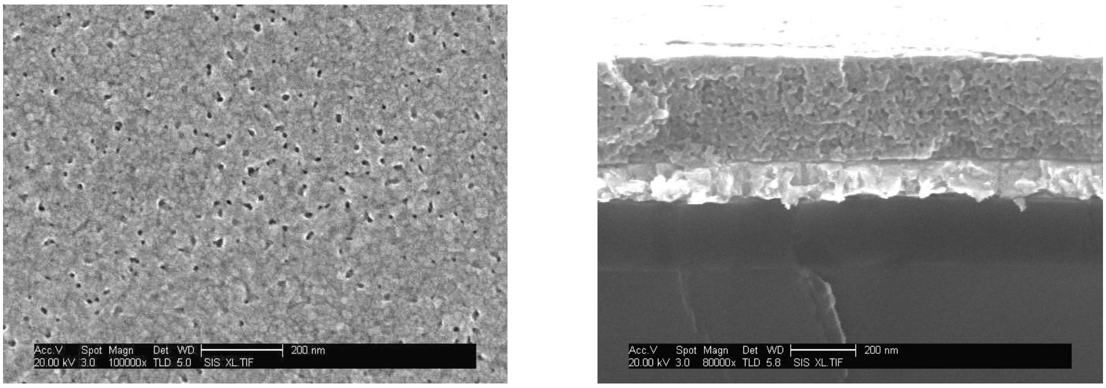

Figure 7.37 SEM images of the surface and section of multilayer structure combining BZT(5/95) and BZT(35/65) layers sequentially as shown in the schematic of figure 7.36.

The SEM micrographs (figure 7.37) show the multilayer film to be nanoporous with a small grain structure. Looking at the sample in section (right-hand SEM image) there are regions where the individual BZT layers are just distinguishable. The composite film appears uniform and reasonably smooth. The surface microstructure was also analysed using AFM (figure 7.38) from which a measurement of surface roughness was obtained (figure 7.39).

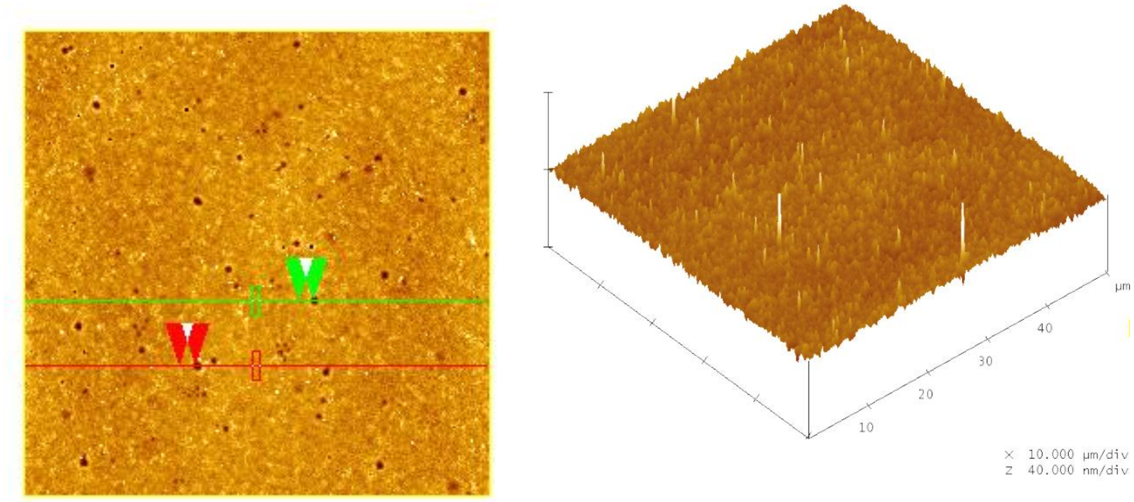

Figure 7.38 AFM image of the BZT multilayer surface including a three dimensional projection. A section analysis was performed on the left-hand image (green and red scan lines). The scan results are shown in figure 7.39.

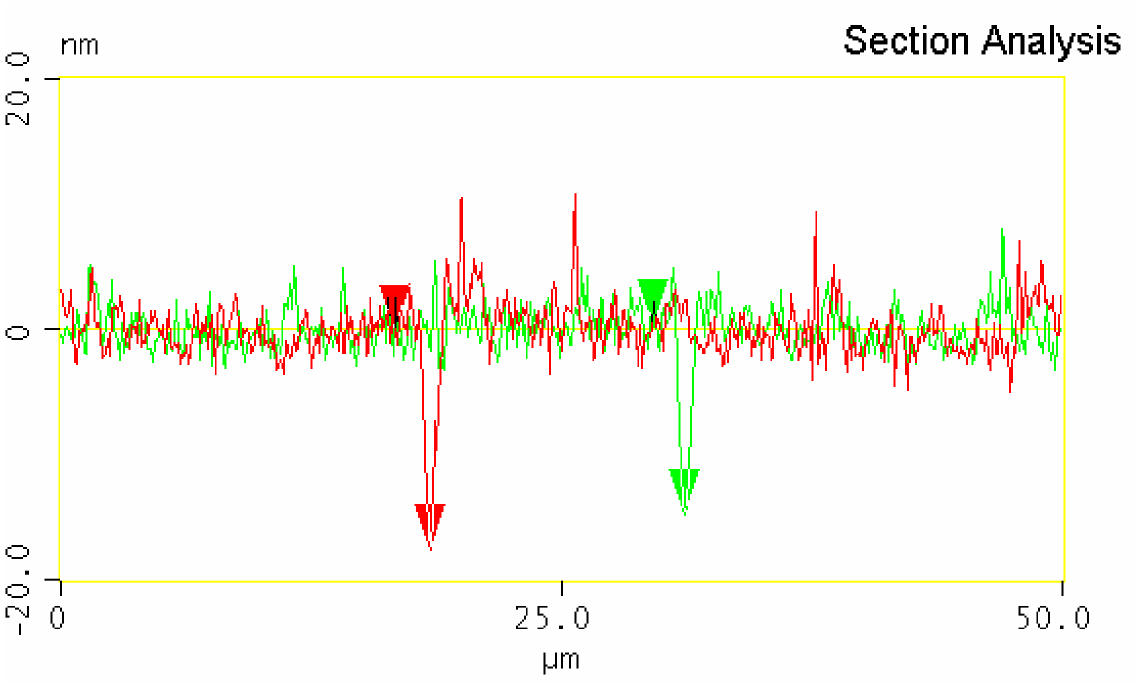

Figure 7.39 Section analysis performed on the AFM image in figure 7.38 for the BZT multilayer structure shown schematically in figure 7.36.

Using the left-hand AFM surface image a section analysis was performed (figure 7.39) from which the surface roughness (R_a) was determined. The measured roughness was 3.3 nm which corroborates the analysis by SEM.

Electrical measurements were taken of the MIM capacitors fabricated using this multilayer structure and the results of dielectric constant and loss as a function of frequency to 300 kHz are shown in figure 7.40.

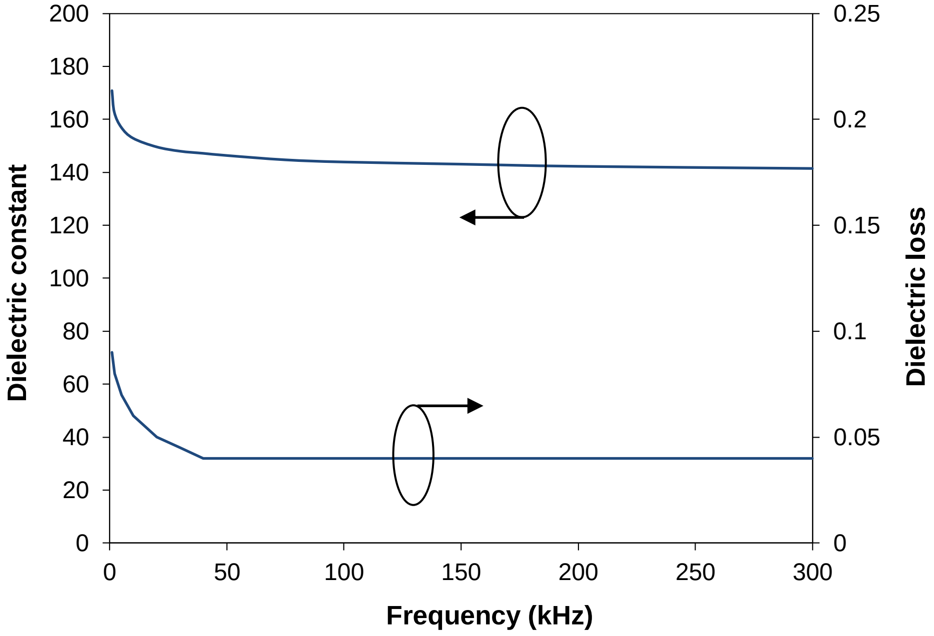

Figure 7.40 Variation of dielectric constant and loss with frequency for multilayer BZT thin film on platinised silicon substrate.

The results in figure 7.40 show a high dielectric constant (145) for the multilayer film over the frequency range to 300 kHz with an increase at the lower frequency end to 170. The increase in dielectric constant at low frequency is accompanied by a corresponding increase in the dielectric loss which is generally a little higher than seen in single compositional thin films. This may be due to interface issues between the different compositional layers. Layers of BZT(35/65) have a higher Zr content than BZT(5/95) layers and will influence grain growth differently due to the larger ionic radius of Zr^{4+} (0.86 Å) compared to Ti^{4+} (0.74 Å). Larger grain growth is expected from BZT(5/95) layers.

Results of the variation of dielectric constant and loss with electric field for BZT multilayer thin film structure are presented in figure 7.41.

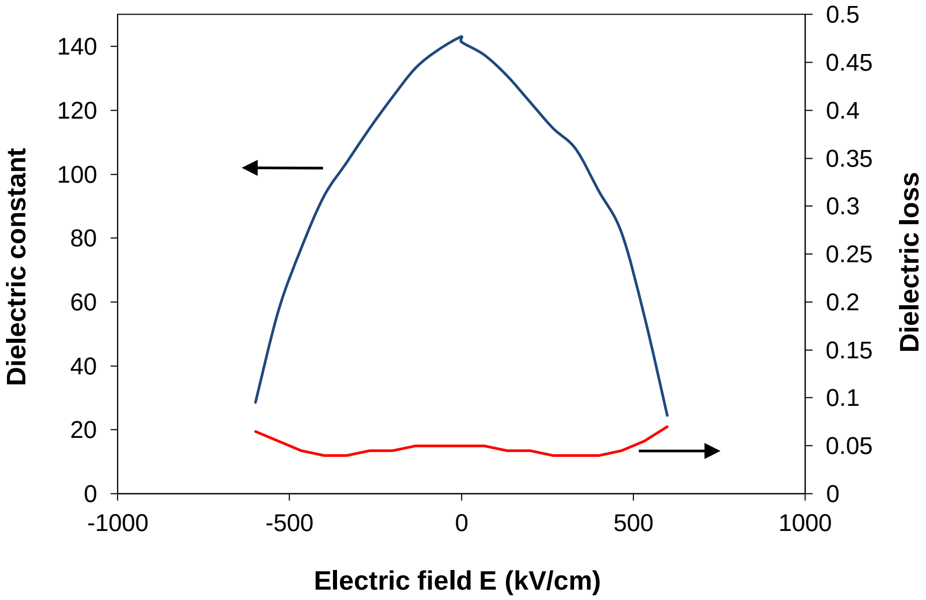

Figure 7.41 Dielectric properties of BZT multilayer thin film as a function of electric field.

The multilayer structure as shown in figure 7.36 gave the highest tunability of 82% at a bias field 600 kV/cm (figure 7.41). This structure was formed from alternate layers of BZT(5/95), a ferroelectric material at room temperature, and BZT(35/65) which is paraelectric at room temperature. A question therefore arises as to whether the composite film behaves as a ferroelectric or paraelectric material. The variation of the dielectric constant with electric field in figure 7.41 might suggest so. However, additional evidence was required in the form of a polarisation versus electric field (P-E) loop to see whether the material displayed the characteristic hysteresis associated with ferroelectrics or not. The BZT multilayer samples used in this investigation were not poled initially because the dielectric properties, including the tunability, had been measured for unpoled material. The sample was poled afterwards to see if the polarisation of the material could be improved upon. The P-E loop measurement for the BZT multilayer sample before and after poling is shown in figure 7.42.

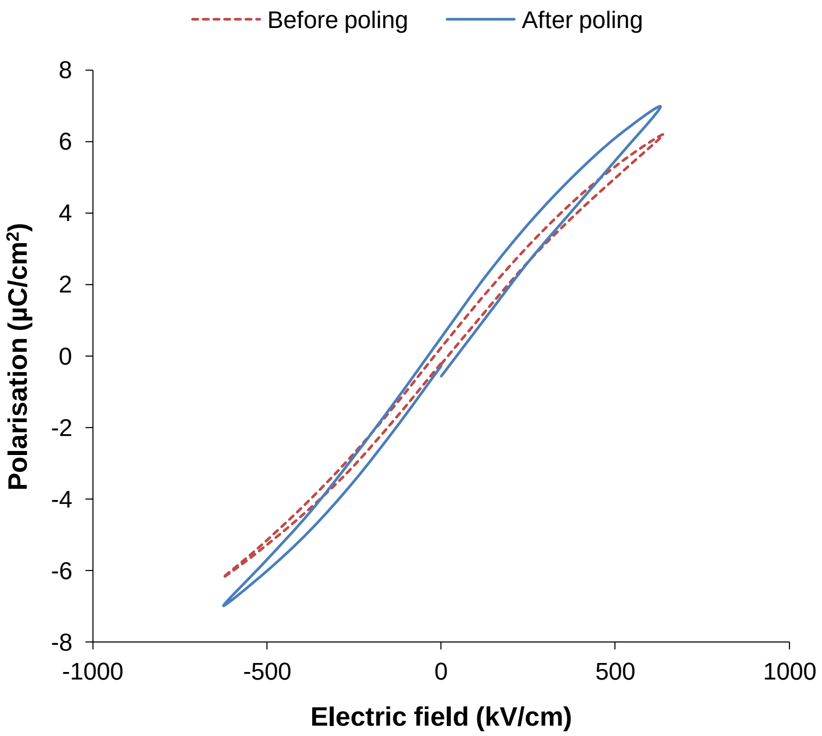

Figure 7.42 Polarisation versus electric field hysteresis loop of BZT multilayer thin film deposited on platinised silicon substrate.

The P-E loops in figure 7.42 shows hysteresis of the BZT multilayer film before poling and a slightly enhanced hysteresis after poling. The remnant polarisation (P_r) and coercive electric field (E_c) obtained from the P-E hysteresis loops are 0.28 $\mu C/cm^2$ and 26.7 kV/cm for unpoled material, and 0.52 $\mu C/cm^2$ and 39.3 kV/cm for poled material, respectively. The very narrow P-E hysteresis loop is characteristic of ferroelectric BZT thin film material in general.

In answer to the earlier question, the composite film made up of alternate ferroelectric and paraelectric BZT layers does clearly behave as a ferroelectric. The multilayer structure of unpoled ferroelectric and non-ferroelectric layers shows a net spontaneous polarisation. It is thought that in the thin (50 nm) ferroelectric layers the domains are better oriented, inducing orientation and charge accumulation in the non-ferroelectric layers.

7.4 Summary of Main Features and Achievements

Two methods were trialled to improve the dielectric properties of sol-gel derived BZT thin film for application to voltage tunable capacitors: (1) the growth of BZT thin film on Au coated silicon, and (2) the deposition of a BZT thin film multilayer stack on platinised silicon.

In the first method there was a preference for using Au bottom electrode due to its lower series resistance compared to using Pt, borne out by the sheet resistance measurements on metal layers (sub-section 7.3.2). Although crystalline BZT thin film was successfully grown on Pt bottom electrode, it was unsuccessful when grown directly on Au coated silicon due to tensile stress and cracking of films. The growth and characterisation of BZT thin film on Au coated silicon has been successfully demonstrated by the introduction of a buffer layer. The methodology for growth of sol-gel derived BZT thin film on Au was:

- BZT thin film grown directly on Au layer but unsuccessfully crystallised.
- Successful growth and crystallisation of BZN thin film on Au bottom electrode with excellent dielectric strength (2 MV/cm), however, relatively poor tunability (25%) compared to BZT.
- Thermal coefficient of expansion of BZN between that of Au and BZT.
- The dielectric properties of a bilayer film incorporating a BZN buffer layer with a BZT main layer optimised using a layered composite model.
- Deposition of a very thin (25 nm) sputtered BZN buffer layer ideal for BZT growth and crystallisation on Au coated silicon, verified by experiment.

The use of a sputtered BZN buffer layer to facilitate the growth and crystallisation of BZT thin film on Au bottom electrode with enhanced tunability (82% on Au compared to 60% on Pt electrode) in the paraelectric phase is deemed a significant achievement and contribution to knowledge.

The second method for improving the dielectric properties of sol-gel derived BZT thin film focused on a BZT multilayer stack. The structure incorporated alternate layers of $Ba(Zr_{0.05}Ti_{0.95})O_3$, a ferroelectric composition at room temperature, and $Ba(Zr_{0.35}Ti_{0.65})O_3$, a composition in the paraelectric phase at room temperature. A total of six layers were deposited, each layer 50 nm thick. Crystallisation of the 300 nm thick film was performed by RTA at 750^oC for 2 minutes. The composite film of ferroelectric and paraelectric layers was shown to behave as a ferroelectric material with characteristic polarisation versus electric field hysteresis. A dielectric constant of 145, loss of <0.05 and tunability of 82% at a bias field of 600 kV/cm was achieved. The combining of BZT ferroelectric and paraelectric phase material in a single film to enhance the tunability is also seen as an important achievement.

8 High-K Zipping Varactor

8.1 Introduction

Many of the current designs of variable capacitor give very nonlinear capacitance change or very small tuning range. The objective has therefore been to develop a device which has a continuously variable capacitance over a wide range. The zipping varactor is a miniature MEMS tunable device that uses the mechanical movement of a cantilever to achieve a large variation in capacitance. A schematic diagram of the zipping varactor is shown in figure 8.1.

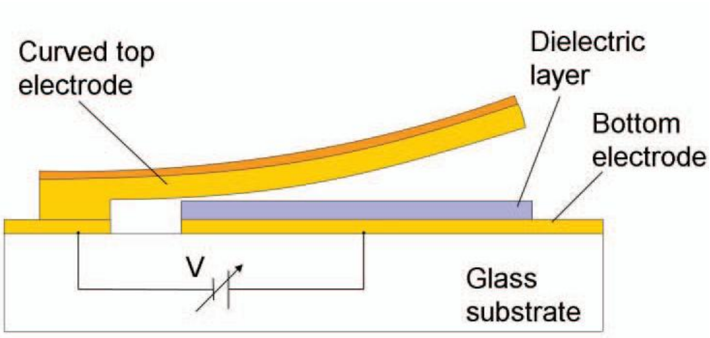

Figure 8.1 Schematic of the zipping varactor on glass substrate [3.125].

Capacitance tuning is achieved when a variable voltage is applied between the top plate of the curved cantilever beam and the fixed bottom plate or electrode of the dielectric thin-film capacitor. The resulting electrostatic force deflects the cantilever beam toward the dielectric and metal electrode layers. In the case of the zipping varactor, the beam is anchored at one end so that maximum deflection occurs at the tip of the beam. The amount that the beam deflects is dependent on the voltage applied and the geometry and mechanical properties of the cantilever beam. The cantilever beam is bilayered with a pre-stressed (tension) top metal layer (sputtered Au) and a thicker unstressed bottom layer (electroplated Au). Stress in the top layer causes the beam to curve. These parameters have been incorporated into the modelling of cantilever beam displacement by Pu *et al*. [3.127]. One objective of this thesis is to compare the modelled data of capacitance as a function of DC bias voltage with the data retrieved from experimental devices incorporating BZN and PZT dielectric films.

The use of PZT dielectric in the zipping varactor is part of a separate parallel investigation to that of BZN, and has been included for comparison purposes only. Fabrication of the zipping varactor was undertaken jointly by Cranfield and Imperial College London. Processing of the capacitor had two distinct phases: (1) the deposition and patterning of the bottom metal electrode and thin insulating dielectric film, and (2) the fabrication, alignment and bonding of the top electrode. Fabricated devices had not been tested at the point of completing this thesis. However, the preliminary research associated with the fabrication of thin BZN films on metallised glass wafers will be discussed in detail.

8.2 Material Specification for Substrate, Bottom Electrode and Dielectric Layer

The substrate material selected for process development of the zipping varactor was based on a set of criteria which included RF compatibility, coefficient of thermal expansion match to device materials, good adhesion between coatings and substrate, and the ability to implement laser transfer and bonding methods. The substrate must therefore be UV-transparent, so films were prepared on reusable glass wafers making for cost efficient processing.

The bottom and top electrode metallisation must be low resistivity with the aim of achieving a low contact resistance (<1Ω) and high Q values (~100-200) for the device. This can be achieved using Au. Original investigations centred on sputtered Au/Cr using a very thick (800 nm) Au layer. This choice was in response to sheet resistance measurements recorded for a range of metal layers, the results of which are presented in sub-section 7.3.2. The sheet resistance of Au(800nm)/Cr was typically 0.05 ±0.01 Ω/sq over the temperature range 300^{o}C to 700^{o}C. This compared favourably to sputtered Au(100nm)/Cr which was also trialled. The sheet resistance of Au(100nm)/Cr was 0.8 ±0.2 Ω/sq over the same temperature range. The as-deposited sheet resistance of Au(800nm)/Cr and Au(100nm)/Cr was 0.04 Ω/sq and 0.5 Ω/sq, respectively. However, there were some processing issues with using the thick and thin Au at the higher temperatures, such as Au/Cr diffusion into the dielectric film. Other metal films successfully trialled were those with a Pt top layer including Pt(100nm)/Ti and Pt(100nm)/Au(200nm)/Ti. The as-deposited sheet resistance of Pt(100nm)/Ti and Pt(100nm)/Au(200nm)/Ti was 1.85 Ω/sq and 0.13 Ω/sq, respectively. More than an order of magnitude reduction in the sheet resistance was achieved through the inclusion of an Au layer. Although the sheet resistance was generally higher for metal films with Pt top layer compared to films with an Au top layer, there was greater thermal stability and no diffusion issues.

When selecting a suitable dielectric thin film material for the zipping varactor, dielectric properties such as dielectric constant (k), loss and breakdown strength must be optimised to give a very large continuous capacitance change in a compact device. Some typical simulated tuning data for devices incorporating low-k (k=4) and high-k (k=200) dielectrics are shown in figure 8.2.

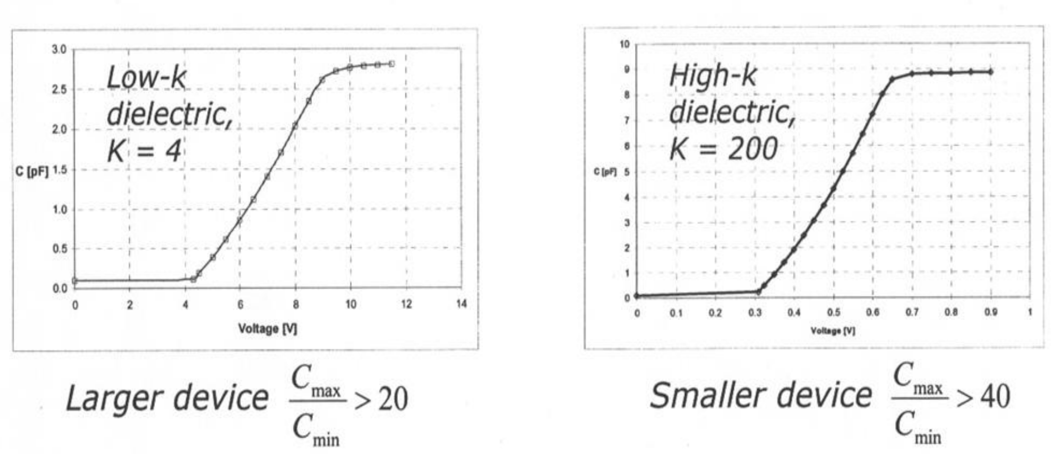

Figure 8.2 Simulated capacitance–voltage characteristics for zipping varactor displaying a capacitance ratio C_r of C_{max}/C_{min}>20 for low-k dielectric and C_{max}/C_{min}>40 for high-k dielectric. Data is courtesy of Imperial College London.

A typical low-k dielectric will be a 300 nm thick SiO_2 film which has a dielectric constant ~4.0. High-k dielectrics currently under investigation include BZN and PZT(30/70). PZT thin film (500 nm thick) deposited by sol-gel method has a dielectric constant of ~380. However, the use of PZT as dielectric in the zipping varactor is not the focus of attention in this work, but rather that of lead-free BZN. The sputtered BZN films have a dielectric constant in the range 80-150.

8.3 Fabrication of Bottom Electrode and Dielectric Layer

The processing routes for the fabrication of dielectric layer and bottom electrode are shown schematically in figures 8.3 and 8.4. There were three principal fabrication stages: (1) material deposition, (2) patterning of dielectric layer, and (3) patterning of the bottom electrode.

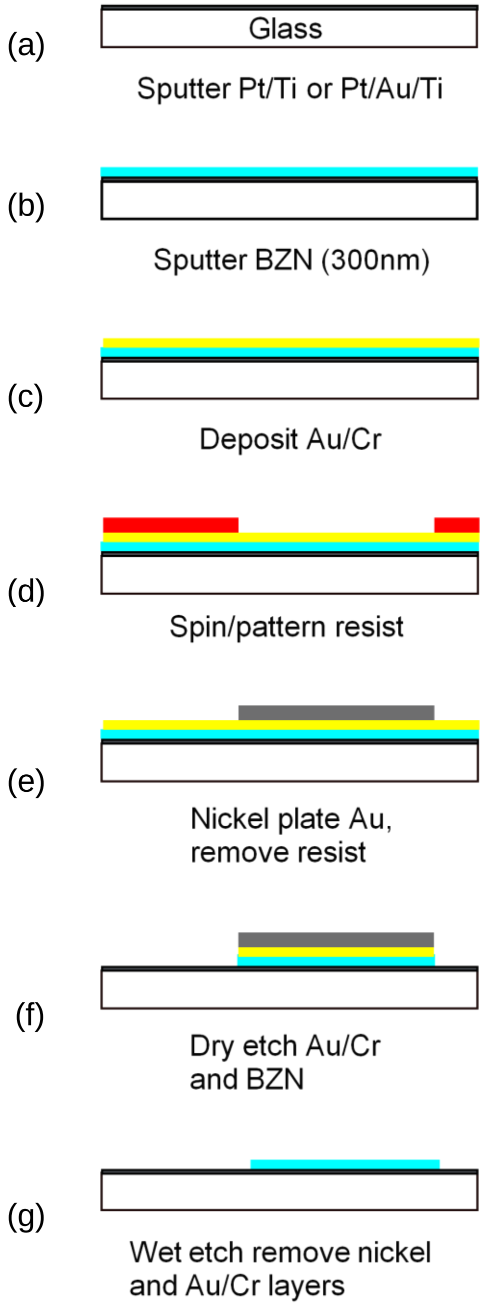

Figure 8.3 Process flow schematic for the patterning of dielectric layer.

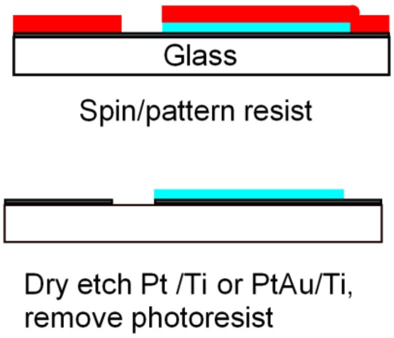

Figure 8.4 Process flow schematic for the patterning of bottom electrode.

8.3.1 Material Deposition

Two 100 mm diameter glass wafers were prepared by sputter depositing a blanket metallisation coating, one with Pt(100nm)/Ti(10nm) and the other with Pt(100nm)/Au(200nm)/Ti(10nm) (figure 98a). The metal layers were deposited on one side of the wafer only using the Nordiko sputtering system described in sub-section 4.3.1. A *circa* 300 nm thick BZN film was RF magnetron sputter deposited over the metal layer at an *in situ* substrate temperature of 300^{o}C using the SVS equipment detailed in sub-section 4.3.4 (figure 8.3b). The BZN sputtering parameters chosen for both wafers were: gas pressure of 40 mTorr, Ar/O_2 gas mixture ratio of 85/15, and RF power of 400 W. After depositing the BZN, the films were *ex situ* crystallised using a new and improved annealing procedure which is discussed in section 8.4. Crystallisation of the BZN thin films at the centre and toward the edge of each wafer was confirmed using XRD.

8.3.2 Patterning of BZN Dielectric Layer

The fabrication steps for the dielectric layer are shown in figure 8.3. To avoid undercutting the small (200 µm x 10 µm) dielectric feature shown in figure 8.5a, dry etching of BZN layer was preferred over that of wet etching. The dielectric finger can also be seen in the complete assembly (figure 8.5b) directly underneath the shaped top electrode. To dry etch BZN, either a soft photoresist mask, or some form of hard masking such as nickel or aluminium can be used. In this case, it was decided to use a nickel hard mask for its durability. However, before proceeding, a test BZN film was immersed in the liquid etchants that would later be used to remove the nickel mask and Au/Cr seed layers after patterning the BZN. Any undercutting of the BZN features at this stage had to be avoided. There was no perceivable etching of the BZN films in all solutions.

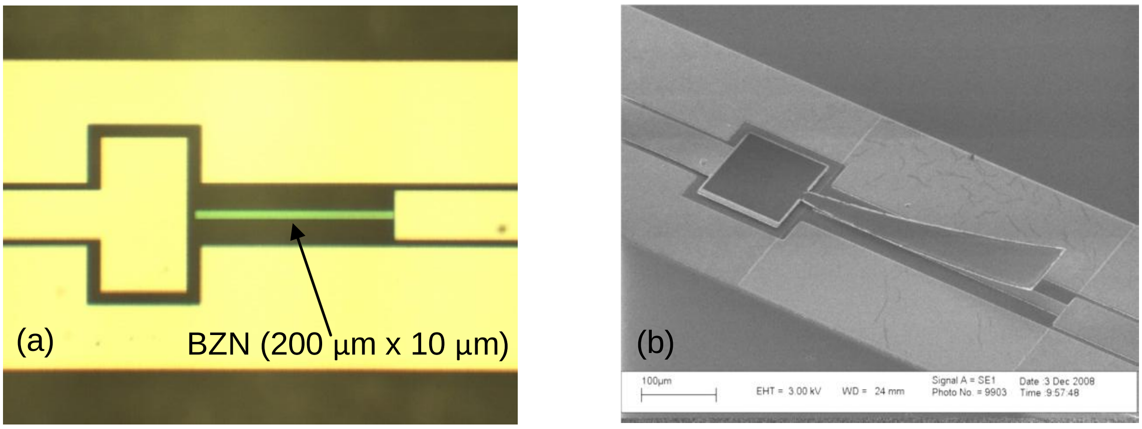

Figure 8.5 Images of (a) BZN dielectric finger (200 µm x 10 µm) and bottom electrode and (b) complete assembly showing shaped top electrode bonded at one end to a square contact pad (bottom metallisation).

A Au(100nm)/Cr seed layer was sputtered to give blanket coverage of the wafer in preparation for nickel plating (figure 8.3c). After depositing the Au/Cr seed layer, S1818 positive photoresist was spin coated at 4000 rpm for 60 seconds. The resist was then baked at 115^{o}C for 60 seconds. The first chrome mask plate for patterning the dielectric layer was aligned and brought into contact with the resist layer using a Karl Suss MA56 Mask Aligner. The resist was UV exposed with a dose 153 mJ/cm^2 before being immersed in MF319 developer for 60 seconds, and then rinsed in a beaker with flowing water. A second rinse of the wafer under flowing ultra-pure water was performed followed by a blow dry with filtered nitrogen. The wafer was inspected optically to check for clearance of the resist and exposure of the Au seed layer within the very fine features, i.e. the 200 µm x 10 µm rectangular window (figure 8.3d).

The exposed Au was nickel plated as described in section 4.3.5 using a plating current of 2.3 mA administered for 26.5 minutes to give a target nickel thickness of 0.3 µm. After nickel plating, the wafer was rinsed thoroughly under flowing water and blow dried. The quality of the plating was inspected optically and found to be satisfactory. The nickel hard mask thickness was measured across a resist alignment feature using the Dektak profilometer and found to be 0.28 µm, close to the target thickness. Having achieved the desired thickness, the photoresist was removed by soaking the wafer in acetone, followed by a rinse with acetone then IPA (to prevent drying stains) before blow drying with filtered nitrogen (figure 8.3e). If the target thickness had not been met, the wafer would have been returned to the plating bath to increase the plating thickness.

Using the newly formed nickel mask, the Au/Cr seed layer was dry etched in a Plasma Technology RIE80 machine using argon (Ar) gas at an RF power of 120 W, DC bias of 340 V, gas pressure 30 mTorr and gas flow of 20 sccm. The etch duration was 12 minutes. This was followed by the dry etching of the thin BZN film using CHF_3/Ar RIE at an RF power of 100 W, DC bias 300 V to 230 V, gas pressure 30 mTorr and gas flow ratio CHF_3/Ar of 10/13 sccm (figure 8.3f). The etch duration was four hours. Finally, RIE with Ar/O_2 was used to etch the polymer or skin often left behind when dry etching with hydrocarbons. The etching parameters used were an RF power of 60 W, DC bias of 100 V, gas pressure 200 mTorr, gas flow of 100 sccm and an etch duration of 60 minutes. The glass wafers were inspected optically to check for complete removal of the skin especially around the edges of the dielectric features. Once the polymer had been fully removed, the nickel plating was stripped off by immersing the glass wafer into ferric chloride ($FeCl_3$) solution for 5 minutes until the Au seed layer underneath was exposed. Finally, the Au and Cr layers were removed by wet etching using chemicals specified in sub-section 4.5.1 (figure 8.3g).

8.3.3 Patterning of Bottom Electrode

Fabrication steps for the bottom electrode are shown in figure 8.4. The partly processed wafers were spin coated with S1818 positive photoresist at 4000 rpm for 40 seconds with a 2 second acceleration and deceleration. The resist was then baked at 115^oC for 45 seconds. The second chrome mask plate for patterning the bottom electrode was aligned and brought into contact with the wafer using the Karl Suss MA56 mask aligner. The resist was UV exposed with a dose 156 mJ/cm^2. The wafer was then immersed for 1 minute in MF319 developer, rinsed in water and blow dried. After inspection optically for correct alignment of resist to dielectric fingers, the resist was flow baked at 115^{o}C for 3 minutes to round off the edges. Using the resist mask, the bottom electrode (Pt/Ti on one wafer and Pt/Au/Ti on the other wafer) was dry etched in the Plasma Technology RIE80 with argon gas. The process parameters were: RF power 120 W, DC bias 300 V, gas pressure 30 mTorr and gas flow rate 20 sccm. The etch duration was typically 100 minutes. However, for the wafer with Pt/Au/Ti bottom electrode it was not possible to remove the very thin (~10 nm) Ti layer since this had oxidised. The TiO_2 was removed in 5 minutes by RIE using CHF_3 at an RF power of 120 W, DC bias 300 V, gas pressure 20 mTorr and gas flow rate 28 sccm. Complete removal of the Ti layer was checked by electrically probing the surface and measuring the surface resistance.

Once the bottom electrode had been completely etched on both wafers, attempts were made to remove the residual photoresist by barrel ashing with Ar/O_2 for one hour in the Polaron PT7160 RF Plasma Barrel Etcher followed by spin cleaning using acetone. After this procedure a very thin skin of material remained which proved difficult to remove even using deep reactive ion etching (DRIE) in pure oxygen for 20 minutes followed by a soak in hot microposit 1165 [N-methyl-2-pyrrolidine (NMP)]. A further soak in hot NMP was required followed by a gentle mechanical wipe over the surface while still immersed in the hot NMP solution. This approach was preferred to an ultrasonic clean which could have resulted in lift-off of the dielectric film and/or bottom metallisation.

After cleaning was completed, the BZN thin film and metallisation thicknesses were measured on the Dektak profilometer. For both wafers the BZN thickness at the centre of the wafer was 350 nm and near to the edge was 300 nm, very close to the target thickness. Capacitors that have a range of dielectric thicknesses at this early trial stage can help determine the optimum dielectric thickness. On the wafer with Pt/Au/Ti bottom electrode where CHF_3 RIE was used to remove a TiO_2 film, Dektak measurements indicated etching of the glass wafer to a depth of ~100 nm. Also, over-etching resulted in complete removal of some of the dielectric and metal layers at the edge of the wafer.

8.4 Results and Discussion

8.4.1 BZN Thin Film Growth Trials on Au Coated Silicon

The most important properties of the dielectric material used in the zipping varactor are high dielectric constant, low dielectric loss and high breakdown strength; good tunability is not a prerequisite. Higher dielectric constant and strength of BZN thin film grown on platinised silicon was achieved by annealing at higher temperatures (700^{o}C) using RTA. Similar trials on the growth of sputtered BZN thin film on Au coated silicon and glass samples were conducted in preparation for work on the zipping varactor. Electrical measurements of films were made using MIM parallel-plate capacitors. Films grown on 100 nm thick Au and Pt electrodes in the same sputtering run were also compared. Sputtering parameters for the deposition of BZN films were: RF power 400 W, Ar/O$_2$ gas ratio 85/15, gas pressure 40 mTorr and substrate temperature 300^{o}C.

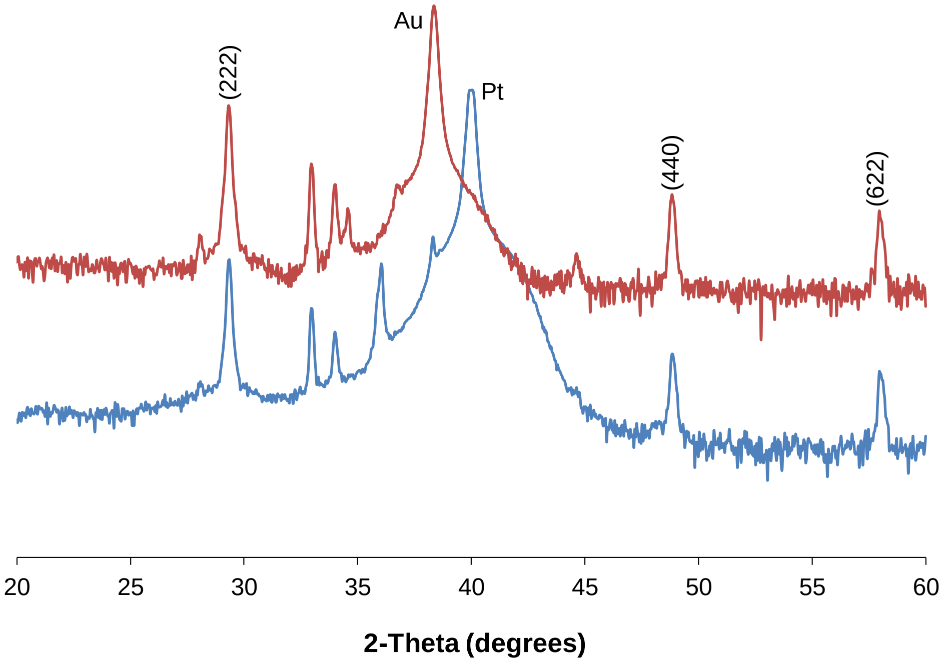

Figure 8.6 XRD diffractograms of BZN thin film on Au and Pt coated silicon.

The XRD patterns of sputtered BZN thin films grown on Pt/Ti and Au/Cr coated SiO_2/Si substrates, and annealed by RTA at 700^{o}C for 1 minute, is shown in figure 8.6. These XRD patterns show excellent crystallisation of BZN thin film grown on both Au and Pt electrodes. Sharp, narrow diffraction peaks indicate a large grain structure as confirmed in the SEM micrograph of the BZN film on Au (figure 8.7a). Films also appear dense and uniform (figure 8.7b). There is no evidence of blistering or pinhole formation. However, there does appear to have been some Cr and Au diffusion through the grain boundaries of the BZN film as can be seen in figure 8.7a. The surface of the BZN film was electrically probed to confirm that there was insufficient diffusion for the film to become conductive. The surface roughness (R_a) of the BZN films on Pt and Au was measured on the Dektak profilometer and found to be 3.2 nm and 2.8 nm, respectively.

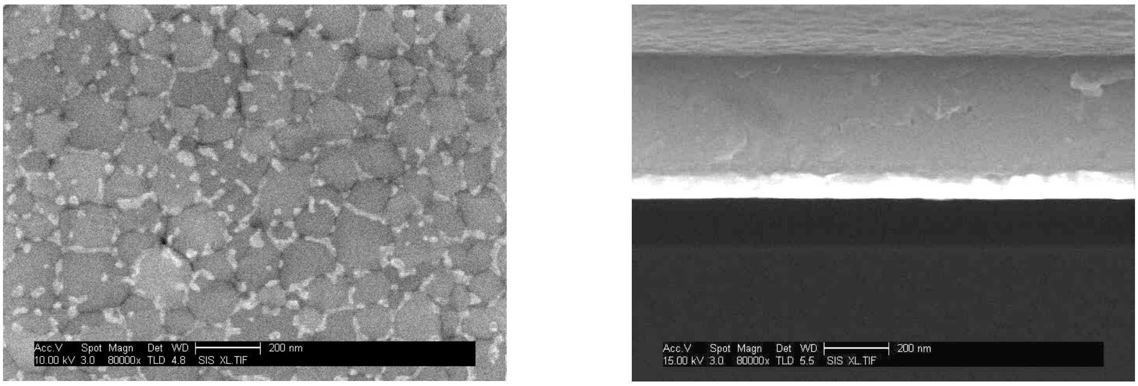

(a) (b)

Figure 8.7 SEM images of (a) the BZN thin film surface and (b) section of BZN film on Au (white layer) coated Si substrate.

Electrical measurement over the low frequency range up to 300 kHz were performed on the BZN dielectric films using the MIM structure with Pt/Ti and Au/Cr bottom electrodes (figure 8.8). It was expected that the dielectric properties of BZN grown on Au would be superior to the dielectric properties of BZN grown on Pt due to the increased conductivity of the Au over that of Pt. However, Au diffusion into the BZN film resulted in a decrease in dielectric constant accompanied by a significant increase in dielectric loss as can be seen in figure 8.8. The dielectric strength of BZN thin film on Pt and Au bottom electrode was 0.43 MV/cm and 1.07 MV/cm, respectively.

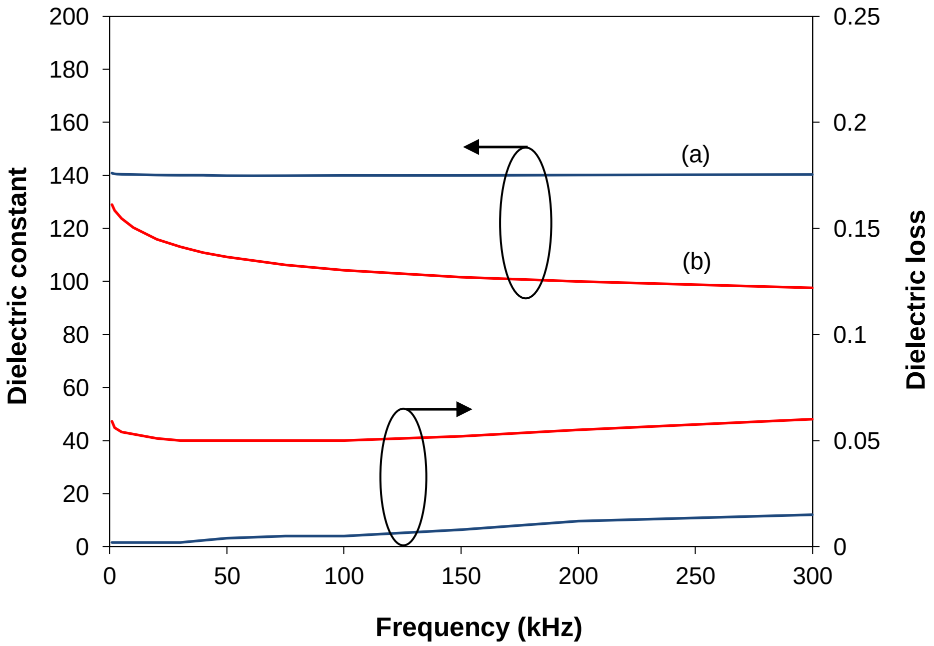

Figure 8.8 Variation in the dielectric constant and loss of BZN thin film grown on (a) Pt electrode and (b) Au electrode. Films annealed by RTA at 700^{o}C.

Due to issues with diffusion of Au/Cr into the BZN film after high temperature annealing and crystallisation, experiments were conducted at lower annealing temperatures in order to achieve material stability. XRD measurements of BZN thin film grown on Au coated silicon in the same sputtering run, and *ex situ* annealed by RTA at temperatures ranging from 250^{o}C to 500^{o}C, are presented in figure 8.9. The dominant crystallographic orientation was the (222) plane and the XRD peak could be seen to change with temperature. At the lowest temperature (250^{o}C) the peak was relatively broad indicating a small grain size. As the temperature was increased the peak became narrower which showed that the grain size was increasing. This variation in peak width could also be seen for the other crystallographic orientations of the polycrystalline BZN film. Full crystallisation occurred at or around a minimum annealing temperature of 250^{o}C since there was no crystallisation observed at 200^{o}C. It is interesting to note that a nanocrystalline structure to BZN existed when the material was first sputtered onto a substrate heated at 300^{o}C. However, when subsequently *ex situ* annealed by RTA at the lower temperature of 250^{o}C, the BZN film became fully crystallised. When annealed by hotplate this did not occur, as much higher temperatures of between 400°C and 500°C were required. The difference was in the method by which the sample was heated. In the case of RTA it was primarily radiant energy, whereas with hotplate annealing it was conducted energy through the substrate. Clearly RTA crystallised the BZN more efficiently.

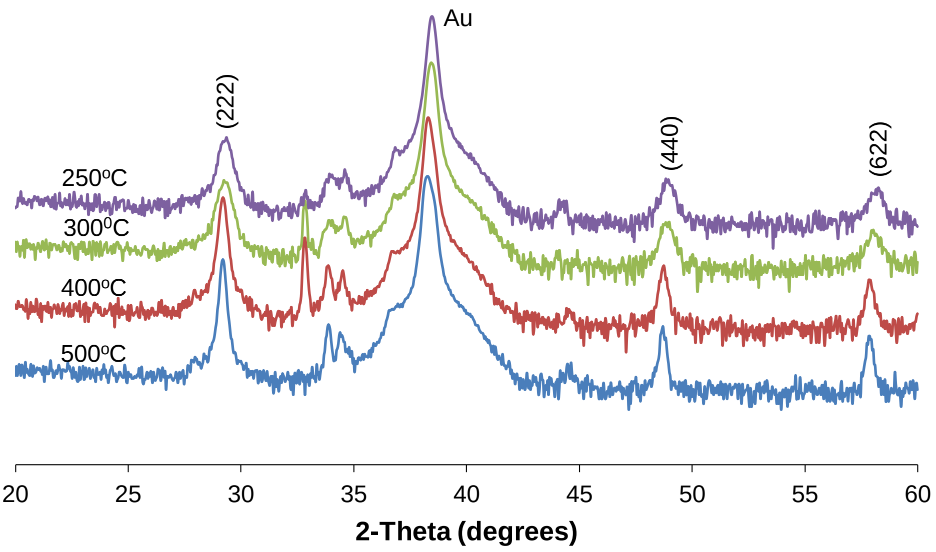

Figure 8.9 XRD diffractograms of BZN thin film on Au coated SiO_2/Si substrate after annealing by RTA at low temperature.

The effect of reducing the annealing temperature on the grain size can be seen in the SEM micrographs of figures 8.10-8.12, and complements the results of peak broadening shown in the XRD patterns of figure 8.9. Variation in the average grain size of BZN film with RTA temperature is shown in figure 8.13.

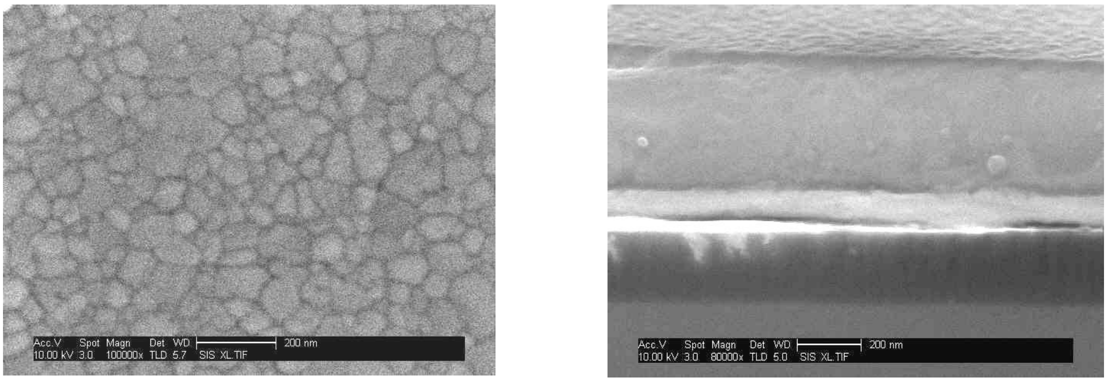

Figure 8.10 SEM images of the surface and section of BZN thin film on Au/Cr/SiO_2/Si substrate after annealing by RTA at 500°C for 3 minutes.

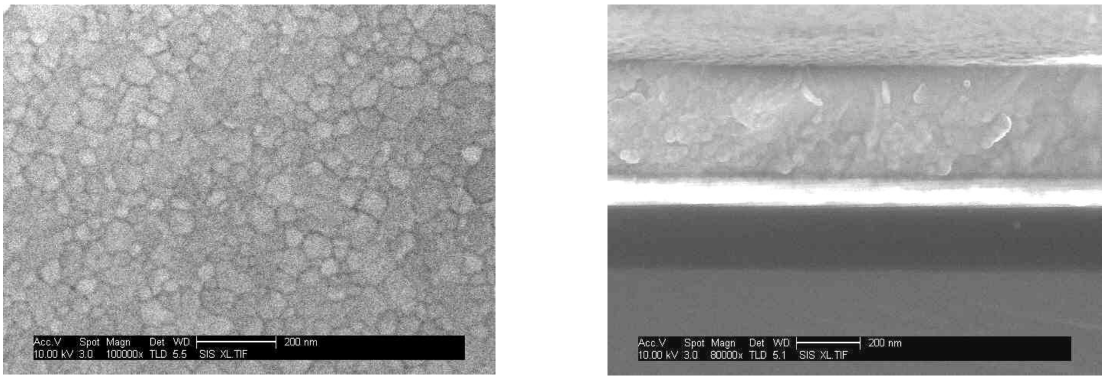

Figure 8.11 SEM images of the surface and section of BZN thin film on Au/Cr/SiO_2/Si substrate after annealing by RTA at 400°C for 3 minutes.

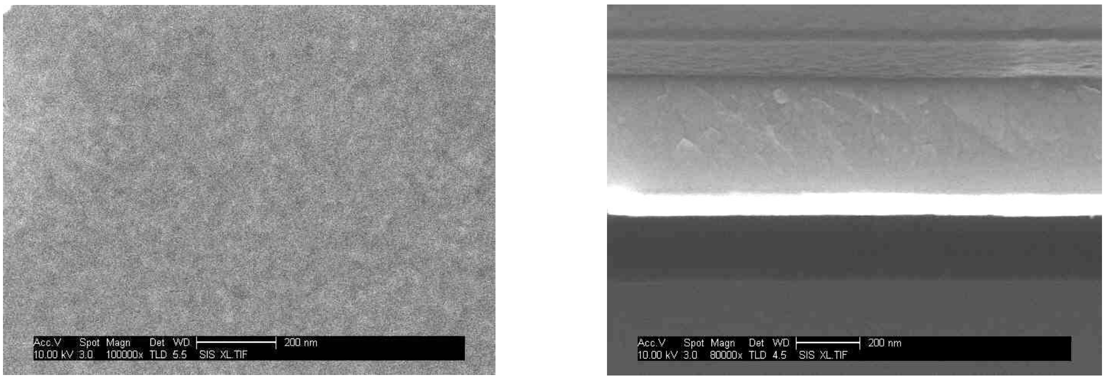

Figure 8.12 SEM images of the surface and section of BZN thin film on Au/Cr/SiO_2/Si substrate after annealing by RTA at 300°C for 3 minutes.

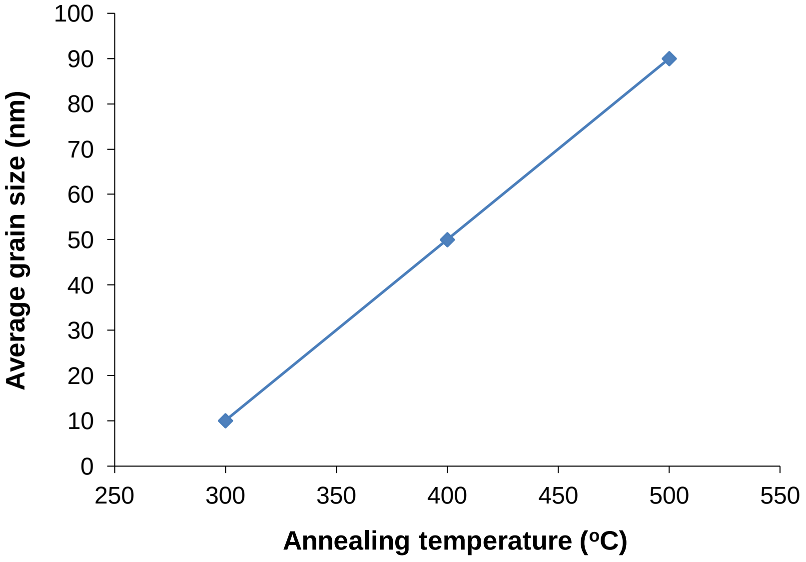

Figure 8.13 Average grain size as a function of RTA temperature for BZN film sputter deposited on Au coated silicon.

The relationship of average grain size with annealing temperature (figure 8.13) shows a general trend to larger grains with increasing temperature. However, the actual grain size for a given sample, particularly at the higher temperature, can vary quite significantly. For example, the variation in grain size for BZN film annealed by RTA at 500°C ranged from *circa* 30 nm to 150 nm, at 400°C the grain size ranged from 15 nm to 85 nm, and at 300°C was ~10 nm or less.

Dielectric properties measured at low frequency for BZN thin film on Au bottom electrode are displayed in figure 8.14. With the exception of BZN annealed at 400°C, the dielectric constant of BZN thin film on Au bottom electrode annealed by RTA at low temperature was ~80 and the dielectric loss close to 0.02 over the frequency range 1 kHz to 300 kHz.

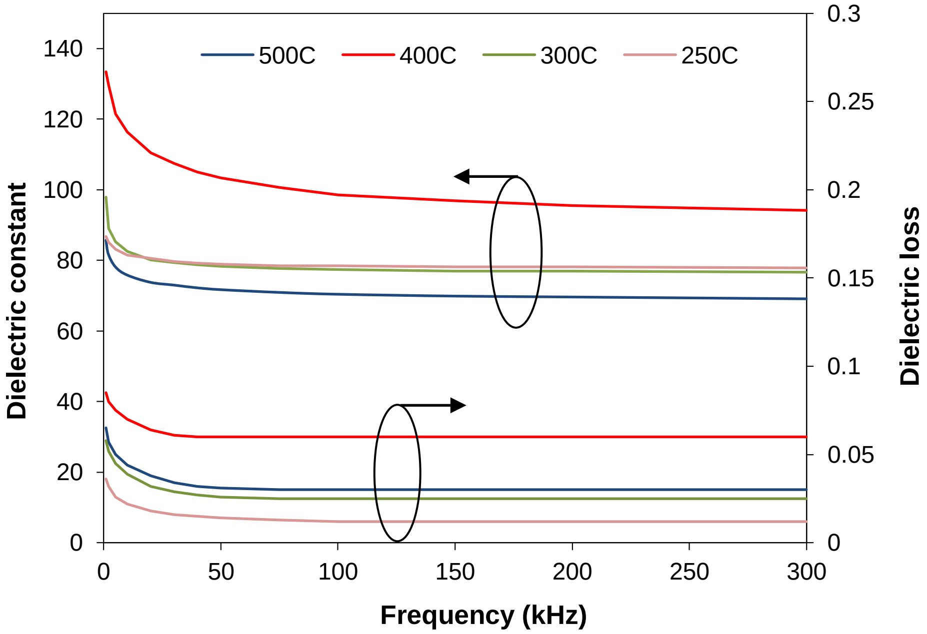

Figure 8.14 Dielectric constant and loss as a function of frequency for BZN thin film on Au/Cr bottom electrode at different BZN crystallisation temperatures.

There was little variation in the dielectric constant and loss over the frequency range 10 kHz to 300 kHz but an increase was seen at the low frequency end below 10 kHz. The dielectric strength of BZN on Au electrode was between 1.0 MV/cm and 2.0 MV/cm, much higher than that of BZN deposited on Pt electrode which had typical breakdown strength of between 0.4 MV/cm to 0.7 MV/cm. The higher breakdown strength of BZN when grown on Au bottom electrode was due to the higher conductivity, and hence lower contact resistance, of Au compared to Pt. Also, there was a difference in the microstructure of BZN film grown on Au compared to Pt which likely gave rise to the lower dielectric constant. It may have been possible that some Au/Cr diffusion into the BZN film was causing a thin layer of BZN at the interface with the bottom electrode to become conductive thus effectively reducing the dielectric thickness.

Having shown that low temperature annealing enabled BZN thin films to be successfully grown on Au(100nm)/Cr bottom electrode without diffusion of Au into the BZN film, three other electrode metals Au(800nm)/Cr, Au(100nm)/Ti and Pt(100nm)/Au(200nm)/Ti were trialled using a new, improved, low temperature annealing process involving both hotplate and RTA. Samples were annealed by initially heating on the hotplate gradually from room temperature to 350^{o}C according to the ramp profile shown in figure 4.10. The sample was held on the hotplate at 350^{o}C for 5 minutes before being transferred hot to the RTA furnace and further annealed at 300^{o}C for 3 minutes. XRD scans showed excellent crystallisation of BZN thin films on all electrode metals on silicon. The SEM micrographs of BZN film on Pt(100nm)/Au(200nm)/Ti bottom electrode display a nanocrystalline structure as can be seen in figure 8.15.

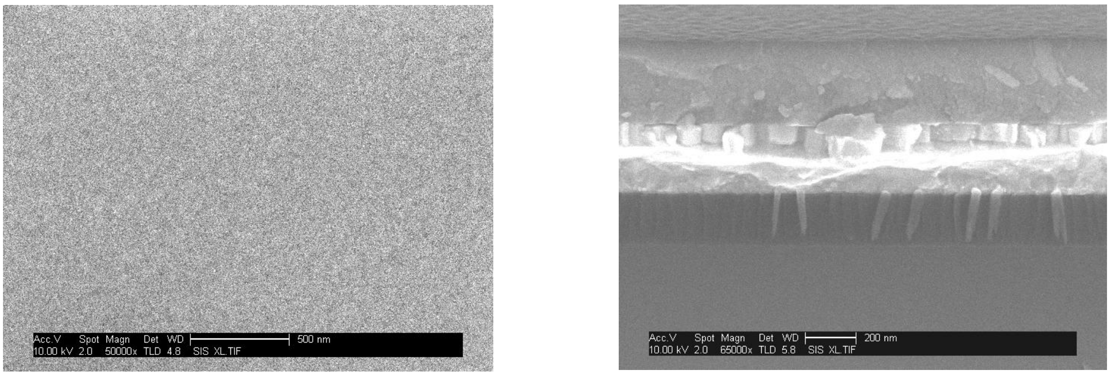

(a) (b)

Figure 8.15 SEM images of (a) surface and (b) section of BZN film on Pt/Au/Ti/SiO$_2$/Si substrate. The columnar structure of the 100 nm thick Pt layer can be seen between the BZN film and 200 nm thick Au layer. The dark band below the Pt/Au metal layer is the 200 nm thick SiO$_2$ buffer layer.

The microstructure of BZN film on Au(100nm)/Ti was very similar to that of BZN film on Pt/Au/Ti in figure 8.15. However, the microstructure of the 350 nm thick BZN film on thick (800 nm) Au was very different as can be seen in figure 8.16.

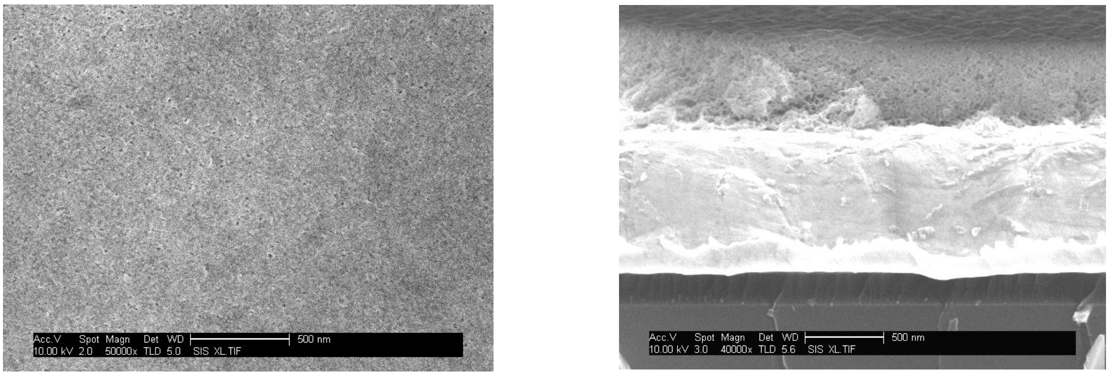

(a) (b)

Figure 8.16 SEM micrographs of (a) surface and (b) section of 350 nm thick BZN film on 800 nm thick Au bottom electrode (bright layer).

The microstructure of BZN film on thick (800 nm) Au is clearly nanoporous according to the surface and sectional SEM images in figure 8.16.

Low frequency electrical measurements were taken and the variation of dielectric constant and loss with frequency for BZN film grown on the different metal electrodes were compared (figure 8.17). The results in terms of the variation of dielectric constant and loss for BZN film on Au(100nm)/Cr electrode annealed using the new thermal process was very similar to that recorded in figure 8.14 for BZN film annealed by RTA at 300^{o}C, i.e. dielectric constant ~85 and loss 0.028. The thin BZN film on Au(800nm)/Cr electrode displayed a low dielectric constant (45) due to its nanoporous microstructure (figure 8.16); the dielectric loss was also very low (0.002). Thin-film BZN grown on Au(100nm)/Ti and Pt(100nm)/Au(200nm)/Ti electrodes showed the highest dielectric constant of 102 and very low loss of 0.005 and 0.0015, respectively. The low measured values of dielectric loss relate to the sheet resistance measurements recorded as a function of RTA temperature for the various metal layers as shown in figure 7.9. At an RTA temperature of 300^{o}C the metal layers with the lowest sheet resistance (starting with the lowest) were Au(800nm)/Cr, Pt/Au/Ti, Au/Ti and Au(100nm)/Cr. To optimise the dielectric properties of thin-film BZN the ideal choice of bottom electrode out of those trialled was either Au/Ti or Pt/Au/Ti. BZN grown on these metal layers produced the highest dielectric constant, low dielectric loss and high breakdown strength (1.25 MV/cm for BZN grown on Au/Ti and 1.95 MV/cm for BZN film on Pt/Au/Ti).

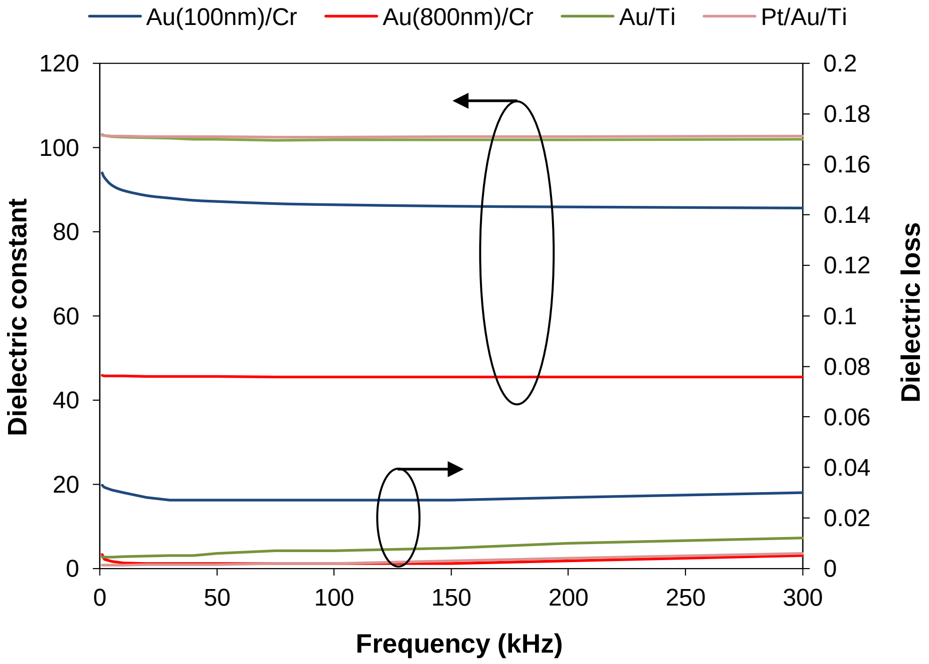

Figure 8.17 Dielectric properties as a function of frequency to 300 kHz for BZN thin films on various bottom metal electrodes annealed by RTA at 300°C.

As a starting point, the dielectric properties of BZN thin films grown on various metal electrodes on silicon have been well characterised in this section. The intention was to use BZN as the dielectric in the zipping varactor, but fabricated on Au coated glass substrate rather than silicon. This will be discussed in the following sub-section.

8.4.2 BZN Thin Film Growth Trials on Au Coated Fused Silica and 100 mm Diameter Device Quality Glass Substrates

Based on the results of BZN thin film grown on Au(800nm)/Cr/SiO_2/Si substrate which demonstrated the lowest dielectric loss, and the fact that the contact or series resistance for this metal layer was particularly low (<1 Ω), it was decided to use the thick Au layer on fused silica substrate to grow BZN. Samples were initially prepared on 30 mm diameter, 0.5 mm thick, circular fused silica substrates. Half of the glass circular substrate was sputter deposited with 10 nm of Cr and 800 nm of Au. A 350 nm thick BZN film was then sputter deposited onto the Au coated and bare glass areas of the substrate at an RF power of 400 W, gas pressure 40 mTorr, Ar/O_2 gas ratio 85/15 and *in situ* substrate temperature 300^{o}C. After sputtering, the substrates were cleaved into two equally sized pieces for annealing trials. XRD analysis showed that BZN thin film on Au coated fused silica crystallised at higher temperatures compared to films grown on Au coated silicon. For instance, when using RTA, the lowest crystallisation temperature for BZN film on Au coated glass substrate was 350^{o}C compared to 250^{o}C on silicon. A similar difference was observed for BZN film on Au coated glass and silicon when annealed by hotplate, but at a higher temperature of 550^{o}C and 450^{o}C, respectively. This was due to the difference in thermal conductivity of the glass and silicon substrates.

The microstructure of the thin BZN film (~350 nm) grown on thick (800 nm) Au bottom electrode on fused silica substrate is shown in figure 8.18. As can be seen in figure 8.18b the microstructure of the BZN layer is granular and mimics the granular structure of the thick Au layer.

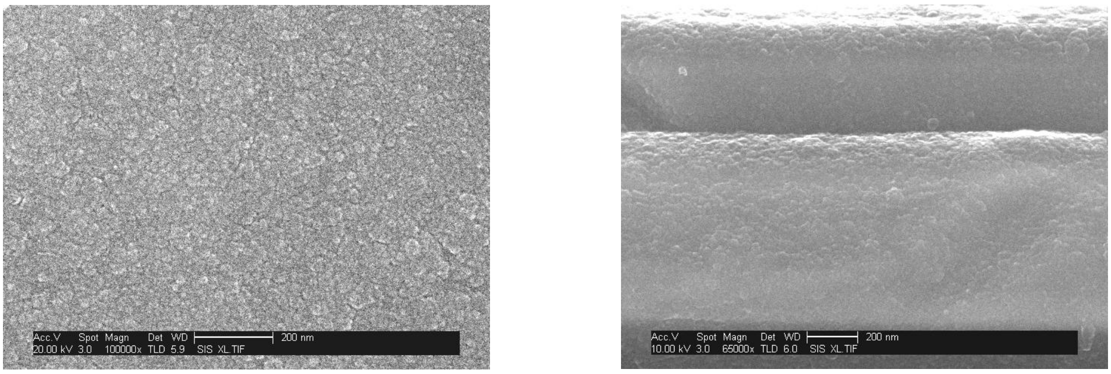

(a) (b)

Figure 8.18 SEM images of the (a) surface and (b) section of BZN thin film on 800 nm thick Au bottom electrode on fused silica substrate after annealing by RTA at 400^{o}C.

The 350 nm thick BZN film appears dense with no visible defects (pinholes and hillocks). The surface roughness was 4.9 nm as measured on the Dektak profilometer. Electrical measurements on the BZN thin film over the low frequency range 1 kHz to 300 kHz gave a value for the dielectric constant of 100 and dielectric loss of 0.01. However, the breakdown strength of BZN film on thick Au and fused silica substrate was very low, only 0.4 MV/cm.

Further trials were conducted on 100 mm diameter glass wafers of the type that will be used in the fabrication of real devices. A thick Au(800nm)/Cr layer was sputter deposited on the glass. Over the Au a *circa* 350 nm BZN film was sputter deposited and *ex situ* annealed by RTA at 400^{o}C. Visual inspection of the wafer after annealing showed micro-cracking and blistering of the BZN film as seen in the optical images of figure 8.19. Micro-cracking was observed at the centre of the glass wafer and blistering toward the edge of the wafer.

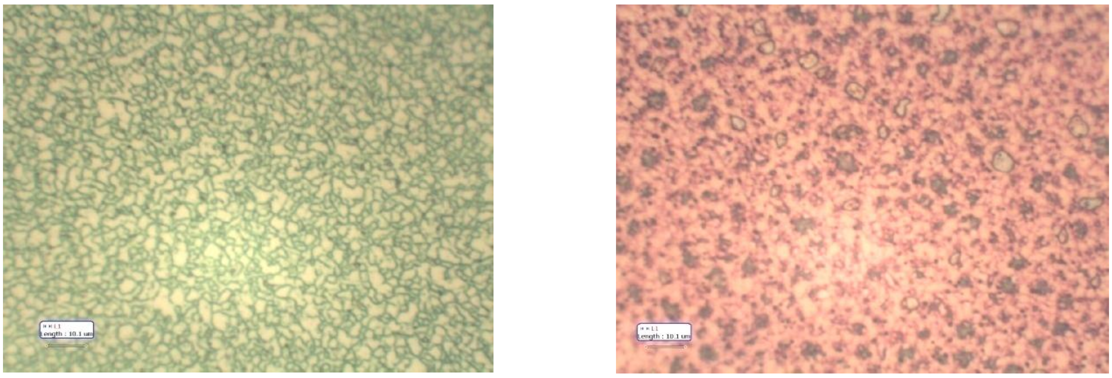
(a) Dimension bar 10 µm.

(b) Dimension bar 10 µm.

Figure 8.19 Optical images at 50x magnification showing (a) micro-cracking and (b) blistering of BZN thin film on thick Au coated 100 mm diameter glass wafer.

Surface roughness of the BZN film as measured by Dektak was 16.2 nm. The cracking and blistering of the BZN film was due to stress developed in the film by the thick (800 nm) Au layer over the large wafer area. The BZN film was electrically probed and found to be conductive indicating metal diffusion through the BZN. EDX analysis showed this to be primarily Cr and not Au. This was substantiated by observing the underside of the glass wafer. The silver Cr layer was visible before processing but not after, only the yellow Au layer was visible.

In order to lower the stress in the BZN film, the Au thickness was reduced to 400 nm. However, after sputtering the BZN at an *in situ* wafer temperature of

300^{o}C the BZN film appeared cloudy due to increased surface roughness. The BZN film was again electrically probed and found to be conductive due to metal (likely Cr) diffusion. The experiment was repeated with only 100 nm of Au but proved unsuccessful. After sputtering the BZN film, the surface appeared cloudy and was conductive indicating diffusion of mainly Cr. It was not possible to successfully grow a thin BZN film on Au/Cr electrode over a 100 mm glass wafer, whereas, it had been possible to grow BZN on smaller Au/Cr coated fused silica and silicon wafer pieces. Alternative electrode metal combinations must be used that do not have Au as the top layer onto which the BZN is grown.

8.4.3 BZN Thin Film Growth on 100 mm Glass Device Wafers

Due to the problems associated with growing BZN directly on Au coated glass substrate, together with the issue of Au/Cr diffusion, the bottom electrode metallisation used in the two device wafers were sputtered Pt(100nm)/Ti and Pt(100nm)/Au(200nm)/Ti. BZN thin films 350 nm thick were deposited by RF magnetron sputtering using the same sputtering parameters as previously (RF power 400 W, working gas pressure 40 mTorr, Ar/O_2 gas ratio 85/15, *in situ* substrate temperature 300^{o}C and sputtering duration 100 minutes). Deposited bottom electrode metal layers and BZN film covered entirely one side of the 100 mm wafer. The BZN film was then *ex situ* annealed and crystallised using an improved heat treatment procedure based on sound experimental evidence.

Trial experiments were conducted using the new, improved, low temperature annealing process as first described in sub-section 8.4.1. This involved using both hotplate and RTA. Samples were annealed by initially heating on the hotplate gradually from room temperature to 350^{o}C according to the ramp profile shown in figure 4.10. The sample was then held at 350^{o}C for 5 minutes before being transferred hot to the RTA furnace and further annealed at 350^{o}C for 3 minutes. By avoiding a sudden temperature rise (thermal shock) the stress in the film was reduced. However, the effectiveness of heating by radiant energy rather than by conductive was maintained. After a number of trials, the new annealing procedure was ready for use on device wafers.

The crystallisation of BZN thin film for the two device wafers was verified using XRD. The XRD scans of the polycrystalline films are displayed in figure 8.20. As for previously sputtered BZN films, the dominant crystallographic peak is at (222). The fairly broad peak is indicative of a small grain size which is characteristic of BZN thin film annealed by RTA at a low temperature of 350^{o}C.

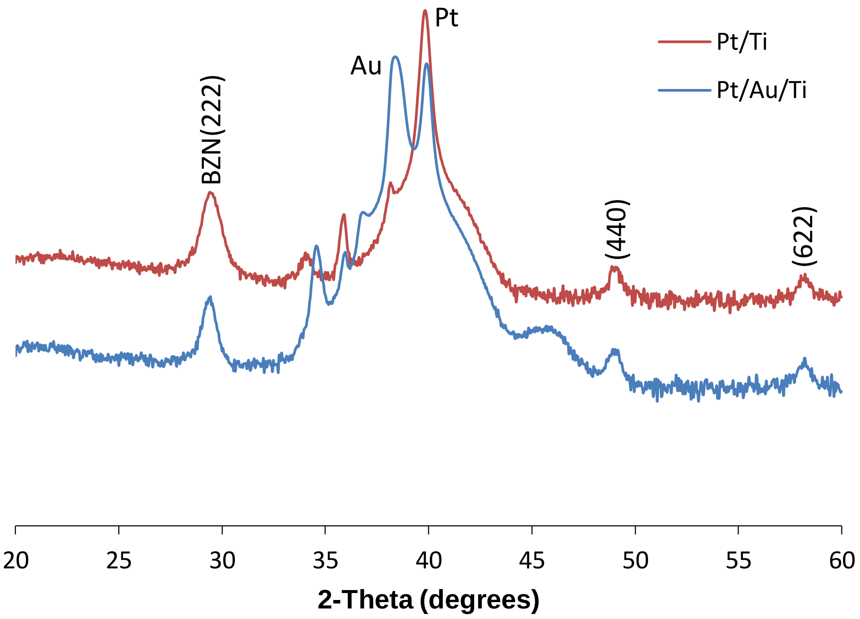

Figure 8.20 XRD scans of crystallised BZN thin films deposited on 100 mm diameter glass device wafers with Pt/Ti and Pt/Au/Ti bottom electrodes.

The BZN films covering one side of each of the two device wafers appeared smooth and defect free. A colour change (broad concentric rings) across the wafer indicated a gradual variation in the BZN thickness, decreasing from centre to edge. Experiments that looked at the variation in BZN thickness for material sputter deposited over a 100 mm diameter silicon wafer, and for different oscillation conditions, were discussed in sub-section 4.3.4. This gradual change in the BZN thickness over the wafer enabled the fabrication and testing of zipping devices that support a range of dielectric thicknesses. No further analysis was performed on the BZN to avoid any contamination of the film or damage to the wafer.

8.4.4 Reactive Ion Etching of Thin-Film BZN

The reactive ion etching (RIE) of thin-film BZN was performed using CHF_3/Ar, and the etch rate as a function of RF power and CHF_3 to Ar gas ratio measured. Nickel was used as a hard mask when dry etching BZN on device wafers. Since there were sputtered BZN thickness non-uniformity issues over the area of the wafer, it was important to have good etching selectivity between BZN film and the Au and Pt in the bottom electrode. Etch rate trials were performed on relatively small samples (2 cm^2) using a demarcation created by the painting on of S1818 photoresist and then cured on the hotplate at 115°C for 5 minutes. Samples of BZN, Au and Pt layers on silicon and glass substrates were prepared. Using this approach, many quick trials could be performed. Results that show the variation in etching rate of BZN, Au and Pt with RF power over the range 50 W to 200 W using a CHF_3/Ar gas mixture are displayed in figure 8.21. Other fixed process parameters were: CHF_3/Ar gas ratio and flowrates of 10/13 sccm (i.e. 56.5% Ar), and gas pressure 30 mTorr. Linear trendlines have been drawn through the data points for ease of comparison.

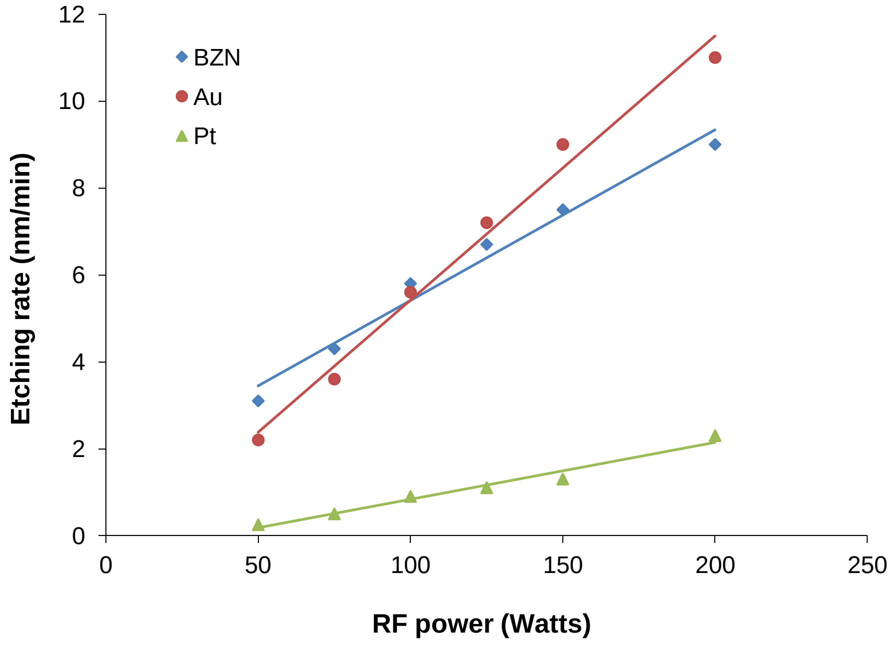

Figure 8.21 Etching rates of BZN, Au and Pt layers as a function of RF power in CHF_3/Ar plasma.

Excellent selectivity of BZN over Pt has been demonstrated, with the etch rate of BZN being typically 6 times that of Pt at 100 W (figure 8.21). The etching selectivity of BZN over Au was not so impressive due to the higher sputter yield of Au compared to Pt. At close to 100 W RF power the etch rate of BZN and Au was the same. To achieve increased selectivity of BZN to Au, a power below 100 W must be used, e.g. at 50 W the BZN etch rate was 1.5 times faster than that of Au. However, the etch rate of BZN at 50 W (~3.0 nm/min) was somewhat reduced compared to the etch rate at 100 W (~6 nm/min).

The selectivity could also be improved by changing the CHF_3/Ar gas ratio. A graph of the etch rate of BZN, Au and Pt as a function of Ar% in CHF_3/Ar at 100 W RF power and 30 mTorr gas pressure is presented in figure 8.22. Unlike the approximated linear variation of etch rate with power (figure 8.21), the variation of etch rate with gas ratio for the three materials is clearly nonlinear.

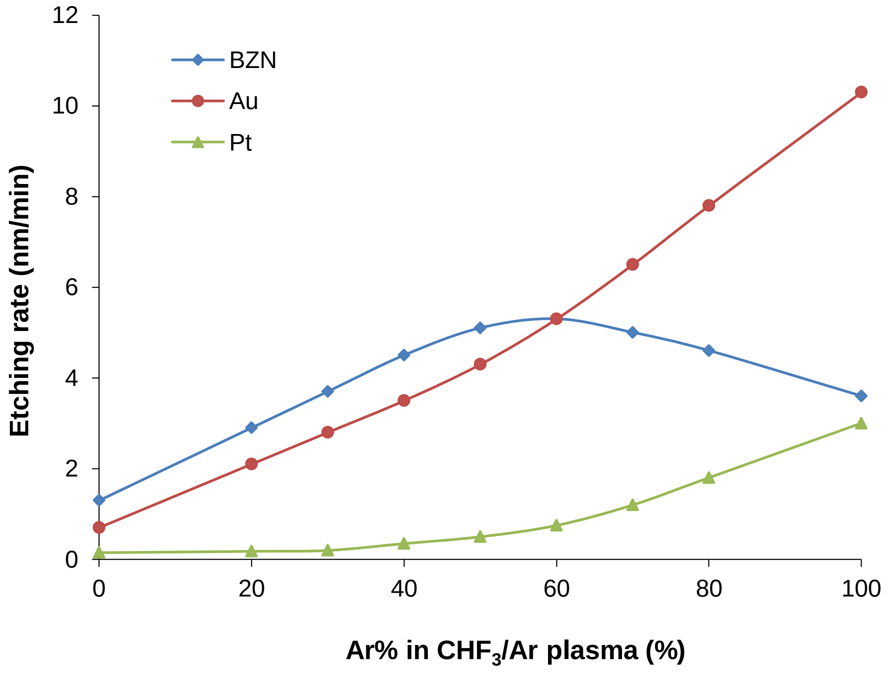

Figure 8.22 Etching rates of BZN, Au and Pt layers as a function CHF_3/Ar gas ratio at a fixed power of 100 W and gas pressure 30 mTorr.

The graph in figure 8.22 shows the effect on etch rate of using different RIE plasmas ranging from pure CHF_3 (0% Ar) through CHF_3/Ar (50% Ar) to pure Ar

(100% Ar). As can be seen from the results, there was a physical component (sputter yield) and a chemical component (cracking of CHF_3 in the plasma to produce reactive species) to the etching. Layers of Au and Pt were etched solely by the physical mechanism of sputtering as evidenced by the etch rate continuing to rise with increasing Ar content in the plasma gas. BZN was etched by a combination of physical sputtering and chemical erosion (i.e. by reaction with the free fluorine in the dissociation of CHF_3). The chemical etching was enhanced by ion bombardment of the reacting surface. This is characterised in figure 8.22 by the BZN curve which shows the etch rate rising to a peak of 5.3 nm/min at ~60% Ar and then reducing to 3.6 nm/min at 100% Ar. In a purely CHF_3 plasma there was a small amount of etching of Au and Pt which was due to sputtering alone. Although the sputter yield of BZN is lower than that of Au, the etch rate of BZN in CHF_3 was higher because of the additional chemical component of etching. As the proportion of Ar in the CHF_3/Ar plasma was increased beyond 50% there was a sharp increase in the etch rate of Au and Pt. This was due to reduced CHF_3 present in the plasma resulting in fewer collisions with Ar^+ ions primarily responsible for the sputtering action.

It has been observed that the etch rate of BZN decreases as the area of BZN exposed to the plasma is increased, referred to as the “loading effect”. Hence, the transition from small (~2 cm^2) samples to the 100 mm glass wafers resulted in a reduction in etching rate of BZN by as much as 50% due mainly to the loading effect. This loading effect can significantly reduce not only the etch rate but also the etch rate uniformity. Suggestions for improvement to the etching rate, based on information in the literature review in section 3.12, include the introduction of chlorine containing gases as well as fluorine (eg. CCl_2F_2).

The etch rate data presented in this section has been used to successfully etch BZN thin film, Pt/Ti and Pt/Au/Ti bottom electrode layers on the two glass device wafers. Modest etch rates and good selectivity over Pt was achieved for BZN using CHF_3/Ar RIE. This completed the fabrication of high permittivity dielectric and bottom electrode assembly on 100 mm diameter glass substrate as shown in figure 8.23.

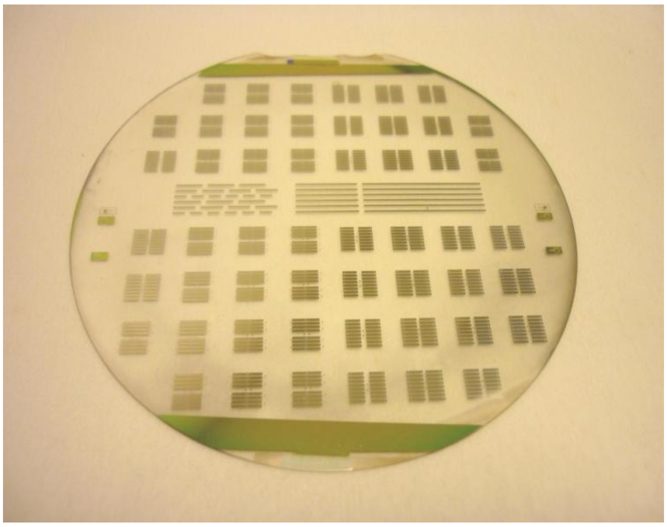

Figure 8.23 Glass wafer supporting arrays of dielectric (BZN) and bottom electrode metallisation with some test structures in the centre.

A single array of eight combined dielectric and bottom electrode structures is shown in figure 8.24.

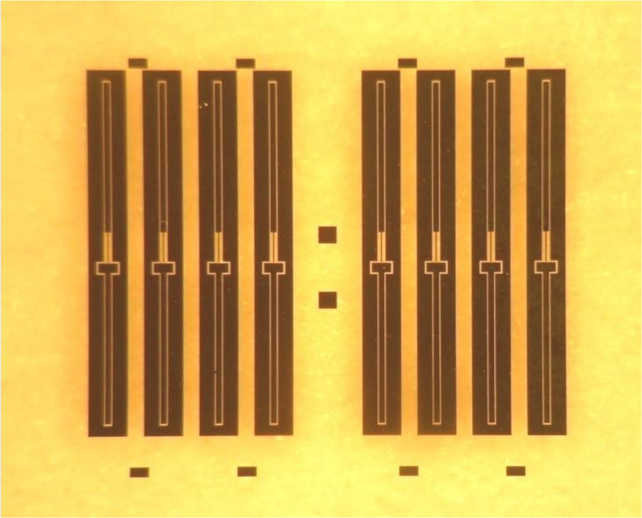

Figure 8.24 Array of structures incorporating high-k dielectric (BZN) and bottom electrode metallisation (dark regions).

The fabrication, alignment and bonding of the curved top electrode were carried out by the research team at Imperial College London. The testing of assembled devices will also be undertaken at Imperial when the manpower is available. As a consequence, there is no test data currently available on the assembled zipping varactor with BZN high-k dielectric thin film, or PZT for comparison.

8.5 Summary of Main Features and Achievements

The fabrication of bottom electrode and dielectric layer for the zipping varactor has been detailed including, material deposition by sputtering, patterning of dielectric film and metal electrode using photolithography, soft and hard masking, and wet and dry etching.

The preferred metallisation for bottom electrode was Au/Cr due to its low series resistance and based on experimental evidence using small sample pieces. For example, the deposition and crystallisation of BZN thin film on thick (800 nm) Au coated silicon and fused silica was successful for small sample pieces provided the RTA temperature was kept low (300°C-400°C). However, due to processing issues with BZN on Au/Cr when scaled to device wafer size, Pt/Ti and Pt/Au/Ti were chosen for the bottom electrode metallisation thus avoiding an interface between Au and the BZN film. Growth of 300 nm thick BZN film on Pt/Au/Ti/SiO_2/Si substrate resulted in a dielectric constant of 100, very low dielectric loss of 0.0015 and high breakdown strength of 1.95 MV/cm.

Growth and crystallisation of BZN thin film on Pt/Ti and Pt/Au/Ti bottom electrode on 100 mm diameter glass device wafer was not without issues. In order to grow and crystallise a defect free BZN film a new improved heat treatment regime was devised and trialled. It involved slowly heating the wafer on a hotplate from room temperature to 350°C, then swiftly transferring the wafer hot to the RTA furnace and crystallisation annealing at the extremely low temperature of 350°C. This heat treatment process when used on the sputtered BZN thin films eliminated the blistering and pinhole formation usually associated with compressive stress and is viewed as an important achievement.

A further noteworthy achievement was the dry etching of thin-film BZN using fluorine chemistry not previously reported elsewhere. The reactive ion etching of BZN and metal layers was performed using CHF_3/Ar and Ar, respectively. At an RF power of 100 W the etching rate of the BZN thin film was ~6 nm/min, with excellent selectivity over Pt, typically 6:1. The BZN dielectric film and Pt/Ti and Pt/Au/Ti electrodes were successfully patterned on the two glass device wafers.

9 Conclusions and Future Work

9.1 Conclusions

The work detailed in this thesis focuses on the successful development of barium zirconate titanate (BZT) and bismuth zinc niobate (BZN) as dielectric thin film materials for application to fixed value, voltage tunable and zipping variable capacitors. Significant improvement in the dielectric properties of these materials were achieved as a result of some novel experimental processes devised. BZT and BZN thin films have been integrated into planar devices using established growth and fabrication techniques. Experimental rigour enabled each of the primary research objectives listed in section 2.2 to be met.

Some problems were encountered with blistering and pinhole formation in BZN films due to compressive stress when crystallised using RTA at higher temperatures (>500^{o}C). The defect density in the films was dramatically reduced by using hotplate annealing followed immediately by RTA. The annealing process was refined by heating the material firstly on the hotplate, then transferring the sample to the RTA furnace whilst hot and immediately annealing at the higher temperature. This avoided undue thermal shock of the dielectric film yet achieved good crystallisation of the material. The improved thermal treatment procedure also allowed the crystallisation temperature to be kept much lower, down to 300^{o}C.

It has been shown that fixed value MIM capacitors with low dielectric constant (2 to 15) and high breakdown strength (~1.3 MV/cm) can be fabricated using amorphous BZT deposited by the sol-gel method on Au coated silicon. The ultra-low permittivity was achieved by the introduction of porosity into the film when pyrolysed, after spin-coating the BZT sol at a reduced speed (2500 rpm).

Control of the microstructure and dielectric constant of thin-film BZN was achieved using the two-step sputtering deposition method. By growing a second BZN film on a pre-crystallised BZN layer annealed by RTA it was possible to introduce porosity into the second film. By increasing the thickness of the second grown film relative to the first film deposited, the dielectric constant of the composite structure was reduced from 170 to 70. For all films measured, the dielectric loss was at or below 0.005.

Fixed value capacitors fabricated with dense amorphous or nanocrystalline BZN dielectric layers deposited by RF magnetron sputtering were found to have a dielectric constant of ~50 with a reduced dielectric strength of 0.35 MV/cm. It was possible to increase the dielectric strength to 0.56 MV/cm by growing the BZN film on a thin (50 nm) BZT seed layer which produced a columnar, as opposed to a granular, microstructure.

The very low temperature of crystallisation (down to 250^{o}C) of thin-film BZN has had positive implications for growth and crystallisation of BZN on low melting point (~320^{o}C) polymer substrates such as LCP. Trial experiments have been already conducted with BZN thin-film MIM capacitors on polymer substrate, and reported on in sub-section 6.3.5. They have demonstrated that low loss (0.005) dielectric films can be deposited on Au coated LCP.

For tunable capacitor applications experiments were conducted using three $Ba(Zr_xTi_{1-x})O_3$ compositions, x=0.05, 0.20 and 0.35, that have some interesting and varied properties. At a zirconium content of 0.05 the material is ferroelectric at room temperature and so was characterised by high tunability (80%) due to the spontaneous polarisation. At a zirconium content of x=0.20 a morphotropic phase boundary (MPB) between the tetragonal, orthorhombic and rhombohedral ferroelectric phases and the paraelectric phase exists at or around room temperature. For BZT composition where the zirconium content is x=0.35 the BZT thin film material is paraelectric at room temperature. This was of particular interest since in the paraelectric state the material has lower dielectric loss due to the disappearance of ferroelectric hysteresis. However, the tunability of the material in the paraelectric phase was somewhat reduced, only 60% compared to 80% achieved for material of ferroelectric composition. The approach devised to increase the tunability while maintaining the dielectric loss low was to grow the BZT on Au bottom electrode using a BZN buffer layer inserted between electrode and dielectric film. This was a novel approach that worked very successfully, producing peak tunability in the paraelectric BZT film of 82% at an applied field of 1.25 MV/cm and measurement frequency 300 kHz. A similarly high tunability (83%) at a bias field of only 600 kV/cm (measurement frequency 300 kHz) was achieved for a multilayer BZT thin film structure that incorporated alternate ferroelectric and paraelectric single layers of composition $Ba(Zr_{0.05}Ti_{0.95})O_3$ and $Ba(Zr_{0.35}Ti_{0.65})O_3$, respectively. The resultant multilayer BZT film displayed ferroelectric properties (P-E loop hysteresis) despite being 50% composed of paraelectric material. The remnant polarisation and coercive electric field obtained for poled thin film material was 0.52 $\mu C/cm^2$ and 39.3 kV/cm, respectively.

Significant progress was made in developing a high-k dielectric material suitable for the zipping variable capacitor. The integration of BZN dielectric thin films into the zipping varactor has been demonstrated. Dielectric constant of 100 and loss of 0.0015 were achieved for BZN thin film grown on Pt/Au/Ti bottom electrode at a measurement frequency of 100 kHz. Since activation voltages for the zipping device can be quite high (~60 V), a thin film material with a high dielectric strength was sought. BZN appeared to be an appropriate choice since a breakdown strength of ~2.0 MV/cm was recorded for BZN thin film on Pt/Au/Ti when crystallised at 350^oC using the improved annealing procedure described in sub-sections 8.4.1 and 8.4.3. The small feature sizes (10 µm x 200 µm) associated with the zipping device were successfully dry etched into BZN dielectric thin film for the first time by reactive ion etching (RIE) using a CHF_3/Ar plasma. At the chosen power level of 100 W, the BZN thin film etching rate was ~6 nm/min with excellent selectivity of 6:1 over the underlying Pt layer. BZN thickness variations across the device wafers meant that zipping varactors with a range of dielectric film thicknesses could be fabricated and tested. The zipping varactor with high permittivity dielectric layer such as thin-film BZN can result in a device with large tuning range and reduced size. A suitable application for the zipping varactor is in mobile handset devices, e.g. for tunable RF mobile antennas, such as the varactor tuned antenna for Digital Video Broadcast to a Handheld (DVB-H) application designed to operate primarily in the usable UHF-band (470 MHz to 862 MHz, or a portion of it).

9.2 Future Work

Within the framework of this thesis it has not been possible to include all of the background research that is necessary for a fully comprehensive treatment of the subject. There is clearly a call for more research. Several suggestions contained in this section relate to further work on the processing and characterisation of BZT and BZN and to finding additional materials that can be used in fixed value, tunable and zipping variable capacitors.

To extend the research on BZT thin-film capacitors the dielectric properties of sputtered BZT material should be compared to that of sol-gel derived BZT thin films for each of the three compositions studied (i.e. Zr/Ti ratios 5/95, 20/80 and 35/65). Similarly for BZN the dielectric properties of sol-gel prepared films can be compared with those obtained for sputtered material. For example, by employing sol-gel grown BZN films subtle compositional changes to the starting materials could be performed. Du *et al*. found that a compositional change to BZN through the substitution of strontium (Sr) significantly affected the dielectric properties of bulk ceramic [3.46]. In bulk ceramic form Sr^{2+} ions substituted for Zn^{2+} ions at the A site in $(Bi_{1.5}Zn_{0.5})(Zn_{0.5}Nb_{1.5})O_7$ crystal lattice resulted in an increase in relative permittivity without significantly affecting the dielectric loss. The temperature coefficient of the dielectric constant (in ppm/^{o}C) was reported to increase substantially from -515 to +515 at 85^{o}C for the composition $(Bi_{1.5}Zn_{0.5-x}Sr_x)(Zn_{0.5}Nb_{1.5})O_7$ where x=0 to 0.5. In addition to Sr-doped BZN, other substitutions in bulk ceramic form that have not been demonstrated in thin film form include, for example, that of Ti substituted on the B site of BZN [3.45].

The future work programme should include research into other dielectric materials that complements the work on BZT thin films and that are suitable for fabricating fixed value and tunable capacitors. These could include, for example, thin-film calcium titanate ($CaTiO_3$) and magnesium titanate ($MgTiO_3$) [9.1, 9.2]. Experiments to deposit thin films of $CaTiO_3$ on Pt and Au coated silicon by RF magnetron sputtering were undertaken and some preliminary results obtained. The dielectric constant was typically 160, dielectric loss 0.002

and dielectric strength 2 MV/cm measured at 100 kHz. The dielectric properties of thin-film $CaTiO_3$ are similar to those of bulk $CaTiO_3$. The temperature coefficients of the dielectric constants of thin-film $CaTiO_3$ and $MgTiO_3$ are about -1340 ppm/^oC and +260 ppm/^oC, respectively. Hence, magnesium calcium titanate [$(Mg_xCa_{1-x})TiO_3$] films with controlled Mg and Ca ratio [9.3], and multilayered thin films of $MgTiO_3/CaTiO_3$ (MT/CT) [9.4], could conceivably be used to control the dielectric constant and the temperature coefficient of dielectric constant more precisely resulting in improved temperature stability. The further possibility of looking at composite structures such as BZT/CT and BZT/MT is founded on work done by Gao *et al.* on $Ba(Zr_{0.2}Ti_{0.8})O_3/MgTiO_3$ (BZT/MT) heterostructured thin films prepared by sol-gel [1.28].

Composite BST/BZT and BST/BZN multilayer thin films with significantly improved dielectric properties over that of thin-film BST have been demonstrated by other researchers [1.29-1.32]. This provides the impetus to develop new BZT/BZN multilayer thin-film capacitors which may have improved electrical performance compared to BZT and BZN thin-film capacitors.

Another ferroelectric material that has been little researched but is a promising candidate as dielectric film in the tunable capacitor is barium strontium zirconate titanate (BSZT) [9.5-9.8]. The substitution of Ba^{2+} ions by Sr^{2+} ions in the A site of $BaTiO_3$ to form $(Ba_xSr_{1-x})TiO_3$ (BST) has been widely studied and well documented. The substitution of Ti^{4+} ions by Zr^{4+} ions in the B site of $BaTiO_3$ to form $Ba(Zr_xTi_{1-x})O_3$ is one of the main materials studied as part of this thesis and has highlighted some interesting properties, with some advantages over BST. Both BST and BZT have well characterised ferroelectric to relaxor behaviour. By adjusting the cation ratios at the A and B sites of the ABO_3 perovskite structure, the benefits of the two systems can be combined. Similar ferroelectric to relaxor behaviour is evidenced when both A and B sites are substituted, as in the case of barium strontium zirconate titanate [$(Ba,Sr)(Zr,Ti)O_3$] (BSZT) thin films and bulk ceramic material. The sol-gel method can be used to deposit BSZT thin films. Sols are synthesised using barium acetate [$Ba(CH_3COO)_2$], strontium acetate [$Sr(CH_3COO)_2$], zirconium isopropoxide [$Zr(OC_3H_7)_4$] and titanium isopropoxide [$Ti(OC_3H_7)_4$] [9.5]. Typical room temperature dielectric constant of ~420 and dielectric loss ~0.02 can be realised for BSZT thin films grown by sol-gel. The high dielectric constant of this material makes it an ideal alternative candidate for dielectric thin film in the zipping varactor.

When depositing thin dielectric films on Pt/Ti bottom electrode at elevated temperatures (>600^{o}C) Ti diffusion into the Pt along Pt grain boundaries can result in hillock formation causing electrical breakdown of the dielectric. This can be resolved by oxidising the Ti layer prior to depositing the Pt. A further investigation should therefore be undertaken to look at the effect that a TiO_2 layer has on the adhesion and resistivity of the Pt, and how this impacts on the MIM tunable capacitor performance using BZT and BZN dielectric thin films. Due to issues with diffusion of Pt/Ti and Au/Cr from the bottom electrode into the dielectric layer during thermal processing, XPS analysis could be used to profile the extent of the diffusion. In the case of the voltage tunable capacitor, the interfaces between BZT thin film, BZN buffer layer and Au/Cr electrode should be examined thoroughly.

Although evaporated Au/Cr was routinely used for the top electrode in the MIM configuration in this work, experiments should be conducted to trial and compare sputtered Au/Cr, Au/Ti and Pt/Ti top electrodes. The top electrodes could also be more accurately defined using photolithography with a lift-off or etching process rather than employing a shadow masking technique.

Premature electrical breakdown within dielectric films can affect the quality and reliability of thin-film capacitors. The breakdown condition is reached when a conducting path is created from one electrode/dielectric interface to the other. Reliability properties of MIM (and MFM) thin-film capacitor structures and the mechanisms that cause capacitor failure can be investigated by performing time dependent dielectric breakdown (TDDB) tests on BZT and BZN dielectrics. This involves the statistical analysis of dielectric strength. Weibull distributions are used to describe the statistical properties of dielectric breakdown in capacitors and other devices (e.g. gate dielectric in MOSFET).

The work of growing thin BZT films on Au coated silicon substrates using a BZN buffer layer inserted between BZT film and Au electrode resulted in improved dielectric properties compared to BZT films deposited on platinised silicon. However, an understanding of the growth mechanism of sol-gel prepared perovskite BZT thin film on sputtered pyrochlore BZN layer is also required. To accomplish this, FIB-TEM and XPS should be used to analyse the growth surface and microstructure at the interface between BZN buffer layer and BZT main film.

Further characterisation of BZT and BZN dielectric thin films, together with BZT multilayer structures, is required at frequencies 300 kHz to ~15 GHz. The high frequency measurements can be obtained using a much smaller (typically 5 μm^2) MIM capacitor structure (top electrode) patterned by photolithography.

Relaxor ferroelectrics are characterised by a dielectric permittivity that is both frequency and temperature dependent. To thoroughly investigate the dielectric properties of relaxors (e.g. $Ba(Zr_xTi_{1-x})O_3$ with a composition $x \geq 0.25$) and the diffuseness of the ferroelectric phase transition it is therefore essential to examine these materials over a wide frequency and temperature range. This necessitates testing material at temperatures well below ambient. Low temperature analysis is further justified with reference to work carried out by Thayer *et al*. who reported increased tunability of thin-film BZN after cooling the material to 77 K [3.51]. The decrease in electronic conductivity that resulted enabled higher fields to be applied without dielectric breakdown. Unfortunately, low temperature analysis was not possible due to there being no suitable test facility. This analysis should therefore form part of a future work programme.

Although thin-film BZN was successfully dry etched by RIE using CHF_3/Ar gas, there is a need to conduct further dry etching experiments on BZN thin films using other halogenous gases (e.g. CF_4, SF_6, $CBrF_3$ and CCl_2F_2) in an attempt to increase the etching rate of BZN and to improve the selectivity over that of Au, Pt and photoresist. These gases are often used in combination with Ar and/or O_2. Some form of real-time plasma analysis should also be incorporated such as optical emission spectroscopy, mass spectrometry or Langmuir probe.

References

[1.1] G.H. Haertling; Ferroelectric ceramics: history and technology; *J. Am. Ceram. Soc.* 82, 4 (1999) 797-818

[1.2] A.K. Tagantsev, V.O. Sherman, K.F. Astafiev, J. Venkatesh, N. Setter; Ferroelectric materials for microwave tunable applications; *Journal of Electroceramics* 11 (2003) 5-66

[1.3] A.K. Tagantsev, V.O. Sherman, K.F. Astafiev, J. Venkatesh, N. Setter; Erratum: Ferroelectric materials for microwave tunable applications; *Journal of Electroceramics* 14 (2005) 199-203

[1.4] S.S. Toncich; Potential impact of ferroelectric technology for PCS and cellular communications; *Integrated Ferroelectrics* 28 (2000) 37-47

[1.5] S.A. Wolf, D. Treger; Frequency agile materials for electronics (FAME) – progress in the DARPA programmes; *Integrated Ferroelectrics* 42 (2002) 39-55

[1.6] H.C. Kim, K. Chun; RF MEMS technology; *Trans. on Electrical and Electronic Eng.* 2 (2007) 249-261

[1.7] G.M. Rebeiz; RF MEMS – Theory, design, and technology; Wiley Interscience (2003)

[1.8] D. Damjanovic; Ferroelectric, dielectric and piezoelectric properties of ferroelectric thin films and ceramics; *Rep. Prog. Phys.* 61 (1998) 1267-1324

[1.9] P. Chandra, P.B. Littlewood; A Landau primer for ferroelectrics; *Topics in Applied Physics,* 105 (2007) 69-116

[1.10] O.G. Vendik, S.P. Zubko; Modeling microwave dielectric characteristics of thin ferroelectric films for tunable planar structures; *Integrated Ferroelectrics* 34 (2001) 215-226

[1.11] S.P. Zubko; Modeling dielectric response and losses of ferroelectrics at microwave frequencies; *Integrated Ferroelectrics* 49 (2002) 71-80

[1.12] O.G. Vendik; Microwave tunable components and subsystems based on ferroelectrics: Physics and principles of design; *Integrated Ferroelectrics* 49 (2002) 181-190

[1.13] M.E. Lines, A.M. Glass; Principles and applications of ferroelectrics and related materials; Clarendon Press (1977)

[1.14] Y. Hotta, G.W.J. Hassink, T. Kawai, H. Tabata; Artificial control of order degree state of B-site ions in Ba(Zr,Ti)O_3 by a superlattice technique; *Jpn. J. Appl. Phys.* 42 (2003) 5908-5912

[1.15] B. Guigues, J. Guillan, E. Defay, P. Garrec, D. Wolozan, B. Andre, F. Laugier, R. Pantel, X. Gagnard, M. Aid; $SrTiO_3/BaTiO_3$ multilayer thin films for integrated tunable capacitors applications; *J. Europ. Ceram. Soc.* 27 (2007) 3851-3854

[1.16] F.M. Pontes, E.R. Leite, E.J.H. Lee, E. Longo, J.A. Varela; Dielectric properties and microstructure of $SrTiO_3/BaTiO_3$ multilayer thin films prepared by a chemical route.; *Thin Solid Films* 385 (2001) 260-265

[1.17] G. Koebernik, W. Haessler, R. Pantou, F. Weiss; Thickness dependence on the dielectric properties of $BaTiO_3/SrTiO_3$ multilayers; *Thin Solid Films* 449(2004) 80-85

[1.18] H-H. Huang, F-Y. Hsiao, N-C. Wu, M-C. Wang; Preparation and characterisation of $SrTiO_3/BaTiO_3$ thin multilayer films deposited on Pt/Ti/SiO_2/Si substrates by radio frequency magnetron sputtering; *J. of Non-Crystalline Solids* 351 (2005) 3809-3815

[1.19] H. Liu, X. Gong, J. Liang, X. Li, D. Xias, J. Zhu, Z. Pu; Enhanced dielectric and ferroelectric properties of $Pb(Zr_{0.8}Ti_{0.2})O_3/Pb(Zr_{0.2}Ti_{0.8})O_3$ multilayer films; *Applied Physics Letters* 91 (2007) 122906 1-3

[1.20] J. Wang, L.Y. Zhang, X. Yao, J.K. Li; Characterisation of PZT/PT multilayer thin film by sol-gel; *Ceramics International* 30 (2004) 1517-1520

[1.21] L. Sun, O.K. Tan, W. Liu, W. Zhu, X. Chen; Characterisation of sol-gel derived $Pb(Zr_{0.3}Ti_{0.7})O_3/PbTiO_3$ multilayer thin films; *Ceramics International* 30 (2004) 1835-1841

[1.22] F. Zhang, J. Chen, X. Li, M. Shen; Morphotropic phase boundary (MPB) effect in $Pb(Zr,Ti)O_3$ rhombohedral/tetragonal multilayer films; *Materials Letters* 60 (2006) 2733-2737

[1.23] L.H. Chang, W.A. Anderson; Single and multilayer ferroelectric $PbZr_xTi_{1-x}O_3$ (PZT) on $BaTiO_3$; *Thin Solid Films* 303 (1997) 94-100

[1.24] S. Alkoy, E.M. Alkoy, K. Uchiyama, T. Shiosaki; Fatigue behaviour of $Pb(Zr,Ti)O_3/PbZrO_3$ multilayer ferroelectric thin films; *Jap. J. of Appl. Phys.* 45 (2006) 7275-7278

[1.25] T-L. Ren, L-T. Zhang, L-T. Liu, Z-J. Li; Electrical properties of a silicon-based PT/PZT/PT sandwich structure; *J. Phys. D: Appl. Phys.* 33 (2000) L77-L79

[1.26] X. Li, N. Wang, J. Bao, T. Chen, J. Xu, H. Feng, S. Li; Voltage drop at interfaces in multilayer ferroelectrics; *Applied Physics Letters* 82 (2003) 1589-1591

[1.27] M.D. Glinchuk; Ferroelectric thin films and multilayer structures based on them; *Powder Metallurgy and Metal Ceramics* 39 (2000) 345-354

[1.28] L.N. Gao, J.W. Zhai, X, Yao, Z.K. Xu; Dielectric properties of heterostructured BZT thin films prepared by sol-gel technique; *Materials Letters* 62 (2008) 3198-3200

[1.29] W.F. Qin, J. Xiong, J. Zhu, J.L. Tang, W.J. Jie, Y. Zhang, Y.R. Li; Enhanced electrical properties of multilayer

$Ba(Zr_{0.2}Ti_{0.8})O_3/Ba_{0.6}Sr_{0.4}TiO_3/Ba(Zr_{0.2}Ti_{0.8})O_3$ thin films for tunable microwave applications; *J. Mater. Sci*. 43 (2008) 409-412

[1.30] X. Yan, W. Ren, P. Shi, X. Wu, X. Chen, X. Yao; $Ba_{0.5}Sr_{0.5}TiO_3/Bi_{1.5}Zn_{1.0}Nb_{1.5}O_7$ multilayer thin films prepared by sol-gel method; *Applied Surface Science* 255 (2008) 2129-2132

[1.31] L. Yan, L.B. Kong, L.F. Chen, K.B. Chong, C.Y. Tan, C.K. Ong; $Ba_{0.5}Sr_{0.5}TiO_3$-$Bi_{1.5}Zn_{1.0}Nb_{1.5}O_7$ composite thin films with promising microwave dielectric properties for microwave device applications; *Applied Physics Letters* 85 (2004) 3522-3524

[1.32] S-X. Wang, M-S. Guo, X-H. Sun, T. Liu, M-Y. Li, X-Z. Zhao; Tunable, low loss $Bi_{1.5}Zn_{1.0}Nb_{1.5}O_7/Ba_{0.6}Sr_{0.4}TiO_3/Bi_{1.5}Zn_{1.0}Nb_{1.5}O_7$ sandwich films; *Applied Physics Letters* 89 (2006) 212907 1-3

[1.33] P. Shi, W. Ren, X. Wu, R. Huang, L. Zhang, X. Yao; Preparation and dielectric properties of $Bi_{1.5}Zn_{1.0}Nb_{1.5}O_7$-$Ba_{0.5}Sr_{0.5}TiO_3$ composite thick films; *Ferroelectrics* 357 (2007) 138-141

[1.34] W. Fu, H. Wang, L. Cao, Y. Zhou; $Bi_{1.5}Zn_{1.0}Nb_{1.5}O_7$/Mn-doped $Ba_{0.6}Sr_{0.4}TiO_3$ heterolayered thin films with enhanced tunable performance; *Applied Physics Letters* 92 (2008) 182910 1-3

[1.35] W. Fu, L. Cao, S. Wang, Z. Sun, B. Cheng, Q. Wang, H. Wang; Dielectric properties of $Bi_{1.5}Zn_{1.0}Nb_{1.5}O_7$/Mn-doped $Ba_{0.6}Sr_{0.4}TiO_3$ heterolayered films grown by pulsed laser deposition; *Applied Physics Letters* 89 (2006) 132908 1-3

[1.36] M.L. Calzada, I. Bretros, R. Jimenez, H. Guillon, L. Pardo; Low-temperature processing of ferroelectric thin films compatible with silicon integrated circuit technology; *Adv. Mater.* 16 (2004) 1620-1624

[2.1] W.C. Booth, G.G. Colomb, J.M. Williams; The craft of research; *The University of Chicago Press*, 2nd Edition (2003)

[3.1] W.X. Cheng, A.L. Ding, X.Y. He, X.S. Zheng; Characterization of $Ba(Zr_{0.05}Ti_{0.95})O_3$ thin film prepared by sol-gel process; *J. Electroceram.* 16 (2006) 523-526

[3.2] A.J. Moulson, J.M. Herbert; Electroceramics – Materials, properties, applications; Chapman and Hall (1997)

[3.3] I. Levin, T.G. Amos, J.C. Nino, T.A. Vanderah, C.A. Randall, M.T. Lanagan; Structural study of an unusual cubic pyrochlore $Bi_{1.5}Zn_{0.92}Nb_{1.5}O_{6.92}$; *J. of Solid State Chem.*, 168 (2002) 69-75

[3.4] H. Wang, X. Wang, X. Yao; Phase transformation and phase distribution of pyrochlore structure in Bi_2O_3-ZnO-NB_2O_5 system; *IEEE International Symposium on Applications of Ferroelectrics* 2 (1996) 787-790

[3.5] M.A. Subramanian, G. Aravamudan, G.V. Subba Rao; Oxide pyrochlores – A review; *Pro. Solid St. Chem.* 15 (1983) 55-143

[3.6] J. Zhai, D. Hu, X. Yao, Z. Xu, H Chen; Preparation and tunability properties of $Ba(Zr_xTi_{1-x})O_3$ thin films grown by a sol-gel process; *J. Europ. Ceram. Soc.* 26 (2006) 1917-1920

[3.7] C. Gao, J. Zhai, X. Yao; Preparation and dielectric properties of $Ba(Zr_xTi_{1-x})O_3$ thin films grown by a sol-gel process; *Integrated Ferroelectrics* 74 (2005) 147-153

[3.8] C. Hofer, S. Halder, R. Waser; Influence of thickness and Zr content on $Ba(Ti_xZr_{1-x})O_3$ thin films; *Ferroelectrics* 332 (2006) 153-157

[3.9] J. Zhai, X. Yao, J. Shen, L. Zhang, H. Chen; Structural and dielectric properties of $Ba(Zr_xTi_{1-x})O_3$ thin films prepared by a sol-gel process; *J. Phys. D: Appl. Phys*. 37 (2004) 748-752

[3.10] A. Dixit, S.B. Majumder, P.S. Dobal, R.S. Katiyar, A.S. Bhalla; Phase transition studies of sol-gel deposited barium zirconate titanate thin films; *Thin Solid Films* 447-448 (2004) 284-288

[3.11] J. Zhai, X. Yao, L. Zhang, B. Shen, H. Chen; Orientation control and dielectric properties of sol-gel deposited Ba(Ti, Zr)O_3 thin films; *Journal of Crystal Growth* 262 (2004) 341-347

[3.12] J. Zhai, X. Yao, B. Shen, L. Zhang, H. Chen; Dielectric and ferroelectric properties of $Ba(Zr_{0.35}Ti_{0.65})O_3$ thin films grown by a sol-gel process; *Journal of Electroceramics* 11 (2003) 157-161

[3.13] A. Dixit, S.B. Majumder, A. Savvinov, R.S. Katiyar, R. Guo, A.S. Bhalla; Investigations on the sol-gel-derived barium zirconium titanate thin films; *Materials Letters* 56 (2002) 933-940

[3.14] C. Hofer, M. Hoffmann, U. Boettger, R. Waser; Relaxors as high-ε-materials for multilayer and thin film capacitors; *Ferroelectrics* 270 (2002) 179-184

[3.15] A. Dixit, S.B. Majumder, R.S. Katiyar, A.S. Bhalla; Relaxor behavior in sol-gel-derived $BaZr_{(0.40)}Ti_{(0.60)}O_3$ thin films; *Applied Physics Letters* 82 (1983) 2679-2681

[3.16] X.G. Tang, H.L.W. Chan, A.L. Ding; Structural, dielectric and optical properties of Ba(Ti, Zr)O_3 thin films prepared by chemical solution deposition; *Thin Solid Films* 460 (2004) 227-231

[3.17] A. Dixit, S.B. Majumder, R.S. Katiyar, A.S. Bhalla; Studies on the relaxor behavior of sol-gel derived $Ba(Zr_xTi_{1-x})O_3$ ($0.30 \leq x \leq 0.70$) thin films; *Journal of Materials Science* 41 (2006) 87-96

[3.18] W.S. Choi, B.S. Jang, D-G Lim, J. Yi, B. Hong; Characterization of $Ba(Zr_{0.2}Ti_{0.8})O_3$ thin films deposited by RF-magnetron sputtering; *Journal of Crystal Growth* 237-239 (2002) 438-442

[3.19] W.S. Choi, B.S. Jang, Y. Roh, J. Yi, B. Hong; The effect of deposition temperature on the electrical and physical properties of the $Ba(Zr,Ti)O_3$ thin films; J. of Non-Crystalline Solids 303 (2002) 190-193

[3.20] J. Xu, W. Menesklou, E. Ivers-Tiffee; Investigation of BZT thin films for tunable microwave applications; *J. Europ. Ceram. Soc.* 25 (2005) 2289-2293

[3.21] J. Xu, W. Menesklou, E. Ivers-Tiffee; Annealing effects on structural and dielectric properties of tunable BZT thin films; *Journal of Electroceramics* 13 (2004) 229-233

[3.22] T.B. Wu, C.M. Wu, M.L. Chen; Highly insulative barium zirconate-titanate thin films prepared by rf magnetron sputtering for dynamic random access memory applications; *Applied Physics Letters* 69[18] (1996) 2659-2661

[3.23] M-C. Wang, C-Y. Chen, C-S. Hsi, N-C. Wu; Influence of deposition parameters on the dielectric properties of rf magnetron sputtered $Ba(Zr_xTi_{1-x})O_3$ thin films; *J. Europ. Ceram. Soc.* 23 (2003) 2307-2314

[3.24] M-C. Wang, C-Y. Chen, C-S. Hsi, N-C. Wu; Characteristics and crystal structure of the $Ba(Zr_{0.2}Ti_{0.8})O_3$ thin films deposited by RF magnetron sputtering; *Journal of Crystal Growth* 246 (2002) 99-107

[3.25] H-J. Shy, T-B. Wu; Structural and electrical characteristics of $Ba(Zr_{0.12}Ti_{0.88})O_3$ thin films deposited on $LaNiO_3$ electrode by RF magnetron sputtering; *Jpn. J. Appl. Phys.* 37 (1998) 5638-5644

[3.26] W.C. Xu, D.Y. Wang, X.G. Tang, Y. Wang, H.L.W. Chan; Tunable dielectric behaviors of barium zirconate titanate thin films; *Integrated Ferroelectrics* 80 (2006) 443-449

[3.27] X.G. Tang, D.Y. Wang, J. Wang, H.L.W. Chan; Nonlinear dielectric properties of $(Ba,Sr)TiO_3$ and $Ba(Zr,Ti)O_3$ thin films for tunable microwave device applications; *Integrated Ferroelectrics* 77 (2005) 151-156

[3.28] X.G. Tang, Q.X. Liu, Y.P. Jiang, R.K. Zheng, H.L.W. Chan; Enhanced dielectric properties of highly (100)-oriented Ba(Zr,Ti)O_3 thin films grown on $La_{0.7}Sr_{0.3}MnO_3$ bottom layer; *Journal of Applied Physics* 100 (2006) 114105, 1-5

[3.29] Q. Feng, C.J. McConville, D.D. Edwards; Dielectric properties and microstructures of Ba(Ti,Zr)O_3 multilayer ceramic capacitors with Ni electrodes; *J. Am. Ceram. Soc.* 88, 6 (2005) 1455-1460

[3.30] F. Zimmermann, M. Voigts, W. Menesklou, E. Ivers-Tiffee; $Ba_{0.6}Sr_{0.4}TiO_3$ and $BaZr_{0.3}Ti_{0.7}O_3$ thick films as tunable microwave dielectrics; *J. Europ. Ceram. Soc.* 24 (2004) 1729-1733

[3.31] S-J. Jeong, D-S. Lee, E-C. Park, J-S. Song; Piezoelectric properties of a $Ba(Zr_{0.075}Ti_{0.925})O_3$ single crystal induced by poling treatment; *Journal of Electroceramics* 17 (2006) 537-541

[3.32] Z. Yu, R. Guo, A.S. Bhalla; Orientation dependence of the ferroelectric and piezoelectric behavior of $Ba(Ti_{1-x}Zr_x)O_3$ single crystals; *Applied Physics Letters* 77, 10 (2000) 1535-1537

[3.33] Z. Yu, C. Ang, R. Guo, A.S. Bhalla; Dielectric properties and high tunability of $Ba(Ti_{0.7}Zr_{0.3})O_3$ ceramics under dc electric field; *Applied Physics Letters* 81,7 (2002) 1285-1287

[3.34] Z. Yu, C. Ang, R. Guo, A.S. Bhalla; Ferroelectric-relaxor behavior of $Ba(Ti_{0.7}Zr_{0.3})O_3$ ceramics; *Journal of Applied Physics* 92, 5 (2002) 2655-2657

[3.35] Z. Yu, C. Ang, R. Guo, A.S. Bhalla; Piezoelectric and strain properties of $Ba(Ti_{1-x}Zr_x)O_3$ ceramics; *Journal of Applied Physics* 93, 3 (2002) 1489-1493

[3.36] Z. Yu, R. Guo, A.S. Bhalla; Dielectric polarization and strain behavior of $Ba(Ti_{0.92}Zr_{0.08})O_3$ single crystals; *Materials Letters* 57 (2002) 349-354

[3.37] Z. Yu, C. Ang, R. Guo, A.S. Bhalla; Dielectric properties of $Ba(Ti_{1-x}Zr_x)O_3$ solid solutions; *Materials Letters* 61 (2007) 326-329

[3.38] T. Maiti, R. Guo, A.S. Bhalla; Electric field dependent dielectric properties and high tunability of $BaZr_xTi_{1-x}O_3$ relaxor ferroelectrics; *Applied Physics Letters* 89 (2006) 122909, 1-3

[3.39] X.P. Jiang, M. Zeng, H.L.W. Chan, C.L. Choy; Relaxor behaviours and tunability in $BaZr_{(0.35)}Ti_{(0.65)}O_3$ ceramics; *Mater. Sci. and Eng.* A438-440 (2006) 198-201

[3.40] X.G. Tang, K-H. Chew, H.L.W. Chan; Diffuse phase transition and dielectric tunability of $Ba(Zr_yTi_{1-y})O_3$ relaxor ferroelectric ceramics; *Acta Materialia* 52 (2004) 5177-5183

[3.41] A.A. Bokov, M. Maglione, A. Simon, Z-G. Ye; Dielectric behaviour of $Ba(Ti_{1-x}Zr_x)O_3$ solid solution; *Ferroelectrics* 337 (2006) 169-178

[3.42] M. Kobune, K. Yamakawa, T. Yazawa; A barium zirconate titanate-based inorganic dielectric material with high permittivity as a lead-free insulator for semiconductor applications; *Integrated Ferroelectrics* 74 (2005) 155-164

[3.43] J. Li H. Kakemoto, S. Wada, T. Tsurumi, H. Kawaji; Dielectric relaxation in gigahertz region and phase transition of $BaTiO_3$-based ceramics; *Journal of Applied Physics* 100 (2006) 024106, 1-6

[3.44] H. Du, X. Yao; Structural trends and dielectric properties of Bi-based pyrochlores; *J. Mater. Sci: Mater. In Electron*ics, 15 (2004) 613-616

[3.45] H. Du, X. Yao; Investigations on structural evolution and dielectric characteristics of high performance Bi-based dielectrics; *Materials Research Bulletin* 40 (2005) 1527-1535

[3.46] H. Du, X. Yao; Effects of Sr substitution on dielectric characteristics in $Bi_{1.5}ZnNb_{1.5}O_7$ ceramics; *Mater. Sci. and Eng.*, B99 (2003) 437-440

[3.47] I. Levin, T.G. Amos, J.C. Nino, T.A. Vanderah, C.A. Randall, M.T. Lanagan; Structural study of an unusual cubic pyrochlore $Bi_{1.5}Zn_{0.92}Nb_{1.5}O_{6.92}$; *J. of Solid State Chem.*, 168 (2002) 69-75

[3.48] D.P. Cann, C.A. Randall, T.R. Shrout; Investigation of the dielectric properties of bismuth pyrochlores; *Solid State Communications*, 100 (1996) 529-534

[3.49] W. Ren, R. Thayer, C.A. Randall, T.R. Shrout, S. Trolier-McKinstry; Bismuth pyrochlore films for dielectric applications; *Materials Research Society Symposium – Proceedings*, 603 (2000) 137-142

[3.50] S.S. Kim, M.H. Park, J.K. Kim, W-J. Kim; Properties of sol-gel derived bismuth-based pyrochlore thin films; *Integrated Ferroelectrics*, 79 (2006) 147-154

[3.51] R.L. Thayer, C.A. Randall, S. Trolier-McKinstry; Medium permittivity bismuth zinc niobate thin film capacitors; *Journal of Applied Physics*, 94 (2003) 1941-1947

[3.52] H. Wang, R. Elsebrock, T. Schneller, R. Waser, X. Yao; Bismuth zinc niobate ($Bi_{1.5}ZnNb_{1.5}O_7$) ceramics derived from metallo-organic decomposition precursor solution; *Solid State Communications*, 132 (2004) 481-486

[3.53] J. Lu, D.O. Klenov, S. Stemmer; Influence of strain on the dielectric relaxation of pyrochlore bismuth zinc niobate thin films; *Applied Physics Letters* 84 (2004) 957-959

[3.54] J. Park, J. Lu, S. Stemmer, R.A. York; Microwave planar capacitors employing low loss, high-K, and tunable BZN thin films; *IEEE MTT-S International Microwave Symposium Digest*, 1516673 (2005) 607-610

[3.55] J, Lu, S. Schmidt, D.S. Boesch, N. Pervez, R.A. York, S. Stemmer; Low-loss tunable capacitors fabricated directly on gold bottom electrodes; *Applied Physics Letters*, 88 (2006) 112905, 1-3

[3.56] J. Park, J. Lu, S. Stemmer, R.A. York; Microwave dielectric properties of tunable capacitors employing bismuth zinc niobate thin films; *Journal of Applied Physics*, 97 (2005) 084110, 1-4

[3.57] A. K. Tagantsev, J. Lu, S. Stemmer; Temperature dependence of the dielectric tunability of pyrochlore bismuth zinc niobate thin films; *Applied Physics Letters*, 86 (2005) 032901, 1-3

[3.58] J. Park, J.W. Lu, D.S. Boesch, S. Stemmer, R.A. York; Distributed phase shifter with pyrochlore bismuth zinc niobate thin films; *IEEE Microwave and Wireless Components Letters*, 16 (2006) 264-266

[3.59] J. Lu, S. Stemmer; Low-loss, tunable bismuth zinc niobate films deposited by rf magnetron sputtering; *Applied Physics Letters*, 83 (2003) 2411-2413

[3.60] J. Park, J. Lu, S. Stemmer, R.A. York; BZN thin film capacitors for microwave low loss tunable applications; *Integrated Ferroelectrics*, 77 (2005) 21-26

[3.61] N.K. Pervez, J. Park, J. Lu, S. Stemmer, R.A. York; Geometrical scaling effects in high permittivity capacitors; *Integrated Ferroelectrics*, 80 (2006) 437-442

[3.62] K.H. Ko, D.H. Back, Y.P. Hong, J.H. Moon; Phase decomposition and dielectric properties of reactively sputtered bismuth zinc niobate pyrochlore thin films deposited from monoclinic zirconolite target; *Journal of Electroceramics*, 14 (2005) 171-175

[3.63] D.J. Jung, M. Dawber, J.F. Scott, L.J. Sinnamon, J.M. Gregg; Switching dynamics in ferroelectric thin films: An experimental survey; *Integrated Ferroelectrics,* 48 (2002) 59-68

[3.64] J. Yu, L. Wang, Y. Wang, G. Peng, F. Liu, J. Gao; A compact model for the simulation of ferroelectric capacitor; *Integrated Ferroelectrics,* 75 (2005) 35-45

[3.65] R. Ulrich, L Schaper; Materials options for dielectrics in integrated capacitors; *International Symposium on Advanced Packaging Materials*, (2000) 38-43

[3.66] A.I. Kingon, J-P Maria, S.K. Streiffer; Alternative dielectrics to silicon dioxide for memory and logic devices; *Nature*, 406 (2000) 1032-1038

[3.67] L. Peters; Pursuing the perfect low-k dielectric; *Semiconductor International*, Sept 1998, 64-74

[3.68] H. Treichel, C. Goonetilleke; Integration challenges for low dielectric constant materials; *Advanced Engineering Materials*, 3 (2001) 461-464

[3.69] D. Scansen, R. Haythornthwaite, S. Brown; Impact of low k dielectrics on microelectronics reliability; *IEEE CCECE/CCGEI*, (2005) 714-717

[3.70] C.J. Brinker, G.W. Scherer; Sol-Gel Science; Academic Press (1990)

[3.71] M. Veith, S. Mathur, N. Lecerf, V. Huch, T. Decker, H.P. Beck, W. Eiser, R. Haberkorn; Sol-gel synthesis of nano-scaled $BaTiO_3$, $BaZrO_3$ and $BaTi_{0.5}Zr_{0.5}O_3$ oxides via single-source alkoxide precursors and semi-alkoxide routes; *J. Sol-Gel Sci. Techn.* 15 (2000) 145-158

[3.72] V.G. Kessler, G.I. Spijksma, G.A. Seisenbaeva, S. Hakansson, D.H.A. Blank, H.J.M. Bouwmeester; New insight in the role of modifying ligands in the sol-gel processing of metal alkoxide precursors: A possibility to approach new classes of material; *J. Sol-Gel Sci. Techn.* 40 (2006) 163-179

[3.73] S. Ivanovici, M. Puchberger, H. Fric, G. Kickelbick; Coordination behaviour of acetoacetate ligands with attached methacrylate groups containing alkyl-spacers of differenet length to titanium and zirconium alkoxides; *Monatshefte fur Chemie* 138 (2007) 529-539

[3.74] X. Lu, J. Zhu, Z. Liu, X. Xu, Y. Wang; Phase transition related stress in ferroelectric thin films; *Thin Solid Films* 375 (2000) 15-18

[3.75] J.S. Zhu, X.M. Lu, P. Li, W. Jiang, Y.N. Wang; Stress effects in ferroelectric thin films; *Solid State communications* 101 (1997) 263-266

[3.76] M.D. Glinchuk, A.N. Morozovska, V.A. Stephanovich, L. Jastrabik; Surface tension and mismatch effects in ferroelectric thin film properties; *Ferroelectrics* 298 (2004) 83-96

[3.77] M.J. Buehler, A. Hartmaier, H. Gao; Atomistic and continuum studies of crack-like diffusion wedges and associated dislocation mechanisms in thin films on substrates; *Journal of the Mechanics and Physics of Solids*; 51 (2003) 2105-2125

[3.78] H. Gao, L. Zhang, W.D. Nix, C.V. Thompson, E. Arzt; Crack-like grain-boundary diffusion wedges in thin metal films; *Journal of the Mechanics and Physics of Solids*; 47 (1999) 2865-2878

[3.79] D. Fang, B. Liu, C.T. Sun; Fatigue crack growth in ferroelectric ceramics driven by alternating electric fields; *J. Am. Ceram. Soc.* 87 (2004) 840-846

[3.80] K. Yao, F.E.H. Tay, W. Zhu; Self-mending of microcracks in barium titanate glass-ceramic thin films with high dielectric constant; *J. Am. Ceram. Soc.* 85 (2002) 496-498

[3.81] J.A. Thornton, D.W. Hoffman; Stress-related effects in thin films; *Thin Solid Films*, 171 (1989) 5-31

[3.82] F.M. d’Heurle, J.M.E. Harper; Note on the origin of intrinsic stresses in films deposited via evaporation and sputtering; *Thin Solid Films*, 171 (1989) 81-92

[3.83] M. Chinmulgund, R.B. Inturi, J.A. Barnard; Effect of Ar gas pressure on growth, structure, and mechanical properties of sputtered Ti, Al, TiAl, and Ti_3Al films; *Thin Solid Films*, 270 (1995) 260-263

[3.84] H. Tokura, B. Window, D. Neely, M. Swain; Microstructure and mechanical properties of sputtered platinum films; *Thin Solid Films*, 253 (1994) 344-348

[3.85] R. Abermann; Measurements of the intrinsic stress in thin metal films; *Vacuum*, 41 (1990) 1279-1282

[3.86] M.C. Barnes, I-D. Jeon, D-Y. Kim, N.M. Hwang; Generation of charged clusters during thermal evaporation of gold; *Journal of Crystal Growth*, 242 (2002) 455-462

[3.87] S.Y. Kweon, S.K. choi, S.J. Yeom, J.S. Roh; Platinum hillocks in Pt/Ti film stacks deposited on thermally oxidised Si substrate; *Jpn. J. Appl. Phys.* 40 (2001) 5850-5855

[3.88] K. Nakamura, Y. Otani, M. Kurita, S. Okamura, T. Shiosaki; Variation in 111 *d*-space and generation of hillocks in platinum thin-film electrodes by heat treatment; *Jpn. J. Appl. Phys.* 44 (2005) 8096-8101

[3.89] K. Wang, K. Yao, S.J. Chua; Titanium diffusion and residual stress of platinum thin films on $Ti/SiO_2/Si$ substrates; *Journal of Applied Physics* 98 (2005) 013538, 1-5

[3.90] N. Abe, Y. Otani, M. Miyake, M. Kurita, H. Takeda, S. Okamura, T. Shiosaki; Influence of a TiO_2 adhesion layer on the structure and the orientation of a Pt layer in $Pt/TiO_2/SiO_2/Si$ structures, *Jpn. J. Appl. Phys.* 42 (2003) 2791-2795

[3.91] G. Velu, D. Remiens; Electrical properties of sputtered PZT films on stabilised platinum electrode; *J. Europ. Ceram. Soc.* 19 (1999) 2005-2013

[3.92] M.P. Moret, M.A.C. Devillers, F.D. Tichelaar, E. Aret, P.R. Hagerman, P.K. Larsen; Damage after annealing and aging at room temperature of platinized silicon substrates; *Thin Solid Films* 434 (2003) 283-295

[3.93] M. Yamaguchi, A. Yamamoto, Y. Masuda; Thermal stability of platinum bottom electrode for bismuth titanate thin films; *Integrated Ferroelectrics* 79 (2006) 235-243

[3.94] S. Okamura, N. Abe, Y. Otani, T. Shiosaki; Influence of Pt/TiO_2 bottom electrodes on the properties of ferroelectric Pb(Zr,Ti)O_3 thin films; *Integrated Ferroelectrics* 52 (2003) 127-136

[3.95] Y. Matsui, M. Hiratani, Y. Kumagai, H. Miura, Y. Fujisaki; Thermal stability of Pt bottom electrodes for ferroelectric capacitors; *Jpn. J. Appl. Phys.* 37 (1998) L465-L467

[3.96] W. Hu, C. Yang, W. Zhang, G. Liu, D. Dong; The diffusion of Pt in BST films on Pt/Ti/SiO_2/Si substrate by sol-gel method; *J. Sol-Gel Sci. Techn.* 39 (2006) 293-298

[3.97] S.Y. Cha, S.H. Lee, H.C. Lee; Ti thickness effects in Pt/Ti bottom electrode on properties of (Ba,Sr)TiO_3 thin film; *Integrated Ferroelectrics* 16 (1997) 183-190

[3.98] S-T. Kim, H-H. Kim, M-Y. Lee, W-J. Lee; Investigations of Pt/Ti bottom electrodes for Pb(Zr,Ti)O_3 films; *Jpn. J. Appl. Phys.* 36 (1997) 294-300

[3.99] C. Gao, J. Zhai, X. Yao; Effect of seed layers on dielectric properties of $Ba(Zr_{0.3}Ti_{0.7})O_3$ thin films; *Journal of Electroceramics* 21 (2008) 653-656

[3.100] J. Zhai, C. Gao, X. Yao, Z. Xu, H. Chen; Enhanced dielectric tunability properties of $Ba(Zr_xTi_{1-x})O_3$ thin films using seed layers on Pt/Ti/SiO_2/Si substrates; *Ceramics International* 34 (2008) 905-910

[3.101] L. Gao, J. Zhai, X. Yao; Low dielectric loss and enhanced tunability of $Ba(Zr_{0.3}Ti_{0.7})O_3$–based thin film by sol-gel method; *Ceramics International* 34 (2008) 1023-1026

[3.102] L.N. Gao, S.N. Song, J.W. Zhai, X. Yao, Z.K. Xu; Effects of buffer layers on the orientation and dielectric properties of $Ba(Zr_{0.20}Ti_{0.80})O_3$ thin films prepared by sol-gel method; *Journal of Crystal Growth* 310 (2008) 1245-1249

[3.103] J. Zhai, D. Hu, X. Yao, Z. Xu, H Chen; Preparation and tunability properties of $Ba(Zr_xTi_{1-x})O_3$ thin films grown by a sol-gel process; *J. Europ. Ceram. Soc.* 26 (2006) 1917-1920

[3.104] D-P. Kim, C-I. Kim, B-G. Yu; Effects of O_2 annealing after etching $SrBi_2Ta_2O_9$ thin films in $Cl_2/CF_4/Ar$ plasma; *Microelectronics Engineering*, 66 (2003) 904-911

[3.105] D-P. Kim, K-T. Kim, C-I. Kim, A.M. Efremov; Etching mechanisms of $Bi_{4-x}La_xTi_3O_{12}$ films in Ar/Cl_2 inductively coupled plasma; *Thin Solid Films*, 447-448 (2004) 343-348

[3.106] D.Y. Lee, C.W. Chung; Etch characteristics of indium zinc oxide thin films in a C_2F_6/Ar plasma; *Thin Solid Films*, 518 (2009) 372-377

[3.107] G-K. Lee, J-H. Moon, B-T. Lee; Inductively coupled plasma reactive ion etching of ZnO using C_2F_6 and NF_3 based gas mixtures; *Semiconductor Science and Technology*, 21 (2006) 971-974

[3.108] M.H. Shin, M.S. Park, S.H. Jung, J.H. Boo, N-E Lee; Effects of doping elements on ZnO etching characteristics with $CH_4/H_2/Ar$ plasma; *Thin Solid Films*, 515 (2007) 4950-4954

[3.109] T. Zijlstra, M. Kroug, B. Rong, T.M. Klapwijk; Nanoscale niobium trilayer technology using temperature controlled pattern transfer; *Microelectronic Engineering*, 78-79 (2005) 369-373

[3.110] J.M. Martinis, R.H. Ono; Fabrication of ultra small Nb-AlO_x-Nb Josephson tunnel junctions; *Applied Physics Letters*, 57 (1990) 629-631

[3.111] B.J. Curtis, H. Mantle; Reactive ion etching of niobium in SF_6/O_2 to produce sloped sidewall profiles; *J. Vac. Sci. Technol.*, 11 (1993) 2846-2849

[3.112] T.T. Foxe, B.D. Hunt, C. Rogers, A.W. Kleinsasser, R.A. Buhrman; Reactive ion etching of niobium; *J. Vac. Sci. Technol.*, 19 (1981) 1394-1397

[3.113] T.T. Piotrowski, A. Piotrowski, E. Kaminska, Z. Szopniewski, S. Kolesnik, J. Wrobel, P. Gierowski, S. Lewandowski; Electron beam lithography and reactive ion etching of nanometer size features in niobium film; *Material Science and Engineering*, C15 (2001) 171-173

[3.114] J.L. Jackel, R.E. Howard, E.L. Hu, S.P. Lyman; Reactive ion etching of $LiNbO_3$; *Applied Physics Letters*, 38 (1981) 907-909

[3.115] D.A. Darbyshire, A.P. Overbury, C.W. Pitt; Ion and plasma assisted etching of holographic gratings; *Vacuum*, 36 (1986) 55-60

[3.116] R. Boucher, U. Hubner, W. Morgenroth, H. Roth, H.G. Meyer, M. Schmidt, M. Eich; Etching of sub-micron high aspect ratio holes in oxides and polymers; *Microelectronic Engineering*, 73-74 (2004) 330-335

[3.117] D.A. Darbyshire; Waveguide and microlens components for optical signal processing and communications; *MSc Dissertation, University of London* (1987)

[3.118] G.D. Gray, M.J. Morgan, P.A. Kohl; Electrostatic actuators with expanded tuning range due to biaxial intrinsic stress gradients; *J. of Microelectromechanical Systems*, 13 (2004) 51-62

[3.119] C-Y. Lee, E.S. Kim; Piezoelectrically actuated tunable capacitor; *J. of Microelectromechanical Systems*, 15 (2006) 745-755

[3.120] Z. Feng, W. Zhang, B. Su, K.F. Harsh, K.C. Gupta, V. Bright, and Y.C. Lee; Design and modeling of RF MEMS tunable capacitors using electro-thermal actuators; *Proc. IEEE MTT-S Int. Microwave Symp. Digest*, 4 (1999) 1507–1510.

[3.121] T. Ketterl, T. Weller, D. Fries; A micromachined tunable CWP resonator; *IEEE MTT-S Int. Microwave Symp.Digest*, (2001) 345-348

[3.122] E.S. Hung, S.D. Senturia; Tunable capacitors with programmable capacitance-voltage characteristics; *Solid-State Sensors and Actuators Workshop*, (1998) 292-295

[3.123] G.V. Ionis, A. Dec, K. Suyama; A zipper-action differential micro-mechanical tunable capacitor; *Proc. of IEEE Int. Conf. on Micro-Electro-Mechanical Systems*, (2001) 29-32.

[3.124] C-Y. Lee, S-J. Chen, D. Chi, H. Yu, E.S. Kim; Surface micromachined GHz tunable capacitor with 14:1 continuous tuning range; *Proc. of IEEE Int. Conf. on Micro-Electro-Mechanical Systems (MEMS)*, art. no. 4443829 (2008) 1008-1011

[3.125] S.H. Pu, A.Laister, A. Holmes, E.Yeatman, R. Miles, I. Robertson, G. Dou; High-Q continuously tunable zipping varactors with large tuning range; *Proc. 2008 Asia Pacific Microwave Conference*, art. no. 4958046

[3.126] S.H. Pu, A.S. Holmes, E.M. Yeatman, C. Papavassilion, S. Lucyszyn; Stable zipping RF MEMS varactors; *J. of Micromechanics and Microengineering*, 20(3) (2010) art. no. 035030

[3.127] S.H. Pu, A.S. Holmes, E.M. Yeatman; Design and simulation of zipping variable capacitors; *Proc. Micro Mechanics Europe Workshop*, Guimaraes, Portugal 16-18 Sep (2007) 147-150

[4.1] J. Lu, Z. Chen, T.R. Taylor, S. Stemmer; Composition control and dielectric properties of bismuth zinc niobate thin films synthesised by radio-frequency magnetron sputtering; *J. Vac. Sci. Technol.* A21(5), (2003) 1745-1751

[4.2] F.M. Smits; Measurement of sheet resistivities with the four-point probe; *The Bell Systems Technical Journal,* May 1958, 711-718

[5.1] V.O. Sherman, A.K. Tagantsev, N. Setter, D. Iddles, T. Price; Ferroelectric-dielectric tunable composites; *J. of Appl. Phys.* 99 (2006) 074104 1-10

[5.2] V.O. Sherman, A.K. Tagantsev, N. Setter; Tunability and loss of the ferroelectric-dielectric composites; *2004 IEEE Int. Ultrasonics, Ferroelectrics and Frequency Control Joint 50th Anniversary Conference* 33-38

[5.3] K.F. Astafiev, V.O. Sherman, A.K. Tagantsev, N. Setter; Can the addition of a dielectric improve the figure of merit of a tunable material? *J. Europ. Ceram. Soc.* 23 (2003) 2381-2386

[5.4] A.K. Tagantsev, V.O. Sherman; Composite tunable materials with low loss-factor at microwaves; *35th European Microwave Conference Proceedings 2* (2005) 913-916

[6.1] H. Chen, C. Yang, C. Fu, J. Zhang, J. Liao, L. Hu; Effects of interface on the dielectric properties of $Ba_{0.6}Sr_{0.4}TiO_3$ thin film capacitors; *Applied Surface Science,* 254 (2008) 3175-3179

[6.2] Q. Zhang, S. Corkovic, C.P. Shaw, Z. Huang, R.W. Whatmore; Effect of porosity on the ferroelectric properties of sol-gel prepared lead zirconate titanate thin films; *Thin Solid Films*, 488 (2005) 258-264

[7.1] S. Alkoy, E.M. Alkoy, K. Uchiyama, T. Shiosaki; Fatigue behaviour of $Pb(Zr,Ti)O_3/PbZrO_3$ multilayer ferroelectric thin films; *Jap. J. of Appl. Phys.*, 45, (2006) 7275-7278

[9.1] B.D. Lee, K.H. Yoon, E.S. Kim, T.H. Kim; Microwave dielectric properties of $CaTiO_3$ and $MgTiO_3$ thin films; *Jpn. J. Appl. Phys.* 42 (2003) 6158-6161

[9.2] C-L. Huang, Y-B. Chen; Structure and electrical characteristics of RF magnetron sputtered $MgTiO_3$; *Surface and Coatings Technology* 200 (2006) 3319-3325

[9.3] B.D. Lee, H.R. Lee, K.H. Yoon, Y.S. Cho; Microwave dielectric properties of magnesium calcium titanate thin films; *Ceramics International*, 31 (2005) 143-146

[9.4] B.D. Lee, H.R. Lee K.H. Yoon; Effect of stacking layers on the microwave dielectric properties of $MgTiO_3/CaTiO_3$ multilayered thin films; *J. Am. Ceram. Soc.*, 88 (2005) 1197-1200

[9.5] A. Dixit, D.C. Agrawal, Y.N. Mohapatra, S.B. Majumder, R.S. Katiyar; Studies on the dielectric and relaxor behaviour of sol-gel derived barium strontium zirconate titanate thin films; *Materials Letters* 61(2007) 3685-3688

[9.6] S.H. Choy, D.Y. Wang, J.Y. Dai, H.L.W. Chan, C.L. Choy; Barium strontium zirconate titanate (BSZT) thin films for optical waveguide applications; *Integrated Ferroelectrics* 80 (2006) 107-114

[9.7] J-Y. Ha, J-W. Choi, C-Y. Kang, J-S. Kim, S-J. Yoon, D.J. Choi, H-J. Kim; Improvement of dielectric loss of $(Ba,Sr)(Ti,Zr)O_3$ ferroelectrics for tunable devices; *J. Europ. Ceram. Soc.* 27 (2007) 2747-2751

[9.8] X.G. Tang, X.X. Wang, K-H. Chew, H.L.W. Chan; Relaxor behaviour of $(Ba,Sr)(Zr,Ti)O_3$ ceramics; *Solid State Communications* 136 (2005) 89-93

Appendix 1

Material Parameters for Substrates, Metal Layers and Dielectric Films.

1. Introduction

Material parameters including ionic radii, lattice constants and room temperature linear thermal expansion coefficients are important for gaining an improved understanding of thin-film dielectrics in the form of complex oxides, and their interaction with metal layers and various substrate materials. Among researchers there is some disagreement about the values assigned to some of the parameters, so estimated values are given in certain cases. For example, in a paper by Lu *et al*. the thermal expansion coefficient of BZN was assumed to be the same as that of $Bi_{1.5}Zn_{1.0}Sb_{1.5}O_7$ (α=7.92x10^{-6} K^{-1}) [3.53].

2. Ionic Radii

BZT:	Ba^{2+} (1.42 Å)	Zr^{4+} (0.87 Å)	Ti^{4+} (0.68 Å)
BZN:	Bi^{3+} (1.17 Å)	Zn^{2+} (0.90 Å)	Nb^{5+} (0.64 Å)

3. Lattice Constants

Silicon a=0.5431 nm   Pt (fcc) a=0.3924 nm   Au (fcc) a=0.4078 nm

$Ba(Zr_{0.05}Ti_{0.95})O_3$: a=0.402 nm, c=0.419 nm
$Ba(Zr_{0.20}Ti_{0.80})O_3$: a=0.404 nm, c=0.408 nm
$Ba(Zr_{0.35}Ti_{0.65})O_3$: a=c=$c_{bulk}$=0.406 nm

BZN a=1.056 nm (unit cell)

4. Thermal Expansion Coefficients (10^{-6} K^{-1})

Silicon (2.6), SiO_2 (5.8), Al_2O_3 (7.3), MgO (12.8), Pt (8.9), Au (14.1)
$BaTiO_3$ (~6.0), $BaZrO_3$ (~6.9), BZN (~7.92)

Appendix 2

Calculation of Starting Material Weights for BZT Sol Synthesis

For each of the BZT compositions synthesised the aim was to produce a 50 ml solution of 0.25 M concentration.

Starting materials and associated formula weights (FW) include:

Barium acetate, $Ba(OAc)_2$:	FW = 255.43
Zirconium propoxide, $Zr(O^nPr)_4$:	FW = 327.58 (purity 75%)
Titanium butoxide, $Ti(O^nBu)_4$:	FW = 340.36 (purity 98%)

Amount of substance (y) in a 50 ml solution to give 0.25 M concentration:

y:50 = 0.25:1000 y = 0.25(50/1000) = 0.0125 mol

- Barium acetate (same for all three BZT compositions):

Weigh out $Ba(OAc)_2$: 0.0125x255.43 = **3.193 g**

- Zirconium propoxide and titanium butoxide (dependent on Zr:Ti ratio):

$Ba(Zr_{0.05}Ti_{0.95})O_3$

$Zr(O^nPr)_4$ y:0.0125 = 0.05:1 y = 0.05x0.0125 = $6.25\text{x}10^{-4}$ mol
Weigh $Zr(O^nPr)_4$: $6.25\text{x}10^{-4}$x327.58(100/75) = **0.273 g**

$Ti(O^nBu)_4$ y:0.0125 = 0.95:1 y = 0.95x0.0125 = $1.1875\text{x}10^{-2}$ mol
Weigh $Ti(O^nBu)_4$: $1.1875\text{x}10^{-2}$x340.36(100/98) = **4.124 g**

$Ba(Zr_{0.20}Ti_{0.80})O_3$

$Zr(O^nPr)_4$ y:0.0125 = 0.20:1 y = 0.20x0.0125 = $2.5\text{x}10^{-3}$ mol
Weigh $Zr(O^nPr)_4$: $2.5\text{x}10^{-3}$x327.58(100/75) = **1.092 g**

$Ti(O^nBu)_4$ y:0.0125 = 0.80:1 y = 0.80x0.0125 = 0.01 mol
Weigh $Ti(O^nBu)_4$: 0.01x340.36(100/98) = **3.473 g**

$Ba(Zr_{0.35}Ti_{0.65})O_3$

$Zr(O^nPr)_4$ y:0.0125 = 0.35:1 y = 0.35x0.0125 = 4.375×10^{-3} mol

Weigh $Zr(O^nPr)_4$: $4.375 \times 10^{-3} \times 327.58(100/75)$ = **1.911 g**

$Ti(O^nBu)_4$ y:0.0125 = 0.65:1 y = 0.65x0.0125 = 8.125×10^{-3} mol

Weigh $Ti(O^nBu)_4$: $8.125 \times 10^{-3} \times 340.36(100/98)$ = **2.822 g**

An accurate balance with digital readout was used to weigh the barium acetate powder. The zirconium propoxide and titanium butoxide liquids were dispensed into a glass flask and weighed on a digital balance inside a glove box.

Appendix 3

BZT Sol Synthesis Variants Featured in Literature

The following BZT sol-gel process flow diagrams show five variants in sol synthesis as developed by other researchers. The process flows developed by Dixit *et al.* (figure A3.1) [3.13] and Zhai *et al*. (figure A3.2) [3.12] were the basis for the initial work on $Ba(Zr_{0.05}Ti_{0.95})O_3$ presented in this thesis. However, problems arose with precipitation when synthesising sols with higher Zr content. This process was later modified and improved to enable synthesis of BZT sols which have the higher Zr content (i.e. 0.20 and 0.35).

In the work by Dixit *et al*. the zirconium-titanium solution was chelated with acetic acid. Ethylene glycol was added to the barium acetate and acetic acid solution prior to the addition of the Zr-Ti complex sol (figure A3.1).

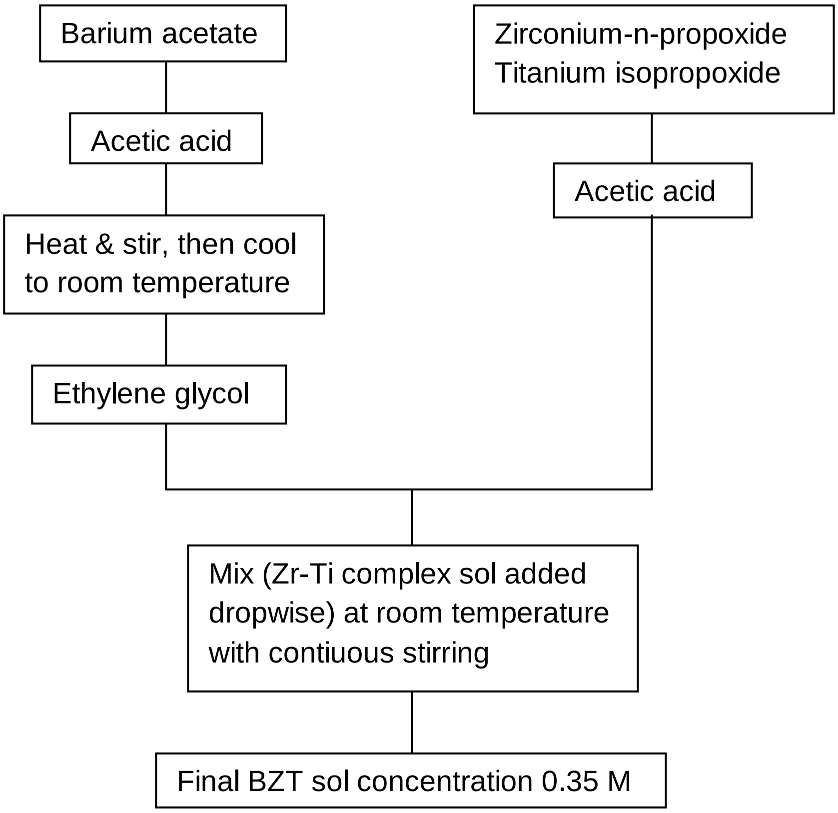

Figure A3.1 $Ba(Zr_xTi_{1-x})O_3$ sol synthesis route employed by Dixit *et al.* [3.13].

The work reported by Zhai *et al*. [3.12] on the growth of $Ba(Zr_{0.35}Ti_{0.65})O_3$ thin films shows a slightly different approach to that of Dixit *et al*. [3.13] in that the zirconium-titanium solution was added without a chelating agent directly to the barium acetate and acetic acid. Once these solutions were mixed, then the ethylene glycol was introduced. Finally the solution was refluxed for one hour, cooled to room temperature and aged for 24 hours (figure A3.2). The final concentration of this sol was 0.1 M, but Zhai *et al*. also produced an identical sol to this with a much higher concentration of 0.6 M. This approach, alongside that of Dixit *et al*. (figure A3.1) is probably the simplest to execute.

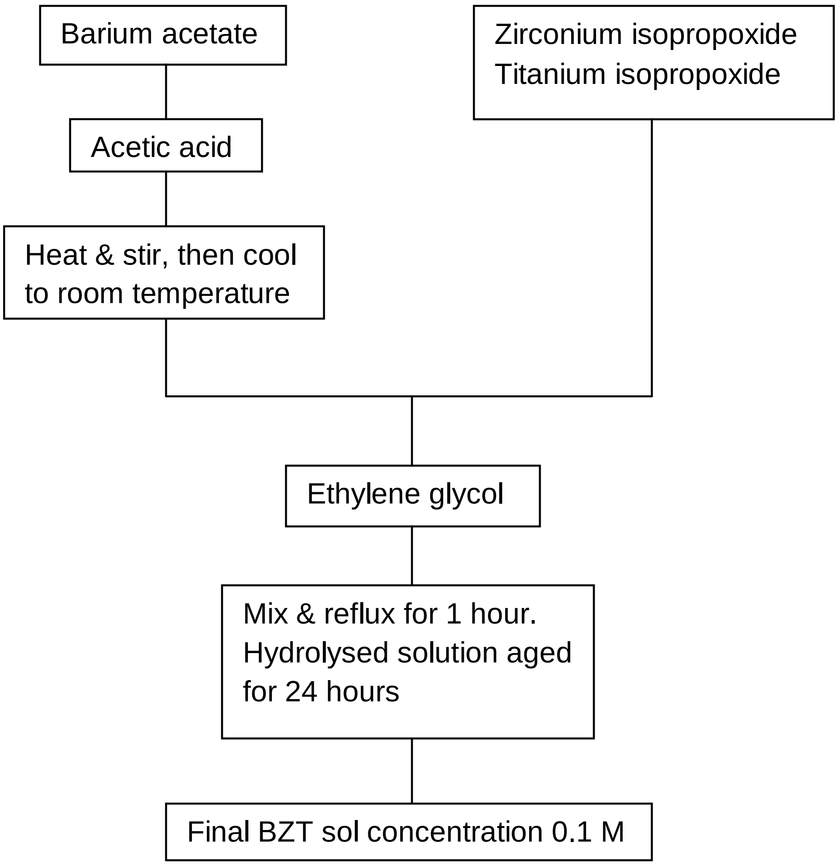

Figure A3.2 BZT sol synthesis route developed by Zhai *et al*. for the growth of $Ba(Zr_{0.35}Ti_{0.65})O_3$ thin films [3.12].

A further paper by Zhai *et al*. gave details of the growth of $Ba(Zr_xTi_{1-x})O_3$ thin films with Zr content x=0.05 to 0.35 and using the sol synthesis process detailed in figure A3.3 [3.9]. Note the use of 2-methoxyethanol as a solvent and to adjust the viscosity of the final solution. However, this chemical is extremely toxic.

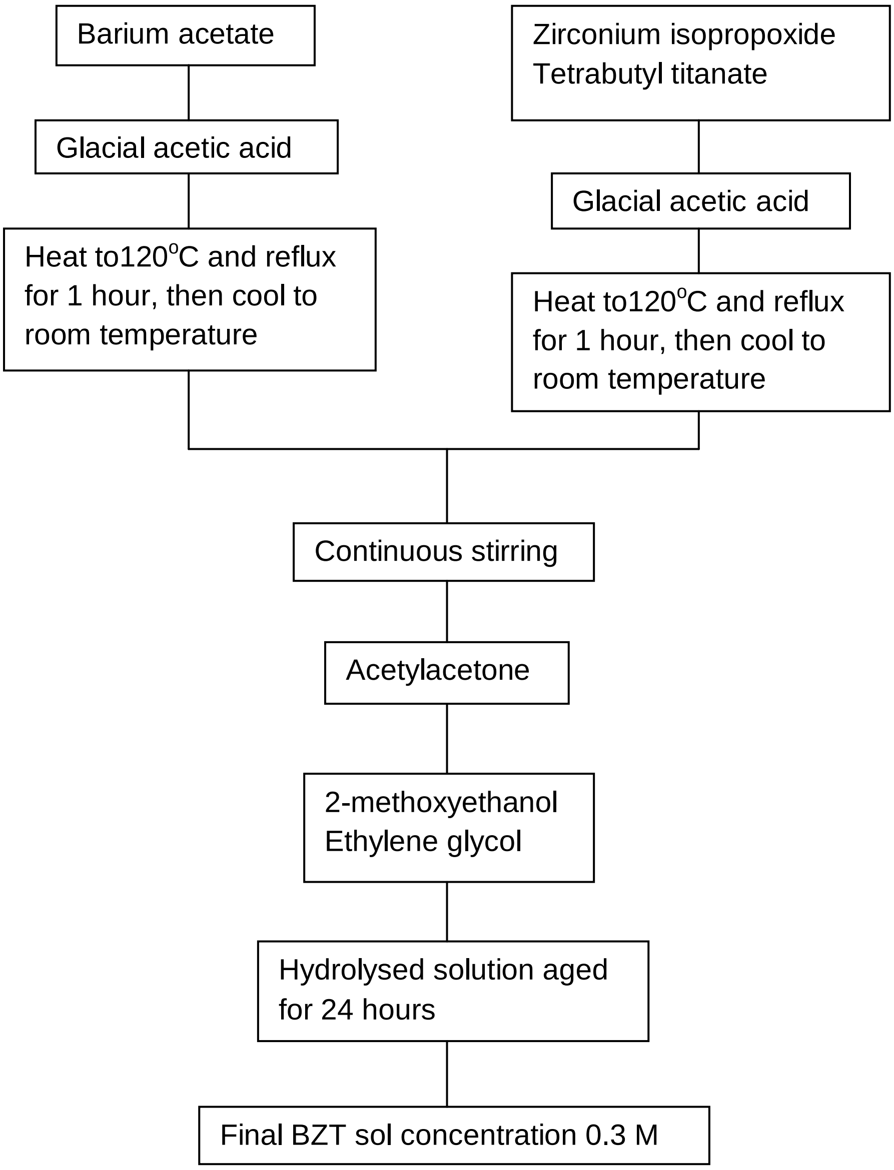

Figure A3.3 An alternative BZT sol synthesis route developed by Zhai *et al*. for the growth of $Ba(Zr_xTi_{1-x})O_3$ thin films [3.9].

In the case of work carried out by Gao *et al*. they looked at the growth of $Ba(Zr_{0.35}Ti_{0.65})O_3$ thin films prepared by sol-gel method [3.102]. The sol synthesis route selected was that shown in figure A3.4 in which acetylacetone, monoethyl ether and ethylene glycol were added to control the solution viscosity and cracking of films. The final BZT sol concentration was 0.05 M the lowest of those surveyed in the literature (cf. the highest of those surveyed 0.6 M). The target concentration of the BZT sols used in this work and detailed in the thesis was initially 0.3 M later reduced to 0.25 M to avoid cracking of films.

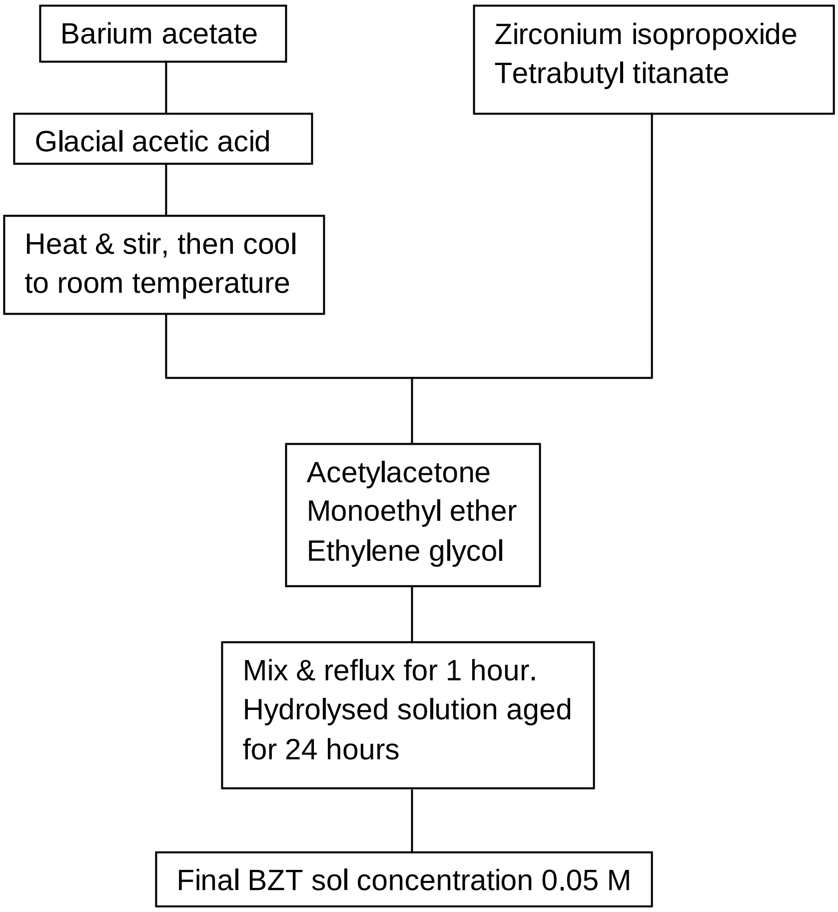

Figure A3.4 BZT sol synthesis route established by Gao *et al*. for the growth of $Ba(Zr_{0.20}Ti_{0.80})O_3$ thin films [3.102].

Cheng *et al*. developed and characterised $Ba(Zr_{0.05}Ti_{0.95})O_3$ thin films formed from the sol synthesised using the process shown in figure A3.5 [3.1]. Interestingly, the 2-methoxyethanol (extremely toxic) and acetylacetone were added to the Zr-Ti complex solution before being mixed with the barium acetate and acetic acid in order to improve the stability of the final sol. Also, no ethylene glycol had been added which would normally be introduced toward the end of the process to stabilise the solution and control cracking of the BZT films.

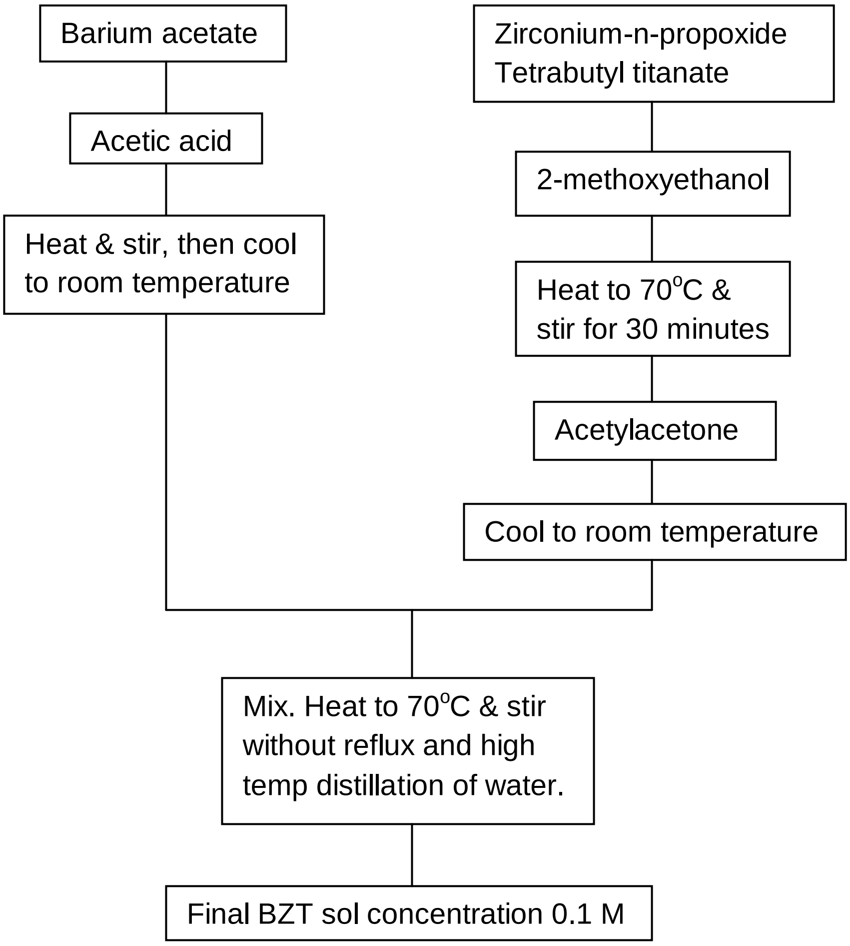

Figure A3.5 BZT sol synthesis route developed by Cheng *et al*. for the growth of $Ba(Zr_{0.05}Ti_{0.95})O_3$ thin films [3.1].

Appendix 4

Process Summary for Sol Batches BZT1 to BZT10 (Table 4.1)

Appendix 4 summarises the successes and failures of the various sol batches.

BZT1 (5/95): The concentration of sol was reduced from 0.3 M to 0.25 M to reduce the cracking and peeling of films (figure A4.1). The sol synthesis route chosen was successful for the BZT composition Ba($Zr_{0.05}Ti_{0.95}$)O_3 but failed to produce stable sols for compositions with higher Zr content (i.e. 0.20 and 0.35).

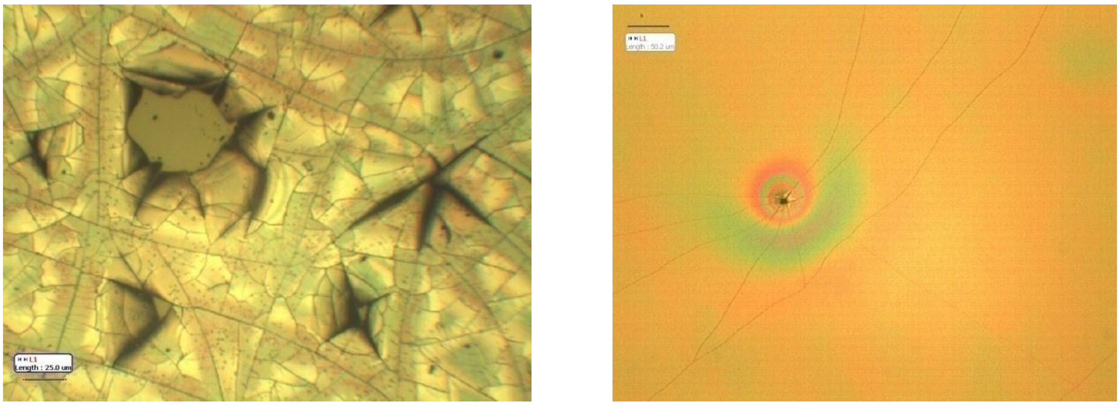

(a) Dimension bar 25 µm.

(b) Dimension bar 50 µm.

Figure A4.1 Optical images of (a) BZT film deposited from a 0.3 M concentration sol with evidence of substantial cracking and peeling, and (b) cracks propagating from a defect in the BZT film deposited from the lower concentration (0.25 M) sol. Areas on the wafer away from defects were crack free with no evidence of peeling.

BZT2 (20/80): Synthesis route the same as for BZT1 final solution but needed to add monoethanolamine (MEA) at the end of the process to reduce the viscosity and eliminate precipitation. This resulted in a change to the surface morphology of annealed thin films (figure A4.2), although no significant change to the crystalline structure was perceived.

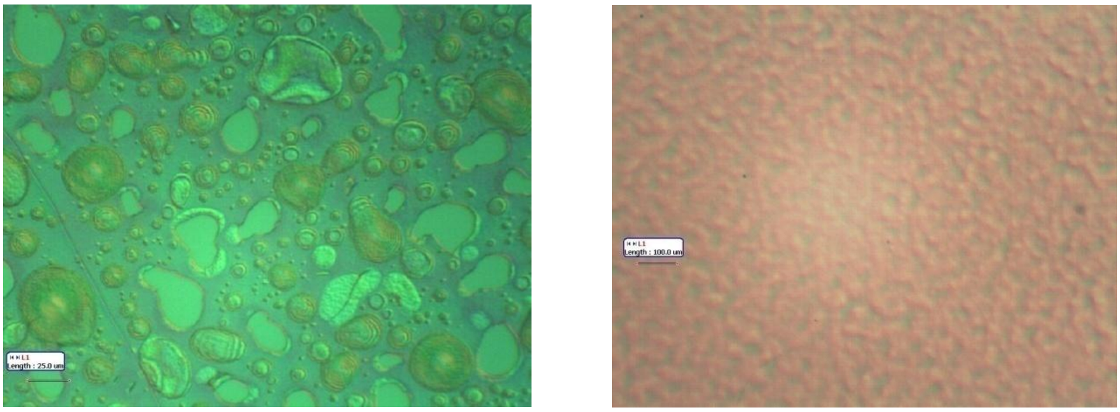

(a) Dimension bar 25 µm.

(b) Dimension bar 100 µm.

Figure A4.2 Optical images of the surface of $Ba(Zr_{0.20}Ti_{0.80})O_3$ thin films after (a) final anneal at 600°C by RTA for 3 minutes and (b) annealing at 600°C by RTA for 3 minutes after the 1st, 4th and 8th (final) spun layer.

BZT3 (5/95): Similar recipe to that of BZT1. After adding 10 ml of acetic acid to the Zr-Ti complex mixture, 2 ml of acetylacetone was added turning the solution yellow. Initially no ethylene glycol added. As a consequence, films cracked and peeled after annealing by RTA at low temperature (550°C) (figure A4.3a). Subsequently added 1 ml of ethylene glycol to the final solution which significantly reduced the cracking and eliminated the peeling (figure A4.3b).

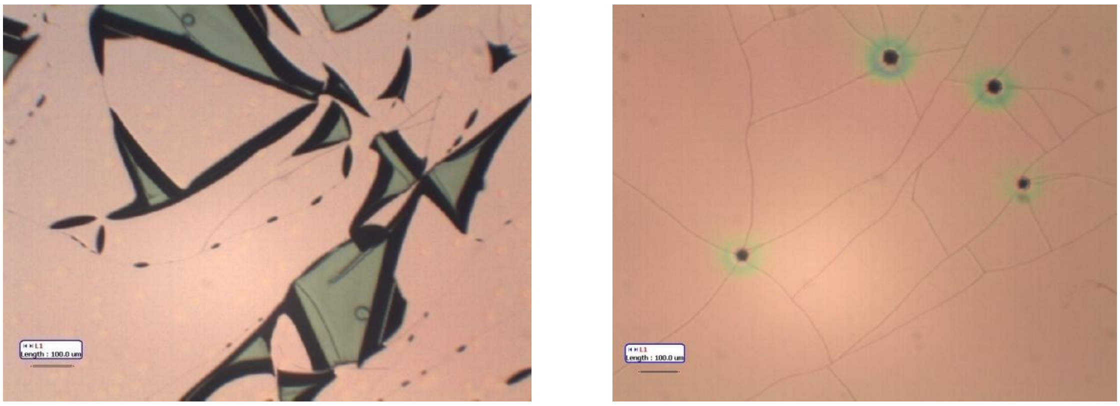

(a) Dimension bar 100 µm.

(b) Dimension bar 100 µm.

Figure A4.3 Optical surface images of films deposited from BZT3 sol (a) with no ethylene glycol added and (b) with 1 ml of ethylene glycol added to final solution.

BZT4 (35/65): Process route generally the same as for BZT3. After the Zr-Ti solution was added to the barium acetate solution the combined sol was heated and refluxed for 1 hour with continuous stirring. Cooled and stirred overnight. Final process step was to add 1 ml of ethylene glycol.

BZT5 (35/65): As for BZT4 but pure acetic acid used in place of glacial acetic acid. Also, no heating and reflux of the final solution performed. Lastly, 2 ml of ethylene glycol was added. The surface structure of the pre-annealed and crystallised BZT thin film produced from this sol is displayed in figure A4.4.

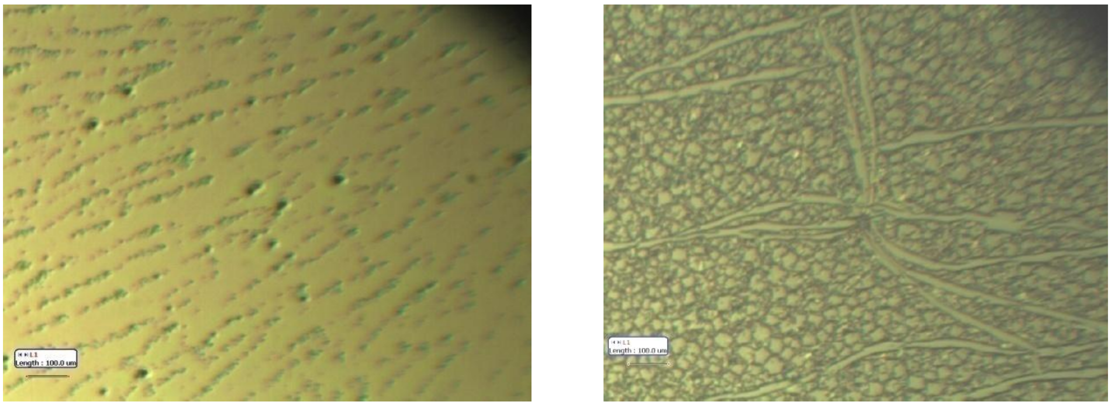

(a) Dimension bar 100 µm.

(b) Dimension bar 100 µm.

Figure A4.4 Optical surface images of BZT thin films deposited from sol BZT5 which contained a precipitate. The two images show the surface (a) before annealing and (b) after annealing at 650°C for 15 minutes on the hotplate followed by RTA at 700°C for 1 minute.

BZT6 (35/65): The same procedure was employed as for BZT3 sol except weights of starting materials were halved in a 25 ml solution to give 0.25 M concentration. A cloudy solution resulted as before. Water was then mixed with the final solution in the ratio 1:1 and 5 ml of ethylene glycol added. The final sol was heated to 70°C for approximately 10 minutes until the solution was clear. This resulted in a 50 ml solution of 0.125 M concentration.

BZT7 (5/95), BZT8 (20/80) and BZT9 (35/65): Modifications and improvements were made to the sol synthesis which culminated in successful batches for each of the three BZT compositions. This resulted in sols with no precipitation and that remained clear for several months of use. Further details of the modified process are given in sub-section 4.1.1 of this thesis.

BZT10 (95/5): This was an attempt to produce a sol with a very high Zr content [i.e. $Ba(Zr_{0.95}Ti_{0.05})O_3$] close to $BaZrO_3$ using the successful synthesis route formulated for sols BZT7-BZT9. The final solution was cloudy and viscous and no amount of stirring, heating and refluxing could dissolve the precipitation. Reducing the concentration from 0.25 M to 0.15 M by the addition of further quantities of acetic acid also failed to address the problem. Clearly an alternative synthesis route needs to be found. This should form part of a future work programme. Once a suitable route has been established, the synthesis of other BZT sols of compositions in the range $Ba(Zr_{0.50}Ti_{0.50})O_3$ to $BaZrO_3$ should also be investigated with a view to developing amorphous and crystalline BZT thin films for application to fixed value and tunable capacitors.